



University of
Salford
MANCHESTER

Design of a Swept-Wing High-Altitude Long-Endurance Unmanned Air Vehicle (HALE UAV)

by

Ahmad Abdulkarim Mahdi Alsahlani

A thesis submitted in partial satisfaction of the requirements for the degree of
Doctor of Philosophy

Supervisor:

Dr Thurai Rahulan

Co-supervisor

Dr Edmund Chadwick



School of Computing, Science & Engineering
Engineering Research Centre
University of Salford
Greater Manchester, United Kingdom
September-2017

TABLE OF CONTENTS

TABLE OF CONTENTS	I
LIST OF PUBLICATIONS AND PRIZES	IV
LIST OF TABLES	V
LIST OF FIGURES	VI
ACKNOWLEDGEMENTS	X
LIST OF SYMBOLS.....	XI
ABSTRACT	XV
1 INTRODUCTION	1
1.1 SOLAR AVIATION.....	2
1.2 THE FLYING WING.....	5
1.3 CHALLENGES OF FLIGHT AT HIGH ALTITUDE	7
1.3.1 Aerodynamic performance at low Reynolds number	8
1.3.2 Elastic Deformation.....	9
1.3.3 Stability.....	10
1.3.4 Power Requirements.....	11
1.4 AIMS AND OBJECTIVES	13
1.5 MOTIVATION FOR THE DESIGN MISSION	14
1.6 THESIS LAYOUT	15
1.7 ORIGINAL CONTRIBUTIONS.....	16
2 BACKGROUND AND LITERATURE REVIEW.....	17
2.1 EXISTING HIGH-ALTITUDE UAVS	17
2.1.1 Consumable-Fuel HA UAVs.....	19
2.1.2 Solar-Powered HA UAVs.....	20
2.2 HALE AIRCRAFT CONFIGURATIONS.....	22
2.3 AEROFOIL ISSUE	30
2.3.1 Aerofoil Selection.....	30
2.3.2 Aerofoil Shape Design.....	33
2.4 STRUCTURAL ANALYSES - WEIGHT PREDICTION ISSUES	35
2.5 AERODYNAMIC ANALYSIS	41
2.6 OPTIMISATION ALGORITHMS	43
2.7 SOLAR POWERED AIRCRAFT SIZING.....	44
2.8 STABILITY & CONTROL OF FLYING WING AIRCRAFT	46
2.9 OVERVIEW	47
3 METHODOLOGY FRAMEWORK.....	49
3.1 OVERALL DESIGN PROCEDURE.....	49
3.2 CONCEPTUAL DESIGN TOOL	51
3.3 AEROFOIL DESIGN & SELECTION.....	51
3.4 PRELIMINARY DESIGN TOOL.....	52
3.4.1 Aerodynamic Solver (Quasi 3DM).....	53
3.4.2 Composite Structure Model.....	54
3.4.3 Optimisation tool	56

4	CONCEPTUAL DESIGN OF SP HALE UAVS.....	57
4.1	POWER FOR LEVEL FLIGHT (PLEV).....	58
4.2	POWER MANAGEMENT.....	59
4.3	MASS ESTIMATIONS MODELS.....	60
4.3.1	Structure Mass Prediction.....	60
4.3.2	Mass of the Solar cells.....	61
4.3.3	Mass of the Maximum Power Point Tracker.....	61
4.3.4	Mass of the Storage System.....	62
4.3.5	Mass of the Propulsion Group.....	63
4.3.6	Mass of the Avionics and Landing Gear.....	64
4.3.7	Gross Weight of Aircraft.....	64
4.3.8	Aerodynamic Performance Estimation.....	66
4.4	VALIDATING THE CONCEPTUAL DESIGN MODEL.....	73
4.5	AVAILABLE SOLAR RADIATION AT HIGH ALTITUDES.....	75
4.6	STUDY OF THE MISSION REQUIREMENTS ON THE DESIGN OF SOLAR-POWERED HALE UAV.....	78
4.6.1	Availability of Solar Energy in Iraq.....	78
4.6.2	The Influence of the Reference Altitude, Latitude and Duration.....	82
4.6.3	Aerodynamic Performance study.....	88
4.6.4	Payload Requirement Study.....	91
4.6.5	Conclusion.....	91
5	AERODYNAMIC ANALYSIS.....	94
5.1	TORNADO VORTEX LATTICE METHOD.....	95
5.2	TWO-DIMENSION INVISCID/VISCOUS MODEL (IVM).....	96
5.2.1	Inviscid Model (2D Panel Method).....	97
5.2.2	Viscous Model (Integral boundary layer).....	97
5.2.3	The Code IVM.....	102
5.2.4	Validating the 2D Inviscid/Viscous Model (IVM).....	104
5.3	QUASI-THREE-DIMENSIONAL AERODYNAMIC SOLVER.....	109
5.3.1	Validation of the Quasi-Three-Dimensional Aerodynamic Solver.....	113
6	COMPOSITE STRUCTURE MODEL.....	116
6.1	COMPOSITE WING SIZING APPROACH.....	116
6.1.1	Non-spar Elements Estimation.....	119
6.1.2	Spar Sizing Approach.....	119
6.2	FINITE BEAM ELEMENT.....	124
6.3	CRITICAL DESIGN LOADS.....	127
6.4	STATIC AERO-ELASTIC MODELLING.....	128
6.5	VALIDATING THE STRESS ANALYSIS AND DEFORMATION.....	131
6.6	VALIDATING THE WEIGHT ESTIMATION MODEL.....	133
7	AEROFOIL SELECTION.....	140
7.1	EXISTING AEROFOILS FOR FLYING WING AIRCRAFT.....	140
7.2	AEROFOIL SHAPE OPTIMISATION TOOL.....	143
7.2.1	Aerofoil Shape Parameterisation.....	143
7.2.2	The aerodynamic solver.....	146
7.2.3	Problem formulation.....	147
7.3	THE NEWLY DESIGNED AEROFOILS.....	148
7.4	CFD MODELS.....	152
7.4.1	The Aerodynamic Performance of ZMR-17.....	153
7.4.2	Laminar Bubbles.....	158
7.4.3	Flow Aspect at Stall Areas.....	158

8	CONCEPTUAL AND PRELIMINARY DESIGN OF SUMER UAV	164
8.1	CONCEPTUAL DESIGN OF SUMER.....	164
8.2	PRELIMINARY DESIGN OF SUMER	169
8.2.1	Aircraft layout and its Components	170
8.2.2	The Static Stability Parameters.....	172
8.2.3	Optimisation Tool.....	176
8.2.4	Required Sweep.....	182
8.3	THE DESIGN CASES.....	184
8.3.1	Optimisation Results – Aerodynamic Only (AerO series).....	187
8.3.2	Optimisation results - Static Aeroelasticity (AerEl series)	191
8.3.3	Concluding Remarks from the Design Cases	203
8.4	FINAL DESIGN.....	204
8.4.1	Final Design of SUMER.....	207
8.4.2	Performance at Different Flight Speeds.....	210
8.4.3	Assessment of the performance of SUMER	213
8.4.4	CFD Validation of the Design of SUMER	216
9	OVERALL DISCUSSION	224
9.1	CONCEPTUAL DESIGN TOOL	224
9.2	AEROFOIL SHAPE OPTIMISATION	225
9.3	PRELIMINARY DESIGN TOOLS	226
9.4	DESIGN AN AFT-SWEPT FLYING WING (HALE UAV).....	227
10	CONCLUSIONS AND RECOMMENDATIONS.....	229
10.1	CONCLUSIONS	229
10.2	RECOMMENDATIONS	230
10.2.1	Recommendations for the Developed Tools	230
10.2.2	Recommendations for the Design Procedure	231
11	APPENDICES	233
	APPENDIX I: OPTIMISER CODE (CANONICAL GENETIC ALGORITHM)	233
	I-1 Canonical Genetic Algorithm (CGA).....	233
	I-2 The Optimiser Code	236
	APPENDIX II: CONCEPTUAL DESIGN TOOL	238
	APPENDIX III: PANEL METHOD	241
	APPENDIX IV: THE 2D INVISCID-VISCOUS AERODYNAMIC MODEL (IVM)	245
	APPENDIX V SPAR SIZING	253
12	REFERENCES	266

LIST OF PUBLICATIONS AND PRIZES

Conference papers

1. Alsahlani, A., L.J. Johnston, and P.A. Atcliffe, "Design of a High Altitude Long Endurance Flying-wing Solar-Powered Unmanned Air Vehicle", 6TH European Conference for Aeronautics and Space Sciences (EUCASS2015). 2015, EUCASS: Krakow, Poland.
2. Alsahlani, A., T. Rahulan, and N. Abdulhassan, "Composite Structural Analysis of a High Altitude, Solar Powered Unmanned Aerial Vehicle", International Conference on Aerospace Engineering (ICOAE 2016). 2016, Embry-Riddle Aeronautical University, Bauman Moscow State Technical University and Science an Engineering Institute: Moscow, Russia.
3. Alsahlani, A. and T. Rahulan, "Aerofoil Design for Unmanned High-Altitude Flying-Wings", Applied Aerodynamics Conference. 2016, The Royal Aeronautical Society: Bristol / UK.
4. Alsahlani, A. and T. Rahulan. "Design of a High Altitude Long Endurance Flying-wing Solar-Powered Unmanned Air Vehicle", CSE 2016 Annual PGR Symposium (CSE-PGSym 16). 2016. Salford, UK: University of Salford
5. Alsahlani, A. and T. Rahulan, "Weight Estimation of a Conceptual Wing for a High Altitude, Solar Powered Unmanned Aerial Vehicle", in 5th Aircraft Structural Design Conference 2016, The Royal Aeronautical Society: Manchester / UK.
6. Alsahlani, A. and T. Rahulan. "The impact of altitude, latitude, and endurance duration on the design of a high altitude, solar powered unmanned aerial vehicle". International Conference for Students on Applied Engineering (ISCAE), IEEE. 2016. Newcastle / UK: IEEE.
7. Alsahlani, A. and T. Rahulan. "Conceptual and Preliminary Design Approach of A High Altitude, Long Endurance Solar-Powered UAVs". In CSE Annual PGR Symposium (CSE-PGSym 17). 2017. Salford, UK: University of Salford
8. Alsahlani, A. and T. Rahulan. "The Influence of Spar Location on the Elastic Deformation and the Weight Estimation of a Swept-back, High Altitude, Solar Powered Flying Wing UAV" accepted at the 7TH European Conference for Aeronautics and Space Sciences (EUCASS2017), Milano, Italy

Journal papers

1. Alsahlani, A., L.J. Johnston, and P.A. Atcliffe. "Design of a High Altitude Long Endurance Flying-wing Solar-Powered Unmanned Air Vehicle". Progress in Flight Physics, EDP Sciences, Volume 9 (2017) page 3-24.
2. Alsahlani, A., T. Rahulan, and N. Abdulhassan, "Composite Structural Analysis of a High Altitude, Solar Powered Unmanned Aerial Vehicle". International Journal of Mechanical Engineering and Robotics Research, IJMERR, 2017. 6(1): p. 71-76.
3. Alsahlani, A. and T. Rahulan, "Aerofoil Design for Unmanned High-Altitude Aft-swept Flying-Wings", Journal of Aerospace Technology and Management, accepted in April 2017.
4. Alsahlani, A. and T. Rahulan. "A Mathematical Model of a Conceptual Design Approach of High Altitude Solar Powered Unmanned Aerial Vehicles", International Review of Aerospace Engineering Journal, Volume10, No.4, September 2017.

Posters

1. "Aerodynamic Challenges in the Design and Operation of A High-Altitude, Long-Endurance UAV", in SPARC 2015 from University of Salford
2. "Design of a High Altitude, Long Endurance, Flying-wing Solar-Powered UAV", 6TH European Conference for Aeronautics and Space Sciences (EUCASS2015). 2015, EUCASS: Krakow, Poland.

Prizes awarded

1. The best Student Paper Award from the 6th European Conference for Aeronautics and Space Sciences EUCASS 2015. Poland 2015
 2. The best Poster award in SPARC 2015 from University of Salford.
 3. The best Paper Award from the CSE PGR Symposium 2016 in University of Salford.
 4. The best paper award from The International Conference for Students on Applied Engineering ICSAE, Newcastle UK 2016
 5. The runner-up of the best paper prize in the CSE PGR Symposium 2017 in University of Salford
-

LIST OF TABLES

Table 2-1 Number of existing HA UAVs.....	18
Table 2-2 Summary of the typical aerofoil characteristics for different aircraft configurations	31
Table 2-3 Comparison of the CFD methods, from (Jan Mariens, 2012)	41
Table 4-1 The constant parameters of the design	71
Table 4-2 The characteristics of SHAMPO.....	74
Table 4-3 Validation result of SHAMPO	75
Table 4-4 Constants definitions of the solar radiation model (Min Chang et al., 2014).....	78
Table 4-5 Starting dates and Endurance of Missions	79
Table 4-6 Available solar energy and daytime hours at different altitudes at a latitude of 32°	79
Table 4-7 Available Solar Energy and daytime hours at Different Latitudes.....	81
Table 4-8 The fixed mission and aerodynamic performance parameters	82
Table 5-1 Aerofoils used in the validation of the IVM.....	104
Table 5-2 Drag analysis obtained by IVM and Xfoil	104
Table 5-3 Three Experimental cases for the Quasi-3DM validation	113
Table 5-4 Error analysis of the Quasi-3DM for the swept wing (45 degree sweep-case 1)	114
Table 5-5 Error analysis of the Quasi-3DM for the tapered wing (case 2).....	114
Table 5-6 Error analysis of the Quasi-3DM for the swept tapered wing (case 3)	114
Table 6-1 Lamina properties defined by ANSYS.....	131
Table 6-2 Validation results of the composite structural model	132
Table 6-3 Helios P03 Configurations	133
Table 6-4 Weight estimation for the Helios P03	134
Table 6-5 The properties of epoxy carbon T800/M18 (Montagnier & Bovet, 2010)	135
Table 6-6 Plies Stacking in Each Wing-box Station.....	137
Table 7-1 Number of flying wing aerofoils, at $Re = 5 \times 10^5$, evaluated by Xfoil	141
Table 7-2 Aerodynamic performance of the new aerofoils	148
Table 8-1 The mission requirement of the case study SUMER.....	166
Table 8-2 The main characteristics of the SUMER.....	168
Table 8-3 Design cases when only aerodynamic performance factors are considered.....	184
Table 8-4 Design cases when aeroelastic effects are considered.....	186
Table 8-5 Aerodynamic performance at trim condition for varying wing sweep angles for AerO cases	187
Table 8-6 Aerodynamic performance at trim condition for varying static margin for AerO cases	189
Table 8-7 Aerodynamic performance at trim condition for varying spar locations for AerEl cases	192
Table 8-8 Aerodynamic performance at trim condition for varying static margin for AerEl cases.....	196
Table 8-9 Aerodynamic performance at trim condition for varying wing sweep angles for AerEl cases	199
Table 8-10 Aerodynamic performance at trim condition for varying spar locations for AerEl cases	204
Table 8-11 The weight of the spar and non-spar elements of the SUMER	208
Table 8-12 Plies stacking at each spar section in the semi-span of SUMER.....	208
Table 8-13 Results achieved by the design stages	214

LIST OF FIGURES

Figure 1-1 Timeline of solar cell efficiency since 1976	2
Figure 1-2 Solar Impulse-2 aircraft	3
Figure 1-3 Some Significant Flying-Wing Aircraft.....	5
Figure 1-4 X-HALE UAV (Jones & Cesnik, 2015)	6
Figure 1-5 Pathfinder Plus UAV	7
Figure 1-6 The elastic twist due to pure up-bending load of the swept flying wing.....	10
Figure 1-7 Typical solar powered aircraft system	12
Figure 1-8 Marshes of Iraq	14
Figure 2-1 Notable consumable-fuel HA UAVs HA UAVs.	19
Figure 2-2 Timeline of Aero-Vironment / NASA prototypes (Noll et al., 2004)	21
Figure 2-3 NASA Helios P03 UAV	21
Figure 2-4 Qinetiq Zephyr UAV	21
Figure 2-5 Facebook’s Aquila UAV	22
Figure 2-6 The four configurations considered in (Zdobysław et al., 1999).	23
Figure 2-7 Comparison of PW configurations presented in (Goraj et al., 2004).	23
Figure 2-8 Rectangular braced-wing configuration in (Baldock & Mokhtarzadeh, 2006).....	24
Figure 2-9 Number of configurations studied by NASA (Craig L. Nickol 2007)	25
Figure 2-10 Metric results for the solar-powered configurations of NASA’s study (Craig L. Nickol 2007)..	25
Figure 2-11 SHAMPO Configuration in (E. Cestino et al., 2007)	26
Figure 2-12 HELIPLAT Configuration in (E. Cestino et al., 2007)	27
Figure 2-13 Configurations Considered in (Rizzo & Frediani, 2008)	28
Figure 2-14 Optimal Configuration in (Mattos et al., 2013).....	28
Figure 2-15 Baseline geometry adopted in (Morrisey, 2009).....	29
Figure 2-16 X-HALE Concept (Ref. https://www.umich.edu/)	29
Figure 2-17 Structure of laminar separation bubble	32
Figure 2-18 Aerofoil performance at different Reynolds numbers (John & Michael, 1980)	32
Figure 2-19 PARSEC Variable Definition in (Della Vecchia et al., 2014).	34
Figure 2-20 Aerofoil geometry and Bezier control points defined by twelve parameters presented in (P. Salunke et al., 2014).....	34
Figure 2-21 Sketch of the Structural Wing Model in (Ajaj et al., 2013; Seywald, 2011).....	36
Figure 2-22 Structures Module Running in Self-Design Mode (Seywald, 2011).....	37
Figure 2-23 Wing structural of Helios.....	38
Figure 2-24 wing structural of Heliplat (G. Frulla & Cestino, 2008)	38
Figure 2-25 Wing configuration of X-HALE (Cesnik et al., 2010).....	39
Figure 2-26 Wing configuration (Montagnier & Bovet, 2010)	40
Figure 2-27 Comparison of the Quasi 3D method with experimental data and a high order CFD, conducted in (Jan Mariens, 2012)	42
Figure 3-1 Overall design procedure	50
Figure 3-2 Concept of the quasi-three-dimensional aerodynamic solver	53
Figure 3-3 The concept of the 2D Inviscid/Viscous Model (IVM) for the aerofoil	54
Figure 3-4 Overview of the composite structure model	55
Figure 3-5 Optimisation flow	56
Figure 4-1 Fuel Cell Subsystem, Including Storage of Reactant Gases in the Wing Spar (Colella & Wenneker, 1994).....	63
Figure 4-2 Drag coefficient of ZMR-17 at maximum Lift/Drag versus Reynolds number	68
Figure 4-3 The design space of the conceptual design model	71
Figure 4-4 Overview of the conceptual design approach	72

Figure 4-5 External view of SHAMPO (E. Cestino et al., 2007)	73
Figure 4-6 The design space of SHAMPO	75
Figure 4-7 Dissipation of the beam radiation energy through the atmosphere, number obtained from (Rizzo & Frediani, 2008)	77
Figure 4-8 Map of Iraq	79
Figure 4-9 Solar irradiance per unit area and daytime hours versus time, for different altitudes at 32° latitude	80
Figure 4-10 Solar irradiance per unit area and daytime hours versus time for different latitude at 17 km altitude	81
Figure 4-11 Density and dynamic viscosity of air versus altitude	82
Figure 4-12 Effect of the flight altitudes on gross weight, corresponding wingspan, wing aspect ratio, the ratio of solar cells area and operational Reynolds number for different flight durations. At latitude= 31.01°.	83
Figure 4-13 The effect of the reference altitude on the weight estimation for the durations	84
Figure 4-14 Effect of the flight latitudes on gross weight, corresponding wingspan, wing aspect ratio and the ratio of solar cells area for different flight durations, altitude=17 km	86
Figure 4-15 The effect of the reference latitude on the weight estimation for the durations	87
Figure 4-16 Effect of the reference lift coefficient on the aircraft weight and on its main configurations, latitude=31.01°, altitude=17 km, for Duration 2, span efficiency=0.95, payload=100kg, payload power=1250 W	89
Figure 4-17 Effect of the span efficiency on the optimal aircraft weight and on its main configurations, latitude=31.01°, altitude=17 km, for Duration 2, CL_{ref} =0.85, payload=100 kg, payload power=1250 W....	90
Figure 4-18 Effect of the payload weight on the optimal aircraft weight and on its main configurations, latitude=31.01°, altitude=17 km, for Duration 2, CL_{ref} =0.85, span efficiency=0.95, power of payload=0...	92
Figure 4-19 Effect of the power of payload on the optimal aircraft weight and on its main configurations. CL_{ref} =0.85, span efficiency=0.95, payload=100 kg	93
Figure 5-1 Procedure of the Quasi 3D Aerodynamic model	95
Figure 5-2 The lifting surface and the horseshoe vortex layout for the Vortex Lattice Method.....	96
Figure 5-3 Discretization of an Aerofoil Contour into Panels	97
Figure 5-4 The definition of the displacement and the momentum thicknesses (Wauquier, 2009)	99
Figure 5-5 The conception of entrainment (Moran, 2003)	101
Figure 5-6 Sample of the IVM prediction for NACA0012, $Re = 1.44 \times 10^6$, 16 degrees AoA	103
Figure 5-7. IVM validation with Xfoil and experimental data for NACA-1408 Aerofoil, $Re = 6 \times 10^6$	106
Figure 5-8. IVM validation with Xfoil and experimental data for NACA-0012 Aerofoil, $Re = 1.44 \times 10^6$	107
Figure 5-9. IVM validation with Xfoil and experimental data for S7055 Aerofoil, $Re = 0.3 \times 10^6$	108
Figure 5-10 Procedure of the Quasi-3DM	109
Figure 5-11 Aerofoil section perpendicular to the sweep line of a tapered wing	110
Figure 5-12 Angles and Forces Present in the Quasi-3D Method	111
Figure 5-13 Steps to finding the effective angle of attack (α_{eff}) and profile drag	112
Figure 5-14 Validation results of the Quasi 3DM with the three experimental cases	115
Figure 6-1 Sketch of the Structural Wing Model and Wing-box Idealization	116
Figure 6-2 Overview of the wing sizing methodology	118
Figure 6-3 Layout of the spar partition (wing box)	120
Figure 6-4 Wing-box cross-section loading	121
Figure 6-5 Cross-section design methodology	123
Figure 6-6 Structural wing model.....	124
Figure 6-7 Planar beam element and the degrees of freedom.....	125
Figure 6-8 Local and global coordinate system.....	127
Figure 6-9 Elastic vertical deflection as a function of dihedral angles	129
Figure 6-10 Twist distribution pattern in Tornado VLM	129
Figure 6-11 Schematic of the aeroelastic coupling adopted in the CSM.....	130
Figure 6-12 Fixed Cantilever wing-box Subjected to Shear-bending and Pure Torsion	131
Figure 6-13 Directional deflections under pure torsion and bending-shear force evaluated by ANSYS	132

Figure 6-14 NASA Helios P03 HALE UAV (Noll et al., 2004)	133
Figure 6-15 The partitions of the spar	135
Figure 6-16 Weight distribution along the chord-wise direction.....	136
Figure 6-17 The force balance along the semi-span of Helios P03	136
Figure 6-18 The effect of spar height/width ratio on the weight and the elastic deformation under the critical loads at a load factor of 3	138
Figure 6-19 The critical load distributions and the spar deflections at a load factor of 3.....	139
Figure 7-1 Effect of the maximum thickness on the aerodynamic performance for the symmetrical 4-digit NACA aerofoils, obtained by Xfoil.....	142
Figure 7-2 Aerofoil shape optimisation flow.....	143
Figure 7-3 Bezier-Curve for Thickness Distribution.....	144
Figure 7-4 PARSEC parametrization for camber line	145
Figure 7-5 Generated aerofoil from the Bezier and PARSEC parameters	146
Figure 7-6 Aerodynamic performance of the newly designed aerofoils, $Re = 0.5 \times 10^6$	150
Figure 7-7 Aerodynamic performance of the newly designed aerofoils, $Re = 0.5 \times 10^6$	151
Figure 7-8 The schematic of a partial domain of ZMR-17	153
Figure 7-9 The aerodynamic performance of ZMR-17 at $Re=0.5 \times 10^6$	156
Figure 7-10 The aerodynamic performance of ZMR-17 at $Re=0.9 \times 10^6$	157
Figure 7-11 Velocity contour and vector obtained by the transition models for ZMR-17, $Re=0.5 \times 10^6$	159
Figure 7-12 Velocity contour and vector obtained by the transition models for ZMR-17, $Re=0.9 \times 10^6$	160
Figure 7-13 Stream lines around ZMR-17 at different angles of attack using transition SST $k-\omega$ model	161
Figure 7-14 Stream lines around ZMR-17 at different angles of attack using transition $k-kl-\omega$ model.	162
Figure 7-15 Stream lines around ZMR-17 at different angles of attack using Spalart-Allmaras model.....	163
Figure 8-1 Solar irradiance per unit area and daytime hours versus days, for 31.01° latitude at 17 km altitude	166
Figure 8-2 The design space for the given mission requirements of the SUMER.....	167
Figure 8-3 The weight distribution of SUMER.....	168
Figure 8-4 Initial layout of the SUMER.....	171
Figure 8-5 The front-side view of half wing of the SUMER and its weight distribution along the semi-spanwise direction.....	172
Figure 8-6 The weight distribution along the chordwise direction of the SUMER	172
Figure 8-7 Representations of aerodynamic parameters.....	175
Figure 8-8 Optimisation flow	178
Figure 8-9 Manufactured twist distribution pattern.....	179
Figure 8-10 Effect of number of spanwise and chordwise panels on the coefficients of lift, induced drag and pitching moment about the $0.25x/c$ root axis.....	181
Figure 8-11 Optimisation flow for the AerO cases.....	185
Figure 8-12 Optimal manufactured twist distribution and aerodynamic performance parameters for the cases AerO at varying wing sweep angles: static margin=0.05	188
Figure 8-13 Optimal manufactured twist distribution and aerodynamic performance parameters for the cases AerO at varying static margin values: sweep angle= 9°	190
Figure 8-14 Optimal manufactured twist distribution and aerodynamic performance parameters for the cases AerEl at varying spar locations: sweep angle= 9° , static margin=0.05.....	193
Figure 8-15 Elastic twist deformation, respect to the flow direction, for the cases AerEl at varying spar locations: sweep angle= 9° , Static margin=0.05.....	194
Figure 8-16 Elastic vertical deflections for the cases AerEl at varying spar locations: sweep angle= 9° , static margin =0.05	195
Figure 8-17 Optimal manufactured twist distribution and aerodynamic performance parameters for the cases AerEl at varying static margin values: sweep angle= 9° , spar locus= $0.35 x/c$	197
Figure 8-18 Elastic deformations, respect to the flow direction, for the cases AerEl at varying static margin study: sweep angle= 9° , spar locus = $35\% x/c$	198

Figure 8-19 Optimal manufactured twist distribution and aerodynamic performance parameters for the cases AerEl at varying wing sweep angles: static margin=0.05, spar locus= 0.35 x/c	200
Figure 8-20 Elastic twist deformation, respect to the flow direction, for the cases AerEl at varying sweep angles: spar locus= 0.35 x/c, static margin=0.05	201
Figure 8-21 Elastic vertical deflection for the cases AerEl at varying sweep angles: spar locus= 0.35 x/c, static margin=0.05	202
Figure 8-22 Optimal manufactured twist distribution and aerodynamic performance parameters for the cases AerEl at varying spar locations: static margin=0.05, sweep=8°	205
Figure 8-23 Elastic deformation for the cases at varying spar locations: sweep angle=8°, static margin=0.05	206
Figure 8-24 Local lift distribution along spanwise direction at varying angles of attack	207
Figure 8-25 Computerised rendering of the SUMER in cruise condition	209
Figure 8-26 Aerodynamic performance parameters for the final case (AerEl 08-05-34) at varying airspeeds:	211
Figure 8-27 Elastic deformation for the final case at varying flight speeds	212
Figure 8-28 The aerodynamic efficiencies of the SUMER at different angles of attack, airspeed=30.53 m/s, altitude 17km.....	214
Figure 8-29 Front-side of the wing shapes in flight at angles of attack 0 and 10 degrees	216
Figure 8-30 Orthogonal view fluid domain and wing grid	218
Figure 8-31 Comparison of the aerodynamic performance obtained from Quasi-3DM and CFD	219
Figure 8-32 Pressure contours of the upper and lower surfaces of SUMER at varying angles of attack	220
Figure 8-33 Transition points predicted by the Quasi-3DM at varying angles of attack.....	222
Figure 8-34 Upper surface transition line obtained by Quasi-3DM and CFD at AoA= 6.91°	222
Figure 8-35 Turbulent intensity contours of the upper and lower surfaces of SUMER at varying angles of attack	223
Figure 11-1 Discretization of an aerofoil contour into panels	241
Figure 11-2 The components of the velocity induced at a point due to the sources (Houghton & Carpenter, 2003).....	242
Figure 11-3 The components of the velocity induced at a point due to the vortices (Houghton & Carpenter, 2003).....	243
Figure 11-4 Enclosed area of the cross-section contour	253
Figure 11-5 Stress system of a ply respect to the 1-2 axis.....	254
Figure 11-6 Stress system of a ply respect to the coordinate system.....	255
Figure 11-7 Laminate plate geometry	256
Figure 11-8 The distance (z_p) between the neutral axis and the point on the ply	258

ACKNOWLEDGEMENTS

I am greatly indebted to the Higher Committee for Education Development (HCED-IRAQ), the Ministry of Higher Education & Scientific Research and the University of Basrah in Iraq for supporting my study. Also, special thanks to the entire team of the University of Salford for making possible this research.

I gratefully acknowledge Dr Leslie Johnston, who was my supervisor but sadly he passed away during the second year of my study, for offering me such an amazing subject and supporting me by invaluable advice and recommendations.

Special thanks to Dr Thurai Rahulan, my supervisor, for his support and counselling throughout the last year of my study. His guidance and thoughtful criticism have provided the confidence and incentive necessary to accomplish this research. Also additional thank goes to my co-supervisor Dr Edmund Chadwick.

Special thanks to my colleagues David Monk and Peter Morgan, who always supported me with assistance and helpful accompany.

My sincere gratitude is to my wife W. Alsaad for her sacrifices and patient. Without her support, I would have been quite far from completing this thesis. Also, a great thank goes to my wonderful children; Zainb, Manar and Ridha.

I would like to express my special respects and thanks to my parents, for their prayers and loves which have always been there for me. Many thanks to my brothers and sisters and all my friends.

Ahmad Alsahlani

LIST OF SYMBOLS

A_{sc}	m^2	Area of solar cells
A_{en}	m^2	Enclosed area of the wing spar cross-section
A_{ij}, a_{ij}	-	Laminate extensional stiffness matrix and its inverse respectively
AR	-	Wing aspect ratio
a_{pa}, b_{pa}, c_{pa}	-	Coefficients used with PARSEC parametrisation
a_{en}	m	Height of enclosed area of the spar section
B_{ij}, b_{ij}	-	Laminate coupling stiffness element (N) and its inverse respectively
b	m	Wingspan
b_1, b_2, b_3, b_4	-	Aerofoil parameters for the Bezier curve
b_{en}	m	Width of enclosed area of the spar section
b_f	m	Width of the flange
b_w	m	Height of the web
C_f	-	Skin friction drag coefficient
C_D	-	Whole aircraft drag coefficient
C_L	-	Aircraft lift coefficient
C_M	-	Aircraft pitching moment coefficient
C_{M0}	-	Zero-lift pitching moment coefficient
C_d	-	Aerofoil drag coefficient
C_l	-	Aerofoil lift coefficient
C_m	-	Aerofoil pitching moment coefficient
C_{av}	m	Mean geometric chord
C_r	m	Root chord
c	m	Wing local chord
dh_i	degree	Dihedral angle at wing partition
D_{ij}, d_{ij}	-	Laminate bending stiffness matrix and its inverse respectively
D, d	N	Total and local drag force components respectively
E	N/m^2	Young modulus
E	m/s	Entrainment velocity
E_1, E_2	N/m^2	Elastic constants in the direction of 1 and 2 ply axis respectively
EA_y	N	Axial stiffness in the y direction of the spar
EI_x, EI_z	$N.m^2$	Bending rigidity equivalent in the x and z directions respectively
E_{day}	J	Available solar energy
$E_{elec tot}$	J	Daily total electric energy requirement
e	-	Span efficiency
F_{sh}	N	Shear force
FoS	-	Factor of safety
G	N/m^2	Shear modulus
GJ	$N.m^2$	Torsional rigidity stiffness
G_{12}	N/m^2	Shear modulus in the 1-2 ply axis plane
g	m/s^2	Acceleration due to gravity
H	-	Shape factor (boundary layer equation)
H_1	-	Factor which is a function of H (boundary layer equation)
h_c	m	Local outer height of the spar
I_0	W/m^2	Local radiation intensity
I_{sc}	W/m^2	Solar constant

I_{diff}	W/m ²	Diffused solar radiation
I_{dir}	W/m ²	Direct solar radiation
I_{max}	W/m ²	Maximum irradiance during daytime
I_{tot}	W/m ²	Total solar radiation
K_{aer}	-	Constants used to evaluate profile drag of aerofoil
K_{Glob}	-	Global stiffness matrix
K_{Pav}	W/kg	Power to mass factor of avionics
K_{af}	-	Structural mass constant
K_{av}	-	Avionics weight fraction
K_{enc}	kg/m ²	Mass density of encapsulation
K_{fc}	J/kg	Energy density of fuel cell
K_{lg}	-	Landing gear weight fraction
K_{loc}	-	Local stiffness matrix
K_{mppt}	kg/W	Mass to power factor of the maximum power point tracker
K_{prop}	kg/W	Mass to power factor of the propulsion system
K_{sc}	kg/m ²	Fixed thickness mass density of solar cells
L	-	Correlation equation defined as $L = Re \theta U_e \frac{c_f}{2}$
L, l	N	Total and local lift force component respectively
l_{pa}	m	Length of spar segment
M	Nm	Bending moment
m	kg	Aircraft mass
m_{av}	Kg	Mass of avionics systems
m_{fc}	kg	Mass of fuel cells
m_{lg}	Kg	Mass of the landing Gear
m_{mppt}	Kg	Mass of the Maximum Power Point Tracker
m_{prop}	Kg	Mass of the propulsion system
m_{sc}	kg	Mass of the solar cells
m_{LE}	Kg	Leading edge mass
m_{TE}	Kg	Trailing edge mass
m_{af}	kg	Structural mass
m_{cov}	Kg	Structural skin (covering) mass
m_{non_sp}	Kg	Mass of the non-spar elements
m_{par}	Kg	Mass of the spar segment
$m_{payload}$	kg	Payload
m_{rip}	Kg	Mass of the ribs
m_{spar}	Kg	Total mass of the spar
$P_{elec\ tot}$	W	Daily total electric power consumption
P_{lev}	W	Mechanical power required for level flight
P_{pld}	W	Payload power rating
p	N/m ²	Air pressure
p_1, p_2, p_3, p_4, p_5	-	PARSEC curve parameters for the aerofoil
Q_{ij}	N/m ²	Lamina stiffness matrix
q_s	N/m	Shear flow due to shear load
q_t	N/m	Shear flow due to torsional load
Re	-	Reynolds number
S_e	N/m ²	Maximal in-plane shear
S	m ²	Wing planform area
S_{wet}	m ²	Wetted area of the wing
Sm	-	Static margin

T	N	Thrust
T	Nm	Torque
TR	-	Taper ratio
t/c	-	Maximum thickness to chord ratio of the aerofoil
t_f	m	Flange thickness
t_w	m	Web thickness
T_{day}	s	Daytime duration
T_{night}	s	Night time duration
T_r	-	Transformation matrix
TW_i	degree	Local twist angle at the end of a wing partition
V_∞	m/s	True air speed
U	m or rad	Local elastic deformations matrix
U_e	m/s	Tangential velocity component
U_{Glob}	-	Global elastic deformation matrix
u, v	-	Horizontal and vertical velocity components
w_c	m	Width of the spar section
X_{spar}	-	Location of the spar in the chordwise direction
\bar{X}	m	x- coordinate of the centre of gravity of the aircraft (origin at the nose)
$\bar{\bar{X}}$	m	x-coordinate of the aerodynamic centre
X_c	N/m ²	Maximal longitudinal compressive stress in the longitudinal direction of the ply
X_t	N/m ²	Maximal tensile strength in the longitudinal direction of the ply
x_1		Structural mass area exponent
x_2		Structural mass aspect ratio exponent
x_3	-	Constants used to evaluate the profile drag of the aerofoil
\bar{Y}	m	y- coordinate of the centre of gravity of aircraft (origin at the nose)
Y_c	N/m ²	Maximal compressive stress transverse to the direction of the ply
Y_t	N/m ²	Maximal tension transverse to the direction of the ply
Y_{cam}	-	y-coordinate of the aerofoil's camber line
Y_{thick}	-	y-coordinate of the aerofoil's thickness distribution curve
y_{lo}	-	y-coordinate of the aerofoil's lower surface
y_{up}	-	y-coordinate of the aerofoil's upper surface
\bar{Z}	m	z- coordinate of the centre of gravity of aircraft (origin at the nose)

Greek letters

α	degree	Angle of attack
α_{dep}	degree	Depression angle
α_i	degree	Induced angle
$\beta_1, \beta_2, \beta_3$	-	Coefficients used to represent the angles of attack-lift curve
$\gamma_1, \gamma_2, \gamma_3$	-	Coefficients used to represent the lift-moment curve
γ_{12}	-	Shear strain in the plane of the 1-2 ply axes
δ^*	m	Boundary layer displacement
η_{bec}	-	Efficiency of step-down converter
η_{chrg}	-	Efficiency of fuel cell charge
η_{cbr}	-	Efficiency of the curved solar panels
η_{ctrl}	-	Efficiency of motor controller
η_{dchrg}	-	Efficiency of fuel cell discharge
η_{grb}	-	Efficiency of gearbox
η_{mot}	-	Efficiency of motor
η_{mppt}	-	Efficiency of the maximum power point tracker
η_{plr}	-	Efficiency of propeller
η_{sc}	-	Efficiency of solar cells

η_{wthr}	-	Irradiance margin factor
θ_z	degree	Zenith angle
ω_s	degree	Hour angle due to Earth rotation
ϵ_1, ϵ_2	-	Elastic strains in the 1 and 2 of the ply axis respectively
ν_{12}, ν_{21}	-	Poisson's ratios in the 1 and 2 of the ply axis respectively
Λ	degree	Quarter chord sweep angle
δ	m	Boundary layer thickness
μ	kg/(ms)	Air viscosity
δ	degree	Earth declination angle
θ	m	Momentum thicknesses
λ	-	Correlation equation defined as $\lambda = Re \theta^2 \frac{dU_e}{dx}$
ρ	kg/m ³	Air density
σ	N/m ²	Stress
τ	N/m ²	Shear stress
φ	degree	Latitude
l	m	Undeformed element length (finite element beam)

Abbreviations

AoA	Angle of Attack
AerO	Name for a design case with elastic deformations neglected
AerEl	Name of a design case with elastic deformations included
BL	Boundary Layer
CFD	Computational Fluid Dynamics
CG	Centre of Gravity
CGA	Canonical Genetic Algorithm
GA	Genetic Algorithm
HALE	High-Altitude, Long-Endurance
IPA	Interior Point Algorithm (an optimisation algorithm)
IVM	Inviscid -Viscous Model (2D aerodynamic solver written by the author)
LB	Laminar Bubble
MPPT	Maximum Power Point Tracker device
PM	Panel Method
Quasi 3DM	Quasi-Three-Dimensional Aerodynamic Solver (written by the author)
SP	Solar Powered
SUMER	Name of the finalised aircraft in this study
UAV	Unmanned Aerial Vehicles
VLM	Vortex Lattice Method
ZMR-No.	Name designation format for newly designed aerofoils

Subscript Definition

\perp	Normal direction
∞	Refers to free stream condition
<i>LE</i>	Leading edge
<i>TE</i>	Trailing edge
<i>eff</i>	Effective
<i>in</i>	Induced
<i>max</i>	Maximum
<i>min</i>	Minimum
<i>p</i>	Pressure
<i>prof</i>	Profile
<i>ref</i>	Reference
<i>trim</i>	Trim condition

ABSTRACT

High-altitude aircraft flying in the stratosphere (around 17-30 km altitude) can provide a useful platform for sensors to support a range of military and civilian surveillance tasks. The main topic of the thesis concerns the analysis of solar powered unmanned aerial vehicles designed for extended flight operations at high altitudes. An aft-swept flying wing configuration has been adopted for high altitude applications. Specific topics that were considered focussed on the development of a conceptual design tool and a multi-disciplinary optimisation tool able to converge on the layout for a solar powered HALE UAV.

A true aft-swept flying wing is perhaps the most aerodynamically efficient aircraft configuration but, to date, has not been investigated in any detail for possible application to high-altitude UAVs. Such a configuration would require a moderate amount of wing sweep in order to generate the necessary stability in flight and to provide adequate control power for manoeuvring purposes. All systems and elements can now be placed inside the wing without compromising the weight distribution. This avoids the need for drag inducing mass balancing pods and/or reflexed trailing edge associated with unswept (straight) flying wings. Such features can either increase structural weight and/or overall drag whilst reducing the maximum lift that can be achieved. However, the design, in common with the other more conventional aircraft, represents a substantial challenge due to the simultaneous addressing of numerous inter-related engineering disciplines required for a fairly comprehensive analysis.

The innovative aspect of this study was dedicated to the conceptual and preliminary design of a high altitude long endurance solar powered aft-swept flying wing and study in detail the design challenges along with the general problems associated with flying at high altitudes. Moreover, these aims were achieved by the author developing new design tools. The conceptual design tool was created to include all the aircraft elements and the expected power losses in addition to representing the drag estimation of the wing section rather than using a general expression as only a function of Reynolds number regardless the aerofoil performance. The preliminary design tool, also written by the author, represented by the composite structure model and the quasi 3D aerodynamic solver combined in a multidisciplinary optimisation framework, proved its capability in determining the aircraft geometry, its weight and its aerodynamic and structural performance capabilities.

CHAPTER 1

1 INTRODUCTION

High altitude aircraft flying in the stratosphere (around 17-30 km altitude) can provide a useful platform for sensors to support a range of military and civilian surveillance tasks. These can include real-time monitoring of seismic risks or volcanic areas, early forest fire detection, border security surveillance, pipeline & powerline surveys, telecommunication services, agriculture monitoring and many others (E. Cestino, Frulla, & Romeo, 2007). By flying at such high altitudes, not only does the aircraft provide a wide field of view enabling coverage of a large geographical area but also added protection from the possibility of interception by hostile vehicles. Although a number of research and operational high-altitude aircraft have been developed, there still remain significant challenges in the design and operation of high-altitude, long-endurance (HALE) aircraft. To date, the majority of the existing high altitude aircraft are based on the conventional wing/fuselage/tail/fin configuration. There is currently research being undertaken into the use of Blended-Wing Body configurations for UAV applications because of their perceived advantages in terms of aerodynamic and structural efficiency. A true flying wing is perhaps the most aerodynamically efficient aircraft configuration but, to date, has not been investigated in any detail for possible application to high-altitude UAVs. Such a configuration would require a moderate amount of wing sweep in order to generate the necessary stability in flight and to provide adequate control power for manoeuvring purposes.

This study focuses on the design and analysis of a solar powered long endurance high altitude unmanned air vehicle (SP HALE UAV). The design, in common with the other more conventional aircraft, represents a substantial challenge due to the simultaneous addressing of numerous inter-related engineering disciplines required for a fairly comprehensive analysis. Aircraft flight speed, wing lift coefficient, wing planform area and total aircraft weight are some of the key parameters that will need to be optimised during the design process, to meet the mission requirements in an efficient manner. One objective of the present research work is to investigate the design and optimisation of an aft-swept, flying wing configuration for application to high-altitude operations.

1.1 Solar Aviation

Solar powered aircraft use photovoltaic cells to convert the energy from sunlight directly into electrical energy. The solar cell was first demonstrated by a French physicist Edmond Becquerel in 1839 it had an overall efficiency of 1% (Hantula, 2010). However, during the last few decades, the efficiency of the solar cells was gradually improved as shown in Figure 1-1 in addition to the reduction in weight density and financial costs. The upper surface of the wing in addition to other available surfaces facing the sun are usually covered by thin-film solar cells to generate electric power to drive the propulsion system (electric motor) and to provide the aircraft systems such as avionics and transducer payloads. Moreover, for sustained flight, any excess energy can be stored in batteries or fuel cells for continued operation during night time. The efficiency of the battery during the charging and the discharging has also improved with time. Nowadays, the fuel cell is favoured option over batteries due to its low weight/power factor and its high efficiency (Rizzo & Frediani, 2008).

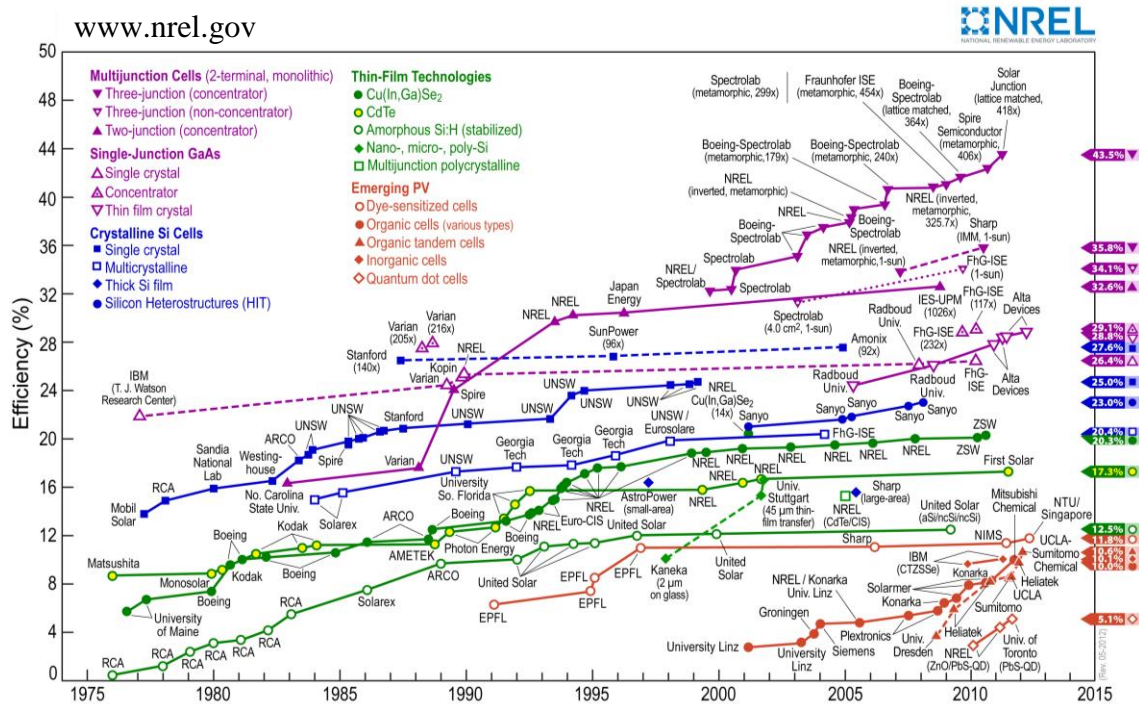


Figure 1-1 Timeline of solar cell efficiency since 1976

The first successful solar powered aircraft was flown about four decades ago as the efficiency reached a point where it could be applied to flying machines. Sunrise-I designed by R.J. Boucher in California, the USA in 1974, was the first to successfully demonstrate a complete sortie with a 20-minute flight. The mission endurance was then extended to four hours during the winter season. The aircraft then sustained permanent damage during a test

flight in a sand storm. Increase in the power/weight factor by about 14% of new generation solar cells, resulted in the improved Sunrise-II designed in 1975 (Boucher, 1984). Since these early days, several attempts were made to design solar powered UAVs with the aim of setting new records for range, altitude and flight endurance in addition to carriage of increased payloads (Noth(a), 2008). Such advances were accompanied by improvements in batteries & fuel cells to extend the flight duration overnight time. Such developments have made a significant contribution and have enabled some solar powered aircraft to continuously fly for several months in recent times (d'Oliveira, Melo, & Devezas, 2016).

The most interesting human-carrying aircraft was that designed by Swiss engineers and scientists who built a single-seat solar-powered monoplane called the Solar Impulse in 2003. The goal was to set a record for the first circumnavigation of the Earth using solar energy. The first version (Solar Impulse-1) was aimed at sustaining a continued flight over a period of 36 hours. This machine proved itself on flights across Switzerland-Spain-Morocco in 2012 and then across various states in the USA in 2013. The lessons learned led to the Solar Impulse-2 which was scheduled to commence the circumnavigation from Abu Dhabi in 2015 and return to the same airfield five months later after a multi-stage journey. Thermal damage to the batteries however caused major delays and it took 16 months for the aircraft to complete the circumnavigation (Solarimpulse.com, 2017).



Figure 1-2 Solar Impulse-2 aircraft

During the last three decades, increasing interest was shown towards high altitude operations using solar power for a variety of possible missions. AeroVironment Inc. with funding from the US government began to investigate the feasibility of building a solar powered aircraft operating at 19 km altitude for long endurance. The findings from the

performance of their first prototype HALSOL indicated inefficient electric power storage which was inadequate for the mission requirements. In 1993, the team produced a new unswept and untapered flying wing machine prototype called the Pathfinder with a gross mass of 254kg including its 45kg payload. This project then became a part of NASA's Environmental Research Aircraft Sensor Technology (ERAST) which enabled the Pathfinder to reach an altitude of 15 km which is regarded as the beginning of the realms of high altitude. After the success of this project, four prototypes were designed for different missions and payloads. The last of the four Helios P03 was flown in 2003 carrying a payload of 284 kg payload to an altitude of 30 km. This aircraft used a fuel cell in place of a lithium battery for higher efficiency and lower weight density (Noll et al., 2004).

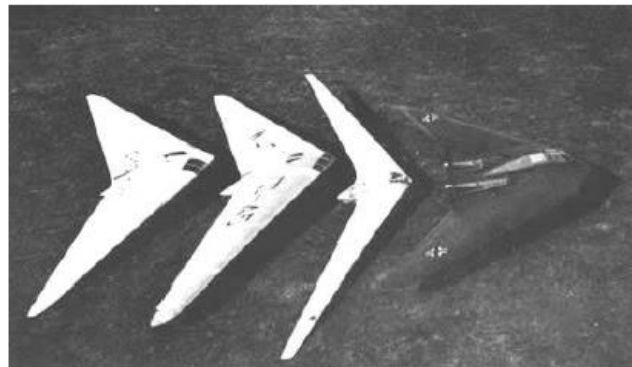
Many projects in Europe were also dedicated to studying high altitude solar-powered aircraft. Some involved small prototypes to assess the feasibility and the validity of their studies such as the DLR project (1997-1998) and the Helinet project (2000-2003) (Noth(a), 2008). A British company QinetiQ manufactured its first solar powered HALE aircraft called Zephyr in 2005. Its newest version is capable of flying continuously at 21 km altitude for several months with a small payload of about 2.26 kg (Rapinett, 2009; Zhu, Guo, Fan, Hou, & Gao, 2014). This project is currently ongoing as a part of an Airbus programme (Pseudo-Satellite (HAPS)) as the intention is to design new versions of Zephyr with increased payload capacity (d'Oliveira et al., 2016). In July 2015, Facebook Company purchased Ascenta, a British company, and built a solar-powered aircraft called the Aquila. It has an aft-swept wing configuration with a 42m wingspan and 400 kg total weight. Its mission was to facilitate 24-hour internet communications in remote parts of the world by carrying its payload at altitudes between 18 to 27 km over a period of three months (d'Oliveira et al., 2016; Guardian, 2015).

1.2 The Flying Wing

Flying wing or “all-wing” aircraft are as old as the human flight itself, and Figure 1-3 illustrates some of the most notable examples. The first successful tailless biplane flying wing aircraft was designed by Englishman John Dunne in 1912 (Weyl, 1945). In Germany, the brothers Walter and Reimar Horten designed and tested a range of successful flying-wing aircraft during the 1931-1944 period. These culminated in a jet-powered combat aircraft, the Horten Ho IX, which flew just before the end of the Second World War. In the USA, Jack Northrop designed and built flying wing aircraft during 1929-1950. None of these designs ever entered operational service. However, the Northrop Grumman company did eventually develop and put into service the B-2 Spirit stealth bomber which shared many of the design features of Jack Northrop’s earlier YB-35 and YB-49 designs (D. F. Anderson & Eberhardt, 2001). The main challenge in the design of such a tailless aircraft was found to be in the control and stability with additional problems associated with the cooling system of the engines. The reasons for adopting this unconventional flying wing configuration (at that time) included lower drag (so that the aircraft can fly at a higher speed for the same engine capacity) and more importantly for military operations, lower levels of detectability by radar thanks to reduced number of reflective surfaces (Whitford, 2007).



The Dunne D.8 designed by John



Four significant Horten designs 1941-1942



Northrop YB-49 (1944-1947)



Northrop Grumman B-2 Spirit

Figure 1-3 Some Significant Flying-Wing Aircraft

High altitude aircraft are characterised by their high aspect ratio wing and ultra-light planform which suggest a flexible structure. The inclusion of an empennage will create additional elastic deformation problems. However, some existing high altitude aircraft such as the Zephyr are tailed aircraft but with low wing loading when compared with some of the NASA prototypes. There is also interest in multi-tailed configurations to prevent or mitigate aeroelastic issues in addition to improving stability and control. This approach has been utilised in the X-HALE and the newest version of the Zephyr (d'Oliveira et al., 2016; Jones & Cesnik, 2015). However, this will create many aeroelastic-related flight control challenges in addition to generating higher drag counts.



Figure 1-4 X-HALE UAV (Jones & Cesnik, 2015)

The straight flying wing configuration was adopted by NASA to build five prototypes. This configuration is efficient from an aerodynamic and structure points of view when compared with tailed aircraft for application at high altitudes but will encounter difficulty with securing an adequate level of stability. Another limitation is the reduced maximum lift coefficient due to the need for reflexed wing section (airfoil) which is necessary to generate a positive pitching moment to balance the aircraft. The weight distribution can lead to achieving a specific static margin and this requirement forced the leading edge of the pods containing systems equipment to be slightly swept forwards in order to ensure correct location of the centre of gravity. This has been adopted in all the NASA's prototypes such as Pathfinder Plus shown in Figure 1-5 (Noll et al., 2004). However, these pods do generate significant drag which is disadvantageous.



Figure 1-5 Pathfinder Plus UAV

Hence the reason as to why an aft-swept flying wing is likely to be more efficient. All systems and elements can now be placed inside the wing without compromising the weight distribution, and, the shaping of the wing can be driven to achieve the stability requirements. This avoids the need for drag inducing mass balancing pods associated with unswept flying wings. Such enhancements will reduce the weight of the aircraft as well. The author was not aware of any research being conducted into the possibility of using this configuration for the application at high altitudes at the start of this study but recently, a swept flying wing high flyer design is being considered for use by the Facebook Company. However, no sufficient aerodynamic or structural data are available as yet. Thus the innovative aspect of this investigation is dedicated to the conceptual design of an aft-swept flying wing and study in fair detail the design challenges along with the general problems associated with flying at high altitudes.

1.3 Challenges of Flight at High Altitude

Sustained flight at high altitudes involves a range of difficulties. The thin air at high altitude is cold at low pressure. For example at an altitude of 25 km, the ambient air pressure and density are about 2.45% and 3.26% respectively of their mean values at sea level whilst the temperature is about -50°C . These physical properties of the air impact upon the ability of the vehicle to generate sufficient aerodynamic lift forces to support its weight. There can also be significant challenges in achieving satisfactory stability and control characteristics for the vehicle when operating at high altitudes. The low air density at high altitudes will

result in the significantly reduced generation of thrust by the propulsion systems (Houghton & Carpenter, 2003). Strong coupling between the aerodynamic and the structural elements can significantly impact trim and stability characteristics. These factors necessitate a delicate balance between optimising the aircraft for better aerodynamic performance and preserving the essential stability characteristics. Therefore, a multidisciplinary design optimisation approach will be vital when designing high-altitude aircraft. The following sections will summarise some of the main challenges.

1.3.1 Aerodynamic performance at low Reynolds number

The flight profiles of solar powered HALE UAVs at high altitudes and moderate flight speeds represent low-Reynolds number operating conditions which places severe demands on the aerodynamic design. The required lift coefficient is high when compared to the more conventional lower-altitude aircraft due to the reduced air density. At low Reynolds number, the viscous effects become more dominant leading to an increase in the drag coefficient whilst at high Reynolds number there will be an increase in the maximum lift coefficient (Greer, Hamory, Krake, & Drela, 1999; Lissaman, 1983). At low Reynolds number, the performance of an aerofoil is limited by laminar separation of the boundary layer. Therefore, the flow becomes unsteady causing the aerodynamic moments and forces to fluctuate with time (Lei, Guo, & Huang, 2013). A separation bubble may form within the boundary layer causing the transition from laminar to turbulent (Lei et al., 2013; Lissaman, 1983). The position of this separation bubble and its intensity depend on the shape of the aerofoil, angle of attack and Reynolds number (Greer et al., 1999). This has the effect of reducing the gradient of the lift curve whilst increasing drag at the same time (Ma & Liu, 2009).

Therefore, the design process needs to have an aerodynamic solver capable of predicting the viscous effect around the wing. However, such a solver would consume a great deal of time to iterate around an optimisation point. Hence it would be prudent to investigate a faster means by which the total drag of the wing could be estimated. In this thesis, a low order analysis model will be introduced to evaluate the total drag in addition to obtaining the locations of the laminar to turbulent transition point and separation of the boundary layer.

1.3.2 Elastic Deformation

In general, high altitude aircraft have a large wingspan and the low weight structure will make it flexible. Therefore, the aerodynamic loads will considerably influence the wing shape and this, in turn, will affect the aerodynamic performance and the stability of the aircraft. If the deflection becomes large, the aeroelastic behaviour will significantly modify and may lead to nonlinear aeroelastic behaviour.

During the initial design stages of high altitude aircraft, the structural sizing is crucial and must be reasonable to reduce the weight and yet withstand the loads and maintain the elastic deformations within acceptable limits. The weight of the structure directly affects the values of the overall design parameters. Such a design tool must consider the structural influence on the shape of the wing in flight.

Particular challenges are expected to be faced with the structural design associated with the nature of flexible swept flying wing configuration. Structurally, it is convenient to consider the bending moment about an axis perpendicular to the elastic axis (spar locus) whilst the local angles of attack (incidences) are measured with respect to the flow direction. In the case of applying pure up-bending load on an aft-swept wing, a decrease of the local wing incidence is produced due to the differences in the elastic vertical displacements at the leading and trailing edges as shown in Figure 1-1. This influence is reversed in the case of bending down the wing, leading to an increase in the local angles of attack. Therefore, the elastic twist of the wing under flight condition will be a part of the torsional elastic twist and the bending deflection. However, the spar location can be used to mitigate the influence of elasticity as will be discussed in chapter 8. Dynamic aeroelasticity is expensive in terms of computational time, therefore, only static aeroelasticity will be considered in the structural design and assessment of aerodynamic performance.

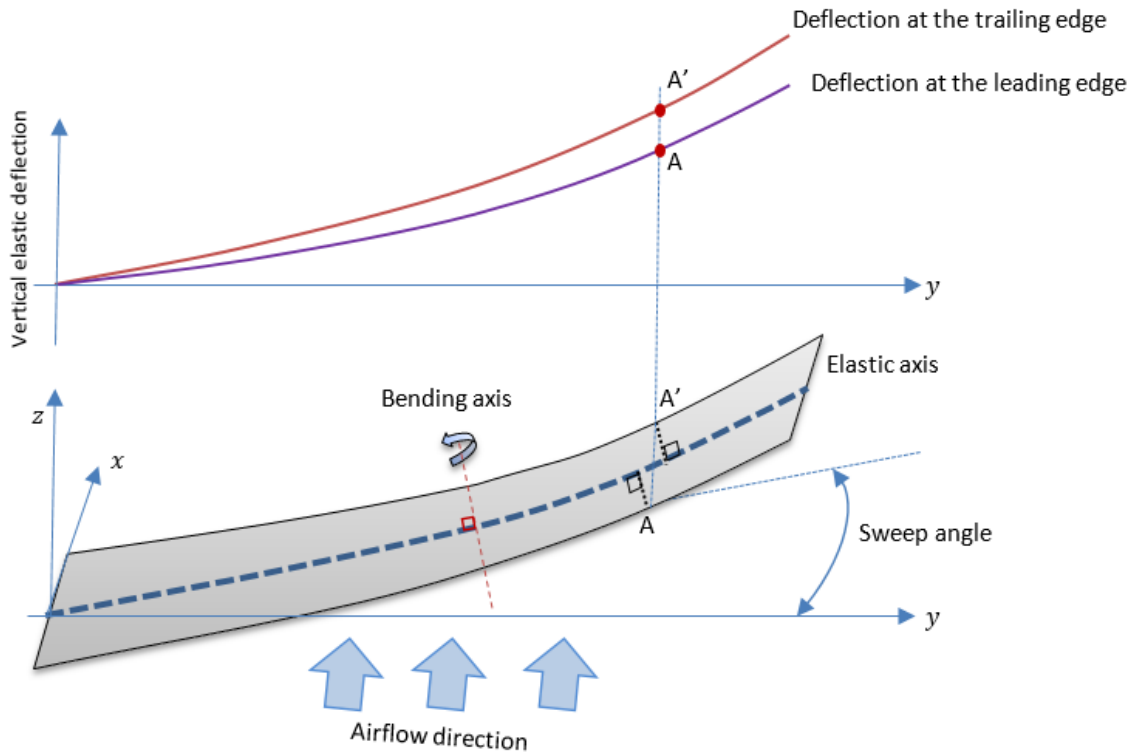


Figure 1-6 The elastic twist due to pure up-bending load of the swept flying wing

1.3.3 Stability

There are two main sets of challenges facing the design process to achieve the stability of such a high-altitude aircraft associated with the layout configuration and structural deformations. The first challenge concerning the tailless aircraft configuration necessitates the offering of an alternative design feature to enhance the stability such as sweeping or/and twisting of the wing in addition to using certain types of aerofoils. As indicated in the previous section, the tailed aircraft, which has good stability, demonstrates lower aerodynamic efficiency due to the drag of the empennage in addition to aeroelasticity problems associated with the attachments.

Using a straight flying wing is one of the design solutions which was adopted in previous studies due to it achieving excellent aerodynamic efficiency but at a low level of stability and low value of maximum lift coefficient. This configuration has a small corresponding tail arm and lack of directional stability. Therefore, a differential of propulsion thrust was used to control the direction of NASA's prototypes. Moreover, this configuration has a poor maximum lift coefficient when the flaps are deflected.

The improved longitudinal stability of a slightly swept back configuration might result in a gain in efficiency when compared with a straight flying wing. Hence, the wing sweep is necessary to provide an adequate moment arm for outboard longitudinal and lateral control surfaces. Such a sweep is needed only for stability reasons because the flight profile of solar powered aircraft is concentrated at low speeds. The sweepback can be useful to achieve the longitudinal, lateral and directional stability (Nickel & Wohlfahrt, 1994). However, this solution will involve a reduction in aerodynamic efficiency and encounter problems with structural elasticity. Adopting a swept flying wing configuration necessitates the use of an aerofoil with a smaller pitching moment, but not excessively low in order to obtain a high lift coefficient.

The second set of challenges is associated with the elastic behaviour highly exhibited by the structure of high altitude aircraft, which impacts the aerodynamic forces and moments, and thus stability. For swept flying wing, wing bending will influence the aerodynamic span load distribution resulting in an inboard shift in centre of load for each wing panel leading to forward shifting in the aerodynamic centre, which in return reduce the longitudinal static stability. Also, this can influence the slope of the lift curve leading to an increase in the trimmed angle of attack. These effects become worse with increasing the sweep angle and the aspect ratio of the wing. Studies conducted on conventional aircraft with swept wings concluded that the torsional deflections had a stabilising influence whilst the bending deformations tended to destabilise (Skoog, 1957). The overall effect of these two influences is dependent on the sweep angle, the location of the spar and the ratio of bending to torsional stiffness values. Moreover, the effects of the static and dynamic aeroelasticity are significantly coupled with the flight dynamics of the aircraft. However, these factors are not the main focus in this study.

1.3.4 Power Requirements

Solar powered HALE UAVs use only the solar irradiance as a source of energy which in turn is dependent on the hour of the day, the day of the year, the latitude and the altitude. For long endurance missions, the aircraft should fly continuously if the energy collected during the daytime is enough to operate the aircraft over a 24 hour period (Gao, Hou, Guo, Liu, & Chen, 2013). During the day, the solar cells convert sunlight energy into electrical power to operate the aircraft and at the same time store energy in the power pack (batteries or fuel cells) for night operations. Such a power storage facility would account for 40-60% of the aircraft weight. However, a certain amount of energy will be lost during the

charging and discharging process in addition to the power lost in the voltage converters which are necessary to supply the power for the various aircraft elements.

In general, the energy and mass balance provides a good starting point for the design of the aircraft. Some of the aircraft items such as motors, solar cell panels, fuel cells or batteries, and avionics are sized on the required power, but at the same time, their own weight will add to the total weight of aircraft which will, in turn, require greater power. High altitude aircraft are characterised by their large wing which means a greater area for the solar cells. However, since the flight conditions of these aircraft at low air density and low speed will mean that the required weight of aircraft need to be minimised (Min Chang, Zhou Zhou, Rui Wang, & Xu, 2014). Therefore it is necessary to support the study using a design tool which is capable of estimating the optimal aircraft weight and size its elements accordingly. This will be of particular interest in this study.

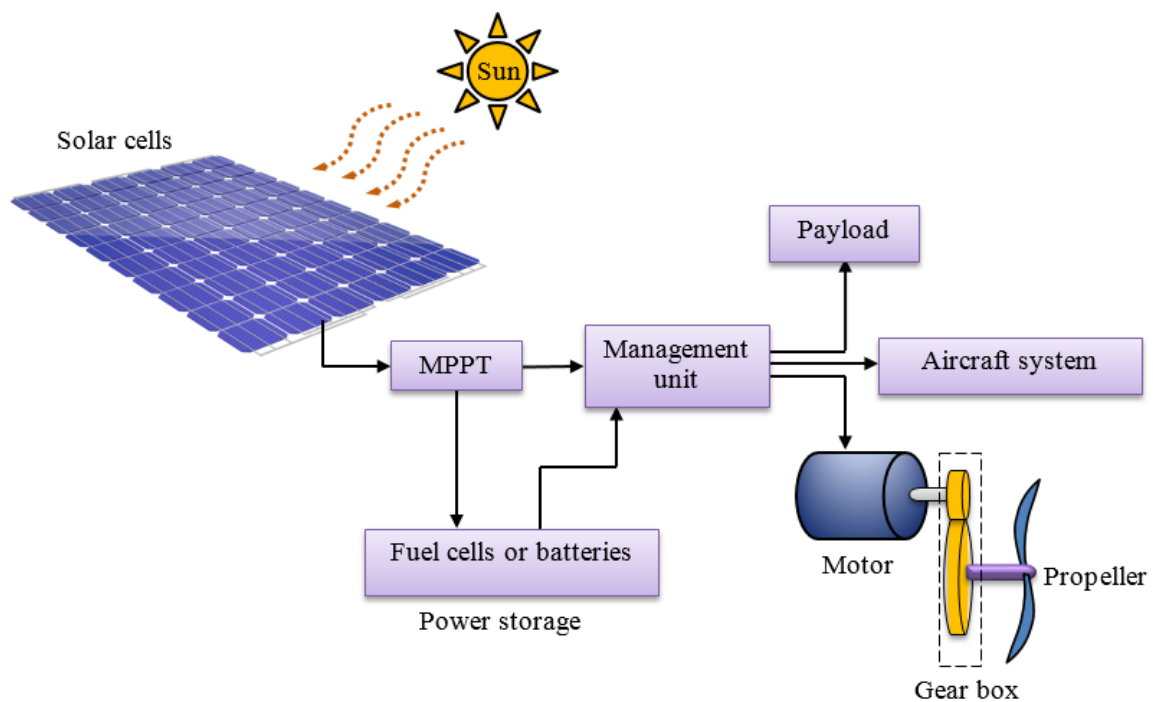


Figure 1-7 Typical solar powered aircraft system

1.4 Aims and Objectives

The main topic of the present research is the analysis of solar-powered unmanned aerial vehicles designed for extended flight operations at high altitudes. An aft-swept flying wing configuration will be designed for particular mission requirements which would possess appropriate science and technology for applications in Iraq. Specific topics to be considered will be the development of a conceptual design tool and a multi-disciplinary optimisation tool able to design and optimise such a solar powered HALE UAV.

To achieve these targets, the following objectives were set:

- 1- Develop a conceptual design model to size the aircraft according to the mission requirements.
- 2- Develop a low fidelity aerodynamic solver to evaluate the aerodynamic performance parameters including the viscous drag.
- 3- Develop a low fidelity composite structure model to size the wing and evaluate the elastic deformation under aerodynamic loads.
- 4- Design and investigate new aerofoils for a swept flying wing configuration for the expected flight conditions.
- 5- Build a multidisciplinary optimisation tool employing the developed aerodynamic and structure models.
- 6- Introduce a specific mission for surveillance purposes to operate over southern Iraq and then use the conceptual design tool to initiate the refinement procedure.
- 7- Propose a new aft-swept flying wing configuration using the key features collected during the conceptual design stage.
- 8- Optimise the aircraft to achieve an operational wing geometry.
- 9- Compare the results obtained during the preliminary and the conceptual design stages to the mission requirements.

1.5 Motivation for the Design Mission

The required mission is to survey the marshlands in southern Iraq adjacent to the historical city Sumer as shown in Figure 1-8. These marshes cover an area of around 3000 square kilometres and are characterised by the diversity of plants and animals which inhabit the region. In particular, the reed Quasab, is the most important plant and is prone to fires every year. The marshes were dried and burned during the 1991-2003 period for security purposes but were subsequently reclaimed after 2004. The Iraqi government is now interested in safeguarding the natural life of the region. Recently, the Iraqi marshlands have been included in the UNESCO's World Heritage List.

There are several relevant survey missions for which a high altitude, long endurance UAV could support this effort, including firefighting, flooding control, monitoring of animal migration ... etc. The required payload for this kind of mission is likely to be an electro-optical camera with infrared capability and may weight about 100 kg. The UAV for this mission would need to cover a large geographical area at an altitude of 17 km which should be sufficiently high to be out of range of possible interception by hostile powers. A flight endurance of around 5 to 6 months would be needed for either autonomous or ground controlled operations.

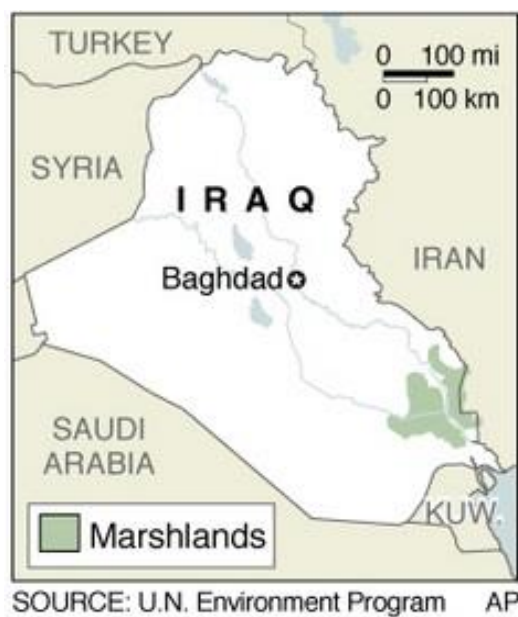


Figure 1-8 Marshes of Iraq

1.6 Thesis Layout

This thesis is structured into nine chapters including the current one.

Chapter 2 presents recent studies and background undertaken in terms of the aircraft configurations, design cases, aerofoils and the analyses of aerodynamic and structural elements.

Chapter 3 presents the framework methodology which was adopted to conduct this study.

Chapter 4 introduces a new developed conceptual design methodology in addition to a study of the influence of the altitude, latitude, endurance and the reference aerodynamic parameters on the weight along with the characteristics of solar powered high altitude UAV at the conceptual design stage.

Chapter 5 presents the development of an aerodynamic solver (quasi 3D aerodynamic solver) which has been built using the Vortex Lattice Method coupled with a two-dimensional inviscid-viscous aerodynamic model to evaluate the profile drag.

Chapter 6 presents the composite structure model developed in this study. It also presents the validation results for this model using a high order commercial package ANSYS in addition to the validating of the weight estimation model using existing data.

Chapter 7 presents the aerofoil design and optimisation tool in addition to the design of 12 new aerofoils in addition to validating one of them using a high order CFD package (FLUENT).

Chapter 8 presents the design procedure of an aft-swept flying wing called SUMER as a case study. The effect of the wing sweep, static margin and the location of the spar on the aerodynamic performance is investigated with and without the structural influences. It is at this stage that the final design and performance data are presented.

Chapter 10 presents the overall discussion for the tools developed in this research and the results obtained.

Chapter 11 presents concluding remarks in addition to recommendations for further work.

Appendices contains extra details in addition to the main program codes.

1.7 Original Contributions

The majority of high altitude aircraft that have been flight demonstrated are based on either empennage type configurations or a pure straight wing. A true swept flying-wing configuration has not been investigated in any detail for possible application for high altitude UAV operations. Therefore, the innovative aspect of this research will aim at investigating the possibility of using a moderately swept flying wing for high altitude long endurance applications. However, many design challenges in term of the required power, elastic deformations and low speed aerodynamic influence must be considered. Therefore, this study will investigate some of the main challenges of the design and this necessitates building more robust design tools for two different stages; conceptual and preliminary.

The design of solar powered high altitude long endurance UAVs represents a substantial challenge since numerous inter-related engineering disciplines are needed for analysis. The aerodynamic performance and the elastic deformation of high altitude aircraft are considerably coupled, and therefore, these items must be addressed during the initial design process. Hence, a multidisciplinary optimisation tool will be developed using low order analysis tools to enable the study of design challenges relating to highly flexible flying wing geometry. Before conducting an in-depth analyses involving aerodynamics and structural stressing, it is necessary to guesstimate the weight and power parameters of the aircraft.

It will be difficult to estimate the weight and power characteristics during the initial design stage due to the clean sheet approach that has been adopted. An analytical approach can be used along with simplified aerodynamic performance predictions at cruise condition. However, the analytical approach in existing studies do not include all the aircraft elements and the power losses. Therefore, an analytical conceptual design approach will be developed to include all the aircraft elements and the power losses.

The main contribution of this research can be summarised as follows:

- Investigated the possibility of using moderate aft-swept flying wing configuration for high altitude application.
- Evolved an analytical approach for the conceptual design stage including the expected power losses and all the aircraft elements prior to more detailed design process.
- Developed a multidisciplinary design/optimisation tool including efficient aerodynamic solver and composite structure model.

CHAPTER 2

2 BACKGROUND AND LITERATURE REVIEW

In this chapter are presented some of the existing high-altitude long-endurance unmanned aerial vehicles HALE UAVs relevant to the present project in addition to the research activities carried out in the areas of structural and aerodynamic analysis. These include the configuration design, aerofoil section, structural and aerodynamic tools, design of solar powered aircraft and the control and stability of a flying-wing.

2.1 Existing High-Altitude UAVs

In this section, some existing high altitude unmanned aerial vehicles (HA UAVs) are surveyed. A number of these vehicles are in operational service for either military or scientific applications. Some of these vehicles were developed to evaluate new technologies in sensors, light structures, aerodynamics and propulsion systems of relevant aircraft configurations (Morrisey, 2009). Table 2-1 documents some notable examples of high altitude aircraft along with their maximum endurance, service ceiling, payload, propulsion system, wing configurations and gross weight. They are classified into two categories; consumable-fuel and solar-powered aircraft. This information has been collected from a variety of sources and their websites (Goraj et al., 2004; Manuel, 2013; Morrisey, 2009; Najafi, 2011; Rapinett, 2009; Symolon, 2009) .

Table 2-1 Number of existing HA UAVs

	Aircraft	Max. Endurance	Max. Altitude km	Propulsion engine	Max. Payload kg	AR	Span m	Chord m	Configurations	Weight kg
Consumable-Fuel	NASA Altus	24 hr	20.72	TC 4-cylinder engine	150	24	16.45	n/a	tailed	975
	Boeing Phantom Eye	4 days	19.8	Liquid hydrogen engine	204	n/a	45.72	n/a	tailed	4445
	Boeing Condor	58 hr	20.42	2 LC, FI 6-cylinder engines	n/a	n/a	60.96	1.82	tailed	9208
	Theseus / Aurora Flight Sciences	30 hr	21.33	2 TC piston engines	340	n/a	21.64	n/a	tailed	2495
	RQ-4B Global Hawk	33 hr	18.28	Single turbofan engine	1360	25	39.89	1.61	tailed	14628
	Global Observer / AeroVironment	7 days	19.8	Liquid hydrogen engine, IC, electrical motors	182	n/a	53.34	n/a	tailed	1814
Solar-Powered	QinetiQ Zephyr	3 months	21.33	2 brushless electric motors	2.26	9.5	18.28	2.13	tailed	32
	NASA Pathfinder Plus	15 hr	24.4	8 electric motors	68	15	36.3	2.438	flying wing	317
	NASA Centurion	14 hr	26.82	2 electric motors	45-272	26	62.78	2.438	flying wing	862
	NASA Helios HP03	several months	30	14 brushless electric motors	284	30.9	75.28	2.438	flying wing	1052
	Facebook, AQUILA	3 months	18-27	4 brushless electric motors	59	n/a	42	n/a	flying wing	400

* TC: twin cams. LC: liquid-cooled. FI: fuel injected. IC: internal combustion. n/a: not available.

2.1.1 Consumable-Fuel HA UAVs

Several different types of engine were used for HA UAVs. These engines in general are four or six-cylinder modified piston types. Global Observer and Boeing Phantom Eye have the best endurance (4-7 days) compared with the other consumable-fuel aircraft thanks to their engines which employ liquid hydrogen as the fuel. The payload fraction of these two vehicles is around 10% and 5% respectively of the total weight. Boeing Condor is a very close competitor to the Global Observer and the Boeing Phantom Eye, with a payload fraction of 8 %, but has an endurance of about 58 hours. It is powered by a six-cylinder opposed, twin turbo-charged liquid-cooled engine. RQ-4B Global Hawk carries a much larger payload than the other vehicles, and can carry the highest payload of any UAV and the service ceiling is about 18.28 km. It is clear from Table 2-1 that hydrogen-fuelled engines can be considered as the best propulsion solution for long endurance and heavy payloads. The same conclusion was reached in a study by NASA, which indicated that the liquid hydrogen internal combustion engine would provide the highest endurance among the engines considered for a future generation of UAVs (Craig L. Nickol 2007). However, this endurance could be considered “limited” for some missions requiring an endurance greater than 7 days with a specific payload.



Figure 2-1 Notable consumable-fuel HA UAVs HA UAVs.

2.1.2 Solar-Powered HA UAVs

Several projects have been funded over the last three decades or so to investigate the design of solar powered UAVs. Further studies were conducted on projects which proved to be successful (d'Oliveira et al., 2016). Table 2-1 shows the characteristics of some notable solar-powered high-altitude aircraft which were test flown in the recent decades. Some of these aircraft were discussed in section 1.1. As mentioned earlier, NASA built five successful solar powered HALE UAVs for scientific and commercial uses as shown in Figure 2-2. The key improvements which drove the developments involved raising the maximum altitude, explore new scientific instrumentation, technologies and/or telecommunications equipment in addition to increasing the payload carrying capability. All NASA prototypes have featured flying wing configurations with neither taper nor sweep. Helios HP03 shown in Figure 2-3 is the latest NASA prototype which reached an altitude of 30 km. The majority of the large wing with a span of 73 m, is covered with photovoltaics cells which power the 14 brushless DC electric motors enabling it to carry a variety of payload (Noll et al., 2004). The other notable recent solar-powered high altitude aircraft are the Zephyr and the Aquila UAVs shown in Figure 2-4 and Figure 2-5 respectively.

From the main characteristics of the aircraft tabulated in Table 2-1, one can conclude that the solar-powered aircraft can last for longer flight durations thanks to sustainable energy harvested from the sun light. However, the payload capacity can be considered limited when compared with consumable-fuel aircraft. The flying wing configurations are the most used on designing the solar power HALE UAVs while the existing tailed solar-powered HALE UAVs were designed to carry a smaller payload. The reason for adopting tailed configuration is to increase stability level, as well as to use a certain wing sections with higher lift coefficient to reduce the required planform wing area, and thus the aircraft weight. However, this approach comes with structural problems due to the flexibility of the wing which may lead to aeroelasticity problems in the wing caused by the load generated at the tail during unsteady flight.

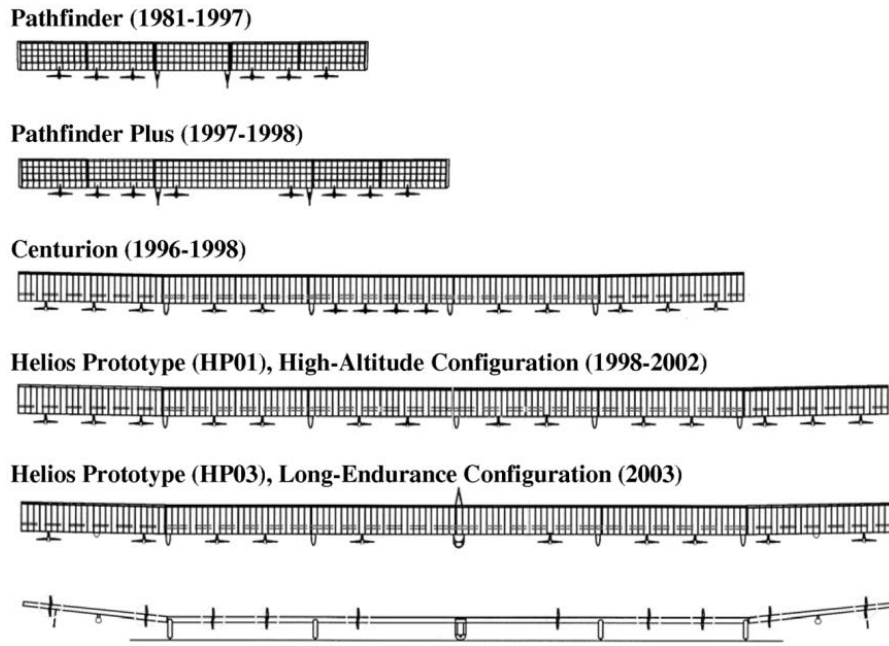


Figure 2-2 Timeline of Aero-Vironment / NASA prototypes (Noll et al., 2004)



Figure 2-3 NASA Helios P03 UAV



Figure 2-4 Qinetiq Zephyr UAV



Figure 2-5 Facebook's Aquila UAV

2.2 HALE Aircraft Configurations

Several attempts have been made to increase the aerodynamic efficiency or structural performance of HALE UAVs. A notable number of these interesting configurations which have appeared in the literature will now be discussed.

Four conceptual designs for HALE UAVs were presented by (Zdobysław, Andrzej, & Jacek, 1999) as shown in Figure 2-6. All of these vehicles were designed to carry the same payload and fuel for a specific mission such as reconnaissance and remote sensing at 27 km altitude, 300 kg payload and 48 hours flight endurance. The turbocharged piston engine in each case is similar to the engine used to power the Strato 2C high-altitude manned aircraft. Panel methods are used to compute the aerodynamic characteristics for different altitude, speed and equilibrium conditions. A performance comparison between these four configurations was made. The results indicate that the flying-wing configuration does not seem to be a good choice because of its large wingspan and its lack of external fuel tanks. However, this configuration did have the lowest zero-lift drag coefficient of all the configurations considered. The authors indicated that increasing the flying-wing aspect ratio (keeping the wing area constant) is not possible because of expected aeroelastic problems. The resulting increase in the mass of the structure will lead to reduced range and endurance. The high-wing monoplane configuration has the best specific endurance and range. In addition, it has the highest speed and rate-of-climb along with the shortest time to reach service ceiling. However, the authors concluded that a biplane with a lifting tail seems to be

a good choice for long endurance and high payload flights, but only in the case when loiter speeds are below the compressible range. The biplane with a lifting tail was recommended because it has a moderate wingspan which can be obtained for a relatively large wing area and a high effective wing aspect ratio. The biplane configuration has a relatively stiff wing structure, with lower induced drag at the same lift condition and wing area as for the equivalent monoplane configuration.

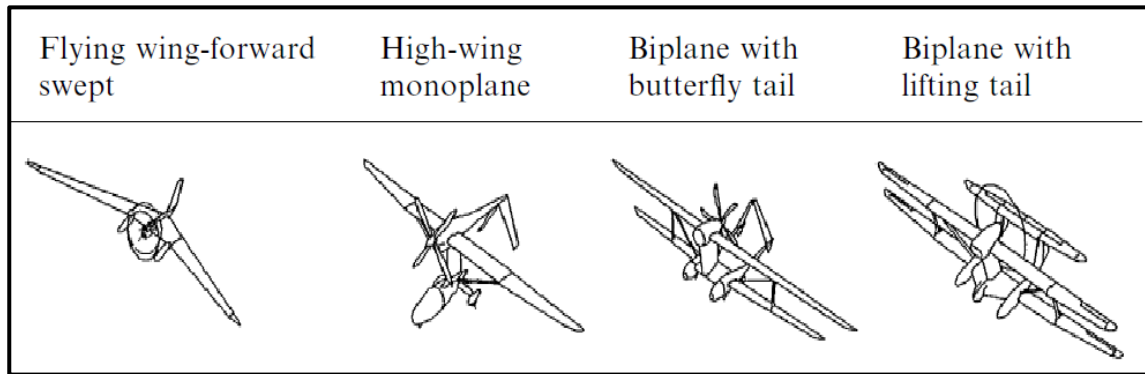


Figure 2-6 The four configurations considered in (Zdobysław et al., 1999).

A design process for a HALE blended-wing aircraft shown in Figure 2-7 was presented by (Goraj et al., 2004). The specified mission was to operate 40 hour mission at high altitude (20 km) for surveillance purposes. The design process started with canard configured PW-111 which was longitudinally unstable. Optimisation studies on various configurations were conducted to improve the stability and the aerodynamic performance characteristics. Figure 2-7 shows the options which were considered and the final choice was based on PW-114. In addition to the central fin, it features wingtip mounted finlets to improve directional stability.

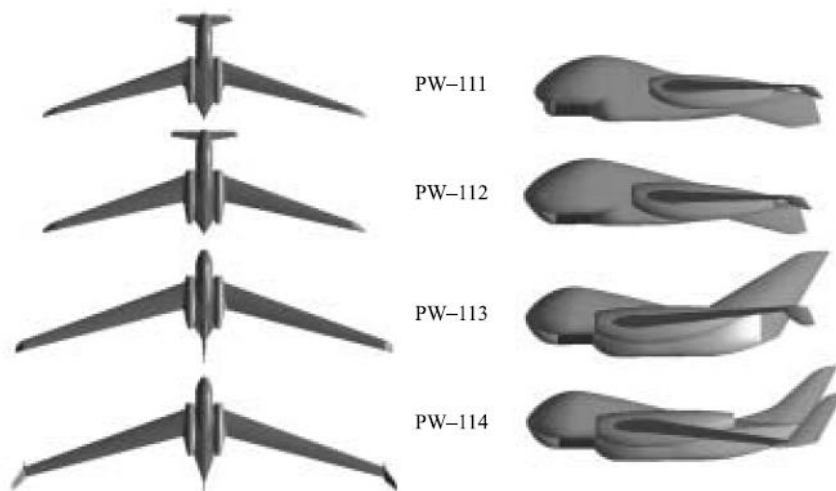


Figure 2-7 Comparison of PW configurations presented in (Goraj et al., 2004).

Baldock and Mokhtarzadeh presented a conceptual design approach to design a basic geometry for a solar-powered HALE UAV (Baldock & Mokhtarzadeh, 2006). The methodology was based on suggesting the aircraft geometry with regards to logical reasoning and analytical constraints, including environmental considerations and structural limitations. The aerodynamics, flight performance and power requirements during the flight condition are then estimated using analytical equations supported by fractions to consider the power losses in the aircraft subsystems. The case study investigated the energy requirements of a rectangular braced-wing configuration, as shown in Figure 2-8, to carry a 100 kg payload. The results showed that this configuration is capable of sustained continuous flight throughout the year at an altitude of 21.3 km and up to latitudes of 10° . Structural analysis, control & stability and optimisation of any sort were not investigated in this study.



Figure 2-8 Rectangular braced-wing configuration in (Baldock & Mokhtarzadeh, 2006)

Several design concepts have been studied by NASA using a multi-disciplinary optimisation tool (Craig L. Nickol 2007; Nickol, Guynn, Kohout, & Ozoroski, 2007). Sixteen configurations were developed which were classified into two groups; lighter than air and heavier than air vehicles. The concepts of heavier than air vehicles were also classified into two groups; consumable fuel and solar-powered aircraft. Each concept focused on two separate operational missions; hurricane science and communications relay. The weight of each aircraft was estimated using a combination of analytical and empirical methods with the weight of some of the elements assumed constant. The sizing of the wing structure was based on the quantity of material which could withstand the predicted loads. The structural arrangement of the solar-powered aircraft was similar to that of AeroVironment Helios design. The study compared the results of each concept for a particular mission. It was concluded that none of these configurations had met the performance specifications in terms of the power and endurance as well as the required

internal volume to house the payload. But the study ranked each design by a metric percentage, denoted by (%P_{regen}), which is the ratio of the power supply against the power of the propulsion system on the worst day during the mission. The metric ratio represents the feasibility of the design to meet the requirements mentioned in the study. The main characteristics and the metric results are shown in Figure 2-10 for both missions. The study also showed that the characteristics of the storage system and the efficiency of the solar cells were key to enhancing the aircraft performance to meet the requirements.

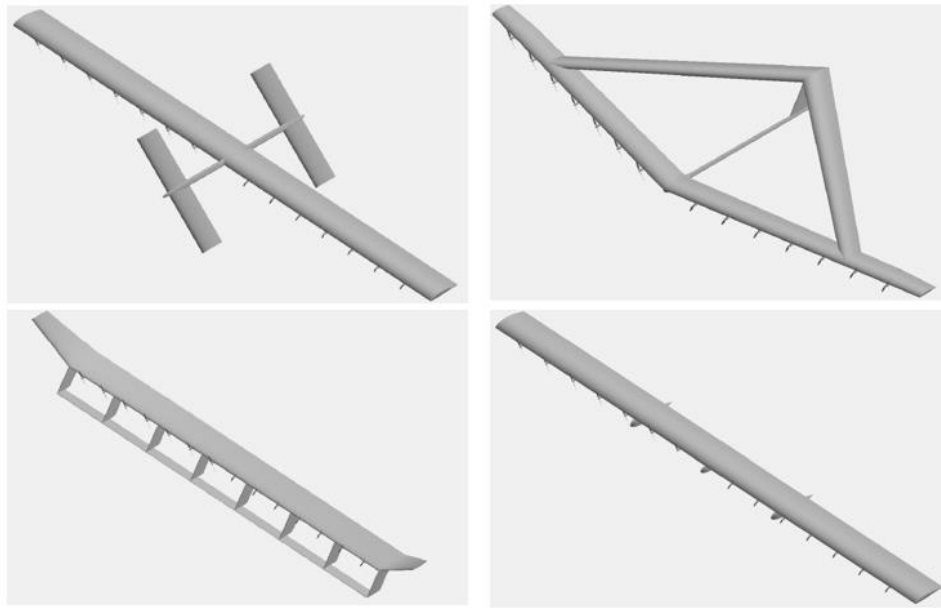


Figure 2-9 Number of configurations studied by NASA (Craig L. Nickol 2007)

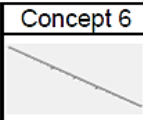
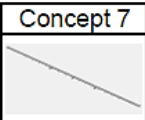
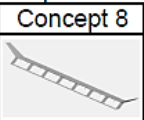
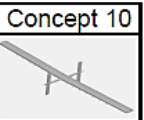
		Concept 6	Concept 7	Concept 8	Concept 9	Concept 10
						
		Solar Regen Fuel Cell	Solar Regen Secondary Battery	Trussed-Wing Secondary Battery	Joined-Wing Secondary Battery	Multi-Surface Secondary Battery
Endurance, days	Hurricane Science	n/a	n/a	n/a	n/a	n/a
	Communications Relay	n/a	n/a	n/a	n/a	n/a
TOGM, kg	Hurricane Science	2610	3210	3590	2690	3800
	Communications Relay	1970	2190	2650	1830	3390
Wingspan (HTA) or Length and Width (LTA), m		100	100	97	80	100
Volume (LTA), m ³		n/a	n/a	n/a	n/a	n/a
%P _{regen} (SR)	Hurricane Science	31	36	31	29	35
	Communications Relay	26	36	35	29	40

Figure 2-10 Metric results for the solar-powered configurations of NASA's study (Craig L. Nickol 2007)

A blended-wing body (BWB) configuration for a solar-powered HALE aircraft called SHAMPO with multi-payload and operation was suggested by (E. Cestino et al., 2007) as shown in Figure 2-11. The study investigated several aerofoil section profiles, wing planforms and wing optimisation to achieve the desired performance characteristics using the Xfoil and the VSAero computational fluid dynamics (CFD) software. A finite-element analysis was used to predict the static and aero-elastic structural behaviour using Msc/Patran/Nastran. The optimal configuration was a blended-wing body with a wing aspect ratio of 28, wingspan of 73 m and 5° quarter-chord wing sweep to carry a 130 kg payload. The mission was to fly for six months, starting on 1st April at an altitude of 17 km and latitudes below 44° N for monitoring sea borders and forest fires during the summer time. The authors concluded that the BWB configuration seems the best compromise of performance and accommodating large surface area (for the solar cells) and volume (for multi-payload purposes). Another aircraft called HELIPLAT was designed using the same tool, mission and altitude. It is a twin-boom tailed configuration such as shown in Figure 2-12. Small scale models were built to perform several experimental flight tests and verify new critical technologies. The flight tests of preliminary design were carried out successfully as indicated in (Romeo, Pacino, & Borello, 2009).

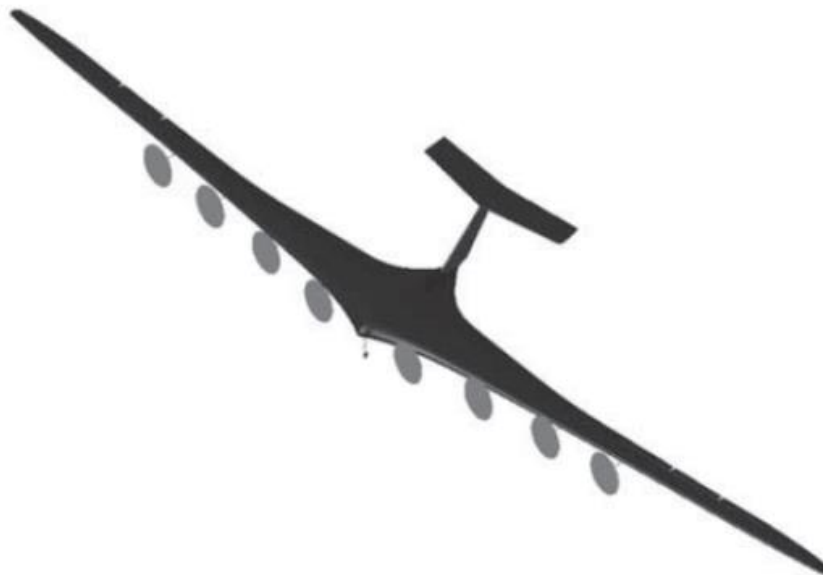


Figure 2-11 SHAMPO Configuration in (E. Cestino et al., 2007)

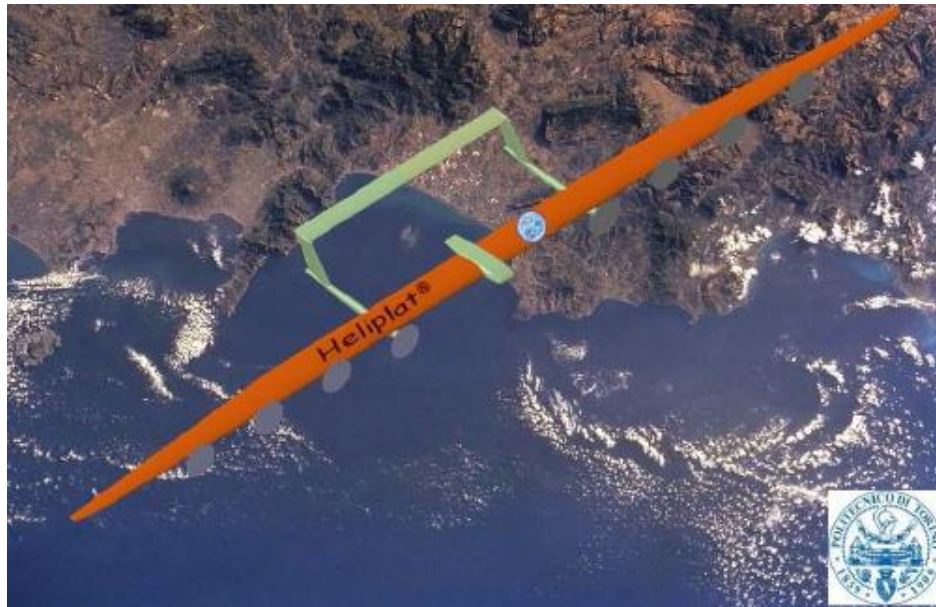


Figure 2-12 HELIPLAT Configuration in (E. Cestino et al., 2007)

A mathematical model for preliminary design of solar-powered aircraft was presented by (Rizzo & Frediani, 2008) based on the energy balance independently of the aerodynamic configuration. The proposed mathematical model was used to compare four different aircraft configurations as shown in Figure 2-13. The planforms were designed to fly at 30 km altitude, 44° N latitude and carry 300 kg payload starting on 25th June. The authors concluded that the reinforced-biplane configuration is the most efficient configuration. Its wing is stiffer and lighter than that of the flying wing. Moreover, the wingspan is reduced by about 15% compared with the flying wing with same wing surface area, and the tip deflection is about 40% of the flying wing with same wingspan and same wing area. However, the flying-wing configuration represented the best solution from the energetic and aerodynamic viewpoints, even though the structural stiffness and weight were critical aspects. The conventional and twin boom configurations showed their need for a larger wing area, particularly at low aspect ratios. The aerodynamic performance and the aerofoil section are not considered in this study. In addition, there is no detail about how the weight and mechanical properties of the wing structure are estimated.

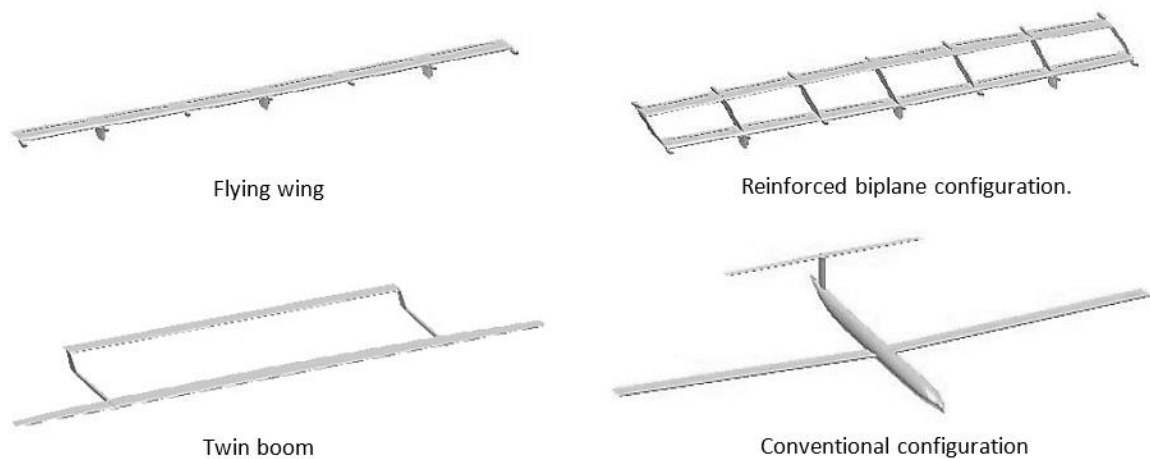


Figure 2-13 Configurations Considered in (Rizzo & Frediani, 2008)

A multi-disciplinary design and optimisation framework to develop a high-altitude, solar-powered UAV was described by (Mattos, Secco, & Salles, 2013). The aircraft baseline configuration was very similar to that of the Zephyr. The disciplines of aerodynamics (using the vortex-lattice method), structures, stability and weight were considered and integrated into a commercial package (modeFRONTIER). The design variables were associated with the shape of the aircraft, including the dimensions of the wing and the horizontal & vertical tails. The optimisation target was chosen to reduce the required power and the weight of the aeroplane. The results showed that the final configuration is quite similar to the baseline aircraft as shown in Figure 2-14.

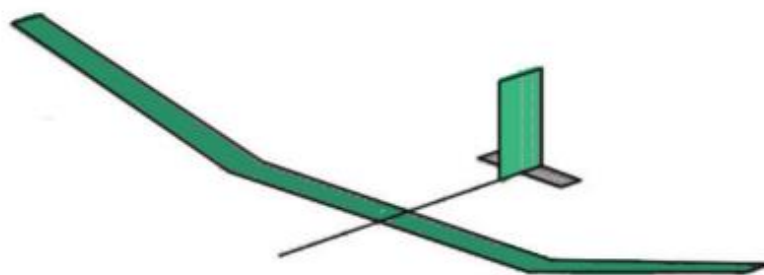


Figure 2-14 Optimal Configuration in (Mattos et al., 2013)

A multi-disciplinary tool was used by (Morrisey, 2009) to design a solar-powered, very-large aspect ratio, unswept, pinned-wing configuration of HALE UAVs. The objective was to study the effect of implementing the segmented-wing concept. The NASA Helios UAV was used as a basis for the comparison. The optimisation tool developed covers the aerodynamic performance (using Athena Vortex Lattice Method), structure analysis, energy

balance and the weight prediction. The results show that the weight of the optimal configuration is reduced by about 17% compared with the baseline aircraft. This reduction was due to a thicker wing section which affected the structural weight which in turn meant lower power requirements and thus reduced weight of the battery. The influence of viscous effects was not considered and the structural analysis was not detailed. In addition, the total weight of the wing was estimated to be 10 % greater than the weight of the spar.



Figure 2-15 Baseline geometry adopted in (Morrisey, 2009)

University of Michigan designed and built a flexible solar powered HALE UAV known as X-HALE. It is a high-aspect-ratio wing-boom-tail type aircraft as shown in Figure 2-16. It has a wingspan of 6 m and its constant chord is 0.2 m. This machine was recently flown for testing and validation of nonlinear aeroelastic solvers by providing an experimental data. The overall aim was to understand the coupling of aeroelastic-flight dynamic and failure modes such as the one experienced earlier with NASA's Helios P03 in 2003 (Cesnik et al., 2010; Jones & Cesnik, 2015).

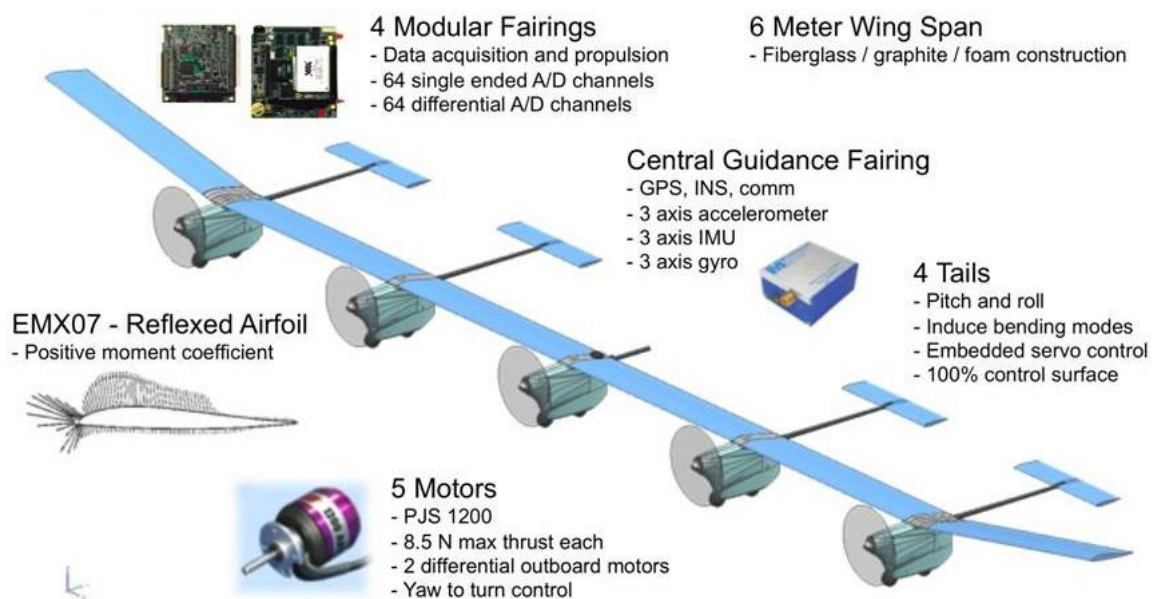


Figure 2-16 X-HALE Concept (Ref. <https://www.umich.edu/>)

2.3 Aerofoil Issue

2.3.1 Aerofoil Selection

The flight profiles of HALE UAVs at low air density and moderate flight speeds represent low Reynolds number operating conditions. The required lift coefficient is high compared to more conventional lower-altitude aircraft. Therefore, the aerofoil section needs to be optimised to operate at high lift coefficients with minimum drag. An additional constraint in selecting suitable aerofoil sections is the thickness required to accommodate either fuel tanks and/or fuel cells in addition to adequate stress members for the required structural stiffness.

Usually, the aerofoil is selected on the performance criterion including the stall characteristics. In the case of tailless aircraft, more attention is paid to the pitching moment of the candidate aerofoil as no horizontal stabilizer is available for usual stability margins (Nickel & Wohlfahrt, 1994). These factors can be summarised as follows:

- I. **Aircraft configuration:** stability requirement can affect the aerofoil selection process depending on the configuration of aircraft:

- (a) **Un-swept flying wing aircraft.**

The pressure distribution in the chord-wise direction is such that the pitching moment about its aerodynamic centre is equal to zero. This is achieved by the incorporation of a reflexed trailing edge but at the cost of reducing the maximum lift coefficient and increased drag (Buckstrom, 1979; Nickel & Wohlfahrt, 1994; Qin et al., 2004). NASA prototypes such as the Helios, Centurion and Pathfinder are examples of this approach.

- (b) **Swept-back flying wing aircraft**

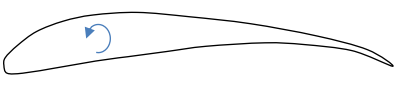
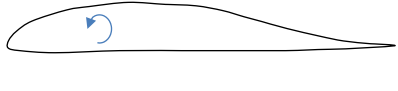
The severity of the reflexed trailing edge becomes less since the sweep-back and washouts are used to supplement the generation of the balancing pitching moment. This will also have the effect of increasing the maximum lift coefficient ($C_{l\ max}$). If the pitching moment is excessive, the sweep and/or washout parameters may turn out to be rather large. Therefore, in general, aerofoils with small pitching moments are preferable for tailless aircraft (Nickel & Wohlfahrt, 1994). This approach has been used in manned flying wing aircraft such as the Horten series (Mader & Martins, 2012) (Li, Zhang, Chen, Yuan, & Lin, 2012).

Uncambered aerofoils with zero pitching moment about the aerodynamic centre are preferable but the maximum lift/drag ratio will suffer (Katz & Plotkin, 2001).

(c) **Tailed-Aircraft type**

This aircraft type can use optimised aerofoils to achieve the highest wing lift/drag ratios as the longitudinal stability and control functions are off-loaded on to the tailplane. However, the designer will have to contend with additional drag from the empennage. The QinetiQ Zephyr, AeroVironment Global Observer, Michigan University X-HALE and the Boeing Phantom Eye are examples of this design (Rapinett, 2009).

Table 2-2 Summary of the typical aerofoil characteristics for different aircraft configurations

Configuration	Typical Aerofoils shape	C_m	$C_{l\max}$	C_d
Tailed aircraft		negative	high	high
Straight Flying wing		positive	low	high
Swept-back Flying wing		Small	moderate	moderate

II. **Low Reynolds Number:** At low Reynolds number, because the viscous effects become more dominant, there will be an increase in the drag coefficient whilst at high Reynolds number there will be an increase in the lift coefficient and hence the $C_{l\max}$ (Greer et al., 1999; Lissaman, 1983). At low Reynolds number the performance of an aerofoil is limited by a somewhat premature separation of the boundary layer. Therefore, the flow becomes unsteady causing the aerodynamic moments and forces to fluctuate with time (Lei et al., 2013). A separation bubble may form within the boundary layer causing the transition from laminar to turbulent as shown in Figure 2-17 (Lei et al., 2013; Lissaman, 1983). The position of this separation bubble and its intensity depend on the shape of the aerofoil, angle of attack and Reynolds number (Greer et al., 1999). This has the effect of reducing the gradient of the lift curve whilst increasing drag at the same time (Ma & Liu, 2009). The majority of the air resistance comes from the pressure drag over the region of the laminar separation bubble. After the separation bubble, the flow reattaches to the

aerofoil and becomes turbulent or may stay separated. If it remains separated, the lift coefficient will sharply drop with a marked increase in the drag coefficient. A number of studies have shown that there is a critical Reynolds number of about 70000 at which the performance of smooth (non-rough skin) aerofoils experience striking changes in lift to drag ratio as shown in Figure 2-18 (John & Michael, 1980). The smooth aerofoils have a higher lift-to-drag ratio than rough aerofoils at about $Re > 10^5$. Below this value, skin roughness will be beneficial as it will delay the separation of the boundary layer (McArthur, 2007).

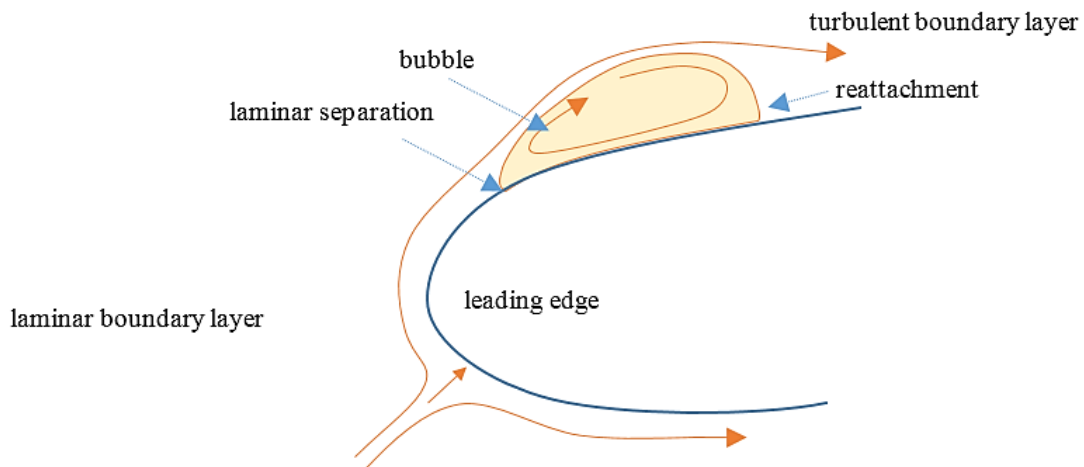


Figure 2-17 Structure of laminar separation bubble

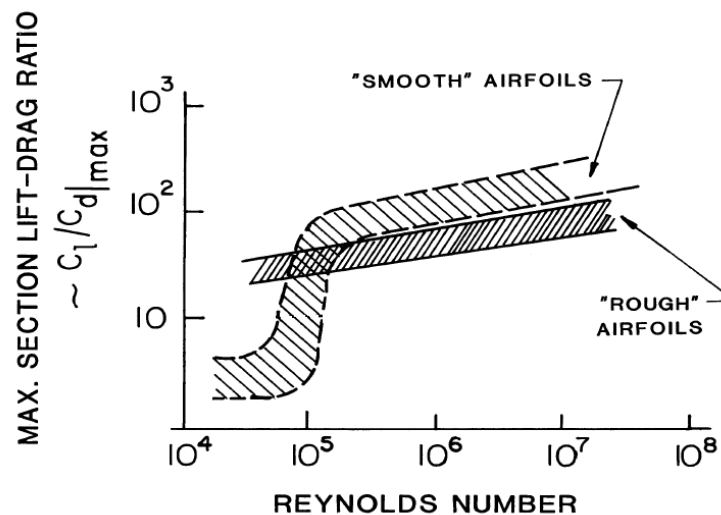


Figure 2-18 Aerofoil performance at different Reynolds numbers (John & Michael, 1980)

III- **Stiffness of the structure and internal volume needed.**

Increasing the aerofoil thickness can obviously increase the wing stiffness and reduce the sensitivity of the wing bending moments which will result in reduced structural weight. Furthermore, it will also provide more space for fuel and payload (Cerra & Katz, 2008). In general, thicker wing sections reduce both the maximum lift/drag ratio and the stall angle (Ma & Liu, 2009).

2.3.2 Aerofoil Shape Design

Two main approaches are introduced in the literature to design aerofoils. The approaches are based on direct numerical optimization and inverse design. The common aspect between these two approaches is that the aerofoil shape is modified until specific goals are satisfied. For the first approach, the goals are usually the aerodynamic performances characteristic such as lift, drag and the pitching moment coefficients whereas the inverse design approach searches for an aerofoil shape until the requirements for a particular flow characteristic such as pressure distributions and skin friction are fulfilled (Della Vecchia, Daniele, & D'Amato, 2014).

The direct numerical optimisation is implemented in a number of existing studies. This process involves varying the aerofoil section geometry until some aerodynamic target is achieved (usually maximum lift coefficient or lift to drag ratio) with some restrictions (e.g. minimum or specific pitching moment coefficient, minimum drag coefficient). A geometric parameterization method needs to be able to accommodate a wide range of possible new aerofoil section shapes to be coupled with an optimisation algorithm. Several parametrizations are used in literature such as B-splines, Bezier curves, Hicks & Henne equation, PARSEC and more which were surveyed by (Samareh, 1999). PARSEC parameterization is a more physically-intuitive method which enables the use of typical aerofoil section parameters to define the aerofoil section geometry (Della Vecchia et al., 2014). Many optimisation studies adopted the PARSEC parameterization such as the once in (Mukesh, Lingadurai, & Selvakumar, 2012; Zetina, Jeong, & Obayashi, 2013). A methodology of this type is presented by Sobieczky (Sobieczky, 1997). Eleven parameters were used and linked directly to the commonly-defined aerofoil section parameters as shown in Figure 2-19.

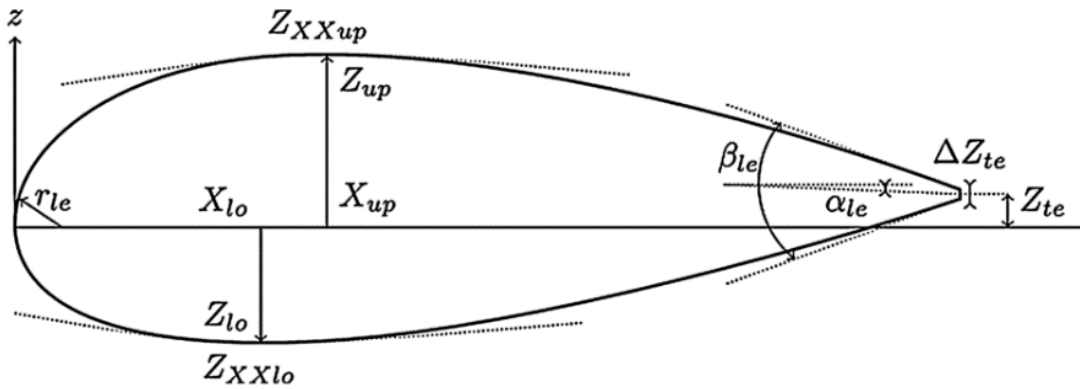


Figure 2-19 PARSEC Variable Definition in (Della Vecchia et al., 2014).

Another popular parametrization is called Bezier curve technique representing the aerofoil by two curves, one for the upper surface and the other for the lower surface, or, one for the camber line and the other for the thickness distribution. The Bezier curve can be created using controlled points which define the shape of the curves as shown in Figure 2-20 (Derksen & Rogalsky, 2010; P. Salunke, Ahamad R. A, & Channiwala, 2014; Park, Han, Lim, Kim, & Lee, 2008).

Several approaches aiming to enhance the representation of the trailing and leading edge shapes were introduced using multiple curves each described by variables. The selection of these curves can have a dramatic effect on optimising accurate representation of the shape of the aerofoil and minimising the computing time. Typically, the coordinates themselves are used as the optimisation variables (Della Vecchia et al., 2014; P. Salunke et al., 2014).

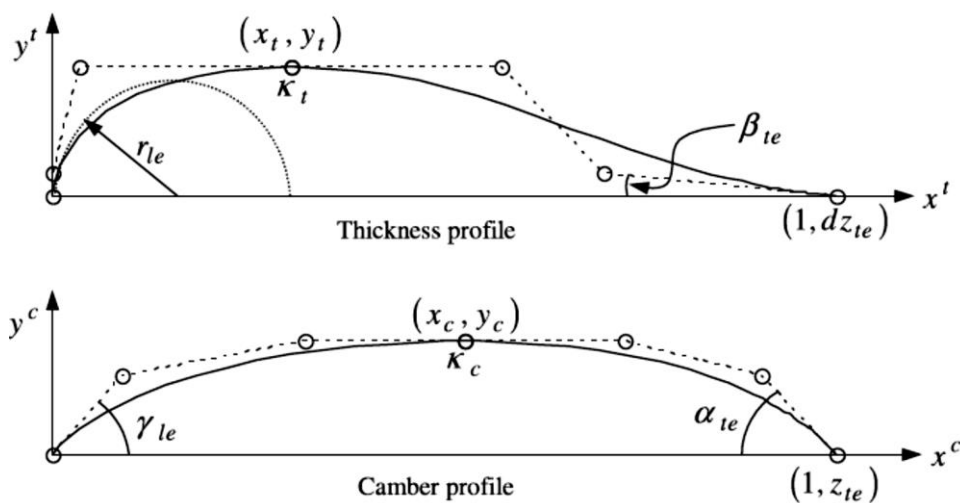


Figure 2-20 Aerofoil geometry and Bezier control points defined by twelve parameters presented in (P. Salunke et al., 2014)

A new aerofoil parametrization technique (Bezier-PARSEC) was introduced by (Derksen & Rogalsky, 2010) by improving the Bezier parametrisation using the PARSEC approach to enhance the matching of representing a wide number of existing aerofoils in addition to accelerating the speed of convergence of the aerodynamic solver.

Numerous studies have attempted to develop or design new aerofoils for low Reynolds number applications. For instance, Selig et al designed and experimentally tested 34 different aerofoils to be operated at low Reynolds number for different applications (Lei et al., 2013; M. S. Selig, Gopalarathnam, Giguere, & Lyon, 2001; M. S. Selig & Guglielmo, 1997). Marten Hepperle designed a number of aerofoils for tailless aircraft operating at different Reynolds number. The aims were to achieve lower drag, lower pitching moment and higher lift/drag ratio compared to existing aerofoils (Hepperle, 1988). However, the maximum thickness to chord ratio of these aerofoils is low. Therefore, they may not be suitable for a large flexible wing structure.

2.4 Structural Analyses - Weight Prediction Issues

The real physical structure of aircraft needs to be simplified if the structural design considerations are to be included in the optimisation process. The purpose of such an optimisation is to find a minimum feasible weight solution, subject to certain criteria. Weight reduction can result in increased payload capability and reduced power requirement. The stiffness of a wing is associated with the maximum thickness of the wing section and the thickness of the various structural elements (spars, ribs, stringers and skin), all of which impacts the wing weight (Chintapalli, 2006). During the optimisation process for the wing structural design, there is a requirement to carry out many structural analysis computations involving a range of geometry variables. The analysis method adopted, therefore, has to be computationally-efficient as well as sufficiently accurate. Nowadays, the majority of modern tools for preliminary wing design are based on beam theory for the analysis of primary structural wing components, supported by statistical analysis for secondary masses (Ajaj, Smith, & Isikveren, 2013). The validity and accuracy of shell and beam theory for wing preliminary design were compared by (Dorbath, Nagel, & Gollnick, 2010). The conclusion was that the beam model provides a sufficiently accurate results when designing the primary structure of a wing.

The cross-sectional geometry of a metallic wing torsion box was idealised by (Ajaj et al., 2013; Jemitola, 2012; Seywald, 2011; Torenbeek, 2013) as shown in Figure 2-21. The wing-box is modelled by means of a three-dimensional finite element beam orientated along the elastic axis of the wing. The wing-box is sized by calculating its thicknesses at each span-wise station according to the critical bending moment, torsion and shear stress applied to each element including static aeroelastic requirements and which then enabled estimation of the weight. Once the thicknesses were determined, the mechanical properties of the structure were calculated and the results were used to evaluate the elastic deformation of the wing using finite-element analysis as shown in Figure 2-22. The method assumes that the wing-box resists all of the external loads and that there is no contribution from wing secondary structures. The weight of the wing ribs is estimated by an empirical formula. This analytical approach was validated by (Ajaj et al., 2013) by applying the method to five different transport aircraft configurations. The conclusion was that this method is sufficiently robust and yields a standard error of about 1.5%. Based on these results, this wing structural idealization was employed in some point in the present research work as in a companion paper (Alsahlani, Johnston, & Atcliffe, 2015) but, later on, a composite structure model has been developed.

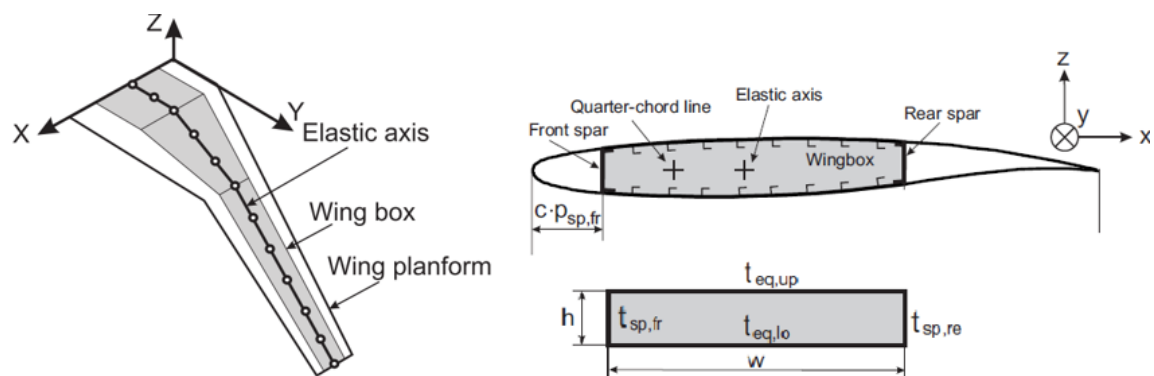


Figure 2-21 Sketch of the Structural Wing Model in (Ajaj et al., 2013; Seywald, 2011).

It is worth mentioning here that there are several empirical formulae in the literature to estimate the weight of the HALE UAV wing which were surveyed and introduced by (Colella & Wenneker, 1994; Hall & Hall, 1984; Jemitola, 2012; Montagnier & Bovet, 2010; Rizzo & Frediani, 2008; Romeo, Danzi, & Cestino, 2014). It may be possible to use some of these empirical equations to validate the results of the wing's structural design, in addition to evaluating the weight of the aircraft's elements.

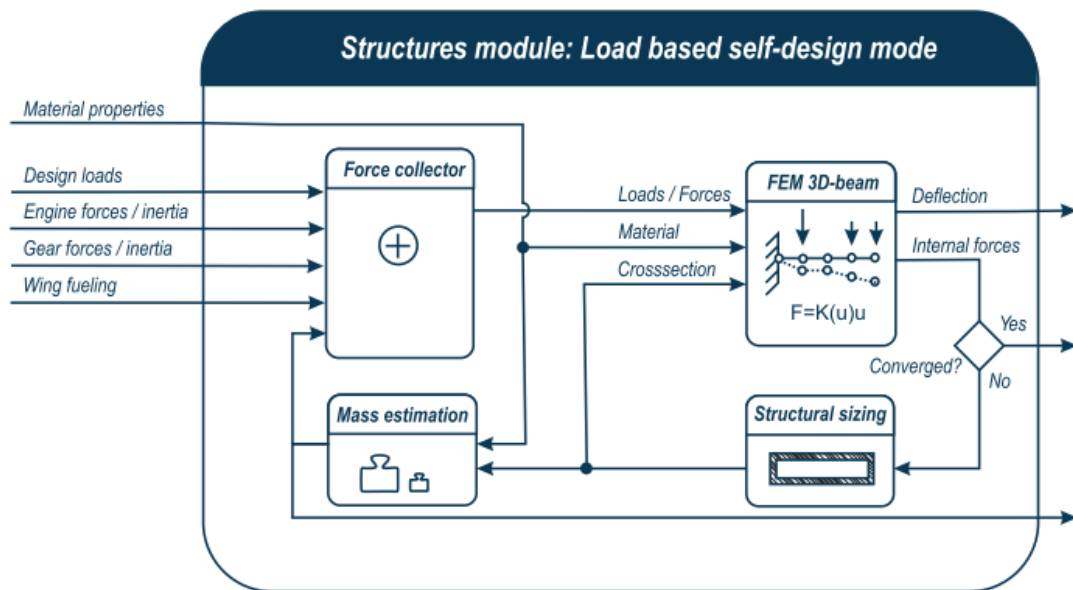
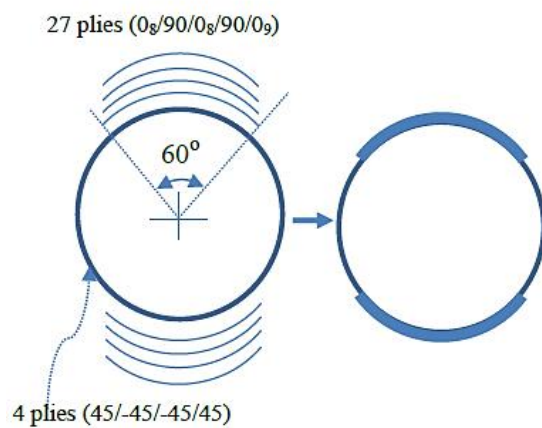
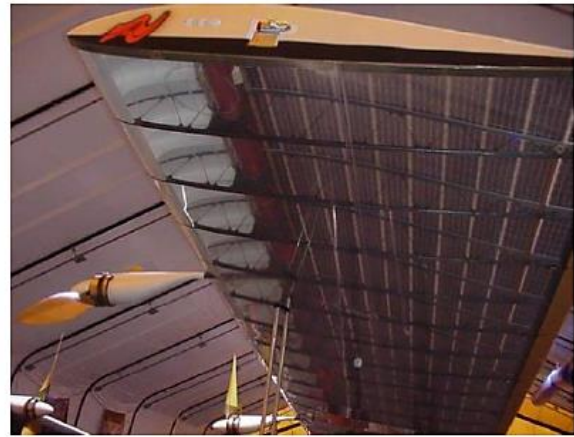


Figure 2-22 Structures Module Running in Self-Design Mode (Seywald, 2011).

High Altitude UAVs tend to possess a high aspect ratio wing to reduce the induced drag. Therefore, it is advisable to exploit the beneficial characteristics of the fibre-based composite materials to increase the stiffness/weight factor. The composite wing is between 34% to 40% lighter than the equivalent metallic wing (Kennedy & Martins, 2012). Helios, Pathfinder, Qinetiq Zephyr and X-HALE and other most existing HALE UAVs use lightweight carbon fibre construction (Giacomo Frulla, 2002; G. Frulla & Cestino, 2008; Romeo et al., 2014; Z. Wang, Chen, Liu, & Mook, 2010). The typical wing structure of most HALE UAVs (such as Helios, Qinetiq Zephyr, and Pathfinder) consists of spars, ribs and skins such as the one shown in Figure 2-23, Figure 2-24 and Figure 2-26. For example, Helios HALE UAV has a single spar which has a circular cross-section. Its spar consists of carbon fibre plies (4 plies of $(\pm 45^\circ)$ and 27 plies of $(0^\circ, 90^\circ)$ plies) reinforced in the 60 degree regions of the top and the bottom of the spar such as shown in Figure 2-23 (Ko, Richards, & Tran, 2007). Another similar example is the structure of Heliplat aircraft shown in Figure 2-24.



Ply Stacking of the main spar as mentioned in (Ko et al., 2007)



Helios Wing Structural (Morrisey, 2009)

Figure 2-23 Wing structural of Helios



Figure 2-24 wing structural of Heliplat (G. Frulla & Cestino, 2008)

Figure 2-25 shows the wing configuration of X-HALE as another example of structure adopted for high altitude aircraft. The wing consists of rectangular composite wing-box (spar) and profile wing skin which are also made from composite materials. The wing was filled in with low weight high compression foam to support the structure against buckling failure and works like a rib (Cesnik et al., 2010). The wing spar is discretised into several segments joined together by Aluminium joiners.

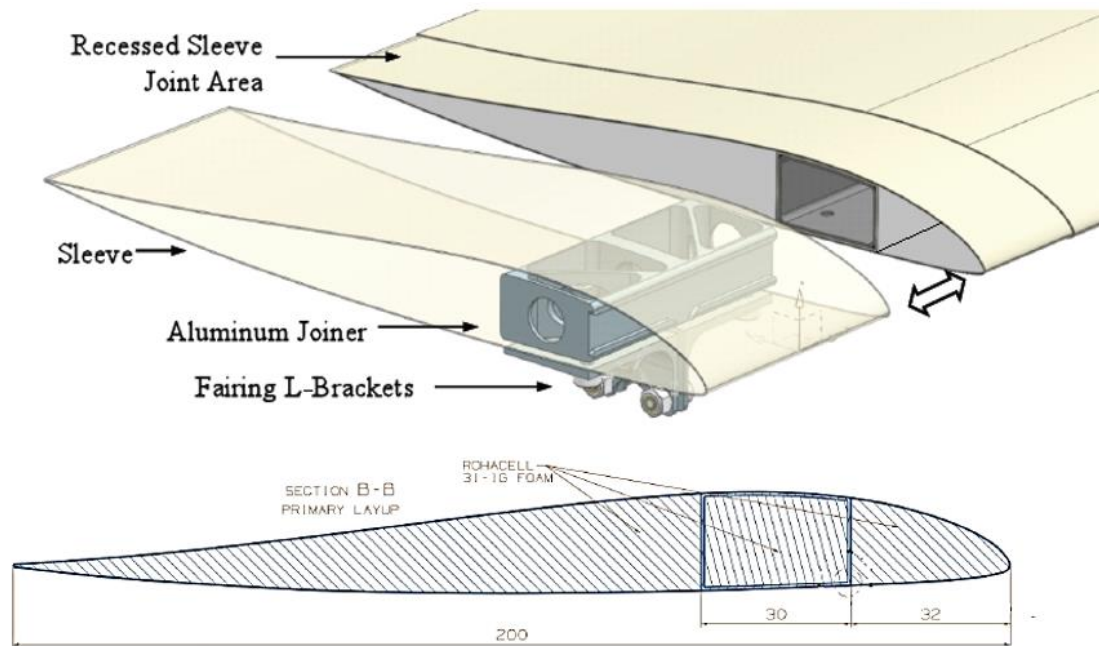


Figure 2-25 Wing configuration of X-HALE (Cesnik et al., 2010)

Several empirical equations were introduced to estimate the weight of the wing elements and other devices according to the mission requirement and aircraft configuration during the preliminary design stage (Colozza, 1993). Lockheed Missiles & Space Company built for NASA, a structure sizing model for high altitude powered platform based on previous designs with other conceptual design efforts (Hall & Hall, 1984). Unfortunately, these estimation models are somewhat outdated due to developments over the last 30 years, especially in term of solar cell and fuel cell efficiencies and their weight densities (Noth(b), 2008). Some of the element weight estimations have been updated by using improved design techniques (Min Chang et al., 2014; P. Guarino, G. L. Cascella, S. Stasi, Dassisti, & Chimienti, 2014; Rizzo & Frediani, 2008; Zhu et al., 2014).

Many studies to design the composite wing spars (wing-box) for aircraft were conducted with the aim of finding the minimum number of plies (lighter weight as possible) capable of withstanding ultimate loads expected with adequate safety margins. Stacking & orientation of plies along with the dimensioning and the location of spars are key parameters when designing a spar. Other component weights are estimated using empirical equations obtained from test results on existing aircraft of the same type. There are only a few studies in literature that model and design a wing structure of a HALE UAV using high order computational analyses. However, they are not suitable for multiple iteration process such as the approach adopted in multi-disciplinary optimisation.

A composite wing-box was designed by (Romeo et al., 2014) for a HALE UAV called SHAMPO using a multi-objective optimisation tool to obtain a lighter structure. Two C-spars were designed and optimised to resist the mechanical, thermal and hygroscopic loads. Buckling failure, cracks, and the maximum tip deflections were investigated. This research was mainly dedicated for structural optimisation in which several parameters necessitated expensive computations.

An analytical mass equation was proposed by (Montagnier & Bovet, 2010) to be implemented in an optimisation tool to find the minimum number of 0° and 45° plies within the spar required to prevent failure under critical loading cases. A circular cross section spar was used as shown in Figure 2-26. The buckling failure was not taken into account but a certain minimum number of plies was adopted to prevent buckling. However, the limitation of this model was that the spar is sized according to a load concentrated on the root section which means that the majority of the spars would have been oversized.

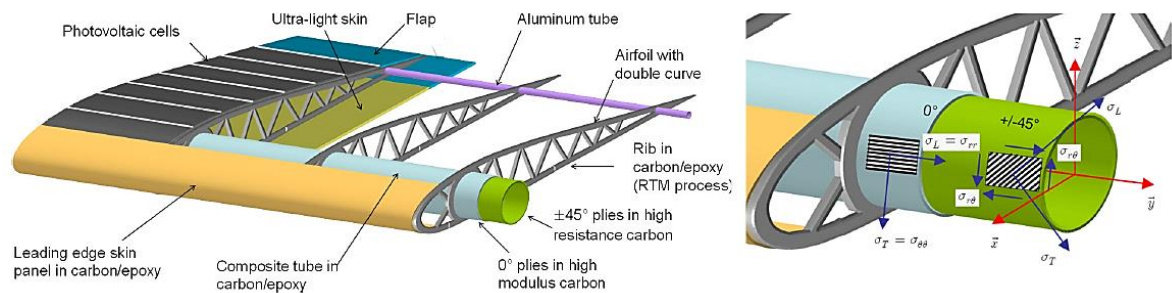


Figure 2-26 Wing configuration (Montagnier & Bovet, 2010)

2.5 Aerodynamic Analysis

HALE UAVs fly at low Reynolds number flight conditions. The aerodynamic characteristics of wing sections at such flight conditions exhibit rapidly-reducing maximum lift-to-drag ratio and possible non-linear behaviour, even at small angles of incidence (Ma & Liu, 2009). Therefore, it is necessary to support the optimisation process by an aerodynamics analysis tool capable of predicting the influence of air viscosity at low Reynolds number and the onset of flow separation. There are many CFD tools giving robust results such as full potential solver, Euler solver, RANS solver and others. However, these tools require excessive computational time and effort and so are not suitable for the multiple solution iterations required by an optimisation algorithm.

The simplest CFD solver methods are based around linear aerodynamics including the Vortex Lattice Method (VLM), Panel Methods (PM) and the Lifting-Line Method (LLM) (Jan Mariens, 2012). These methods are computationally efficient but have several limitations, including neglect of viscous effects as surveyed by (Jan Mariens, 2012) and shown in Table 2-3.

Table 2-3 Comparison of the CFD methods, from (Jan Mariens, 2012)

	Vortex-lattice method	Panel solver	Full potential solver	Euler solver	RANS solver
Governing equations	Linearized potential flow equations	Linearized potential flow equations	Full potential flow equations	Euler equations	RANS equations
Compressibility	using compressibility corrections	using compressibility corrections	'Exact'	'Exact'	'Exact'
Lift coefficient	Yes	Yes	Yes	Yes	Yes
Shockwave prediction	No	No	Inaccurate for strong shocks	Yes	Yes
Pressure distribution on surface	Maybe (inaccurate at leading edge)	Yes	Yes	Yes	Yes
CPU calculation time per case	5 sec. - 1 min.	1 min. - 15 min.	5 min. - 1 hr.	1 - 15 hrs.	Multiple days

The tools Tornado and Athena, which are based on Vortex Lattice Method, are widely-used in the literature, particularly during the preliminary stages of the design process (Ajaj et al., 2013; Jordan Hadjiev, 2013; Khan, Krammer, & Scholz, 2010; M. Martínez, 2012; Rubio, 2013; Seywald, 2011). These inviscid-flow methods give reasonable predictions of lift but can only predict the induced-drag component (Melin, 2001; Pereira, 2012). Viscous effects need to be considered because there are two important physical phenomena governed by fluid viscosity, namely flow separation and transition from laminar to turbulent flow (Houghton & Carpenter, 2003).

A low-order analysis method, called strip method, can be used to evaluate the total drag of the wing. In this approach, the wing induced drag is evaluated using inviscid 3D

aerodynamic solver, whereas the profile drag is evaluated by integrating the section profile drag at corresponding angles of attack and Reynolds number. According to the strip theory, the wing geometry is divided into several two-dimensional spanwise wing sections. Then, for each section, the aerodynamic forces are estimated by using the effective velocity and the effective angle of attack. The aerodynamic performance of each 2D segment is evaluated either using existing experimental data or using a 2D viscous aerodynamic solver. The overall viscous drag is then calculated by integrating the profile drag of the wing segments. However, this approach ignores the three-dimensional nature of the boundary-layer development, particularly important on a swept wing (Houghton & Carpenter, 2003; Jan Mariens, 2012; J Mariens, Elham, & van Tooren, 2014; Moran, 2003; Obert, 2009; Sequeira, Willis, & Peraire, 2006; Trips, 2010).

A quasi-three-dimensional aerodynamic flow solver was developed by (J Mariens et al., 2014) using the concept of the strip method. The method was extended for the implementation of sweep and tapered effects. This solver calculates (by the strip method) the viscous wing drag using the combination of a two-dimensional aerofoil analysis tool (Xfoil) with a 3D Vortex-Lattice code (Athena VLM). The results showed a good agreement with that obtained by a higher-fidelity computational fluid dynamics flow solvers as well as with experimental data as shown in Figure 2-27. This tool was used within a multi-disciplinary optimisation environment to design the wing shape of a typical passenger aircraft.

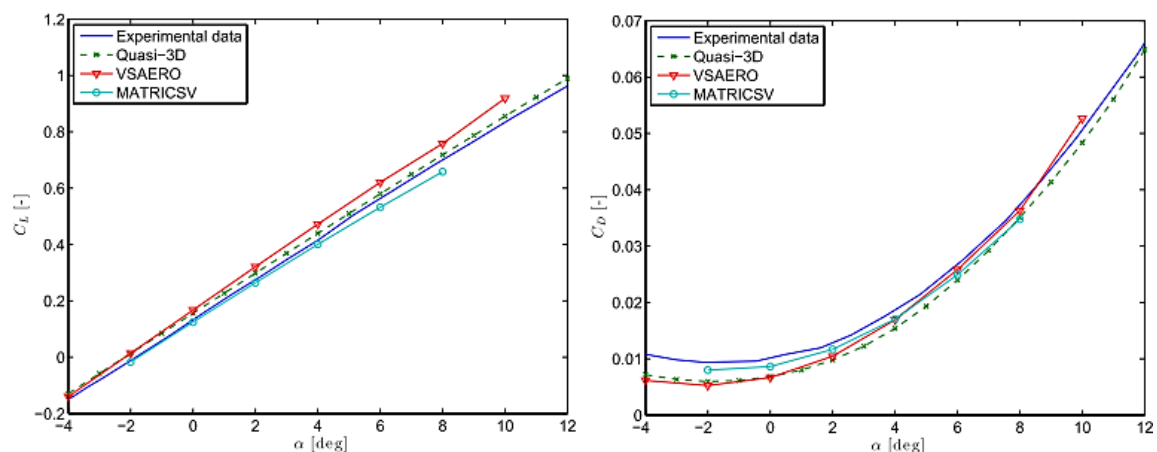


Figure 2-27 Comparison of the Quasi 3D method with experimental data and a high order CFD, conducted in (Jan Mariens, 2012)

2.6 Optimisation Algorithms

Many algorithms to find a global optimum in a solution space have been widely published. These algorithms can be divided into two classes: gradient-based algorithms and non-gradient-based algorithms (Amadori, 2012). In addition, a hybrid algorithm, combining two or more different algorithms, could be facilitated by taking the advantage of the strong points of each algorithm during the optimisation process (Vasseur, 2014).

Genetic algorithms (GA), which are non-gradient based algorithms, have been significantly and successfully used to solve single or multi-objective optimisation problems (Zetina et al., 2013). The GA can deal with the linear and non-linear problems inspired by natural evolution, such as inheritance, mutation, selection and crossover (Coley, 1999; Holland John, 1992). John Holland in 1960 first introduced genetic algorithms and these were developed by Holland and his students and colleagues at Michigan University in the 1960s (Mitchell, 1999). The GA method is widely employed in the field of fluid dynamics. It can search through the entire design variables space (continuous or discrete), which prevents the process being stuck at a locally-optimal design. However, the genetic algorithm approach is computationally more intensive compared to gradient-based algorithms (Della Vecchia et al., 2014; Jan Mariens, 2012).

Gradient-based methods depend on the derivatives of the objective function to direct the search process toward the optimal value. These methods tend to be converged rapidly at an optimal point when compared with non-gradient methods. However, the optimal value may not represent the global optimal and may represent a local optimal value. These problems could be mitigated by defining a probe range for the variables and defining reasonable initial values for the optimisation variables. Examples of these algorithms are the Adjoint Method, the Local Optima Smoothing Principle, Fixed Point Iteration, Interior Point Algorithm (IPA) and Optimiser-Based Decomposition, as well as a few others (Martins, 2002; Morrisey, 2009; Vasseur, 2014).

Nowadays there are many optimisation algorithms facilitated in many design tools or programming platforms, such as the optimisation tools implemented in the MATLAB software.

2.7 Solar powered Aircraft Sizing

Solar powered aircraft use the solar energy and convert it to electrical power. These aircraft can be design to operate for longer endurance flight. To make this work, the daily harvested energy must be enough to operate the aeroplane 24 hours. This means that the solar cells convert the light energy to electricity during the daytime to operate the aircraft and, at the same time, charge the power storage (batteries or fuel cell) by a required power to the night operation. Alternative power storage can be used to eliminate the weight of batteries or fuel cells. This can be called a gravitation potential storage. Its idea came from increasing the altitude of aircraft during the daytime to increase its potential energy. Then at the night time the aircraft will glide without the propulsions system by decreasing its altitude until the sunrise when the solar cell can produce power to drive the thrust system and then again increasing the altitude (Gao et al., 2013). Another approach was suggested by using both the storage power and gravitation potential energy leading to saving in the storage weight (Gao et al., 2013; Zhu et al., 2014).

High altitude aircraft are characterised by their large wing which means a wider covering area can be accommodated by solar cells to supply the needed power for the flight. However, since the flight condition of these aircraft is at low air density, the aircraft weight needs to be minimised (Min Chang et al., 2014).

The energy and mass balance estimates provide a good starting point for the design. Motors, solar cell panels, fuel cells or batteries, as well as avionic systems are characterised according to the power requirements. However, at the same time, the required power depends on the weight of aircraft elements. For this purpose, two different approaches from published literature were adopted to achieve the conceptual design. The first approach is discrete and iterative, and is based on pure estimation for the first set of components (motors, solar cell panels, fuel cell or batteries, and avionic system). From their weight, one can estimate the total weight and required power. The latter power estimation is then compared with the previous estimation, and the process is performed iteratively until a converged solution is found (Noth(b), 2008). The second approach is an analytical and continuous method, which consists of establishing all the relationships between all the components with analytical functions using the component characteristics. Therefore, this approach must be supported by recently developed analytical equations updated with statistical data retrieved from existing relevant aircraft characteristics. The analytical approach can directly provide a unique and optimal design, but requires a robust mathematical model (Mattos et al., 2013;

Noth(b), 2008). The mass and power of each aircraft component can be estimated as a constant fraction of either the structural mass or of the total mass or of the total power. These fractions were evaluated statistically from existing solar powered aircraft data which are likely to improve with future technological developments.

The available solar energy at the service ceiling of aircraft depends on several factors such as operational altitude, latitude, hours of the daylight and day of the year. Other factors which can influence the harvested energy are the shape and the orientation of the solar cells in addition to the overall efficiency (Duffie & Beckman, 1980).

In one of the related studies carried out earlier (Rizzo & Frediani, 2008), a mathematical model was defined to design high altitude long endurance solar-powered UAVs at the conceptual design stage. Their model did not include the weight of the landing gear, avionics, maximum power point tracker device and losses in the electrical instruments. In addition, the parasite drag of aircraft was formulated using a very simple equation which is dependent only on the operational Reynolds number regardless the aerofoil section (thin flat plate analogy). In some of the related work, the drag coefficient was assumed constant regardless of the operational Reynolds number (Noth(b), 2008). In this case the achieved design solution does not represent the problem in adequate detail until a number of iterative design steps were performed at great cost and time. Therefore, employing all the aircraft components and including all the expected losses is likely to produce more accurate estimates. Nevertheless, more accurate results and less effort and time could be achieved if the drag was estimated accurately at the conceptual design stage.

2.8 Stability & Control of Flying Wing Aircraft

A flying wing is essentially a single lifting surface with promises of good aerodynamic and structural properties. However, this comes with several challenges facing designers to achieve a secured level of stability and control.

Only the longitudinal dynamic will be considered in this study due to greater difficulty in achieving adequate control and stability in the absence of a tail. Several design features specific to tailless flying-wing aircraft were utilised or suggested for existing tailless aircraft to enhance vehicle control and stability. Some of the features are summarised below:

- Using reflexed trailing edge aerofoil sections to achieve either positive or low pitching moment necessary to stabilise the aircraft. However, this solution may reduce the lift at a given angle of attack and also reduce the maximum lift coefficient. The location of the maximum camber determines the wing pitching moment but has less influence on the drag polar. Therefore, this feature was used to compensate the reduction in lift in reflexed aerofoils (Buckstrom, 1979; Qin et al., 2004).
- Selecting a suitable combination of sweep and twist distribution to stabilise the aircraft (Li et al., 2012; Mader & Martins, 2012). Sweeping the wing backwards will allow accommodation of the lifting wing area both behind and in front of the aerodynamic centre. A wash-out twist distribution toward the outer section of the wing can be utilised to trim the wing at the cruise condition. Beyond the trim conditions (angles of attack lower than the trimmed angle of attack), the pitching moment resulting from the lift forces generated by the inner sections of the wing which lie in front of the aerodynamic centre, will overcome that generated by the outboard sections which lie behind the aerodynamic centre, leading to positive pitching moment (nose-up). Moreover, opposite case will happen at angles of attack higher than the trimmed angle of attack. Therefore, this technique will offer static stability in the longitudinal mode. Also, sweeping the wing can enhance the stability of the wing in the yaw and roll directions (Nickel & Wohlfahrt, 1994).
- Using the potential for use of differential thrust in multi-engine aircraft to enhance directional stability and control. This approach was used in NASA's HALE UAVs (Cesnik & Su, 2011).
- Using split ailerons and spoiler deflections for yaw control with possible coupling effects in roll and pitch (D. F. Anderson & Eberhardt, 2001; Whitford, 2007).

- Using elevons for roll or pitch control (L. Wang & Wang, 2012).
- Using a suitable dihedral distribution to enhancement the lateral stability (Song, Yang, Zhang, Zhang, & Huang, 2014).
- Using winglets or C-wings to reduce induced drag and enhance directional stability & control (Bolsunovsky et al., 2001; Martinez-Val, Perez, Alfaro, & Perez, 2007).
- Using integrated control systems (electric stability augmentation systems) to manage the coupling between all three axes. This approach has recently become more relevant thanks to the evolution in computer systems (D. F. Anderson & Eberhardt, 2001; L. Wang & Wang, 2012).

High altitude aircraft have a large, light and flexible structure leading to major aeroelastic issue which may affect aircraft stability. Previous studies conducted on flexible wing structure found that the elastic deformations can influence the spanwise aerodynamic loads leading to a forward shifting of the aerodynamic centre. But there will be a reduction in longitudinal stability in addition to reducing the lift-curve slope and hence the trimmed angle of attack (Skoog, 1957; Weyl, 1945).

As far the author knows, the swept flying wing configuration for high altitudes application has not been considered by other researchers at the start of this project. However, swept wing configuration of conventional aircraft were studied and it was concluded that the torsional deflections had a stabilising influence whilst the bending deformations tended to destabilise (Skoog, 1957). The overall effect of these two influences is dependent on the sweep angle, the location of the spar and the ratio of the bending to torsional stiffness factors (Kroo, 1993; Raghavan, 2009).

2.9 Overview

Different high altitude aircraft types such as the tailed and straight flying wing configurations in addition to the conceptual designs based on biplanes were studied in detail. A true swept flying-wing configuration had not been investigated in any detail for possible such applications. Therefore, it will be the interest to study the possibility and the challenges of using this configuration due to higher aerodynamic efficiency than that of corresponding tailed aircraft and more beneficial stability characteristics.

A comparison in terms of the endurance and payload capacity for existing HALE UAVs showed that the achievable endurance of solar-powered aircraft is significantly larger than that of consumable-fuel powered aircraft but with limited payload. A robust conceptual

design tool is needed for estimating and balancing the required power and the expected weight of the aircraft elements. Therefore, employing all the aircraft components and including all the expected losses will also be of interest to produce more accurate estimates for the power and mass of each aircraft element. Also, more accurate results and less effort and time could result if a more robust drag estimation method is considered.

High altitude aircraft with large wingspans and low structural weight will make the airframe more flexible. The wing elastic deformations are influenced by the aerodynamic loads and hence results of the structural analysis during the preliminary design stage will be needed to study the stability characteristics. Previous studies did not adequately address the issues at an elemental level and therefore a low order structural model using composite materials for HALE UAVs is needed for a reasonable estimate for the initial weight and the elastic deformations.

Solar powered HALE UAVs flying at moderate flight speeds at low air density indicate flight at low Reynolds numbers. Therefore, the viscous effects become more dominant leading to an increase in the drag and reduced maximum lift coefficient. However, such a solver would consume a great deal of time to iterate around an optimisation point. Therefore, a quasi-3D aerodynamic solver can be implemented in the optimisation tool due to its faster algorithms and acceptable levels of accuracy for estimating the profile drag.

Several design concepts have been studied by many researchers using multi-disciplinary optimisation tools. A balanced compromise between the inter-disciplinary variables is needed to be produced within a multi-disciplinary optimisation process. The various analysis models within the optimisation environment need to be robust, computationally efficient and as accurate as possible. Therefore, a quasi-3D aerodynamic solver and a low order structural model would be used to develop a design/optimisation tool to produce a reasonable estimate for the aerodynamic and structural performances.

CHAPTER 3

3 METHODOLOGY FRAMEWORK

The overall design process and the major design tools which were developed by the author are presented in this chapter. The conceptual and the preliminary design approaches focusing on a high altitude long endurance solar powered aircraft were developed.

3.1 Overall Design Procedure

In this research, only the conceptual and preliminary design stages are presented using low fidelity design tools coded in the MATLAB environment. At the conceptual design stage, the aircraft weight and its elements are sized using a mathematical approach supported by statistical data retrieved from existing aircraft of similar flight profiles. The outcome from this stage was then utilised as a baseline for the preliminary design stage in which the final wing geometry was designed to meet the mission requirements.

The design process begins with the mission requirements starting with the geographic location (latitude and longitude), flight level (altitude), endurance (including the start and the end dates) and mass & power of the payload system. Then, a solar model was used to calculate the available solar energy at the given mission. The resulting design space from the conceptual design tool led to the initial estimate for the minimum weight of the aircraft. Subsequently, the optimal sweep and twist of the wing was designed using a multi-disciplinary optimisation tool to achieve an operational aircraft. Only the longitudinal static stability was constrained in the optimisation process. The outcome from the preliminary design stage was then assessed relative to the mission requirements and the main characteristics resulting from the conceptual design. The overall design steps are presented in Figure 3-1. The basis of each tool will now be summarised.

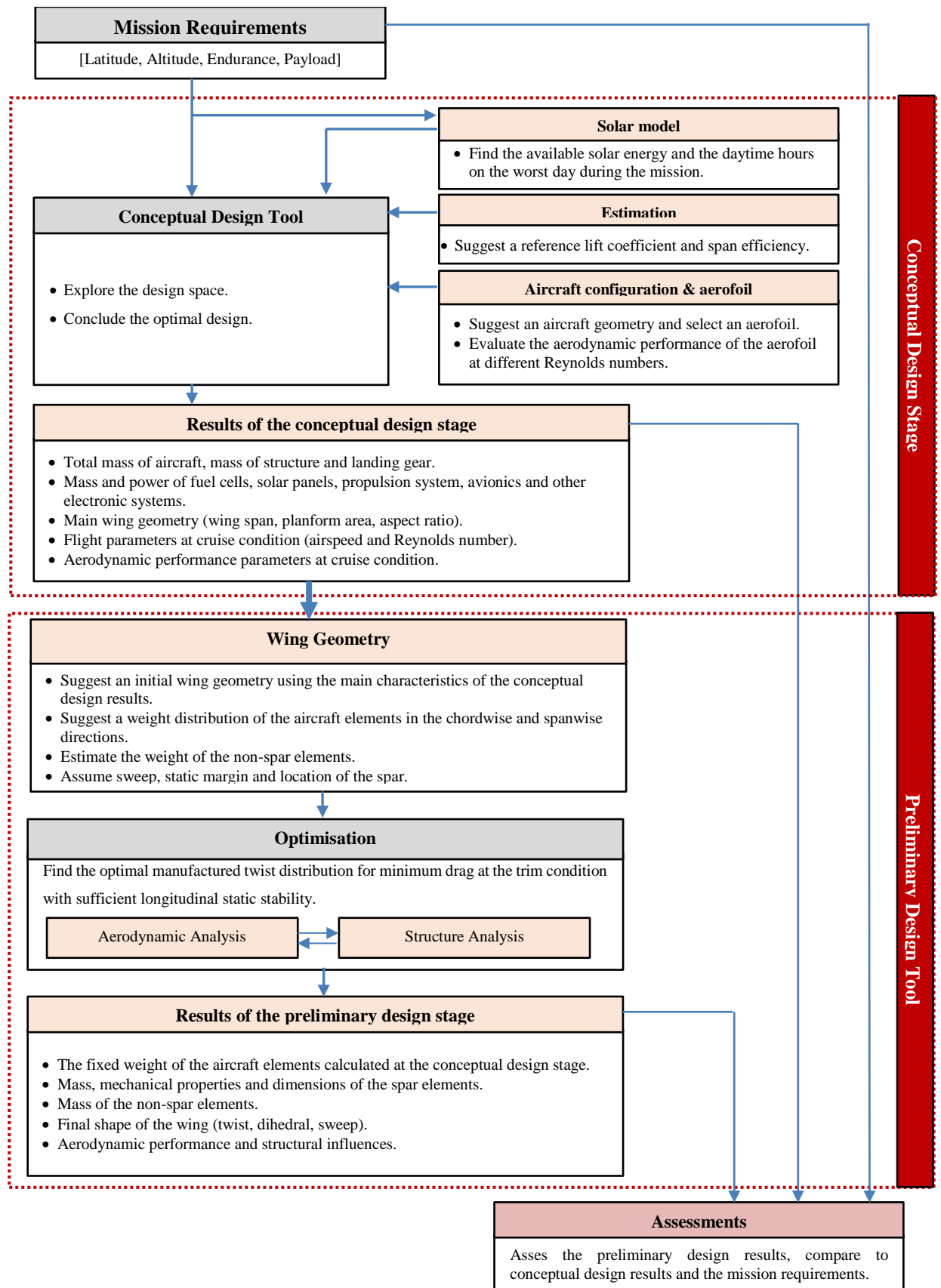


Figure 3-1 Overall design procedure

3.2 Conceptual design tool

A new mathematical model has been developed to represent all aircraft elements and related power requirements. The final equation can be solved in accordance with the wingspan and the aspect ratio. The methodology which has been followed is as follows:

- Develop a mathematical equation for the mass employing all aircraft elements. Mass and/or power of each element are represented as a fraction of the total mass or the required power for the aircraft. The fractions were gathered from data relating to similar studies elsewhere. The resulting equation will be a function of aspect ratio and span in addition to other fixed parameters.
- Consider the expected losses in the power by the aircraft elements.
- Represent the profile drag of the aircraft as a function of the operational Reynolds number and the aerofoil characteristics.
- Build a tool according to this methodology to solve the equation for the mass for a given mission requirement. The design space would be illustrated in order to directly conclude the optimal design.
- Validate the tool by comparing results relating to similar aircraft.
- Investigate the influence of the altitude, latitude, reference aerodynamic parameters (reference lift coefficient and span efficiency) and the payload on the main characteristics of the aircraft.

3.3 Aerofoil Design & Selection

This part is concerned with gathering data from some of the existing aerofoils which were optimised for tailless aircraft in order to study the aerodynamic performance. Also, a low order aerofoil optimisation has been built to investigate how the design constraints can influence the aerofoil performance in addition to designing a number of aerofoils suitable for aft-swept flying wing aircraft at low Reynolds number of about 0.5×10^6 . The study would be completed by selecting a candidate aerofoil appropriate to an aft swept flying wing configuration. The entire process can be summarise as follows:

- 1- Gather information about the aerofoils used within existing high altitude tailless aircraft. Moreover, make a comparison of their aerodynamic performance.
- 2- Build an aerofoil shape optimisation tool to design new aerofoils with different thicknesses and pitching moment coefficients by individually directing the optimisation toward maximising the aerodynamic and endurance efficiencies.

The aerofoil shape optimisation tool has three main parts:

- Aerofoil parametrisation: A combination of PARSEC and Bezier methods has been used to achieve a fast and efficient representation of the aerofoil surfaces.
 - Aerodynamic solver: The Xfoil software has been used as an aerodynamic solver due to its good estimation properties.
 - Optimiser tool: A Genetic Algorithm which has been used in addition to some of the existing algorithms built within the MATLAB environment.
- 3- Select one of the newly designed aerofoils to be used in the aircraft case study.
 - 4- Validate the results using high-order computational fluid dynamic package (FLUENT) at different Reynolds numbers.

3.4 Preliminary design tool

In this tool, the aircraft shape and the wing geometry will be designed using the main characteristics of the aircraft which were obtained from the previous design stage. The outcome would be a flyable aircraft geometry capable of meeting the mission requirements. In addition, the aerodynamic performance of the final design must meet the results obtained at the conceptual design stage. A design optimisation framework has been built within the MATLAB environment containing aerodynamic and structural tools. The aims of this tool were:

1. Build a low order aerodynamic solver capable of predicting the aerodynamic forces including the wing profile drag.
2. Build a composite structure model to conduct the following targets:
 - a. Size the wing and estimate its weight and mechanical properties
 - b. Evaluate the elastic wing deformations
3. Validate each model using either experiment data or a high order analysis package.
4. Build a design/optimisation tool combining the aerodynamic and structure models.
5. Employ static aeroelasticity by coupling the aerodynamic and structural models.

3.4.1 Aerodynamic Solver (Quasi 3DM)

A quasi-three-dimensional aerodynamic solver (Quasi 3DM) has been built using a Vortex Lattice Method coupled with a two-dimensional one-way inviscid-viscous model (IVM). The Tornado VLM was used to evaluate the lift force and the induced drag for the wing geometry. A two-dimensional panel method coupled with an integral boundary-layer method has been built to assess the 2D profile drag in a strip-wise sense. The profile drag of the entire wing is evaluated using the strip theory by integrating the 2D profile drag of the wing sections. The overall components which consisted of the Quasi 3DM are presented in Figure 3-2 while the models of boundary layer equations are presented in Figure 3-3.

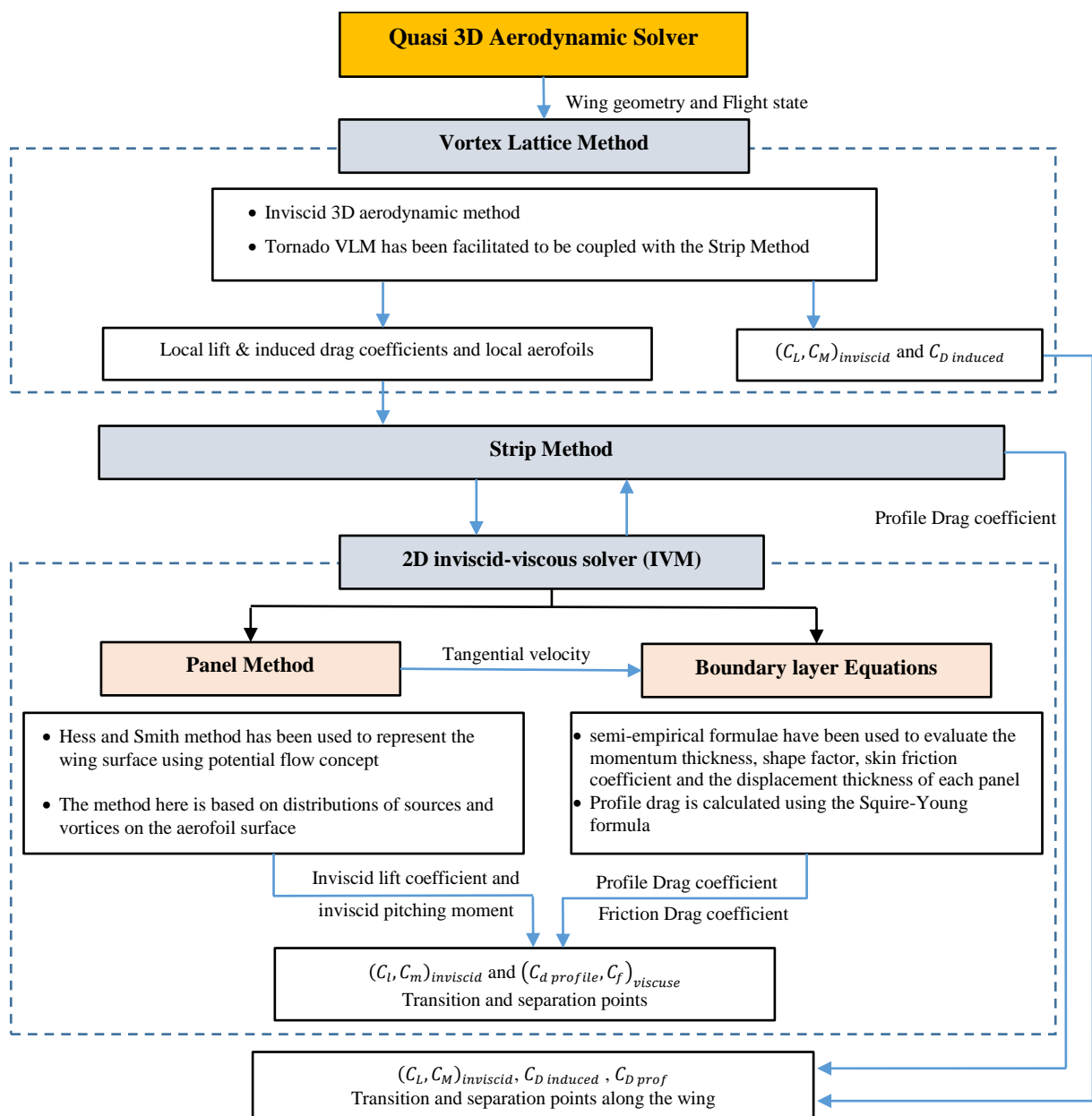


Figure 3-2 Concept of the quasi-three-dimensional aerodynamic solver

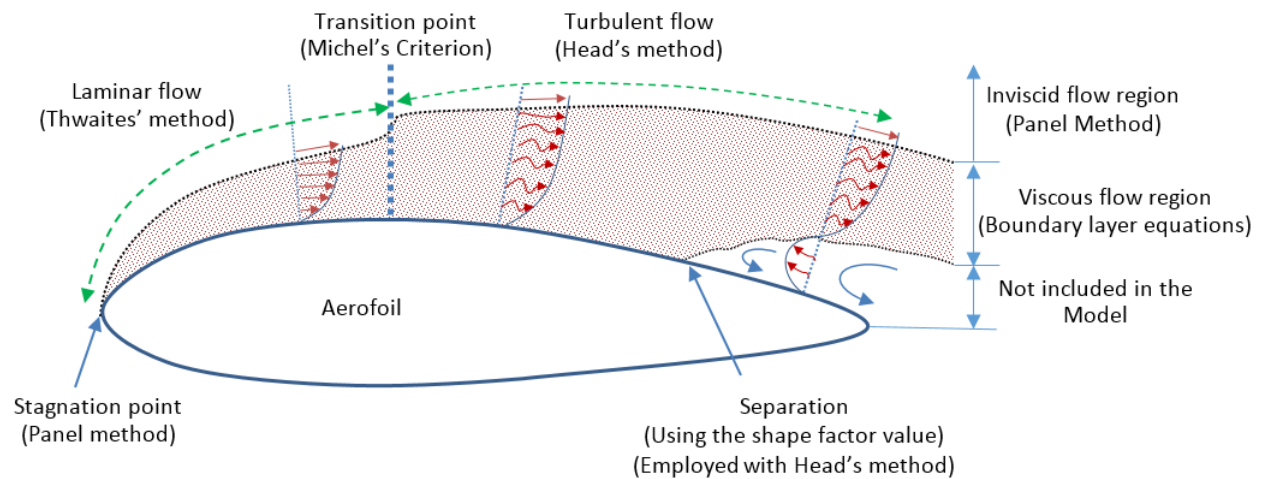


Figure 3-3 The concept of the 2D Inviscid/Viscous Model (IVM) for the aerofoil

3.4.2 Composite Structure Model

This model can design the wing structure for the given critical loads in addition to evaluating the elastic deformation of the wing using linear finite beam elements method. The non-spar elements of the wing were sized using empirical equations which are functions of the wing geometry while the spar element was designed using the concept of the required composite layers within the spar to withstand the ultimate loads. The spar has been modelled as a composite rectangular thin-walled beam and assumed to resist the entire load with no contribution from the secondary wing components. The spar was discretised into segments to be designed according to the critical loads exerted on that segment. An iterative process has been adopted to find the minimum composite layers required in each side (flanges and webs) of each spar segment. Figure 3-4 shows the overall procedure of the structural design process of the wing.

The weight estimation and the stress analysis of the structure model have been validated using existing data for related aircraft (Helios P03) and a high order analysis package (ANSYS) respectively.

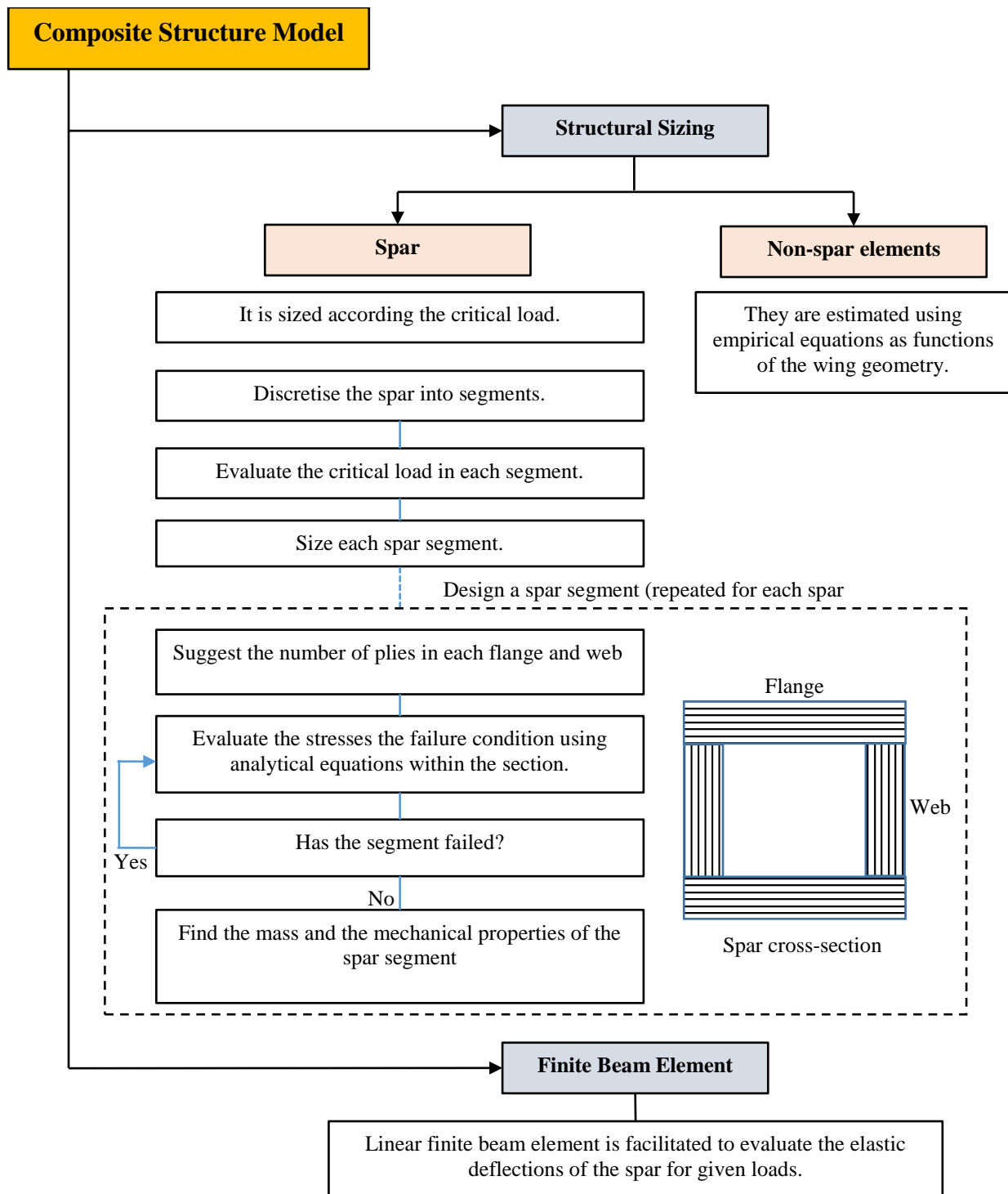


Figure 3-4 Overview of the composite structure model

3.4.3 Optimisation tool

A design optimisation framework has been developed within a MATLAB environment combining the quasi-3D aerodynamic and the composite structure models as indicated in Figure 3-5. The design variables were the manufactured twist distribution of the wing whilst the objective was to minimise the total drag coefficient at the flight trim condition. The aircraft performance at the cruise condition was the design focus and no other operational considerations were addressed. The trim condition would be at the reference lift coefficient that was adopted at the conceptual design stage. Therefore the objective of the optimisation was formulated as follows:

$$\text{minimise } (|C_{L \text{ Ref}} - C_{L \text{ trim}}| + C_{D \text{ trim}})$$

where $C_{L \text{ Ref}}$ is the reference lift coefficient, $C_{L \text{ trim}}$ is lift coefficient at the trim condition and $C_{D \text{ trim}}$ is the total drag coefficient at the trim condition.

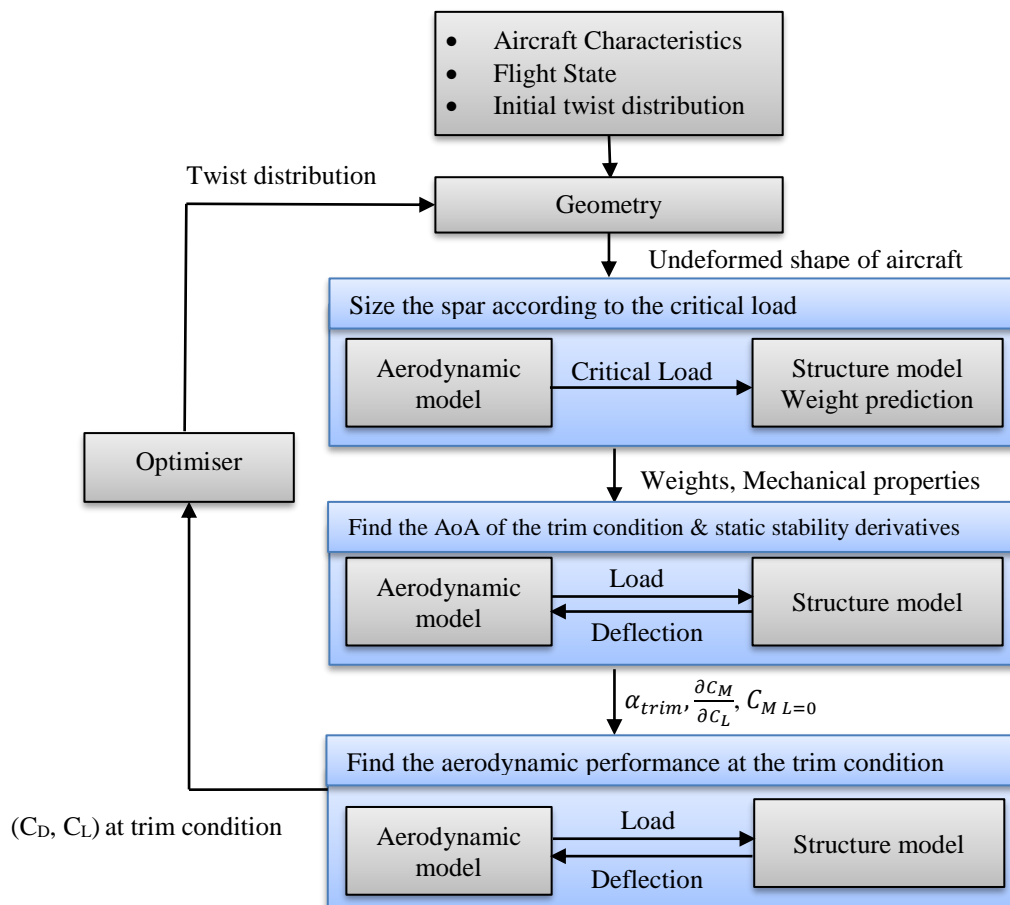


Figure 3-5 Optimisation flow

CHAPTER 4

4 CONCEPTUAL DESIGN of SP HALE UAVs

Solar powered high altitude, long endurance, unmanned aerial vehicles (SP HALE UAVs) use solar irradiance as a source of power, which in turn is a function of the geographical parameters and the capability of solar cell panels. In theory, for long endurance missions, the aircraft can fly continuously if the energy collected during the daytime is adequate to power the aeroplane day and night (Gao et al., 2013). It is apparent that the energy and mass balance estimates provide a good starting point for the design. Motors, solar cell panels, fuel cells or batteries and avionics systems are characterised according to the power requirements. However, at the same time, the required power depends on the weight of the aircraft elements. The mass and power of each aircraft component can be estimated as a constant fraction of either the structural mass or the total mass or the total power (Mattos et al., 2013; Noth(b), 2008). Therefore, this approach must be supported by recently developed analytical equations updated with statistical data retrieved from existing relevant aircraft characteristics.

In this chapter, a mathematical approach has been developed to design high altitude solar-powered aircraft, for given mission requirements at the conceptual design stage. The mass and power requirement of each component are estimated as a fraction of either the structural mass or the total mass or the total power. The drag equation is defined as a function of the Reynolds number and the characteristics of the aerofoil to reduce the effort and time required to compute the results to reasonable levels of accuracy. Another object of this study is to explore the influence of the reference altitude, latitude and endurance on the aircraft weight and its other main characteristics.

4.1 Power for Level Flight (P_{lev})

The governing equations for the balance of forces of aircraft are used to represent the required power for cruise flight. Assuming that the aircraft will be designed to operate at a specified reference altitude for long endurance and no particular manoeuvres, the weight of the aircraft in level flight will be equal to the lift force:

$$Gross\ weight = m\ g = Lift = C_{Lref} \frac{\rho}{2} S V_{\infty}^2 \quad (4.1)$$

where S is the planform wing area, ρ is the air density, C_{Lref} is the design reference lift coefficient of the aircraft and m is the total mass.

Accordingly, air velocity (V_{∞}) can be expressed as:

$$V_{\infty} = \sqrt{\frac{m\ g}{C_{Lref} \frac{\rho}{2} S}} \quad (4.2)$$

Similarly the drag must be equal to the thrust (T):

$$T = Drag = C_D \frac{\rho}{2} S V_{\infty}^2 \quad (4.3)$$

where C_D is the total drag coefficient.

The mechanical power required for level flight (P_{lev}) can be defined as (Gao et al., 2013; Manuel, 2013)

$$P_{lev} = T \cdot V = \frac{C_D}{C_{Lref}^{1.5}} \sqrt{\frac{(mg)^3}{S}} \sqrt{\frac{2}{\rho}} \quad (4.4)$$

Alternatively, by using the definition of the wing aspect ratio AR, the power required for the level flight can be written as:

$$P_{lev} = \frac{C_D}{C_{Lref}^{1.5}} \sqrt{\frac{2AR\ g^3\ m^{1.5}}{\rho\ b}} \quad (4.5)$$

where b is the span. AR is the aspect ratio.

The power losses in the gearbox, propeller, motors and the controller can be considered by taking into account their efficiencies $\eta_{grb}, \eta_{plr}, \eta_{mot}, \eta_{ctrl}$ respectively.

The required power for a given payload (P_{pld}), avionics systems (P_{av}), and, the voltage converter efficiency (η_{bec}) also need to be considered. Thus, the total electric power consumption ($P_{elec\ tot}$) can be given by:

$$P_{elec\ tot} = \frac{1}{\eta_{los}} P_{lev} + \frac{1}{\eta_{bec}} (P_{av} + P_{pld}) \quad (4.6)$$

where:

$$\eta_{los} = \eta_{ctrl} \eta_{mot} \eta_{grb} \eta_{plr} \quad (4.7)$$

4.2 Power Management

The power source for these long endurance aircraft is the solar energy obtained during the daytime (T_{day}) and must be adequate to operate the aircraft over a 24-hour period ($T_{day}+T_{night}$). The solar energy can be saved using efficient storage schemes such as fuel cells or batteries. The performance of the power storage capability during the charging and the discharging cycle may not be ideal and hence this has to be taken into account by employing the charging and the discharging efficiencies η_{chrg} and η_{dchrg} . The total energy required ($E_{elec\ tot}$) over a 24-hour period for level flight can be evaluated by:

$$E_{elec\ tot} = P_{elec\ tot} \left(T_{day} + \frac{T_{night}}{\eta_{chrg} \eta_{dchrg}} \right) \quad [W] \quad (4.8)$$

This amount of energy must be equal to that harvested from sun by the photovoltaic array. The available solar energy depends on several factors such as the altitude, latitude, shaping of the solar panel, the number of daylight hours and the time of the year (P. Guarino et al., 2014; Zhu et al., 2014). A simple model can be used to estimate the solar power consumed by a flat solar cell associated with the maximum irradiance and the daytime period of the operating latitude (Noth(b), 2008). This model assumes that the daytime solar irradiance can be simplified by a sinusoidal function. Therefore, the available solar energy per unite area (E_{day}) will represent the total area under the daily irradiance curve (Duffie & Beckman, 1980; Noth, Siegwart, & Engel, 2007; P. Guarino et al., 2014; Rizzo & Frediani, 2008):

$$E_{day} = \frac{I_{max} T_{day}}{\pi/2} \quad [J/m^2] \quad (4.9)$$

where I_{max} is the maximum irradiance of the daytime period. The available solar energy can be evaluated using an empirical model as a function of the altitude and the solar elevation angle as will be detailed in section 4.5.

The effects of the curvature of the panel, solar cell efficiency, power adapter efficiency and the influence of the weather conditions can be employed in the energy equation according to their efficiencies η_{cbr} , η_{sc} , η_{mppt} , and η_{wthr} respectively:

$$E_{elec\ tot} = \frac{I_{max} T_{day}}{\pi/2} A_{sc} \eta_{cbr} \eta_{sc} \eta_{mppt} \eta_{wthr} \quad [J] \quad (4.10)$$

where A_{sc} is the total solar cell area.

A constant value for $\eta_{cbr}=90\%$ can be set to represent the curvature effect, which means approximately 10 percent energy decrease due to the variation of the incidence angle on the solar cells for a cambered wing during a whole day (Noth(b), 2008). Due to the invariably clear sky at high altitudes, the weather influence will be ignored ($\eta_{wthr}=100\%$).

4.3 Mass Estimations Models

Empirical equations based on data published for existing solar UAVs have been used to estimate the weight of aircraft systems. The mass of each aircraft component can be estimated as a constant fraction of either the total mass or of the power. These fractions were evaluated statistically from existing solar powered UAV data which are likely to improve with future technological developments.

4.3.1 Structure Mass Prediction

In the conceptual design stage, the structural weight (m_{af}) is usually estimated in a parametric manner as a function of the wing span (b) and the wing area (S) in addition to the load factor. Number of statistical equations have been developed using data for existing aircraft such as that proposed by W. Stenderas (Stender, 1969) which was widely adopted in many design cases. Another approach was used by considering the structural weight proportional to the wing area. For instance, Brandt evaluated the structural weight as a ratio 0.97 kg/m^2 for his 61m span HALE UAV (Brandt & Gilliam, 1995); Zhu & et al. assigned 2 kg/m^2 to represent the weight of structure and the solar cells in their design cases (Zhu et al., 2014). For good estimation purposes, some authors modified Stenderas's model by excluding non-related aircraft from the database and develop a new model valid for some aircraft type as surveyed in (Noth(b), 2008). Rizzo (Rizzo & Frediani, 2008) developed an estimation model obtained by interpolating data for NASA prototypes. This model is given by:

$$m_{af} = 15.19 b^{0.656} S^{0.651} \quad [m_{af}: \text{kg}, b: \text{m}, S: \text{m}^2] \quad (4.11)$$

The major aircraft parameters proposed in this study, such as the range of the payload capacity, altitude and endurance, are similar to the NASA prototypes. Therefore, Rizzo's model will be utilised for the conceptual design stage. However, the wing structure will be designed at the preliminary design stage according to the critical aerodynamic loads. Then, the resulting weight will be compared with that obtained at the conceptual stage.

Using the definition of the aspect ratio ($AR=b^2/S$), Rizzo's model can be represented as a function of the span and aspect ratio of the wing as:

$$m_{af} = K_{af} b^{x1} AR^{x2} \quad (4.12)$$

where $K_{af} = 1.548 \left[\frac{\text{kg}}{\text{m}^{1.312}} \right]$, $x1 = 1.312$ and $x2 = -0.0046$.

4.3.2 Mass of the Solar cells

The solar panel usually covers the upper wing surface; hence it should be limited by the wing area during the design iterations. Basically, the efficiency of the solar cell per its mass density is desired to be as high as possible. The required area to be paved by solar cells can be represented as a percentage of the wing planform area can be designed to be maximum as it may not cover the whole wing (e.g. the solar cells cover 75% of the wing area of Pathfinder and 80% of that of the Helios). The mass of the solar cells can be evaluated by

$$m_{sc} = A_{sc}(K_{sc} + K_{enc}) \quad (4.13)$$

where K_{sc} and K_{enc} are the mass density of solar cells and mass density of encapsulation. The area of solar cells can be evaluated using equations (4.8) and (4.10)

$$\frac{I_{max} T_{day}}{\pi/2} A_{sc} \eta_{cbr} \eta_{sc} \eta_{mppt} \eta_{wthr} = P_{elec\ tot} \left(T_{day} + \frac{T_{night}}{\eta_{chrg} \eta_{dchrg}} \right)$$

Therefore the solar cell area can be written as

$$A_{sc} = \left(\frac{Q_1}{\eta_{los}} P_{lev} + \frac{Q_1}{\eta_{bec}} (P_{av} + P_{pld}) \right) \quad (4.14)$$

where:

$$Q_1 = \frac{\pi \left(T_{day} + \frac{T_{night}}{\eta_{chrg} \eta_{dchrg}} \right)}{2 \eta_{cbr} \eta_{sc} \eta_{mppt} \eta_{wthr} I_{max} T_{day}} \quad (4.15)$$

For instance, the solar cell (Triple-Junction ELO Tabbed) manufactured by MicroLink can be used for the design due its high efficiency $\eta_{sc} = 30\%$ and its low mass density $K_{sc} = 0.25 \text{ kg/m}^2$ (MicroLink, 2017).

4.3.3 Mass of the Maximum Power Point Tracker

Using solar cells with varying power density during the day, necessitates adapting the voltage to provide the highest possible power absorption. The use of a maximum power

point tracker instrument is used for this purpose (Gao et al., 2013). Its mass (m_{mppt}) can be assessed according to the solar power consumed $P_{sol\ max}$ by:

$$m_{mppt} = K_{mppt} P_{sol\ max} = K_{mppt} A_{sc} I_{max} \eta_{cbr} \eta_{sc} \eta_{mppt} \quad (4.16)$$

where (K_{mppt}) is the mass density of the maximum power point tracker.

Noth estimated statistically the mass density of the maximum power point trackers developed in a number of solar aircraft and solar cars; it is about $K_{mppt}=0.00047$ kg/W (Noth(b), 2008). A similar value was taken for designing a high altitude solar aircraft with $\eta_{mppt}=95\%$ efficiency in (Gao et al., 2013; Min Chang et al., 2014).

4.3.4 Mass of the Storage System

The fuel cells are used as a power storage instead of batteries because of its low weight to power ratio in addition to its high efficiency. Figure 4-1 shows typical fuel cell components which are used in NASA prototypes UAV (Colella & Wenneker, 1994). The mass of fuel cell components is directly proportional to the energy needed for night time operation which in turn is associated with the total electric power and the night time period. The total mass of the storage system (m_{fc}) can be estimated by

$$m_{fc} = \frac{T_{night}}{\eta_{dchrg} K_{fc}} P_{elec\ tot} \quad (4.17)$$

where K_{fc} is the specific energy of the entire storage system including the fuel cell.

An energy storage system, based on dedicated electrolysis and fuel cells, gives an energy density of 400–600 Wh/kg. The reference value taken in the design of SHAMPO UAV was about $K_{fc}=550$ Wh/kg with a discharge efficiency $\eta_{dchrg}=60\%$ (Enrico Cestino, 2006; E. Cestino et al., 2007). This reference value was taken in different design cases such as in (Najafi, 2011; Rizzo & Frediani, 2008; Zhu et al., 2014).

Now, by substituting the equation for $P_{elec\ tot}$ in the last equation,

$$m_{fc} = \frac{T_{night}}{\eta_{dchrg} K_{fc} \eta_{los}} P_{lev} + \frac{T_{night}}{\eta_{dchrg} K_{fc} \eta_{bec}} (P_{av} + P_{pld}) \quad (4.18)$$

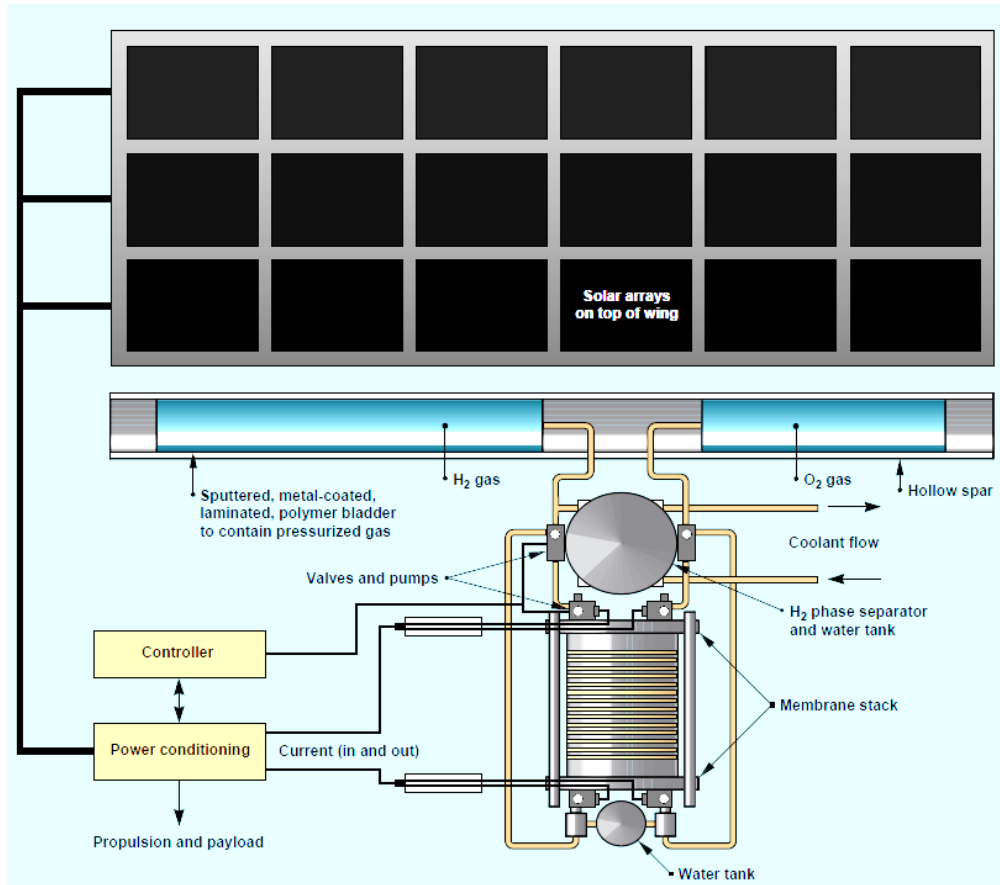


Figure 4-1 Fuel Cell Subsystem, Including Storage of Reactant Gases in the Wing Spar (Colella & Wenneker, 1994).

4.3.5 Mass of the Propulsion Group

The propulsion group consists of the electric motors, propeller, gearbox, and controller. The entire weight of the propulsion system can be simplified to be linearly scaled with the power requirements (Guarino, Stasi, Dassisti, & Chimienti, 2013):

$$m_{prop} = \frac{K_{prop}}{\eta_{los}} P_{lev} \quad (4.19)$$

where: (K_{prop}) is the weight density of the propulsion group.

Data retrieved for brushless electric motors used in NASA's prototypes and SHAMPOO UAV indicate that the mass to power ratio of the propulsion system is $K_{prop} = 0.0045$ kg/W with electric efficiency $\eta_{mot} = 95\%$, propeller efficiency $\eta_{ptr} = 85\%$ and gearbox efficiency $\eta_{grb} = 95\%$ (Enrico Cestino, 2006; Noll et al., 2004).

4.3.6 Mass of the Avionics and Landing Gear

The masses of the avionics systems and the landing gear (m_{av} and m_{lg}) can be estimated as a constant ratio of the total aircraft mass (Min Chang et al., 2014; Montagnier & Bovet, 2010):

$$m_{av} = K_{av}m \quad (4.20)$$

$$m_{lg} = K_{lg}m \quad (4.21)$$

where K_{av} and K_{lg} are the avionics and landing gear weight fractions.

The required power of the avionics systems is scaled with the avionics mass:

$$P_{av} = K_{Pav}m_{av} = K_{Pav}K_{av}m \quad (4.22)$$

where K_{Pav} is the power-to-mass factor of the avionics systems as a whole.

In technical reports accomplished by NASA, the mass of the avionics system was estimated as 3% of the gross weight ($K_{av} = 0.03$) and its power requirement was estimated about $K_{Pav} = 6.0$ W/kg (Bailey & Bower, 1992; Hall, Fortenbach, Dimiceli, & Parks, 1983; Hall & Hall, 1984). Also, the mass of the landing gear was represented as 1.2% ($K_{lg} = 0.012$) of the total mass (Craig L. Nickol 2007).

4.3.7 Gross Weight of Aircraft

The total mass m of the aircraft is the sum of all the component weights:

$$m = m_{payload} + m_{af} + m_{sc} + m_{mppt} + m_{av} + m_{lg} + m_{fc} + m_{prop} \quad (4.23)$$

Using the mass equations of each element:

$$\begin{aligned} m = & m_{payload} + K_{af} b^{x1} AR^{x2} + A_{sc}(K_{sc} + K_{enc}) + K_{mppt} A_{sc} I_{max} \eta_{cbr} \eta_{sc} \eta_{mppt} \\ & + K_{av}m + K_{lg}m + \frac{T_{night}}{\eta_{dchrg} K_{fc} \eta_{los}} P_{lev} + \frac{T_{night}}{\eta_{dchrg} K_{fc} \eta_{bec}} (P_{av} + P_{pld}) \\ & + \frac{K_{prop}}{\eta_{los}} P_{lev} \end{aligned}$$

By substituting P_{av} and A_{sc} in the last equation, and simplifying it:

$$\begin{aligned} m = & m_{payload} + K_{af} b^{x1} AR^{x2} + A_{sc}(K_{sc} + K_{enc} + K_{mppt} I_{max} \eta_{cbr} \eta_{sc} \eta_{mppt}) \\ & + K_{av}m + K_{lg}m + \frac{T_{night}}{\eta_{dchrg} K_{fc} \eta_{los}} P_{lev} \\ & + \frac{T_{night}}{\eta_{dchrg} K_{fc} \eta_{bec}} (K_{Pav} K_{av}m + P_{pld}) + \frac{K_{prop}}{\eta_{los}} P_{lev} \end{aligned}$$

$$\begin{aligned}
m = m_{payload} + K_{af} b^{x1} AR^{x2} + & \left(\frac{Q_1}{\eta_{los}} P_{lev} + \frac{Q_1}{\eta_{bec}} (K_{Pav} K_{av} m + P_{pld}) \right) Q_2 + K_{av} m \\
& + K_{lg} m + \frac{T_{night}}{\eta_{dchrg} K_{fc} \eta_{los}} P_{lev} + \frac{T_{night}}{\eta_{dchrg} K_{fc} \eta_{bec}} (K_{Pav} K_{av} m + P_{pld}) \\
& + \frac{K_{prop}}{\eta_{los}} P_{lev}
\end{aligned}$$

Where:

$$Q_2 = (K_{sc} + K_{enc} + K_{mppt} I_{max} \eta_{cbr} \eta_{sc} \eta_{mppt}) \quad (4.24)$$

Moreover, the mass equation can be simplified as:

$$\begin{aligned}
m = m_{payload} + K_{af} b^{x1} AR^{x2} + P_{lev} & \left(\frac{Q_2 Q_1}{\eta_{los}} + \frac{T_{night}}{\eta_{dchrg} K_{fc} \eta_{los}} + \frac{K_{prop}}{\eta_{los}} \right) \\
& + \frac{Q_2 Q_1}{\eta_{bec}} K_{Pav} K_{av} m + \frac{Q_2 Q_1}{\eta_{bec}} P_{pld} + K_{av} m + K_{lg} m \\
& + \frac{T_{night}}{\eta_{dchrg} K_{fc} \eta_{bec}} K_{Pav} K_{av} m + \frac{T_{night}}{\eta_{dchrg} K_{fc} \eta_{bec}} P_{pld}
\end{aligned}$$

By substituting P_{lev} and re-ordering, the latter equation becomes

$$\begin{aligned}
m^{1.5} \left[\left(\frac{C_D}{b C_{Lref}^{1.5}} \sqrt{\frac{2AR g^3}{\rho}} \right) \left(\frac{Q_2 Q_1 + K_{prop}}{\eta_{los}} + \frac{T_{night}}{\eta_{dchrg} K_{fc} \eta_{los}} \right) \right] \\
+ m \left[\frac{Q_2 Q_1 K_{pav} K_{av}}{\eta_{bec}} + K_{av} + K_{lg} + \frac{T_{night} K_{Pav} K_{av}}{\eta_{dchrg} K_{fc} \eta_{bec}} - 1 \right] \\
+ \left[P_{pld} \left(\frac{T_{night}}{\eta_{dchrg} K_{fc} \eta_{bec}} + \frac{Q_2 Q_1}{\eta_{bec}} \right) + m_{payload} \right. \\
\left. + K_{af} b^{x1} AR^{x2} \right] = 0 \quad (4.25)
\end{aligned}$$

If the drag coefficient is assumed to be constant and not dependent on the operational Reynolds number, this equation can be solved to find the minimum positive real root with varying span lengths (b) and aspect ratios (AR).

4.3.8 Aerodynamic Performance Estimation

At this design stage, no details are available about the wing geometry and its aerodynamic performance. The configuration of solar-powered high-altitude aircraft usually has a straight and large-aspect-ratio wing; therefore, the aerodynamic performance can be simplified so that it will be substituted by the performance of the aerofoil that will be used in the final design.

4.3.8.1 Reference Lift Coefficient

The scope of this thesis is to design a high altitude aircraft can fly for long endurance. Therefore, the flyable lift coefficient should be selected to minimise the required power at level flight. Accordingly, equation (4.5), which represents the required power for the cruise condition, needs to be minimised. This means that the endurance factor $(\frac{C_L^{1.5}}{C_D})$ needs to be maximised.

The total drag coefficient can be approximated as the sum of the profile drag coefficient and the induced drag coefficient of the wing:

$$C_D = C_{D0} + \frac{C_L^2}{e_o \pi AR} \quad (4.26)$$

where e_o is the Oswald factor, C_{D0} is the zero-lift drag coefficient.

If the Oswald factor is assumed constant regardless the influence of elastic deformation on the wing, the lift coefficient corresponding to the minimum power can be found by maximising the endurance factor. By substituting the total drag coefficient in the factor $(\frac{C_L^{1.5}}{C_D})$ and maximising it, the lift coefficient (C_{Lmp}) corresponding to the minimum power will be (Torenbeek, 2013):

$$C_{Lmp} = \sqrt{3 C_{D0} e_o \pi AR} \quad (4.27)$$

However, this lift coefficient must not exceed the maximum lift coefficient. Moreover, a safety requirement must be subjected for the minimum speed (Austin, 2011).

The value of the absolute minimum flight speed is obtained from the lift coefficient equation:

$$V_{min} = \sqrt{\frac{m g}{C_{Lmax} \frac{\rho}{2} S}} \quad (4.28)$$

where C_{Lmax} is the maximum lift coefficient of the aircraft.

But this minimum speed value provides no margin for gust or any air turbulence or aircraft manoeuvre can increase the drag or/and reduce the lift and thus leading the aircraft to stall.

Therefore, a typical value for the operational speed (V_{∞}) is assumed to be 1.3 times the stall speed (Austin, 2011; Torenbeek, 2013; Zhu et al., 2014). This can be formulated as a function of the maximum lift coefficient:

$$V_{\infty} = 1.3 V_{min} \quad (4.29)$$

$$\sqrt{\frac{m g}{C_{Lref} \frac{\rho}{2} S}} = 1.3 \sqrt{\frac{m g}{C_{Lmax} \frac{\rho}{2} S}}$$

Therefore, the flyable lift coefficient (denoted by reference lift coefficient (C_{Lref})) can be estimated by:

$$C_{Lref} = \frac{C_{Lmax}}{1.3^2} \quad (4.30)$$

The maximum lift coefficient of the aircraft will be substituted by the aerofoil maximum lift coefficient ($C_{Lmax} = C_{lmax}$) (Zhu et al., 2014).

4.3.8.2 Drag Coefficient & Span Efficiency

The total drag coefficient can be approximated as the sum of the profile drag coefficient and the induced drag coefficient of the wing assuming that there is no wave drag and no parasite drag of the non-lifting parts. The total drag can be broken down to lift-independent drag which is represented by zero-lift drag coefficient (C_{Do}) and lift-dependant drag coefficient as indicated in equation (4.26). The Oswald factor represents the change in drag with lift of a three-dimensional wing or airplane, as compared to an ideal wing having the same aspect ratio and an elliptical lift distribution.

In the literature, several methods were developed to express the Oswald efficiency as empirical solutions following wind tunnel data or sampling a virtual design space as surveyed in (Niță & Scholz, 2012). Most of existing modelling gave a general form to express the Oswald factor as:

$$e_o = \frac{1}{I_{in} + I_{vi} \pi AR} \quad (4.31)$$

where I_{in} and I_{vi} are factors which are the inviscid and the viscous parts of the lift-induced drag respectively. The values of these two factors are based on experimental data for a set of conventional aircraft where the Oswald factors were known. It is expected that these empirical factors will not be valid for the design case presented in this thesis where no fuselage or horizontal stabiliser are considered.

The total drag coefficient can be represented using the general form of the Oswald factors:

$$C_D = \underbrace{C_{D0} + I_{vi} C_L^2}_{C_{Dprof}} + \frac{C_L^2}{e \pi AR} \quad (4.32)$$

where $e = 1/I_{in}$ is the span efficiency factor from inviscid theory.

The span efficiency factor can be assumed to be equal to $e = 0.95$ ($I_{in} = 1.05$) (Niță & Scholz, 2012; Torenbeek, 2013). Since the majority of high-altitude solar-powered aircraft have a straight wing geometry or feature very little sweep, the profile drag coefficient of the wing (C_{Dprof}) is assumed to be the same as that of aerofoil (C_d) for specific angle of attack or aerodynamic efficiency. The maximum lift to drag ratio will be considered as a reference point of estimating the associated drag coefficient. The profile drag coefficient of the aerofoil depends on two main factors; the operational Reynolds number and the aerofoil geometry. The operational Reynolds number is one of the parameters that can be determined during the conceptual design stage. It depends on the flight speed, wing geometry and air properties. An equation can be produced to estimate the aerofoil drag coefficient as a function of Reynolds number and fractions which are evaluated using the aerodynamic performance of the aerofoil. The equation can be formulated as

$$C_{Dprof} = K_{aer} Re^{-x_3} \quad (4.33)$$

where K_{aer} and x_3 are the constants which can be evaluated using curve-fit methods relating to the C_d versus Re diagrams. For instance, the aerofoil ZMR-17 (see Chapter 7) will be used in this design exercise where the drag coefficient at the maximum lift to drag ratio is represented as a function of Reynolds number as shown in Figure 4-2.

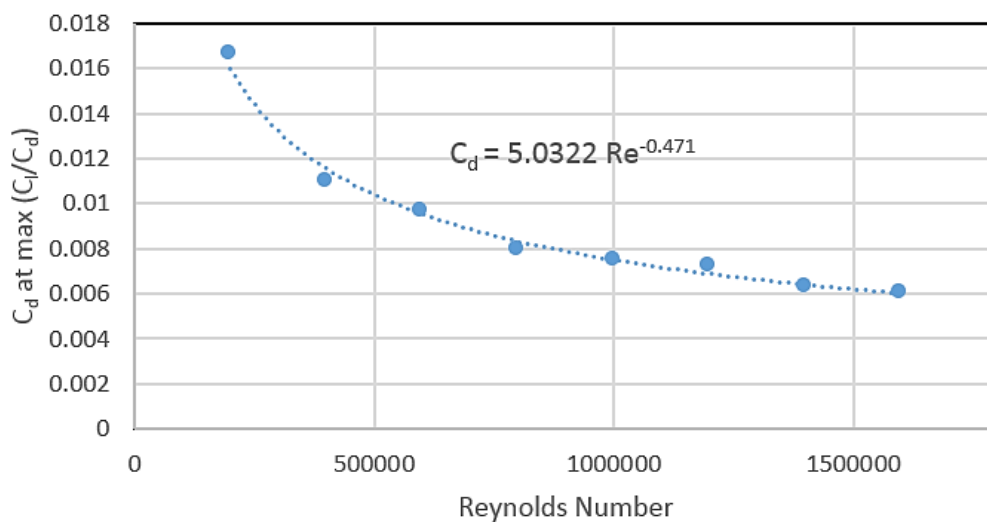


Figure 4-2 Drag coefficient of ZMR-17 at maximum Lift/Drag versus Reynolds number

Now, the demand is to form the drag coefficient as an equation of the aircraft characteristics and employ it in the mass equation (4.25) where the Reynolds number is given by:

$$Re = \frac{\rho}{\mu} V C_{ave} \quad (4.34)$$

where C_{ave} is the mean aerodynamic chord which is a function of the wing span and the aspect ratio. By substituting the airspeed equation (4.2) and the mean chord, Reynolds number becomes:

$$Re = \frac{\rho}{\mu} \sqrt{\frac{m g}{C_{Lref} \frac{\rho}{2} S}} \frac{b}{AR}$$

This leads to:

$$Re = \frac{1}{\mu} \sqrt{\frac{2\rho g}{C_{Lref} AR}} m^{0.5} \quad (4.35)$$

Therefore, C_{Dprof} can be written as:

$$C_{Dprof} = K_{aer} \left(\frac{1}{\mu} \sqrt{\frac{2\rho g}{C_{Lref} AR}} \right)^{-x_3} m^{-0.5x_3} \quad (4.36)$$

By substituting C_{Dprof} in equation (4.32), gives the result

$$C_D = K_{aer} \left(\frac{1}{\mu} \sqrt{\frac{2\rho g}{C_{Lref} AR}} \right)^{-x_3} m^{-0.5x_3} + \frac{C_L^2}{e \pi AR} \quad (4.37)$$

Substituting this in equation (4.25) and rearranging it, yields

$$\begin{aligned} & m^{1.5} \left[\left(K_{aer} \left(\frac{1}{\mu} \sqrt{\frac{2\rho g}{C_{Lref} AR}} \right)^{-x_3} m^{-0.5x_3} + \right. \right. \\ & \left. \left. \frac{C_{Lref}^2}{e \pi AR} \right) \left(\frac{1}{b C_{Lref}^{1.5}} \sqrt{\frac{2AR g^3}{\rho}} \right) \left(\frac{Q_2 Q_1 + K_{prop}}{\eta_{los}} + \frac{T_{night}}{\eta_{dchrg} K_{fc} \eta_{los}} \right) \right] + m \left[\frac{Q_2 Q_1 K_{pav} K_{av}}{\eta_{bec}} + \right. \\ & \left. K_{av} + K_{lg} + \frac{T_{night} K_{pav} K_{av}}{\eta_{dchrg} K_{fc} \eta_{bec}} - 1 \right] + \left[P_{pld} \left(\frac{T_{night}}{\eta_{dchrg} K_{fc} \eta_{bec}} + \frac{Q_2 Q_1}{\eta_{bec}} \right) + m_{payload} + \right. \\ & \left. K_{af} b^{x_1} AR^{x_2} \right] = 0 \quad (4.38) \end{aligned}$$

The final equation after rearranging will be:

$$\begin{aligned}
& m^{1.5-0.5x_3} \left[\left(\frac{1}{\mu} \sqrt{\frac{2g\rho}{C_{Lref}AR}} \right)^{-x_3} \left(\frac{k_{aer}}{bC_{Lref}^{1.5}} \sqrt{\frac{2ARg^3}{\rho}} \right) \left(\frac{Q_2Q_1 + K_{prop}}{\eta_{los}} \right. \right. \\
& \quad \left. \left. + \frac{T_{night}}{\eta_{dchrg} K_{fc} \eta_{los}} \right) \right] \\
& + m^{1.5} \left[\left(\frac{1}{e\pi b} \sqrt{\frac{2g^3}{AR\rho}} \right) \left(\frac{Q_2Q_1 + K_{prop}}{\eta_{los}} + \frac{T_{night}}{\eta_{dchrg} K_{fc} \eta_{los}} \right) \right] \\
& + m \left[\frac{Q_2Q_1 K_{pav} K_{av}}{\eta_{bec}} + K_{av} + K_{lg} + \frac{T_{night} K_{pav} K_{av}}{\eta_{dchrg} K_{fc} \eta_{bec}} - 1 \right] \\
& + \left[P_{pld} \left(\frac{T_{night}}{\eta_{dchrg} K_{fc} \eta_{bec}} + \frac{Q_2Q_1}{\eta_{bec}} \right) + m_{payload} \right. \\
& \quad \left. + K_{af} b^{x_1} AR^{x_2} \right] = 0 \tag{4.39}
\end{aligned}$$

The last equation, denoted ‘the mass equation’, can be solved numerically to find its positive root at varying span lengths (b) and aspect ratios (AR). The fraction values of the components (shown in Table 4-2) are assumed constant during the design process. In this methodology, the design space will be illustrated by suggesting the aspect ratio and span to find a solution for the mass equation. The solution must be constrained so that the value of the solar cell area is less than the planform area. Then, the minimum (optimal) aircraft weight and its corresponding span length and wing aspect ratio will be concluded such as in Figure 4-3.

The final choice can lead to the other component weight estimates includes the weight and power of the propulsion, the solar cells, the fuel cells, the avionics systems, the maximum power tracker and the weights of all other elements. A MATLAB code, which has been written using this methodology, can be used to design solar powered aircraft for given mission requirements during the conceptual design stage. The overview of this methodology is illustrated in Figure 4-4. The code is presented in Appendix II.

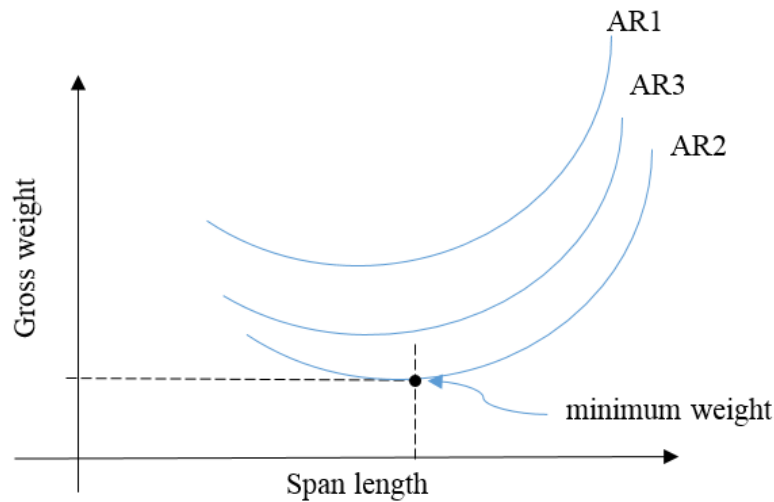


Figure 4-3 The design space of the conceptual design model

Table 4-1 The constant parameters of the design

Parameter	Value	Unit	Description
K_{fc}	550*3600	J/kg	Energy density of fuel cell
K_{sc}	0.25	kg/m ²	Mass density of solar cells
K_{enc}	0.0	kg/m ²	Mass density of encapsulation
K_{mppt}	0.00047	kg/W	Mass to power ratio of max power point tracker
K_{prop}	0.0045	kg/W	Mass to power ratio of propulsion unit
K_{af}	1.548	kg/m ^{1.312}	Structural mass constant
K_{pav}	6	W/kg	Power-to-mass ratio of avionics
K_{lg}	0.012	-	Landing gear weight fraction
K_{av}	0.03	-	Avionic weight fraction
η_{cbr}	0.9	-	Efficiency of the curved solar panels
η_{bec}	0.985	-	Efficiency of step-down converter
η_{sc}	0.3	-	Efficiency of solar cells (Triple-Junction ELO Tabbed Solar Cell (MicroLink))
η_{chrg}	0.99	-	Efficiency of fuel cell charge
η_{ctrl}	0.95	-	Efficiency of motor controller
η_{dchrg}	0.6	-	Efficiency of fuel cell discharge
η_{grb}	0.95	-	Efficiency of gearbox
η_{mot}	0.95	-	Efficiency of motor
η_{mppt}	0.95	-	Efficiency of max power point tracker
η_{plr}	0.85	-	Efficiency of propeller
η_{wthr}	1	-	Irradiance margin factor
$x1$	1.312	-	Structural mass area exponent
$x2$	-0.0046	-	Structural mass aspect ratio exponent

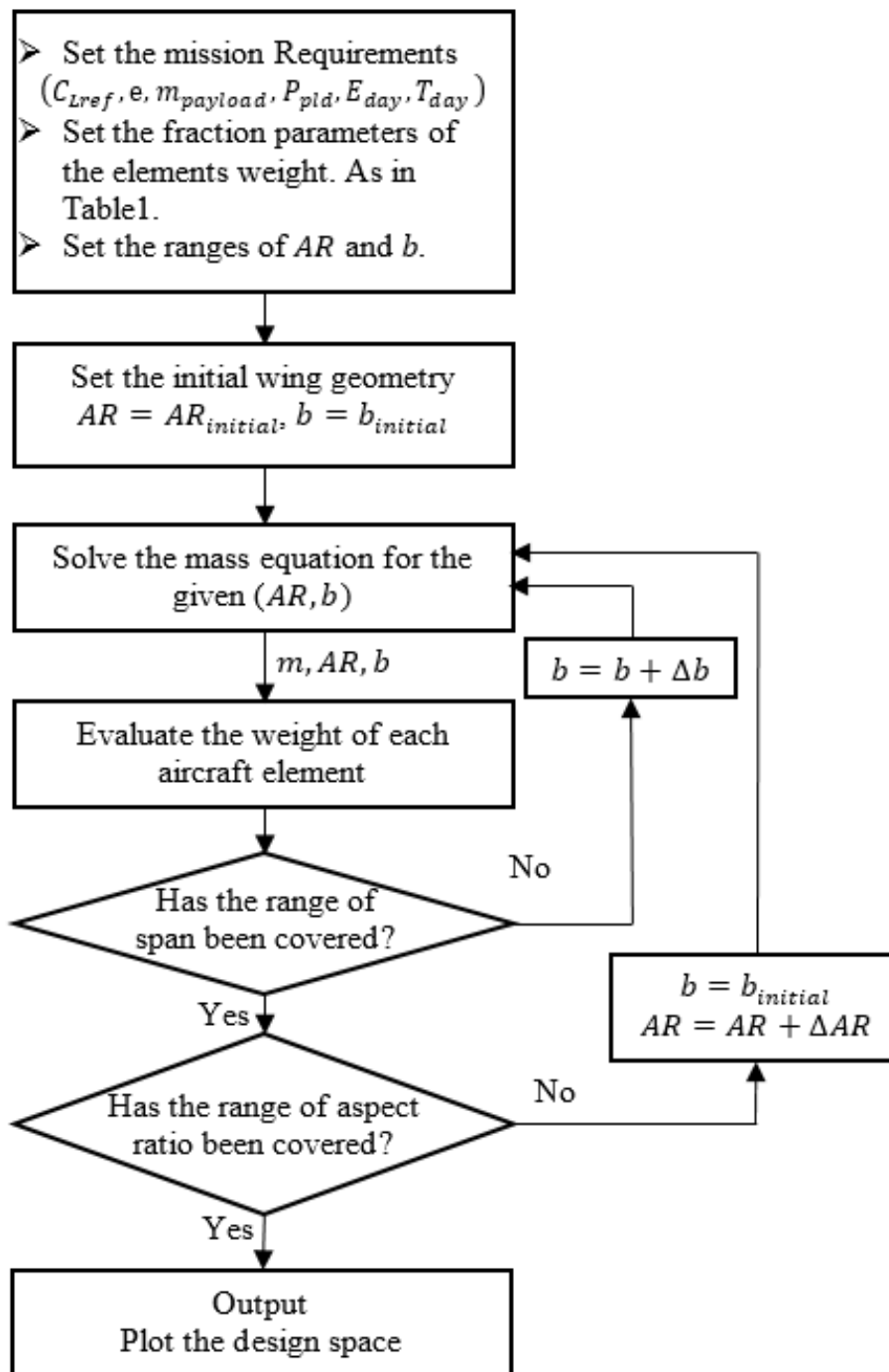


Figure 4-4 Overview of the conceptual design approach

4.4 Validating the Conceptual Design Model

The conceptual design model has been validated using existing data for a design study of a solar powered aircraft, called SHAMPO as shown in Figure 4-5. It is one of the reference configurations which was selected and studied at the Aerospace Department at the Politecnico di Torino under a funded project (Enrico Cestino, 2006; E. Cestino et al., 2007). A small scale model was built to perform experimental flight tests (Romeo et al., 2009). The full model was designed to operate at 17 km altitude for a surveillance mission to carry maximum payload of 130 kg and fly continuously for a few months. The main characteristics of SHAMPO are shown in Table 4-3.

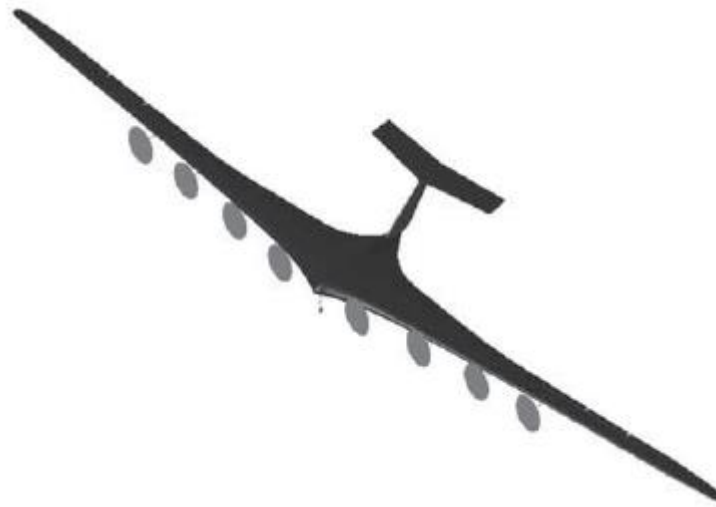


Figure 4-5 External view of SHAMPO (E. Cestino et al., 2007)

To design this aircraft, details such as the aerodynamic performance at the cruise condition, the available solar energy during level flight, daytime hours and other mission requirements will be needed. The properties of the solar cells will be similar to those of SHAMPO. The aerodynamic performance parameters have been estimated using the given gross weight and airspeed values. The aspect ratio for this aircraft was calculated using the total lifting area (planform wing area plus planform tail area). Then, by using a solar model, which is detailed in the next section, the available solar energy and the daytime hours were calculated to be 33.43 MJ/m²/day and 12.83 hours respectively at 38° latitude and 17km altitude on First of April.

Table 4-2 The characteristics of SHAMPO

Aspect ratio (AR)	24	Flight altitude	17 km
Airspeed	25 m/s	Propulsion system efficiency η_{los}	0.85
Wingspan (b)	73 m	Latitude	38°
Planform wing area	192 m ²	Payload	130 kg
Horizontal tail area	25 m ²	Payload power	1300 W
Solar cells efficiency	21%	Reference day	1 st April
Reference lift coefficient	1.092	Solar cells density	0.6 kg/m ²
Total drag coefficient	0.024	Reference air density	0.1382 kg/m ³

The possible design space of the given mission requirements has been generated using the conceptual design tool, as shown Figure 8-2. Two set of validation results, representing the main aircraft characteristics, are compared with the available data of SHAMPO. These results are tabulated in Table 4-4.

The first set of results has been calculated when the spar length and the aspect ratio are the same as that for the SHAMPO (AR=24, b=73m). This result shows excellent agreement in the weight estimates with minor differences.

The second set of results represent the optimal wing characteristics when AR=26 and the span=58m which correspond to the minimum weight as can be concluded from Figure 4-6. The optimal weight is less than that of SHAMPO by about 97 kg. The optimal shape has a smaller wing with a higher aspect ratio when compared with that of SHAMPO. Smaller wing means generation of less lift but it is compensated for, by increasing the airspeed. This interaction can be studied easily by illustrating the design space and presenting their corresponding characteristics.

The conceptual design tool shows that the optimal weight of SHAMPO could be less than the current weight. However, some key mission and aerodynamic performance parameters were estimated using relevant values indicated in references (Duffie & Beckman, 1980; Min Chang et al., 2014). Moreover, power storage for emergency backup and the financial cost constraints were neglected in the validation due to lack of available information. It can be concluded that this method can produce an acceptable estimate of the aircraft characteristics.

Table 4-3 Validation result of SHAMPO

Parameters	SHAMPO AR=24, b=73	Present Model	
		AR=24, b=73	AR=26, b=58
Gross weight (kg)	924	930.27	827.40
Airframe weight (kg)	430	424.71	313.96
Fuel cells weight (kg)	N/A	236.36	243
Avionics weight (kg)	32	27.9	24.82
Total planform area (m ²)	217 (includes the horizontal tail area)	222.04	129.38
Airspeed (m/s)	25	23.32	28.81

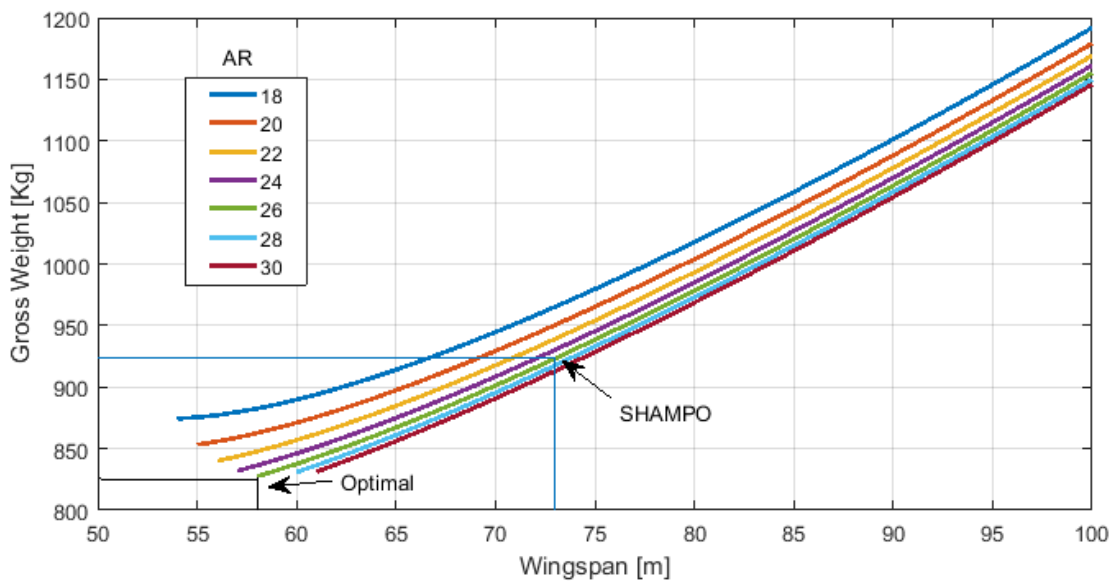


Figure 4-6 The design space of SHAMPO

4.5 Available Solar Radiation at High Altitudes

The emitted radiation from the Sun is nearly constant outside the atmosphere. A useful parameter can be used to measure the solar power outside the atmosphere per unit area normal to the beam direction and per unit time called solar constant (I_{Sc}) and its value is 1367 W/m^2 . The local intensity of radiation (I_0) can be determined using the angle (θ_z) between the direction of the solar beam and the direction perpendicular to the surface of the atmosphere. This angle varies during the day for a given location, which is associated with the latitude and the location of the Earth along its elliptical orbit around the Sun. The solar power available outside the atmosphere per unit area is given by (Duffie & Beckman, 2013):

$$I_0 = I_{Sc} \left(1 + 0.033 \cos \left(n \frac{360}{365} \right) \right) \cos \theta_z \quad (4.40)$$

where n is the day number counts from the first of January ($1 \leq n \leq 365$), θ_z is the zenith angle which can be calculated using the equation:

$$\cos \theta_z = \cos \varphi \cos \delta \cos \omega_s + \sin \varphi \sin \delta \quad (4.41)$$

where φ , δ , and ω_s are the latitude angle, Earth declination angle, and hour angle due to Earth rotation respectively. The latter angles can be calculated using the equations (Duffie & Beckman, 1980):

$$\delta = 23.45 \sin \left(365 \frac{284 + n}{365} \right) \quad (4.42)$$

$$\omega_s = \cos^{-1}(-\tan \varphi \tan \delta) \quad (4.43)$$

The daylight hours can be given by:

$$T_{day} = \frac{24 * 3600}{\pi} \omega_s \quad (4.44)$$

When the solar radiation penetrates the atmosphere, depending on the given altitude and location, a part of the radiation can be scattered towards space and towards the Earth whilst some parts are absorbed by the atmosphere gases (Rizzo & Frediani, 2008) as shown in Figure 4-7. The total solar radiation at high altitude can be classified into three principal components; the direct radiation (I_{dir}), diffuse radiation (I_{diff}), and reflected radiation. At high altitude, due to the relatively cloud-free sky and low humidity, the reflected radiation can be neglected (Rizzo & Frediani, 2008). Therefore, the total solar radiation can be given by:

$$I_{tot} = I_{dir} + I_{diff} \quad (4.45)$$

The direct solar radiation can be evaluated using an empirical model as a function of the altitude and the solar elevation angle which is valued for altitudes higher than 10 km (Keidel, 2000; Meinel, Meinel, & McGowan, 1977; Min Chang et al., 2014):

$$I_{dir} = I_0 \exp \left\{ \frac{c_s \exp \left(-\frac{h}{h_s} \right)}{\left[\sin \left(\frac{\alpha_s + \alpha_{dep}}{1 + \frac{\alpha_{dep}}{90}} \right) \right]^{S_s + \frac{h}{h_b}}} \right\} \quad (4.46)$$

where:

$$\alpha_{dep} = 0.57 + \cos^{-1} \left(\frac{R_E}{R_E + h} \right) \quad (4.47)$$

$$\alpha_s = \frac{\pi}{2} - \theta_z$$

where h is the altitude in km and α_{dep} is the depression angle. All the constants are tabulated in Table 4-5.

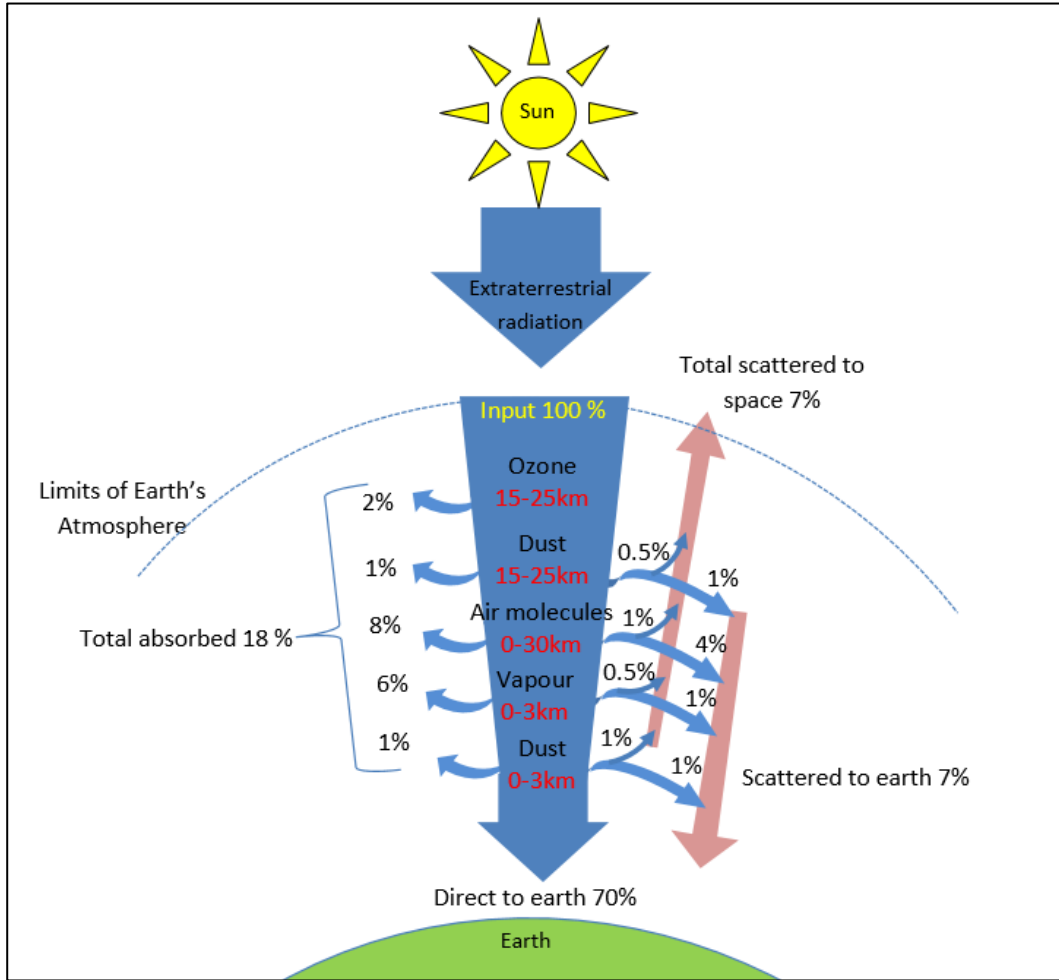


Figure 4-7 Dissipation of the beam radiation energy through the atmosphere, number obtained from (Rizzo & Frediani, 2008)

The diffuse radiation can be defined as a function of the direct radiation and the altitude:

$$I_{diff} = 0.08 I_{dir} \exp\left(-\frac{h}{h_s}\right) \quad (4.48)$$

The total solar energy can be calculated by integrating equation (4.39) for the daytime period:

$$E_{day} = \int I_{tot} dt \quad (4.49)$$

Table 4-4 Constants definitions of the solar radiation model (Min Chang et al., 2014)

Constant	Value	Definition
c_s	0.357	constant
h_s	7 km	Height constant
h_b	40 km	Height constant
S_s	0.678	constant
R_E	6356.8 km	Earth radius

4.6 Study of the Mission Requirements on the Design of Solar-Powered HALE UAV

A study has been conducted using the conceptual design tool to understand how the mission requirements and the aerodynamic performance parameters can influence the resulted main characteristics of the aircraft. This study includes the influences of the endurance of the mission, operational latitude, operational altitude, aerodynamic performance parameters (reference lift coefficient and the span efficiency) and the payload characteristics (mass and power). The main characteristics of aircraft studied in this exercise include gross weight, aspect ratio, span, ratio of the area covered by solar cells divided by the wing area and the operational Reynolds number in addition to representing the mass of each aircraft element. The study was aimed at designing a high altitude long endurance solar powered aircraft for a surveillance mission over a specific area in Iraq.

4.6.1 Availability of Solar Energy in Iraq

The solar radiation model has been used to calculate the available solar energy for different endurance periods at various altitudes and latitudes over a specific area in Iraq which lies between latitudes 29° and 38° N as shown in Figure 4-8. Three different design flight durations have been suggested for the flight endurance as tabulated in Table 4-6 and indicated in Figure 4-9 and Figure 4-10. In each case, the minimum available solar energy per day and the corresponding daytime hours will be considered as reference parameters during the conceptual design process. Generally, in Iraq, the available solar energy is plentiful in the summer season which is about twice that in winter whilst the availability of sunlight varies from 10 to 14 hours.

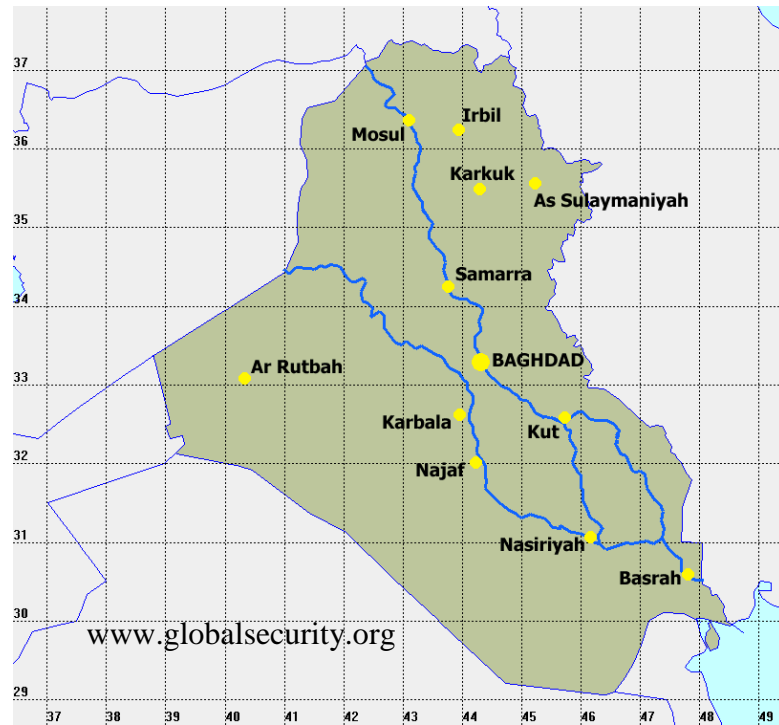


Figure 4-8 Map of Iraq

Table 4-5 Starting dates and Endurance of Missions

Durations	Dates	Endurances [days]
Duration 1	Whole year	365
Duration 2	1 st March – 12 th October	222
Duration 3	1 st May – 14 th August	100

For the altitude study, the available solar energy and the daytime hours are calculated at different altitudes along the 32° N latitude. Figure 4-9 illustrates the variation of the solar energy at different altitudes, in addition to the daytime hours along the days of the year. It can be seen that the scattering and the absorption of energy are more pronounced at lower altitudes, therefore, the available radiation will be more abundant at higher altitudes. The minimum available solar energy and daytime hours are considered as reference parameters for all three cases as tabulated in Table 4-7.

Table 4-6 Available solar energy and daytime hours at different altitudes at a latitude of 32°

Durations	min. daytime[hr]	min. solar energy [MJ/m ² /day] at altitude			
		10 km	15 km	20 km	25 km
Duration 1	9.985	17.83	18.45	18.76	18.91
Duration 2	11.392	26.58	27.54	28.02	28.26
Duration 3	13.254	35.63	37.19	38.00	38.41

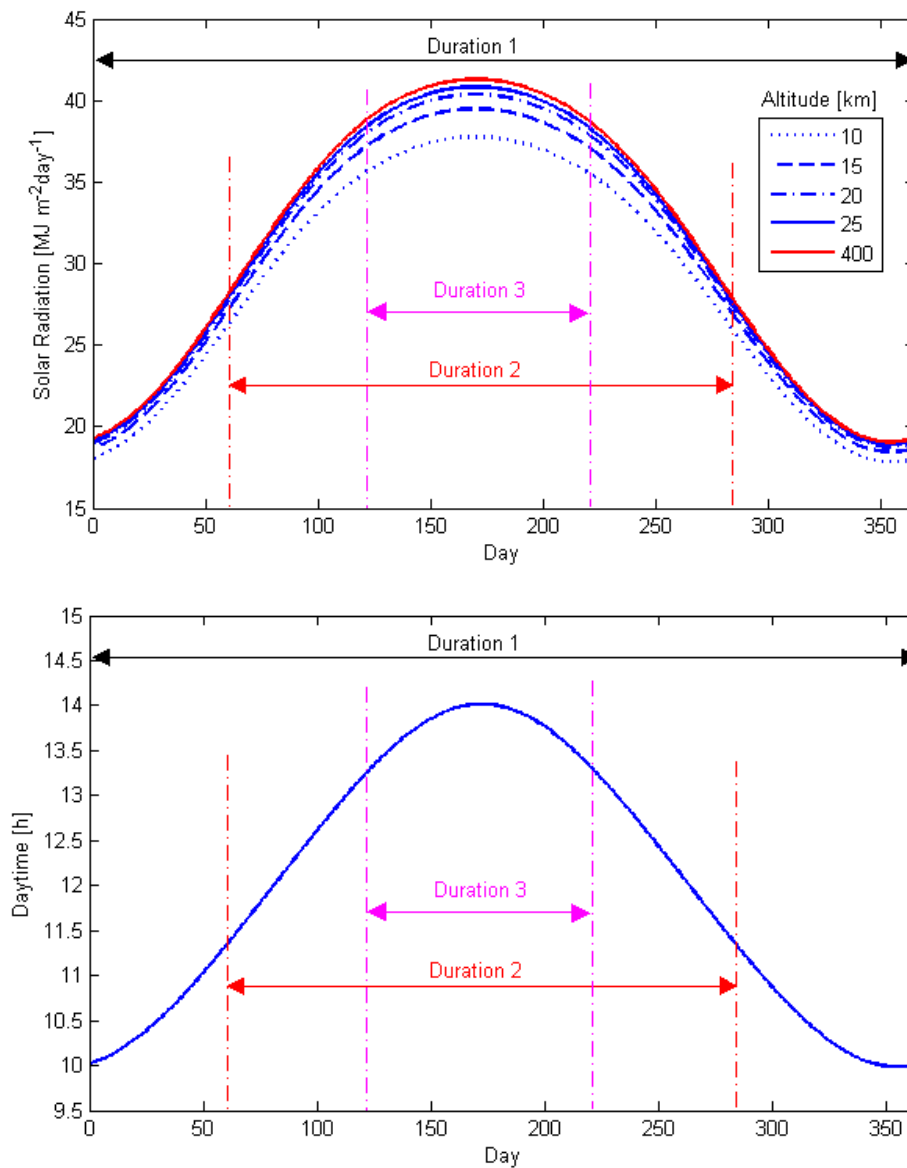


Figure 4-9 Solar irradiance per unit area and daytime hours versus time, for different altitudes at 32^o latitude

For the latitude study, the available solar energy and the daytime hours are calculated along different latitudes at an altitude of 17 km as indicated in Figure 4-10. In general, the calculations show that the available solar energy is plentiful at lower latitudes. However, during June and July, the northern regions of Iraq (higher latitudes) receive much more solar energy per day due to the longer daylight hours. The minimum solar energy for each flight duration is detailed in Table 4-8.

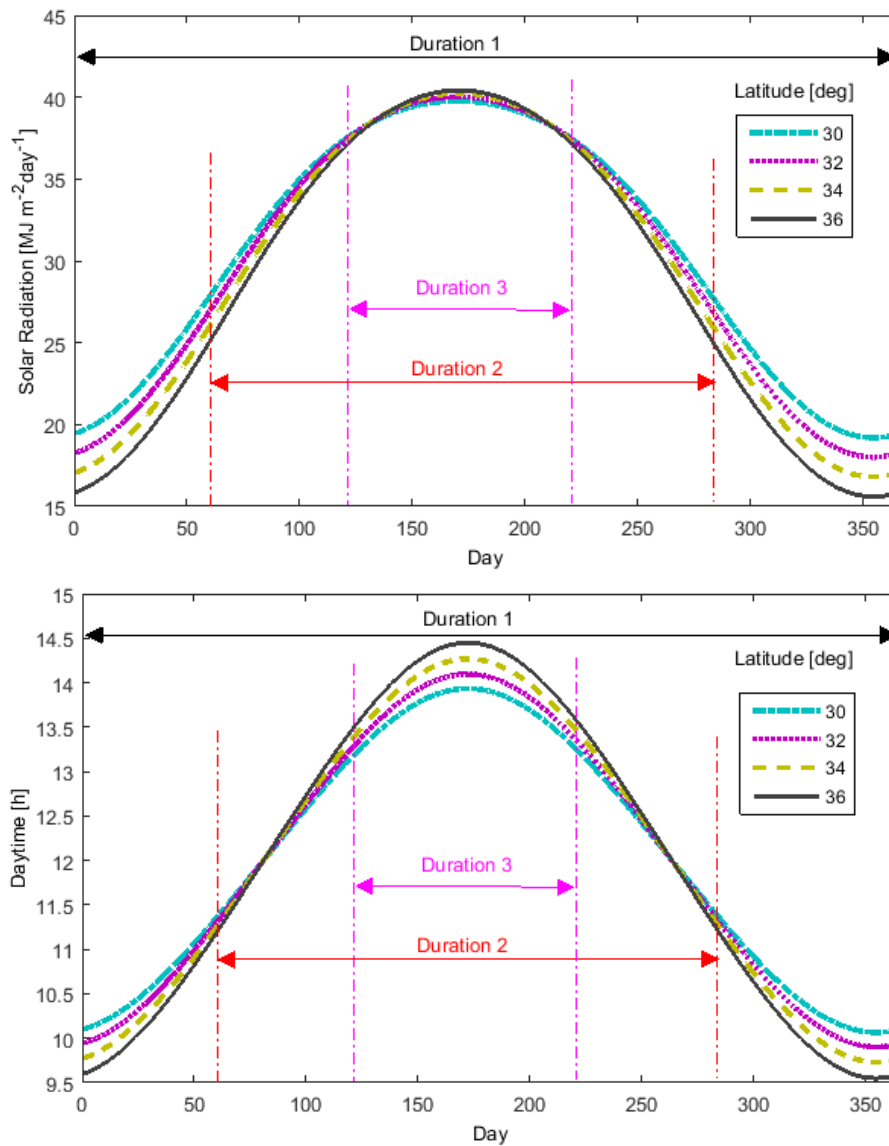


Figure 4-10 Solar irradiance per unit area and daytime hours versus time for different latitude at 17 km altitude

Table 4-7 Available Solar Energy and daytime hours at Different Latitudes

Durations		At Latitude [deg]			
		30 ⁰	32 ⁰	34 ⁰	36 ⁰
Duration 1	min. solar energy [MJ/m ² /day]	19.12	18.01	16.80	15.60
	min. daytime [hr]	10.07	9.90	9.73	9.55
Duration 2	min. solar energy [MJ/m ² /day]	28.41	27.55	26.65	25.73
	min. daytime [hr]	11.45	11.40	11.35	11.30
Duration 3	min. solar energy [MJ/m ² /day]	37.62	37.54	37.41	37.24
	min. daytime [hr]	13.20	13.30	13.41	13.52

4.6.2 The Influence of the Reference Altitude, Latitude and Duration on the Design

The conceptual design tool has been used to study how the reference altitude, latitude and the starting day of the designed duration can influence the main characteristics of aircraft such as gross weight, aspect ratio, span, ratio of solar cells area and operational Reynolds number. The available energy of each design case has been calculated in the previous section. The fixed mission and aerodynamic performance parameters are tabulated in Table 4-9.

Table 4-8 The fixed mission and aerodynamic performance parameters

Parameter	Value	Unit	Description
C_{Lref}	0.85	-	Aeroplane lift coefficient at cruise
e	0.95	-	Span efficiency
$m_{payload}$	100	kg	Payload mass
P_{pld}	1250	W	Payload power consumption

4.6.2.1 Impacts of the Reference Altitude and the Flight Duration

In a previous section it was shown that the available solar energy increases with increasing operational altitude. However, at higher altitudes, the density of air drops considerably, as shown in Figure 4-11. This must be considered in the design. Figure 4-12 shows the influence of the designed flight altitude on the aircraft weight, the corresponding wingspan, the wing aspect ratio, the ratio of the area of the solar cells divided by the wing area and the operational Reynolds number for the three flight durations.

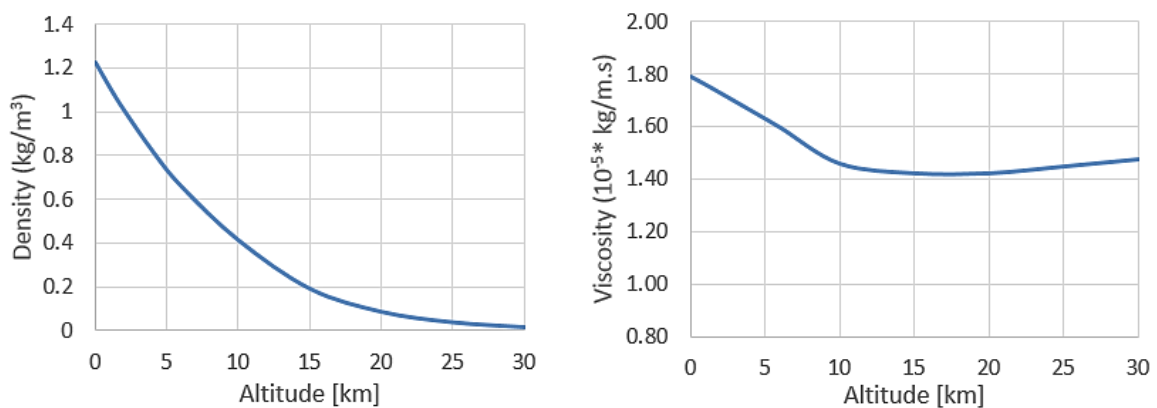


Figure 4-11 Density and dynamic viscosity of air versus altitude

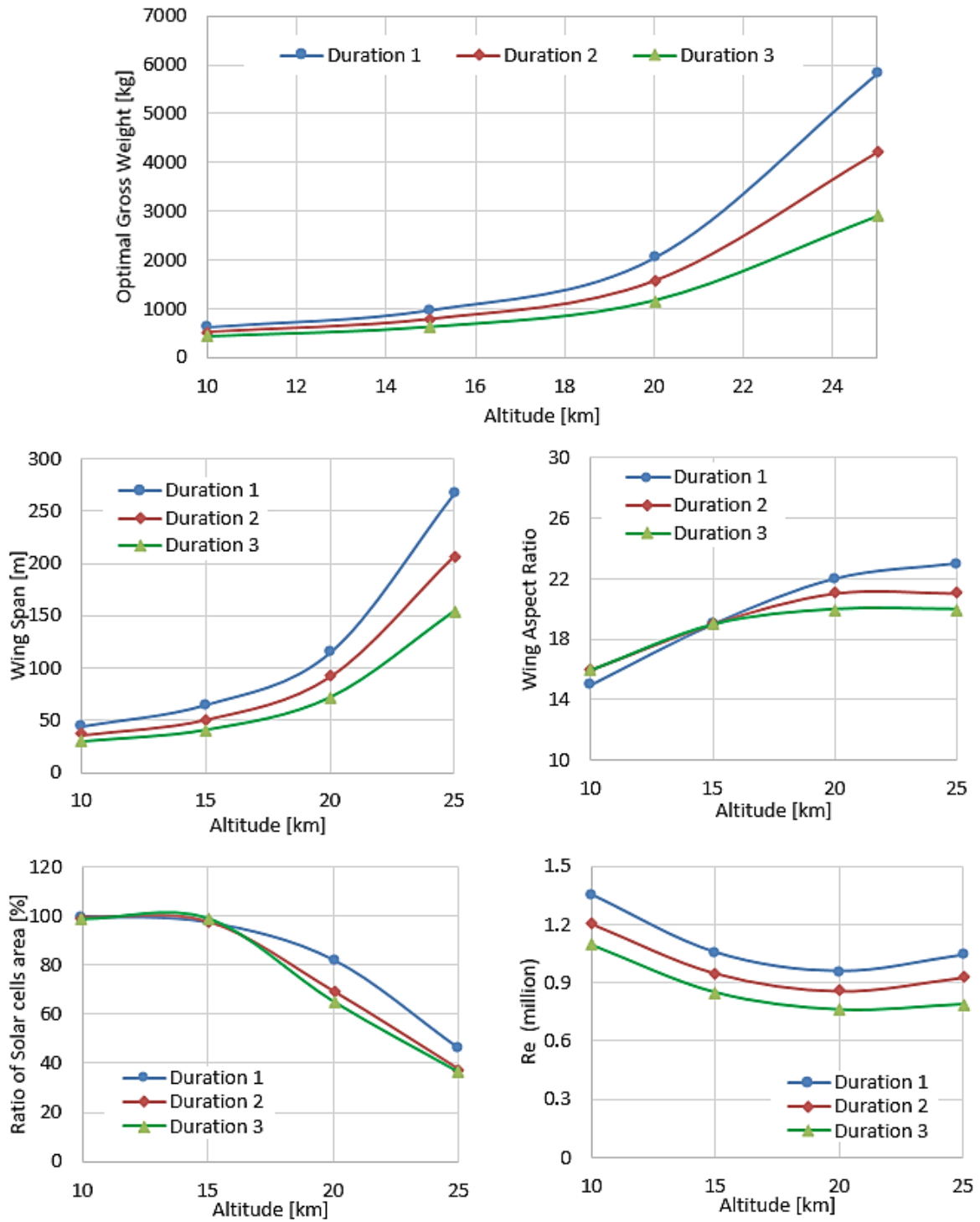


Figure 4-12 Effect of the flight altitudes on gross weight, corresponding wingspan, wing aspect ratio, the ratio of solar cells area and operational Reynolds number for different flight durations. At latitude= 31.01°.

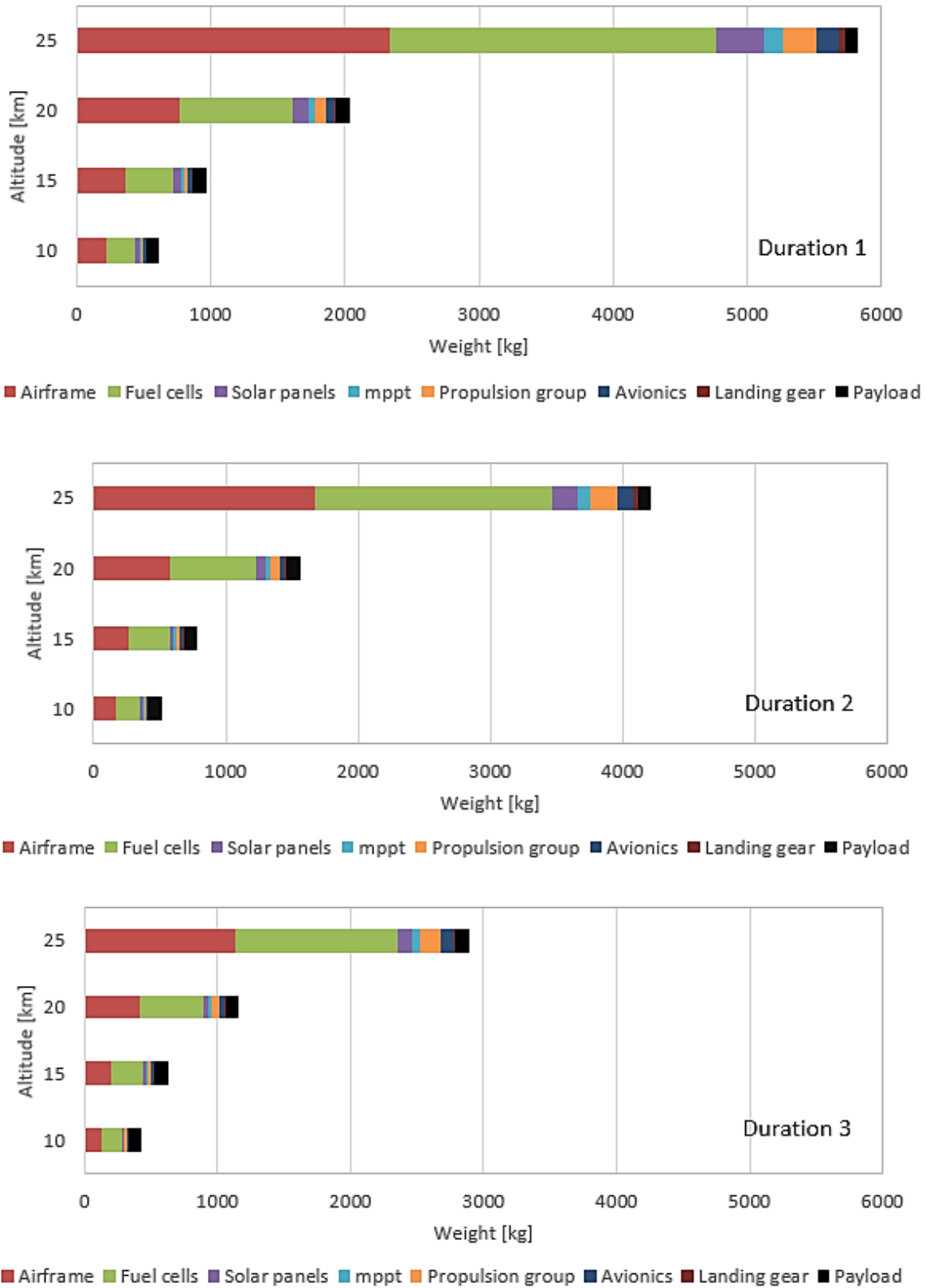


Figure 4-13 The effect of the reference altitude on the weight estimation for the durations

The results show that increasing the reference altitude of the design can lead to a heavier aircraft due to a larger wing requirement. This is accompanied by a proportional increase in the wingspan and aspect ratio of the wing. Moreover, the results indicate that the wing area needed for the solar cells is less than that required for the aerodynamic performance at higher altitudes. This is because of the extreme reduction in the air density which necessitates a large wing area required for generating sufficient lift. Moreover, a high available solar energy which is received at high altitude can reduce the required area of the solar cells.

Since the available solar power for Durations 2 & 3 have increased, the aircraft gross weight and the wingspan are reduced. Due to the relatively higher density at lower altitude, the operational Reynolds number is raised. However, at higher altitude where the air density is low, the optimal design tends to increase the airspeed to compensate for the reduction in the lift force.

4.6.2.2 Impacts of the Reference Latitude and Duration

The effects of the designed operational location (latitude) of aircraft are studied in Figure 4-14. The reference altitude is fixed at 17 km. The results indicate that for each duration, the optimal gross weight is slightly influenced by changes in the selected latitude due to the variation in the angle of incidence of solar radiation and hence the available solar energy and daytime periods.

In Duration 3, the impact of the gross weight differs from that of the cases for Durations 1 & 2 despite the reduction in the available solar energy with increasing latitude. The reason for this is the daytime hours in Duration 3 increasing with increasing the altitude as can be seen in Table 4-8 and Figure 4-10, this aspect is not apparent for Durations 1 & 2. Longer daytime means fewer night-time hours. As indicated in equation (4.17), the weight of the electrical energy storage system depends on the night-time hours and the total electric power. This suggests that the weight of the energy storage system will be less if the aircraft was designed to operate in accordance with the Duration 3 requirements. Therefore, the daytime period is also a noticeable factor besides the available solar energy as it can influence the achievement of the design aims. The span of the wing is affected in much the same manner as the gross weight. Moreover, the results show that the wing aspect ratio is not affected by the variation in the latitude for Durations 1 & 2 while it is slightly affected for Duration 3 case. The ratio of the area covered by the solar cells to the wing area is slightly

increased with increasing latitude for each duration. However, it is affected by the duration factor due to the variation of available solar energy and daytime hours.

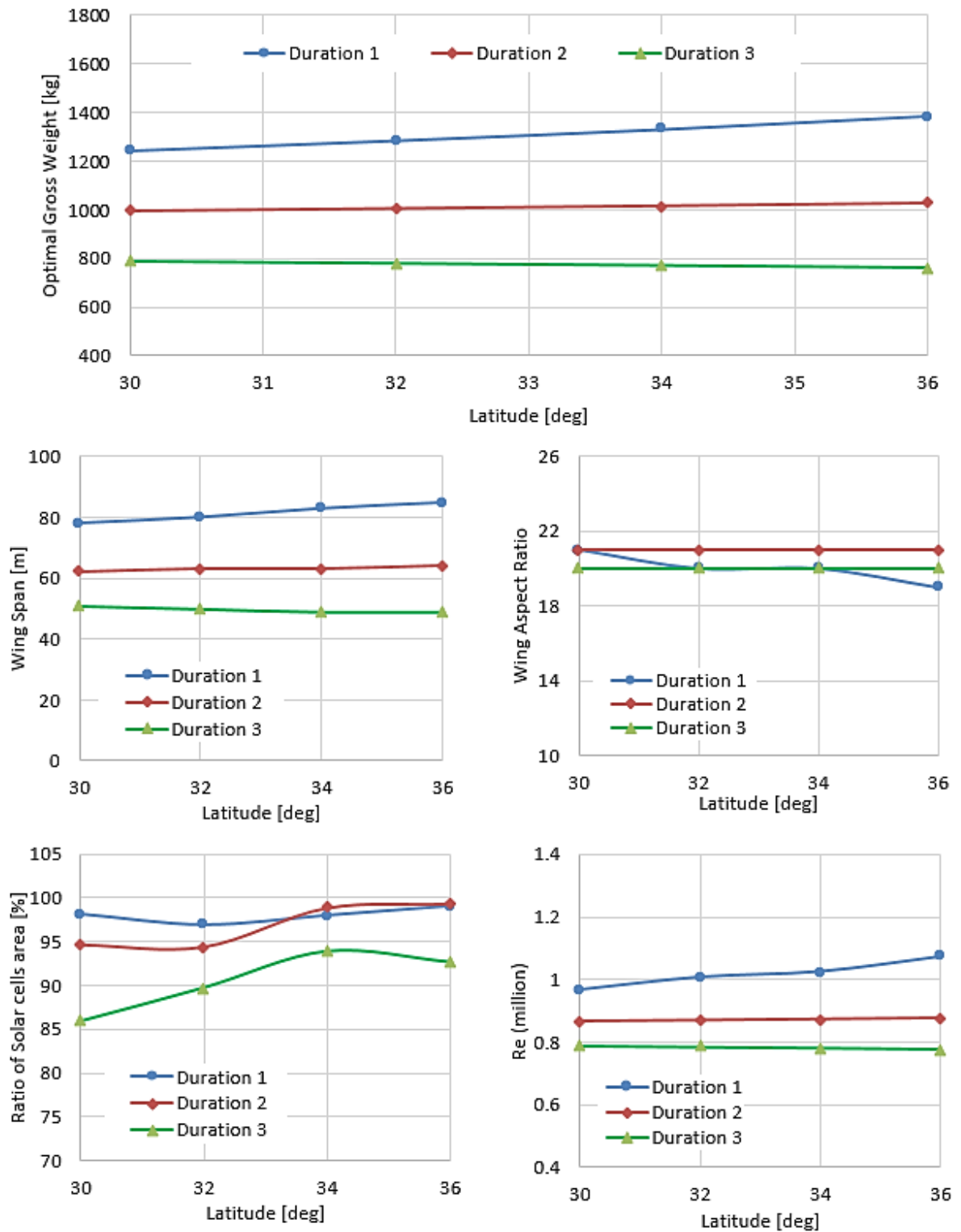


Figure 4-14 Effect of the flight latitudes on gross weight, corresponding wingspan, wing aspect ratio and the ratio of solar cells area for different flight durations, altitude=17 km

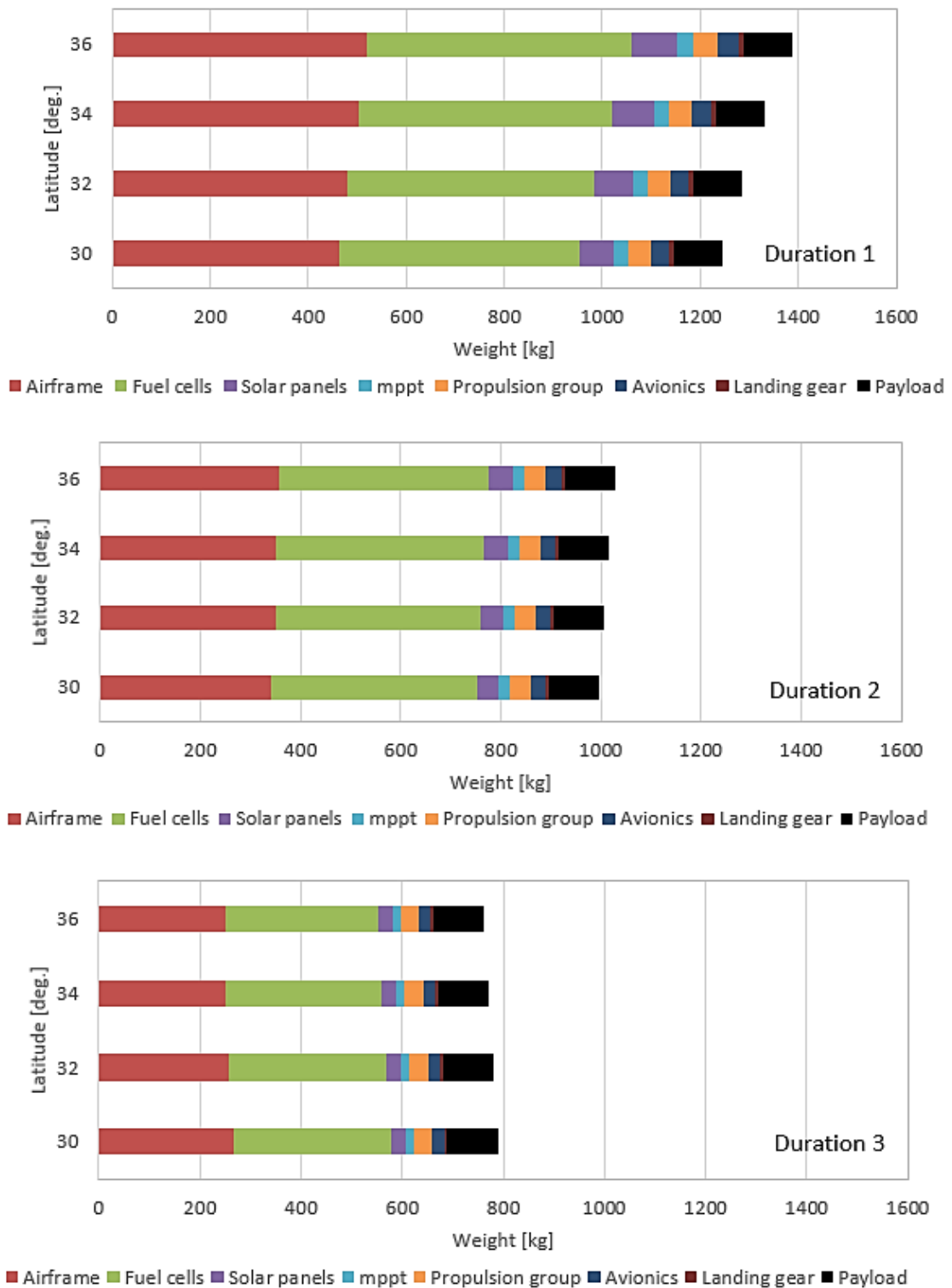


Figure 4-15 The effect of the reference latitude on the weight estimation for the durations

4.6.3 Aerodynamic Performance study

In the conceptual design stage, the aerodynamic performance is usually assumed to be constant at the cruise condition. An accurate estimate of this performance is required in order to reduce the effort and time needed to conduct the calculations. A brief study is carried out to outline the impact of the reference aerodynamic performance parameters such as lift coefficients and the span efficiency on the estimation of the gross weight during the conceptual design stage. This study has been conducted as represented in Figure 4-16 and Figure 4-17 using the same mission requirements shown in Table 4-9 at 17 km altitude and 31.01° latitude, except for the wing performance parameters which were varied.

Figure 4-16 indicates that the optimal gross weight, the corresponding span length and the operational Reynolds number are decreasing with increase to the reference lift coefficient. However, solar cells areas are getting higher with increasing the reference lift coefficient due to a high energy being required, thus heavier fuel cells. The enlarging of the wing area would mostly be in the span wise direction, leading to increasing the aspect ratio and reducing the induced drag. Moreover, from the results it can be concluded that, designing the aircraft with a high lift coefficient can lead to less required airspeed, and thus lower operational Reynolds number. The span efficiency study in Figure 4-17 shows that the gross weight, span, aspect ratio and the ratio of the solar cells area are reduced due to the reduction in the drag with increasing the span efficiency. Therefore, it can be seen, reducing the span efficiency required more power and this necessitates heavier fuel cells thus a heavier structure.

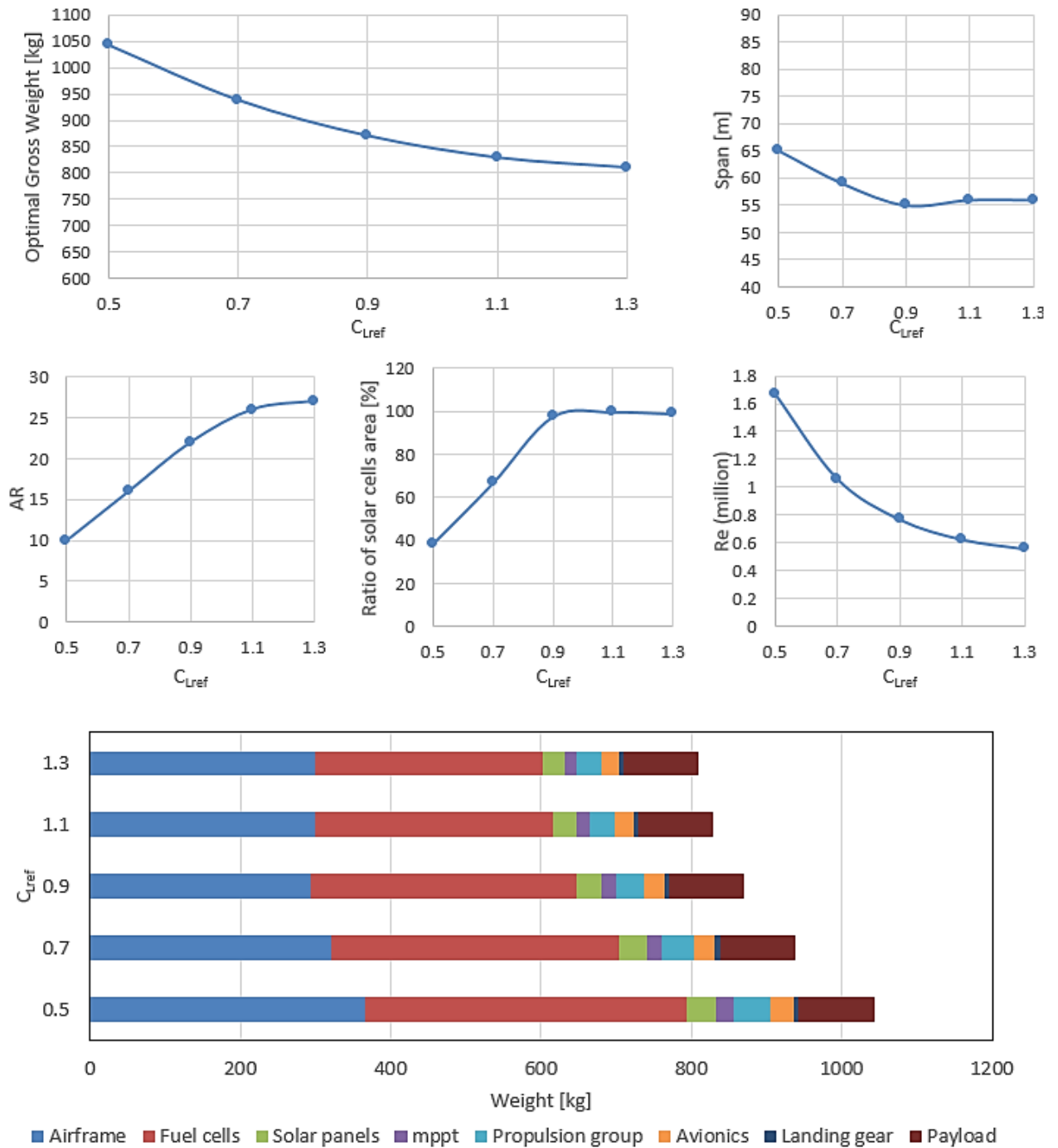


Figure 4-16 Effect of the reference lift coefficient on the aircraft weight and on its main configurations, latitude=31.01°, altitude=17 km, for Duration 2, span efficiency=0.95, payload=100kg, payload power=1250 W

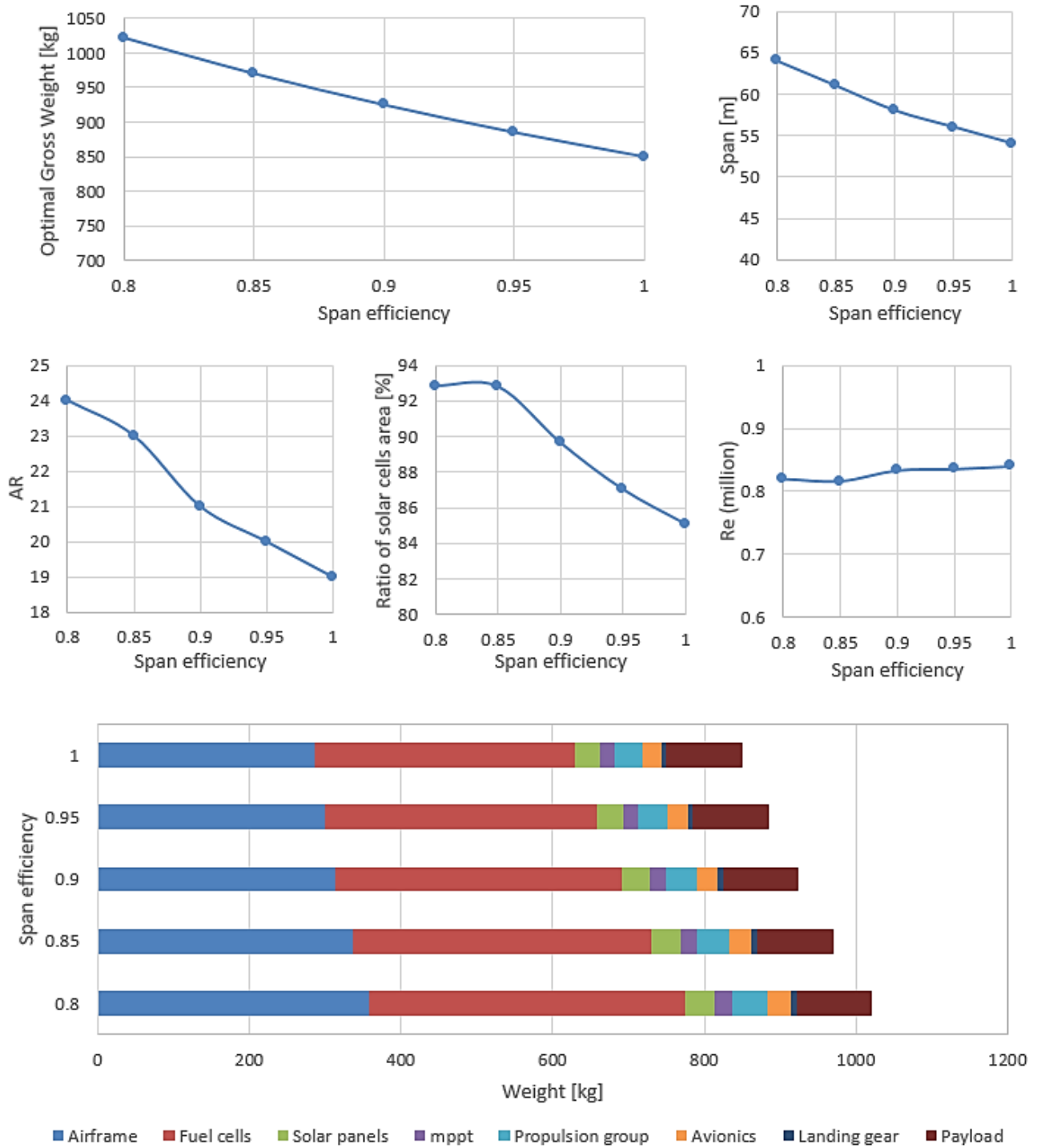


Figure 4-17 Effect of the span efficiency on the optimal aircraft weight and on its main configurations, latitude=31.01°, altitude=17 km, for Duration 2, $C_{Lref}=0.85$, payload=100 kg, payload power=1250 W

4.6.4 Payload Requirement Study

The influences of the payload weight and its required power on the weight estimation and the main characteristics of aircraft have been studied. These two factors can have an intense effect on the gross weight estimation for this type of aircraft as shown Figure 4-18 and Figure 4-19. Increasing the payload weight and its required power necessitates higher required lift force and energy, which in turn need a larger wing area to accommodate sufficient solar panels and to generate sufficient lift leading to an increase in the span, thus increasing the weight.

As shown in Figure 4-18 for this aircraft and its mission characteristics, 100 kg payload can increase the gross weight by about 350 kg due to a larger required wing area to generate sufficient lift. In addition, high capacity fuel cells will be required and this can influence the structural weight thus the total weight. The response of the solar cells area comparing to the required planform area differs and its ratio is reduced due to the domination of the aerodynamic needs. In contrast, in Figure 4-19, the ratio of the solar cells area is increasing with raising the needed power which required larger solar panels.

4.6.5 Conclusion

Several design parameters have been studied using the conceptual design model. Low air density challenge at higher altitudes, dominantly affect the required wing area to generate sufficient lift force if compared with that required to be paved by solar cells. The available solar energy, which is associated with the starting date and duration of the mission, has a noticeable effect on the total weight of the aircraft as heavier fuel cells (high power capacity) will be required when the available solar energy is low. The daytime period also demonstrated a remarkable influence due to it requiring adequate time to charge the fuel cells for the night time flight period. Longer night time means higher capacity & heavier fuel cells and thus larger wing area for generating sufficient lift force leading to a heavier wing structure. It can be concluded that the sensitivity of the total weight toward increasing the required lift force (increasing the wing area) become greater with increasing the altitude due to the decrease in the air density.

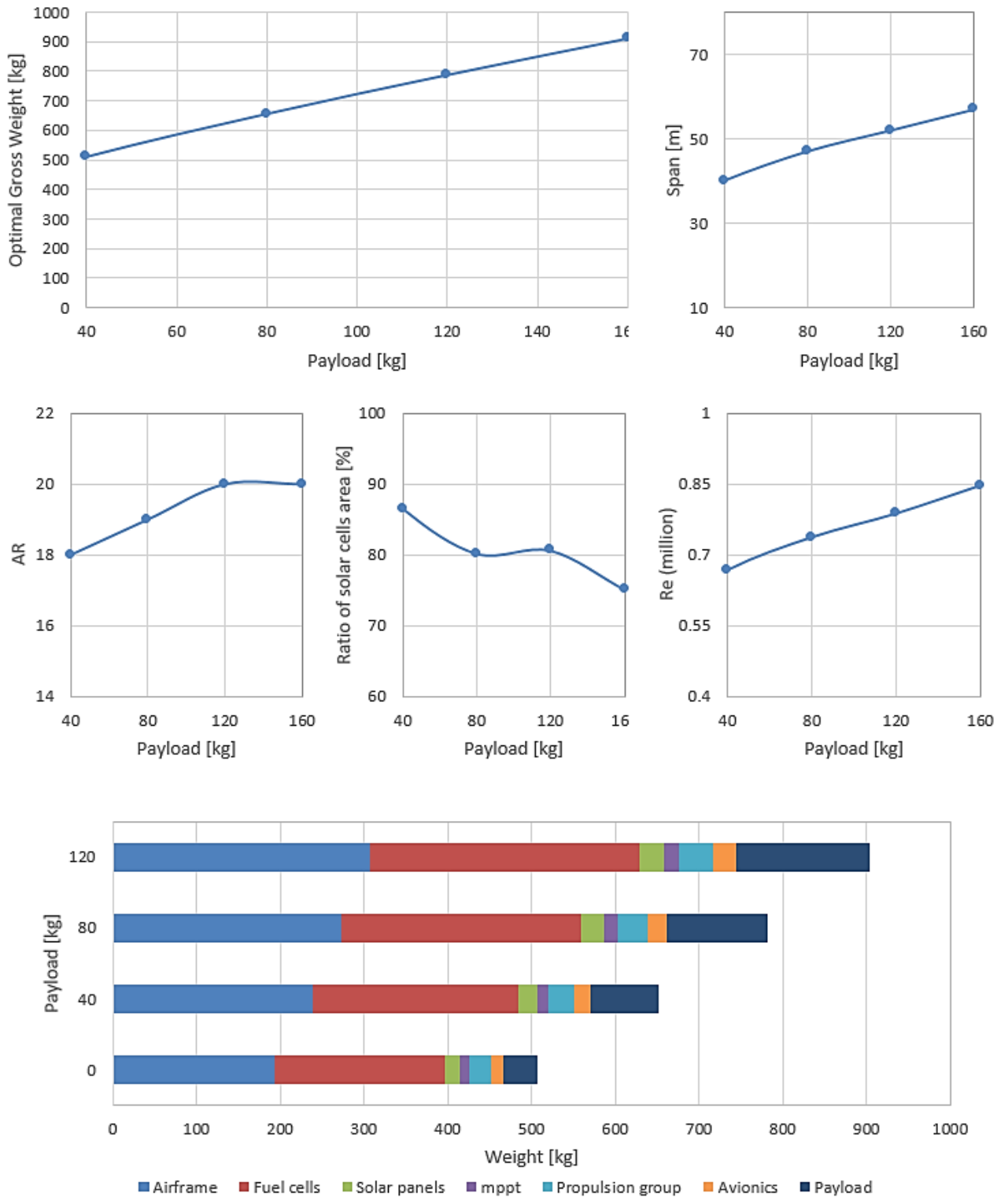


Figure 4-18 Effect of the payload weight on the optimal aircraft weight and on its main configurations, latitude=31.01°, altitude=17 km, for Duration 2, $C_{Lref}=0.85$, span efficiency=0.95, power of payload=0.

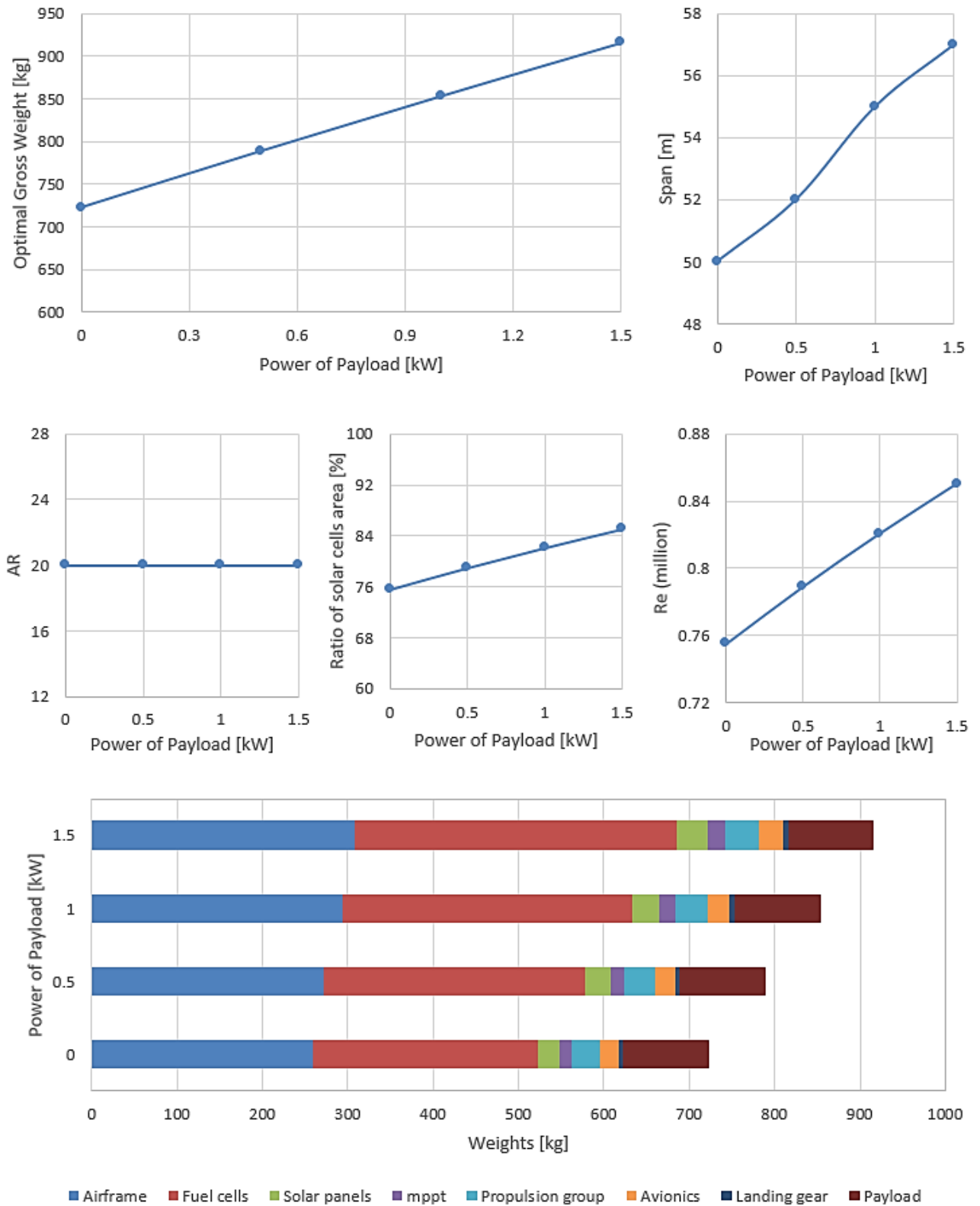


Figure 4-19 Effect of the power of payload on the optimal aircraft weight and on its main configurations. $C_{Lref}=0.85$, span efficiency=0.95, payload=100 kg

CHAPTER 5

5 AERODYNAMIC ANALYSIS

A new low-order analytical piece of software written by the author was used to facilitate efficient computation to deal with multiple optimisation loops often found in engineering analyses. This aerodynamic solver will be a part of the preliminary design tool and will be coupled with a structural model as will be explained in Chapters 6 & 8. In this aerodynamic model, a strip theory has been adopted to evaluate the viscous drag of the wing. Strip Theory implicates discretising the wing geometry into a number of rectangular chord-wise segments of equal span and computing aerodynamic forces on those segments relating to the local velocities and incidence angles. The model consists of two main parts: a three-dimensional inviscid-flow model (Vortex Lattice Method) and a two-dimensional inviscid/viscous flow model. Additional supplementary tools such as an aerofoil section geometry generator and an aerofoil interpolator were employed. The Tornado VLM is used to evaluate the lift and the induced drag forces of the wing geometry. A two-dimensional Panel Method, coupled with an integral boundary-layer method has been built and written in MATLAB to evaluate the two-dimensional profile drag in the longitudinal strip-wise direction. The integration of the profile drag in the span-wise direction will then lead to the evaluation of the profile drag for the whole wing. The overview of this approach is presented in Figure 5-1 and will be detailed in this chapter.

In the literature, the two-dimensional aerodynamic performance is estimated either using experimental data or using a 2D viscous aerodynamic solver such as Xfoil. The experimental data should be prepared in advance for the expected operational range of Reynolds number for the aerofoil that will be used in the design. In the strip theory, the effective angle of attack is found by an iterative process influenced by the inviscid local lift force and the induced angle. Therefore, if the viscous lift of the two-dimensional performance was used to find the corresponding effective angle of attack for the local lift force estimated by inviscid analysis, the accuracy of predicting profile drag could be reduced. This is especially the case, if the viscous drag has a considerable influence on lift generation. Also, the Xfoil is prone to non-convergence problems, or takes a longer time to become converged, which will cause delaying or interrupting for the optimisation process.

In this research, the 2D inviscid lift coefficient is estimated using the Panel Method whilst the viscous drag will be estimated using the Squire-Young formula for the upper and lower surface of the aerofoil as will be detailed later.

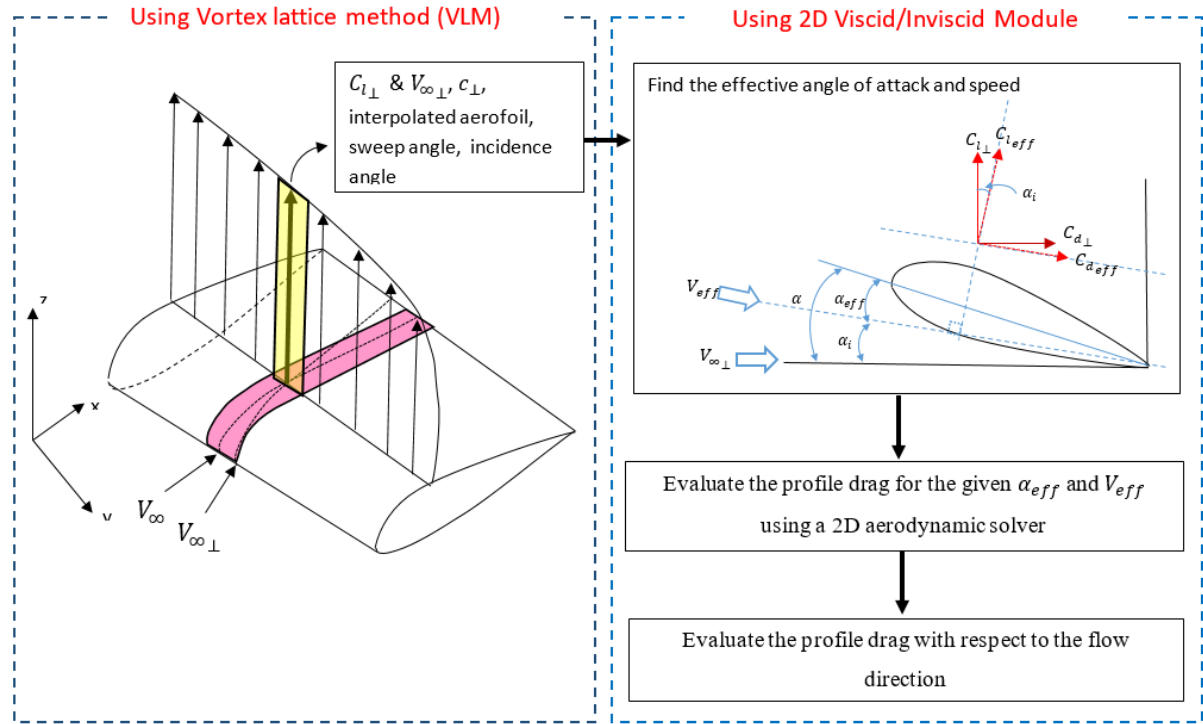


Figure 5-1 Procedure of the Quasi 3D Aerodynamic model

5.1 Tornado Vortex Lattice Method

Tornado VLM is a MATLAB code written by Tomas Melin at the Aerodynamics Department, Royal Institute of Technology (Melin 2001). Tornado is based on standard vortex lattice theory, stemming from potential flow theory. The wing is represented by a thin lifting surface which follows the camber line of the wing sections. The lifting surface is then discretised into quadrilateral elements, the so-called panels. Each panel is then associated with a horseshoe vortex placed on its quarter-chord line with two trailing vortex lines shed from each end such as in Figure 5-2. The required strength of each vortex is then calculated by applying a boundary condition which implies that no-flow penetrates the lifting surface. In this method a variety of three-dimensional wing configurations can be modelled for inviscid, incompressible flow. Thus, Tornado VLM can evaluate the 3D aerodynamic forces and their coefficients.

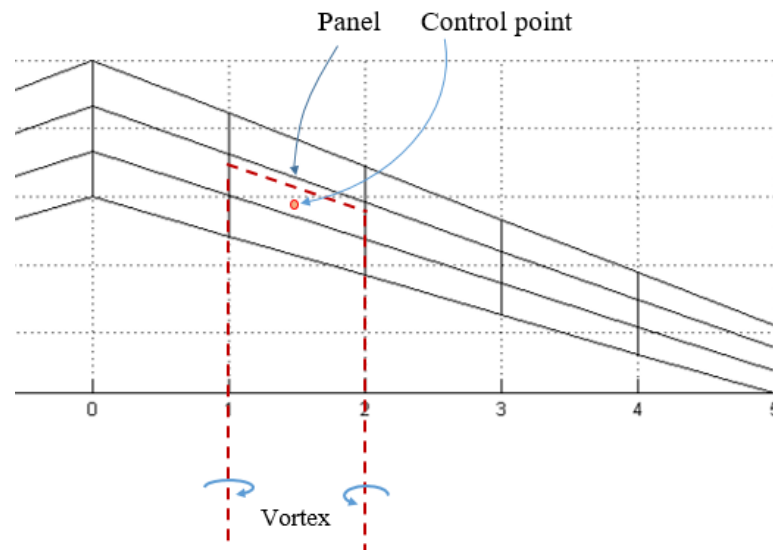


Figure 5-2 The lifting surface and the horseshoe vortex layout for the Vortex Lattice Method

5.2 Two-Dimension Inviscid/Viscous Model (IVM)

In the present application of the incompressible flow around an aerofoil section, viscous effects are significant only in the boundary-layer regions adjacent to the aerofoil surface. In this region, the governing Reynolds-averaged Navier-Stokes equations can be approximated by the so-called boundary-layer equations. Outside this region, the flow can be considered to be inviscid (Katz & Plotkin, 2001; Wauquiez, 2009). The inviscid flow region can be analysed using the Panel Method to find the distribution of the velocity tangential to the aerofoil surface which then can be used as a boundary condition to solve the boundary-layer equations. The boundary layer calculations begin at the stagnation point at the leading edge of the aerofoil, with separate calculations for the upper and lower surface flows. In Xfoil code, the Panel Method and the boundary-layer equations are coupled in an iterative way to modify the region of the viscous flow until a convergence of the air velocity is achieved. Therefore, the Xfoil code can predict the influence of the viscous drag on the flow and, as a result, on the lift and pitching moment coefficients. According to the Strip Theory, the lift distribution is evaluated using an inviscid model. So it is appropriate to use a 2D inviscid aerodynamic model to find the effective angle of attack. Therefore a new model had to be created for use with the Strip Method. The model which is used in this research uses only one-way coupling and hence the resulting lift coefficient will effectively belong to the inviscid part (the Panel Method) and the drag for the viscous part (boundary-layer equations). The reason of utilising a one-way coupling 2D aerodynamic solver is to obtain a rapid solution suitable for an iterative design process. However, attention has to be taken when analysing the flow nearer the stall areas. Therefore, the aerofoil that will be used in

the design has to be studied in advance to keep in mind the appropriate range of angles of attack and operational Reynolds number to obtain valid estimations for the aerodynamic performance parameters.

5.2.1 Inviscid Model (2D Panel Method)

Panel Method is a technique for solving incompressible, irrotational potential flow governed by the Laplace equation around the aerofoil geometry. According to the Panel Method, the aerofoil surface can be represented by straight-line panels as shown in Figure 5-3. In this model, distribution of sources and vortices are assumed around the geometry surface. Along the panels, the vortex distribution is the same on each panel, while the source strength distribution is constant on each panel and differs from panel to panel. The tangential velocity in each panel can be evaluated by applying the boundary condition whereby the normal velocity is zero in each collecting point of each panel, and then the pressure distribution and lift coefficient are evaluated. More detail about this model is placed in Appendix III.

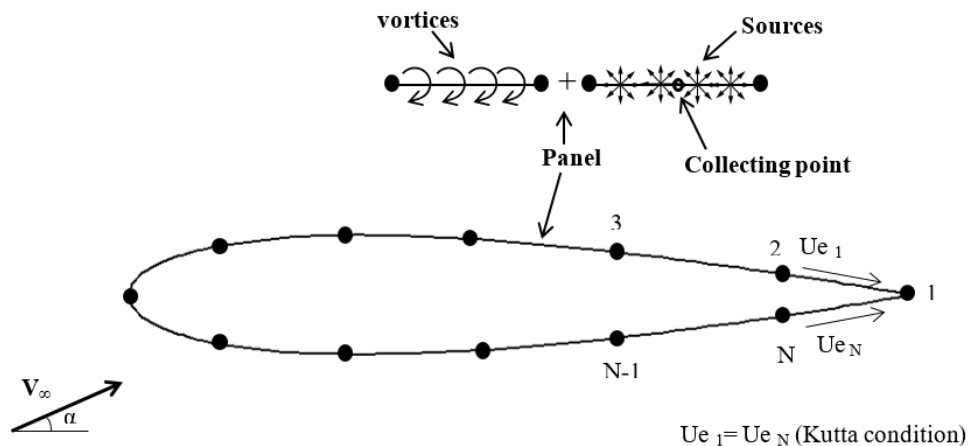


Figure 5-3 Discretization of an Aerofoil Contour into Panels

5.2.2 Viscous Model (Integral boundary layer)

In the boundary layer region, the governing Reynolds-averaged Navier-Stokes equations can be approximated by the so-called boundary-layer equations. For the two viscous-flow field, many semi-empirical formulae have been used to evaluate the momentum thickness, shape factor, skin friction coefficient and the displacement thickness of each panel; this enables computation of the profile drag of the aerofoil. A brief description

of the governing equations used in this model will be discussed next. The full details can be found in references (Houghton & Carpenter, 2003; Moran, 2003; Wauquiez, 2009).

I. Laminar Flow Field:

This field begins from the stagnation point near the leading edge to the transition point from laminar to turbulent flow. Thwaites' model is used to solve the momentum integral equation (Moran, 2003). Additional investigation is brought in to predict the location of the laminar separation which is considered as a transition point (Katz & Plotkin, 2001; Moran, 2003).

The two-dimensional Navier-Stokes equations can be simplified using several assumptions for steady incompressible flow to get the following equations (Prandtl boundary layer):

$$\begin{aligned}\frac{\partial u}{\partial x} + \frac{\partial v}{\partial y} &= 0 \\ \rho \left(u \frac{\partial u}{\partial x} + v \frac{\partial u}{\partial y} \right) &= -\frac{\partial p}{\partial x} + \mu \frac{\partial^2 u}{\partial y^2} \\ \frac{\partial p}{\partial y} &= 0\end{aligned}\tag{5.1}$$

where x and y are the coordinates measured along the aerofoil surface. u and v : are the horizontal and vertical velocity components, p : air pressure, μ : air viscosity, ρ : air density.

From the above equations, the well-known Von Karman integral momentum equation is obtained:

$$\frac{d\theta}{dx} + \frac{\theta}{U_e} (2 + H) \frac{dU_e}{dx} = \frac{1}{2} C_f\tag{5.2}$$

and

$$H = \delta^* / \theta\tag{5.3}$$

where H is the shape factor, δ^* is the displacement as defined in Figure 5-4, θ is the momentum thicknesses and C_f is the skin friction coefficient. They are defined using the following equations:

$$\delta^* = \int_0^\infty \left(1 - \frac{u}{U_e} \right) dy\tag{5.4}$$

$$\theta = \int_0^\infty \frac{u}{U_e} \left(1 - \frac{u}{U_e} \right) dy\tag{5.5}$$

$$C_f = \frac{\mu \left. \frac{\partial u}{\partial y} \right|_{y=0}}{\frac{1}{2} \cdot \rho U_e^2}\tag{5.6}$$

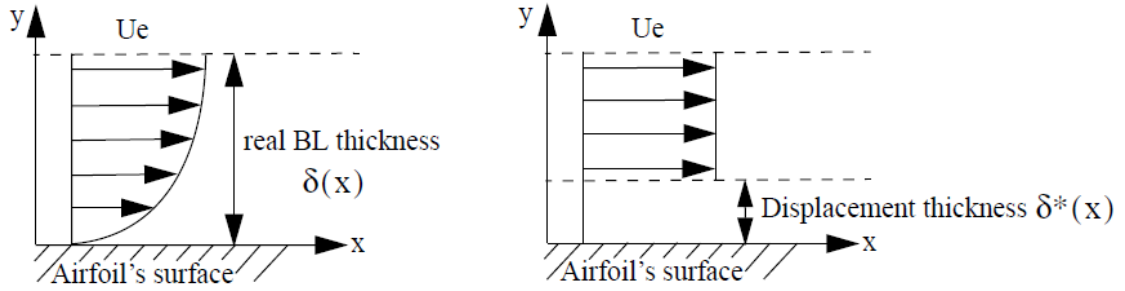


Figure 5-4 The definition of the displacement and the momentum thicknesses (Wauquiez, 2009)

Multiplying equation (5.2) by the Reynolds number (Re) based on the momentum thickness $Re_\theta = Re \theta U_e$ leads to the equation

$$Re U_e \frac{d\theta^2}{dx} = 2[L - (2 + H)\lambda] \quad (5.7)$$

where

$$L = Re \theta U_e \frac{C_f}{2} \quad (5.8)$$

$$\lambda = Re \theta^2 \frac{dU_e}{dx} \quad (5.9)$$

Thwaites proved that the right-hand side of equation (5.7) can be approximated by (Houghton & Carpenter, 2003):

$$2[L - (2 + H)\lambda] \approx 0.45 - 6\lambda \quad (5.10)$$

Therefore, the final equation will be

$$Re \frac{d}{dx} (\theta^2 U_e^6) = 0.45 U_e^5 \quad (5.11)$$

Integrating this equation will evaluate the momentum thickness θ and hence λ . From the semi-empirical formulae given by Cebeci and Bradshaw, the shape factor H and the skin friction coefficient C_f can then be computed (Cebeci & Bradshaw, 2012):

$$H(\lambda) = 2.61 - 3.75\lambda + 5.24\lambda^2 \quad \text{for } 0 < \lambda < 0.1 \quad (5.12)$$

$$H(\lambda) = 2.088 + \frac{0.0731}{\lambda + 0.14} \quad \text{for } -0.1 < \lambda < 0$$

and
$$C_f = \frac{2L(\lambda)}{Re U_e \theta} \quad (5.13)$$

with

$$L(\lambda) = 0.22 + 1.57\lambda - 1.8\lambda^2 \quad \text{for } 0 < \lambda < 0.1$$

$$L(\lambda) = 0.22 + 1.402\lambda + \frac{0.018\lambda}{\lambda + 0.107} \quad \text{for } -0.1 < \lambda < 0 \quad (5.14)$$

II. Laminar Separation

Thwaites' method cannot represent the separation flows and that necessitates checking for either separation or transition of the boundary layer within the laminar flow field. The laminar separation occurs when the factor $L(\lambda)$ in equations (5.14) becomes vanishingly small. Accordingly, the laminar separation will occur when $\lambda \leq -0.0842$ (Moran, 2003).

III. Michel's Transition Criterion

Michel's criterion has been used to indicate the transition point from laminar to turbulent flow (Moran, 2003). The idea of this criterion is that the transition starts at a specific local Reynolds number depending on the pressure gradient imposed on the boundary layer by the inviscid flow and the surface roughness (Houghton & Carpenter, 2003). For incompressible flow around an aerofoil without heat transfer, the transition occurs when

$$Re_{\theta} > Re_{\theta_{\max}} = 1.174 \left(1 + \frac{22400}{Re_x} \right) (Re_x)^{0.46} \quad (5.15)$$

where $Re_{\theta} = ReU_e\theta$ and $Re_x = ReU_ex$

This criterion is valid for $10^5 < Re_x < 4 \times 10^7$.

IV. Turbulent Boundary Layer

After the laminar separation or beyond the transition point, the boundary layer is assumed to become turbulent. In this model, the flow behaviour of the transition area or of the laminar separation bubble is ignored. Therefore, after predicting the laminar separation or transition, the flow will be considered to be turbulent. Head's method has been used to predict the turbulent boundary layer development using a number of semi-empirical correlations of experimental data in addition to the momentum integral equation (Moran, 2003). This model also checks whether separation is occurring and if not, the calculations will continue to the trailing edge.

Head's method bases the concept on the entrainment velocity ($E = dQ/dx$). It is the rate of increasing the volume rate of flow within the boundary layer as shown in Figure 5-5.

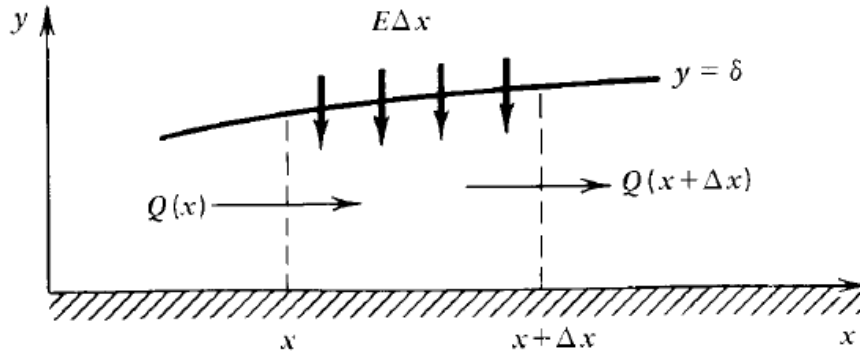


Figure 5-5 The conception of entrainment (Moran, 2003)

$$Q(x) = \int_0^{\delta(x)} u dy \quad (5.16)$$

Combining this equation with the definition of the displacement thickness will yield

$$\delta^* = \delta - \frac{Q}{U_e} \quad (5.17)$$

and so, the entrainment velocity can be written as

$$E = \frac{d}{dx} (U_e \theta H_1) \quad (5.18)$$

where

$$H_1 = \frac{\delta - \delta^*}{\theta} \quad (5.19)$$

Head assumes that the dimensionless entrainment (E/U_e) depends only on H_1 which in turn is a function of $H = \delta^*/\theta$. The Cebeci and Bradshaw's equations can be set with the equations (Cebeci & Bradshaw, 2012)

$$\frac{1}{U_e} \frac{d}{dx} (U_e \theta H_1) = 0.0306 (H_1 - 3)^{-0.6169} \quad (5.20)$$

and

$$\begin{aligned} H_1 &= 3.3 + 0.8234(H - 1.1)^{-1.287} & \text{for } H \leq 1.6 \\ H_1 &= 3.3 + 1.5501(H - 0.6778)^{-3.064} & \text{for } H > 1.6 \end{aligned} \quad (5.21)$$

Moreover, by using the Ludwig-Tillman law, the skin friction can be evaluated by

$$C_f = 0.246 (10^{-0.678H}) \text{Re}_\theta^{-0.268} \quad (5.22)$$

So, to evaluate H_1 , θ , H and C_f , equation 5.20 needs to be integrated using the 2nd order Runge Kutta method.

Turbulent Flow Separation

The typical value for the shape factor (H) at separation point is about 2.4 and it will rapidly increase towards the separation point (Moran, 2003).

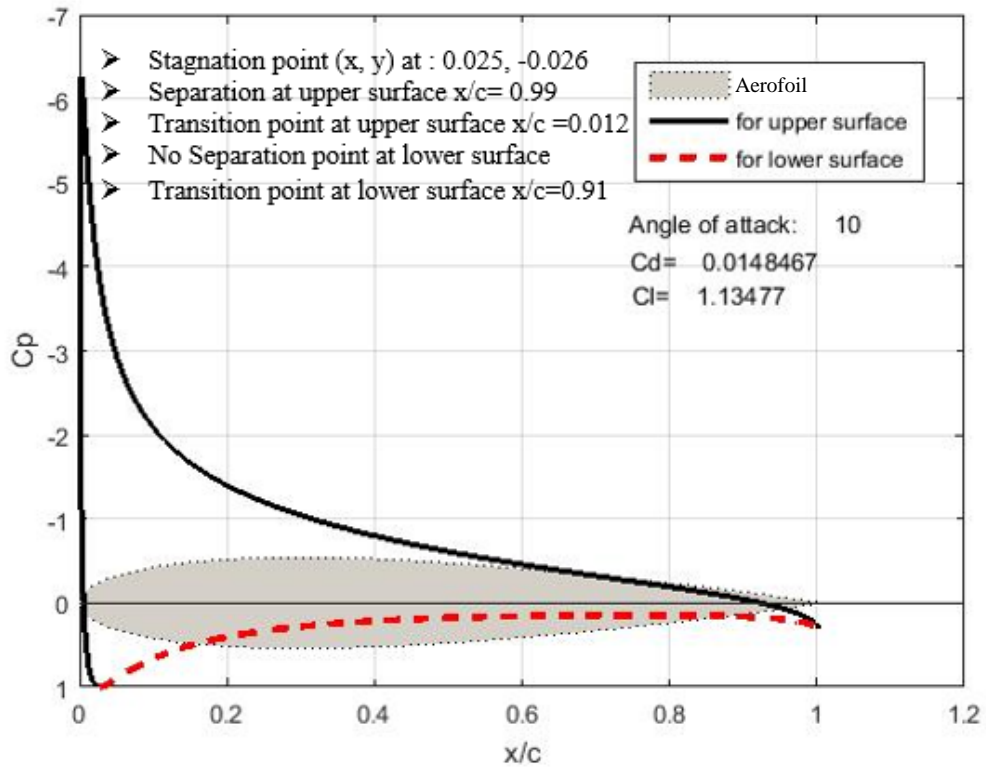
Computation of the Drag Coefficient

The Squire-Young formula can be used to evaluate the profile drag coefficient by the given dimensionless momentum thickness θ , the shape factor H and the dimensionless velocity U_e at the trailing edge of the upper and lower sides (Squire & Young, 1938):

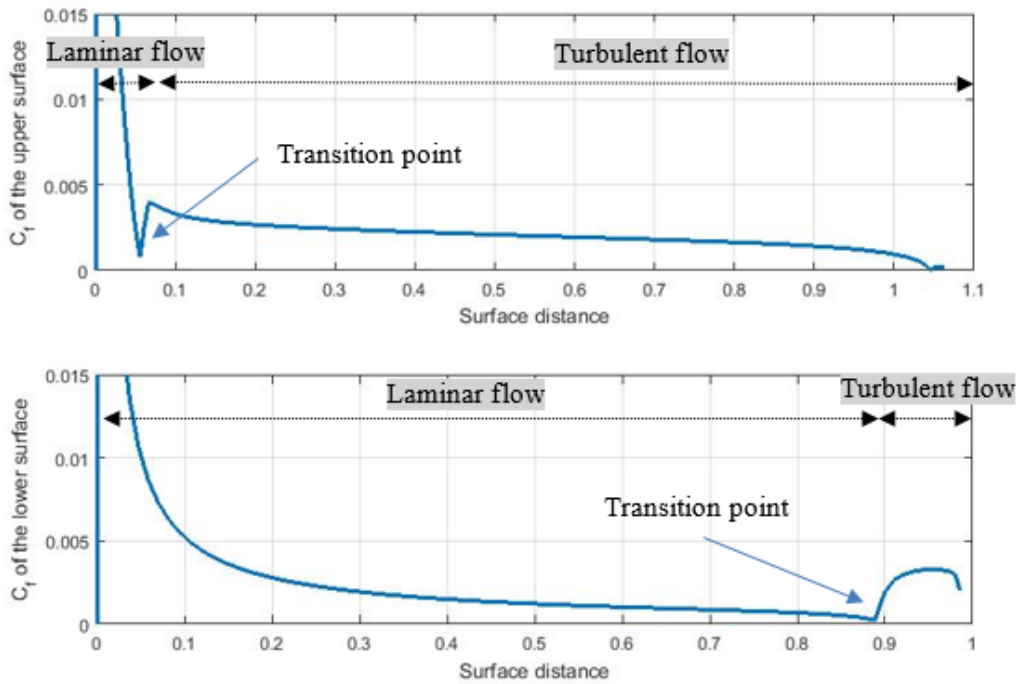
$$C_d = \left[2 \theta_{TE} (U_e)_{TE}^{\frac{H_{TE}+5}{2}} \right]_{Up} + \left[2 \theta_{TE} (U_e)_{TE}^{\frac{H_{TE}+5}{2}} \right]_{Low} \quad (5.23)$$

5.2.3 The Code IVM

A MATLAB code has been written according to the Panel Method (Inviscid Model) and the boundary layer equations (Viscous Model) presented in this chapter. This code is detailed in Appendix VI. The IVM can predict the separation and transition points on the lower and the upper surfaces, as well as the lift and drag coefficients. As an example of the results, the flow analysis around NACA0012 aerofoil at an angle of attack of 16° is presented in Figure 5-6. It is expected that the result of this model will be adequately accurate provided that it does not lie close to a region of separated flow or the trailing edge because the Thwaite's and the Heads' methods do not cater to this. The separation may begin at the trailing edge and then start migrating towards the leading edge with increasing angle of attack. Therefore, it is important to define the validity limit of the solver. Accordingly, it is found for IVM, if the separation was predicted at 98% to 100% of the chord length, the result will be acceptable.



(a) Inviscid Pressure Distribution and Viscous Prediction



(b) Friction Coefficient Distribution for Upper and Lower Surface

Figure 5-6 Sample of the IVM prediction for NACA0012, $Re = 1.44 \times 10^6$, 16 degrees AoA

5.2.4 Validating the 2D Inviscid/Viscous Model (IVM)

The validation of the 2D Inviscid/Viscous Model (IVM) was carried out using experimental data for the three aerofoils operating at different Reynolds number as detailed in Table 5-1. The results using the IVM are also compared with the results of Xfoil. The setting of the Xfoil was set at Mach=0 and Ncrit=9 (standard wind tunnel turbulence level).

Table 5-1 Aerofoils used in the validation of the IVM

Aerofoils	Re	References
NACA-0012	1.44×10^6	(Gregory & O'Reilly, 1973)
NACA-1408	6×10^6	(Abbott & Von Doenhoff, 1959)
S7055	0.3×10^6	(Michael S. Selig, James J. Guglielmo, Andy P. Broeren, & Philippe Giguere, 1995)

The lift and drag curves shown in Figure 5-7, Figure 5-8 and Figure 5-9 show some interesting features. In addition, the pressure distribution, the shape factor, the momentum thickness and the skin friction coefficient obtained by the IVM and Xfoil at angles of attack 0 and 6 degree are displayed. The values of the friction and the pressure drag coefficients are tabulated in Table 5-2.

Table 5-2 Drag analysis obtained by IVM and Xfoil

Aerofoil	Re x10 ⁶	AoA	IVM			Xfoil		
			C_{df}	C_{dp}	C_d	C_{df}	C_{dp}	C_d
NACA1408	6	AoA=0	0.00502	0.00063	0.00566	0.00423	0.00037	0.00460
		AoA=6	0.00381	0.00328	0.00709	0.00439	0.00260	0.00699
NACA0012	1.44	AoA=0	0.00604	0.00076	0.00680	0.00425	0.00091	0.00516
		AoA=6	0.00595	0.00330	0.00926	0.00535	0.00346	0.00881
S7055	0.3	AoA=0	0.00802	0.00032	0.00834	0.00507	0.00286	0.00793
		AoA=6	0.00838	0.00458	0.01297	0.00617	0.00496	0.01110

Since one-way coupling is used in the IVM, the estimated lift is calculated for inviscid flow and hence the expectation is that the lift will be closer to the upper limit when compared to experimental data.

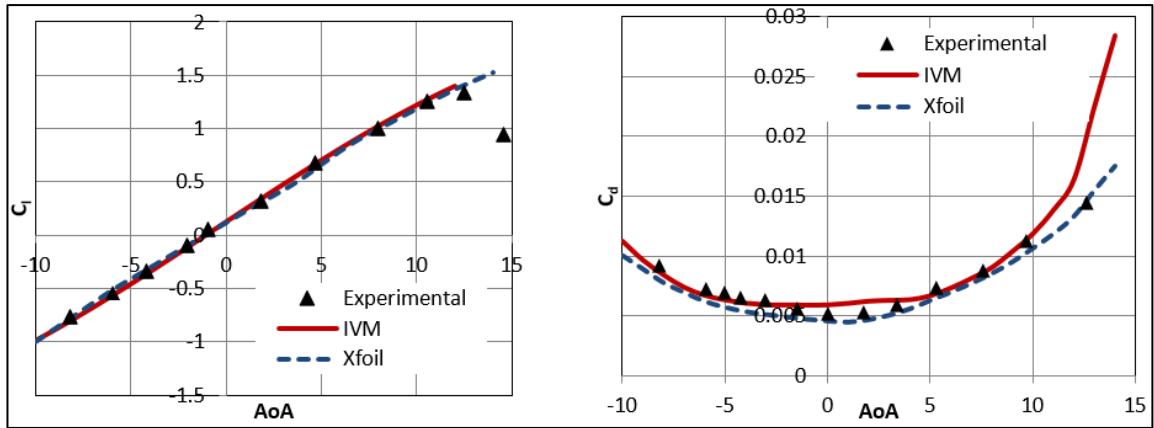
For the case of aerofoil NACA-1408 which was conducted at high Reynolds number of 6×10^6 , the lift coefficient obtained by the IVM are in good agreement with both the experimental data and the Xfoil result due to reduced effects of viscosity as indicated in the pressure distribution curve shown in Figure 5-7. The results of drag obtained by both models were reasonably close to the experimental data but the IVM slightly overestimated it at lower angles of attack and as expected, considerably overestimated it at angles of attack close to the stalling region. The results show that the IVM predicts the transition from laminar to

turbulent boundary layer at an earlier stage than that predicted by Xfoil. However, at higher angles of attack (5-10 degrees), the transition points predicted by both models approach each other leading to good agreement in estimating the drag coefficient.

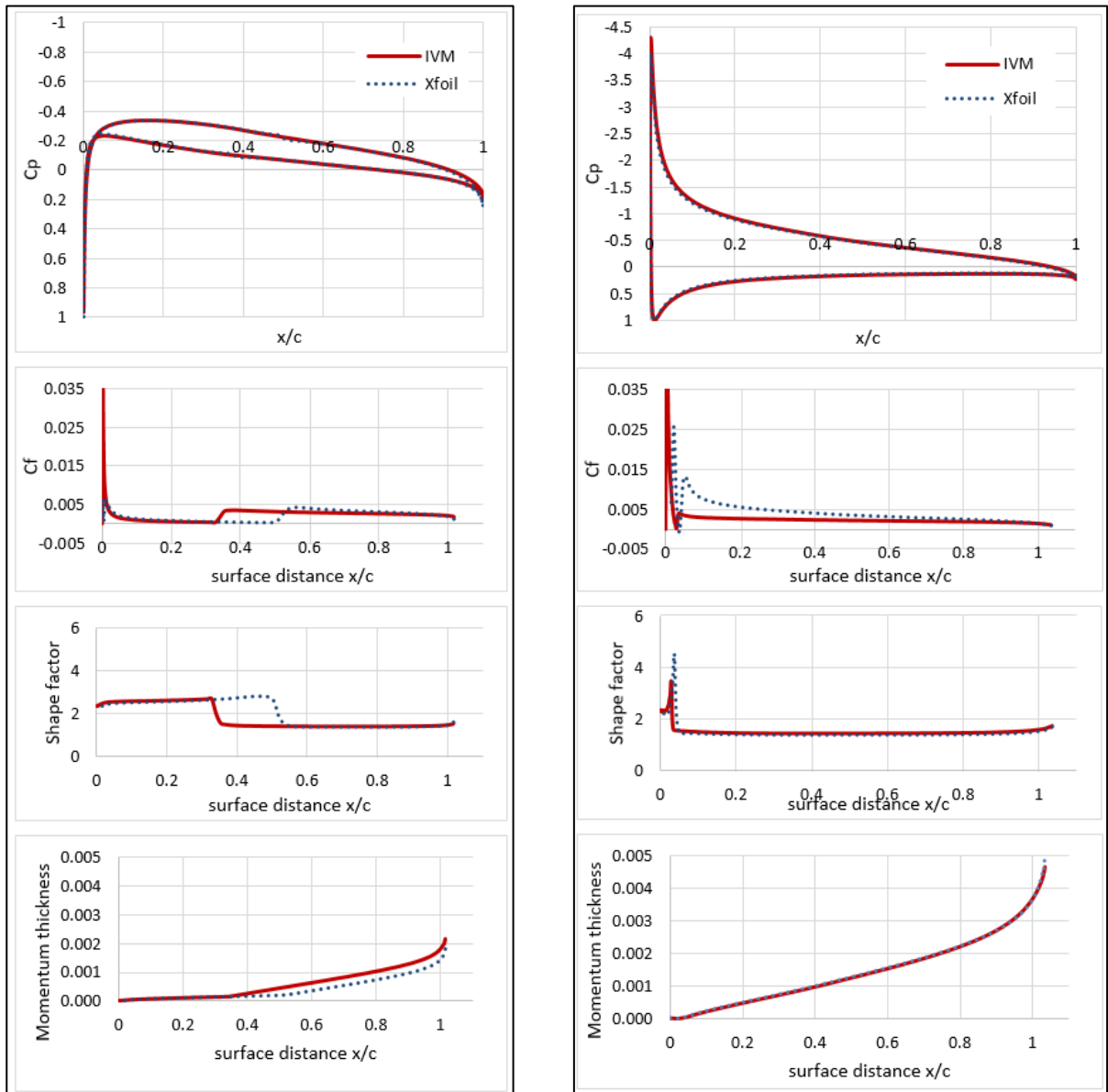
At lower Reynolds number, the influence of the viscosity on the pressure distribution is more noticeable. As expected, the lift coefficient obtained by the IVM is higher when compared to experimental data. This was noticed in the results of NACA0012 shown in Figure 5-8. The results also indicate that the Xfoil estimate for the lift coefficient is more accurate. However, the drag estimated by IVM is in good agreement with experiment and higher than that of the Xfoil due to higher skin friction in the turbulent region.

For the case of aerofoil S7055 which was conducted at low Reynolds number of 0.3×10^6 , nonlinear behaviour predicted by Xfoil in the lift coefficient at lower angles of attack is noticeable. This was caused by a persistent large laminar separation. This can be seen as a significant difference in the shape factor which in turn reduces the skin friction coefficient as shown in Figure 5-9 b. Also, the drag estimated by the Xfoil in this case showed poor results when compared to the one-way coupling solver (IVM). The drag estimated by Xfoil is slightly underestimated and gets worse with increasing angle of attack. It seems that the laminar separation predicted by the Xfoil will affect the overall performance of the aerofoil. The predicted laminar bubble tends to interact with the external flow (due to the two-way coupling between the Panel Method and the boundary layer equations in Xfoil) and appreciably alter the pressure distribution along the aerofoil, and hence affecting its performance. However, this was not noticed in the experimental data. Moreover, this feature is not apparent in the IVM curve because the onset laminar separation is considered as a transition to turbulence and no interaction with the external flow is considered (due to adopting one-way coupling). In conclusion, the large separation predicted by the Xfoil has led to reduced accuracy.

In general, the results indicate that the IVM predicts earlier transition than Xfoil. This explains why the IVM predicts higher drag. The lift coefficient predicted by Xfoil is more robust than that by the IVM because Xfoil performs two-way coupling to capture the viscous effects on the pressure distribution. These results indicate that the IVM produces a reasonably good estimate for the drag coefficient.



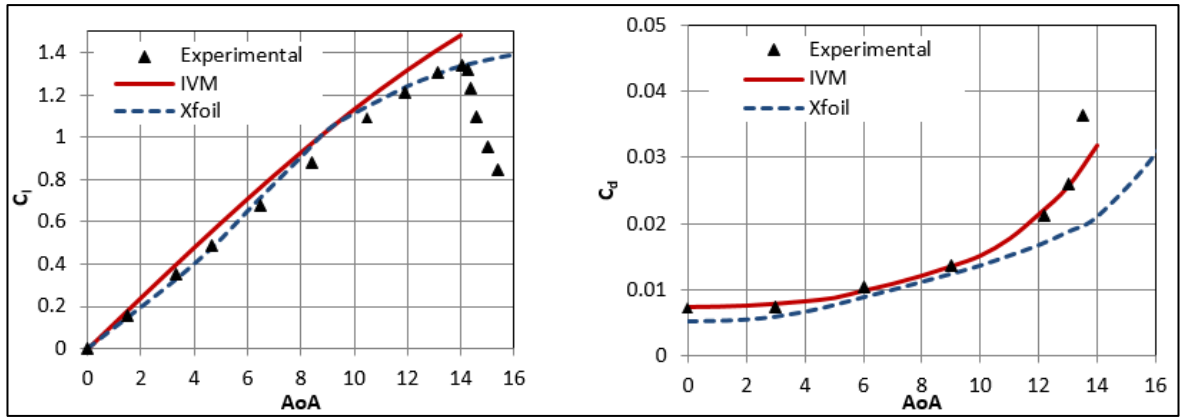
(a) Lift and drag coefficients versus dangle of attack



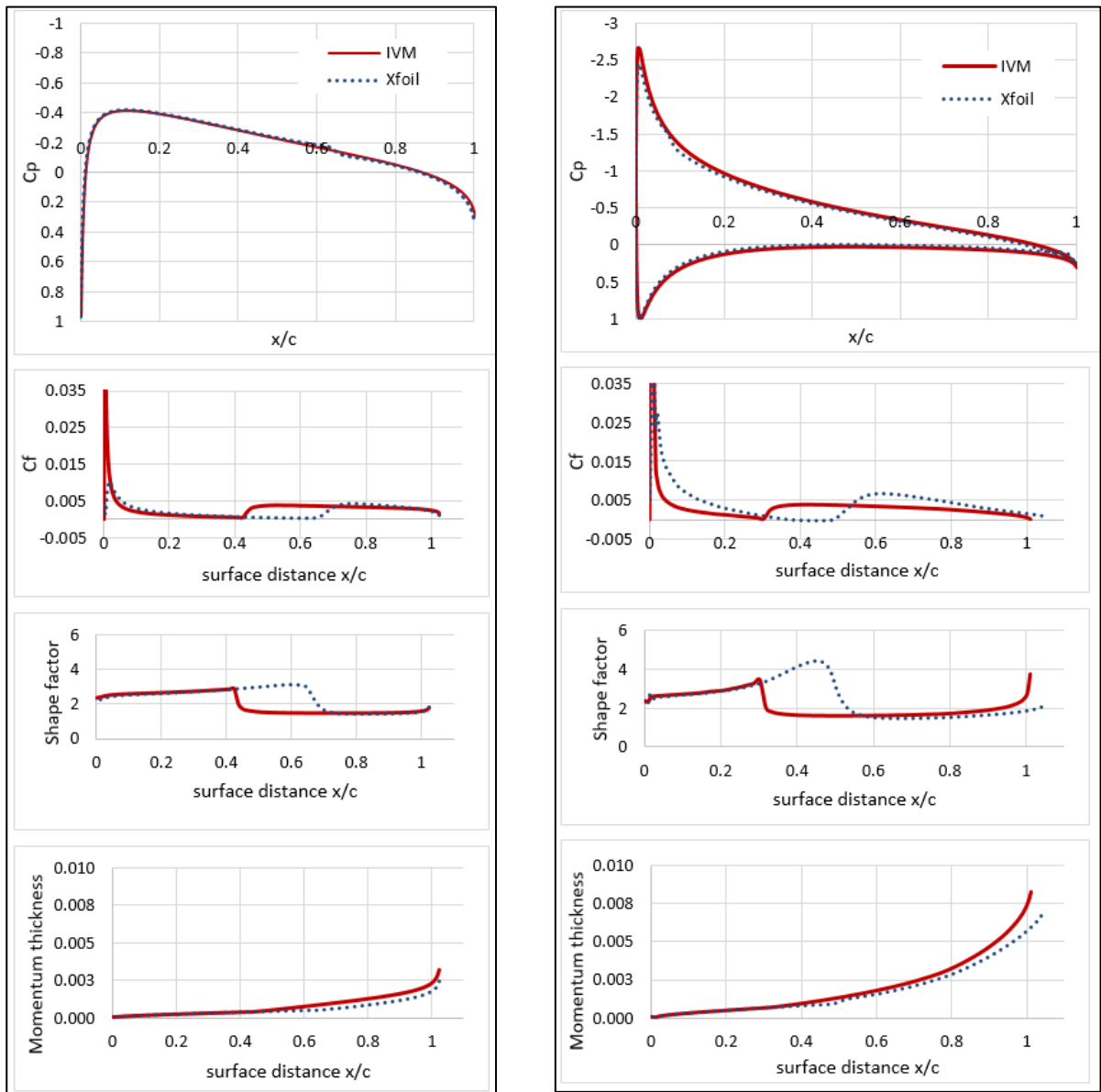
(b) Boundary layer parameters at $AoA=0$

(c) Boundary layer parameters at $AoA=6$

Figure 5-7. IVM validation with Xfoil and experimental data for NACA-1408 Aerofoil, $Re = 6 \times 10^6$



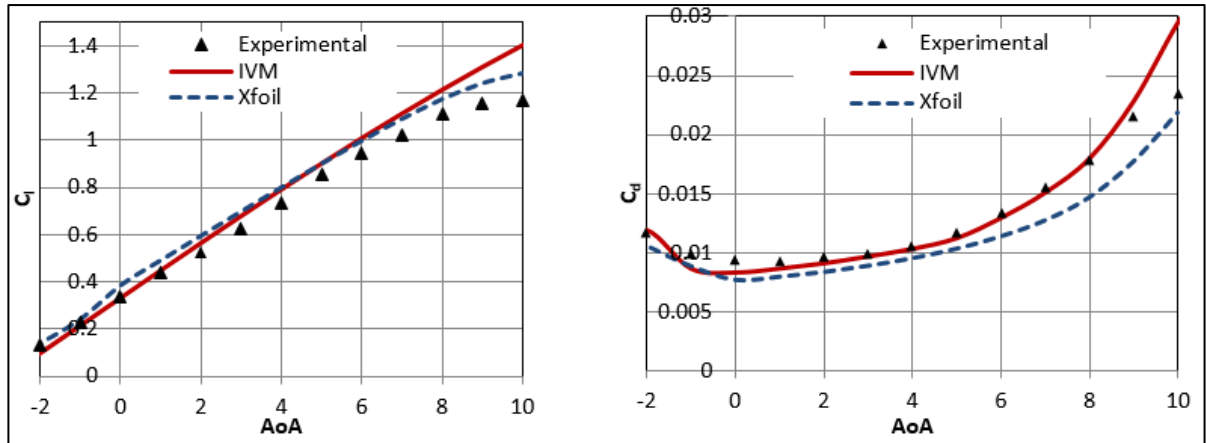
(a) Lift and drag coefficients versus dangle of attack



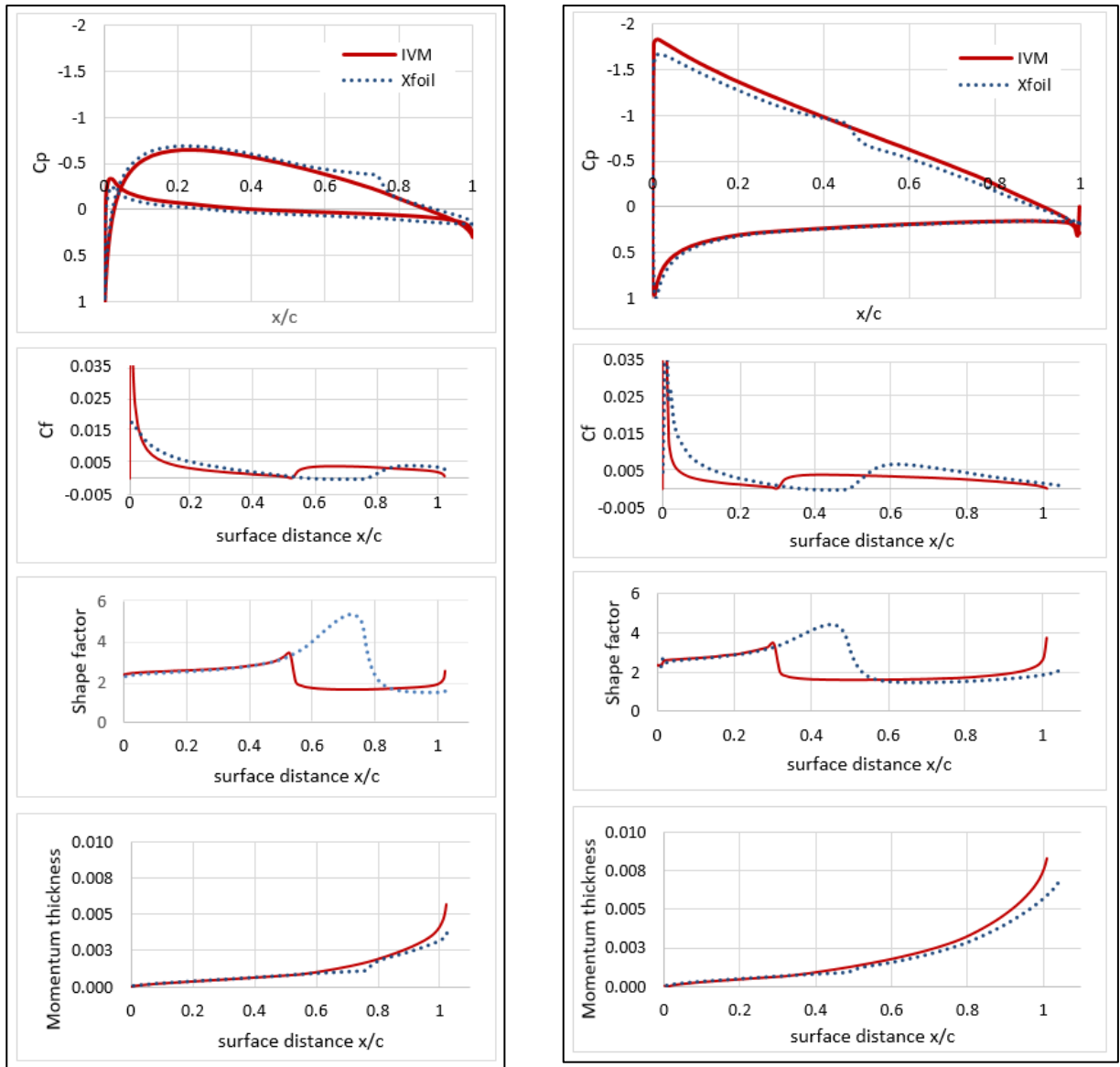
(b) Boundary layer parameters at $AoA=0$

(c) Boundary layer parameters at $AoA=6$

Figure 5-8. IVM validation with Xfoil and experimental data for NACA-0012 Aerofoil, $Re = 1.44 \times 10^6$



(a) Lift and drag coefficients versus dangle of attack



(b) Boundary layer parameters at AoA=0

(c) Boundary layer parameters at AoA=6

Figure 5-9. IVM validation with Xfoil and experimental data for S7055 Aerofoil, $Re = 0.3 \times 10^6$

5.3 Quasi-Three-Dimensional Aerodynamic Solver

In this method, the wing induced drag is evaluated using the Vortex Lattice Method (VLM), whereas the profile drag is evaluated using the Strip Theory (Jan Mariens, 2012). According to the Strip Theory, the wing geometry is divided into several two-dimensional spanwise wing sections and by using the effective velocity and the effective angle of attack, the aerodynamic forces on each segment will be evaluated. The use of the Strip Method has been modified for implementation of sweep and tapered effects as detailed in (Jan Mariens, 2012; J Mariens et al., 2014; Obert, 2009; Trips, 2010). The method could have been simplified by not having to consider the perpendicular velocity component at the wing leading edge as the Reynolds number is relatively small. However, it was not difficult to include the high speed effects. Strip Method ignores the three-dimensional nature of the boundary-layer development which is particularly important for tapered swept wings. The quasi-3D procedure can be divided into three main steps as shown in Figure 5-10.

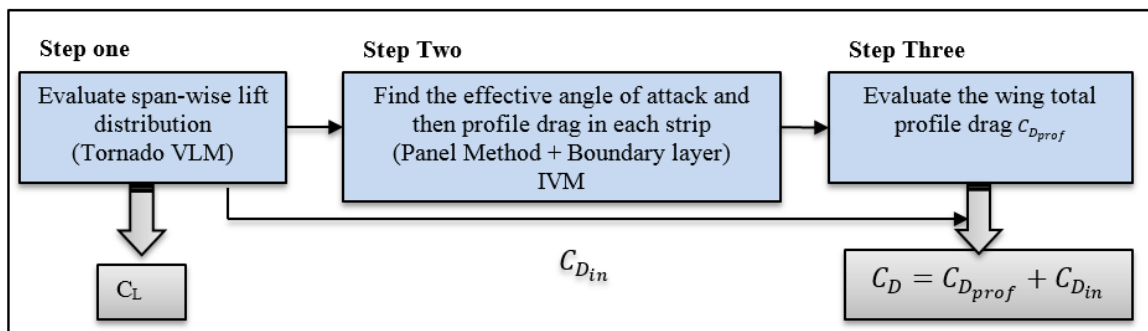


Figure 5-10 Procedure of the Quasi-3DM

Step One:

Tornado VLM is used to evaluate the span-wise lift distribution and induced drag of the given wing geometry and flight state condition. The span-wise lift distribution can be interpolated for each strip, in addition to performing other calculations which are required for the next steps for each strip, such as the strip planform area, the local angle of attack, chord length and the interpolated aerofoil shape which lies perpendicular to the sweep line.

Step Two:

In this step, the effective angle of attack (α_{eff}) and profile drag ($C_{d_{eff}}$) for a given local lift coefficient (from the first step) in each strip, will be calculated using the two-dimensional aerodynamic characteristics of the wing section by applying the Sweep Theory. That means the airspeed V_∞ and aerofoil shape and other geometric parameters that are

involved in the calculation must be based on the direction perpendicular to the sweep line as shown in Figure 5-11. In the present application, the sweep line can be the quarter-chord line while the flight speed is in the subsonic range (Obert, 2009). Therefore, the perpendicular airspeed V_{\perp} and perpendicular chord c_{\perp} will be used instead of V_{∞} and c :

$$V_{\perp} = V_{\infty} \cos \Lambda \quad (5.24)$$

$$c_{\perp} = C_{aft} + C_{front} \quad (5.25)$$

where C_{aft} and C_{front} are shown in Figure 5-11.

For the tapered swept wing case, the aerofoil which lies perpendicular to the sweep line, can be interpolated from its two neighbouring aerofoils as shown in Figure 5-11. The corresponding lift coefficient $C_{l_{\perp}}$ is found using the sweep angle and the local lift coefficient C_l as:

$$C_{l_{\perp}} = C_l \sec^2 \Lambda \quad (5.26)$$

where Λ is the quarter-chord sweep angle.

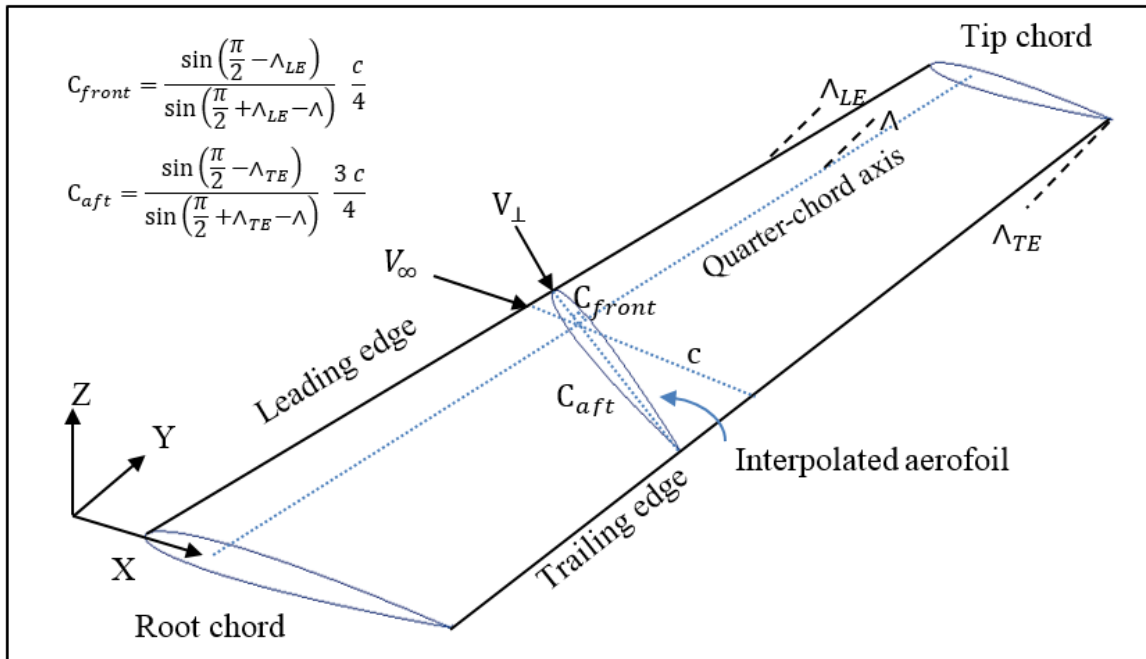


Figure 5-11 Aerofoil section perpendicular to the sweep line of a tapered wing

Figure 5-12 shows the forces and angles at each wing section. The effective lift force can be given as

$$l_{eff} = (l_{\perp} + d_{eff} \sin \alpha_i) / \cos \alpha_i \quad (5.27)$$

Alternatively, the lift and the drag coefficient can be used instead of the forces as shown in the equation below:

$$C_{l_{eff}} = (C_{l_{\perp}} \cos^2 \alpha_i + C_{d_{eff}} \sin \alpha_i) / \cos \alpha_i \quad (5.28)$$

The effective Reynolds number (Re_{eff}) can be evaluated by

$$Re_{eff} = Re_{\infty} \frac{V_{eff} C_{\perp}}{V_{\infty} C_{av}} \quad (5.29)$$

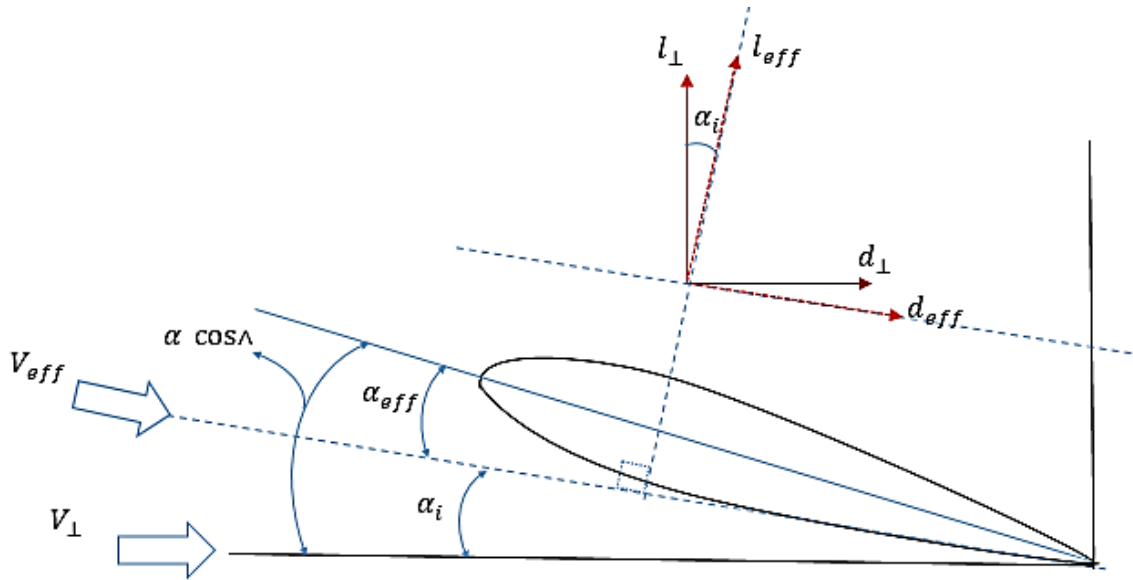


Figure 5-12 Angles and Forces Present in the Quasi-3D Method

The effective angle of attack can be found using an iterative method. The induced angle (α_i) is set to zero at the first iteration and then the effective lift coefficient is evaluated. Then the corresponding effective angle of attack will be found which in turn is used to evaluate the induced angle. This process can be repeated until a convergence in the induced angle is achieved.

Once the effective angle of attack is found, the profile drag can be evaluated as the sum of the pressure and friction drag coefficients given by

$$C_{d_{prof}} = C_{df_{\perp}} + C_{dp_{\perp}} \cos^3 \Lambda \quad (5.30)$$

where $C_{df_{\perp}}$ and $C_{dp_{\perp}}$ are the skin friction and pressure drag components respectively normal to the sweep line. Note that the friction drag is not affected by the sweep as assumed in (Jan Mariens, 2012). The friction and pressure drag coefficients are defined as

$$C_{df_{\perp}} = C_{df_{eff}} / \cos \alpha_i \quad (5.31)$$

$$C_{dp\perp} = C_{dp_{eff}} / \cos \alpha_i \quad (5.32)$$

Figure 5-13 outlines the steps that are followed to find the effective angle of attack and the profile drag.

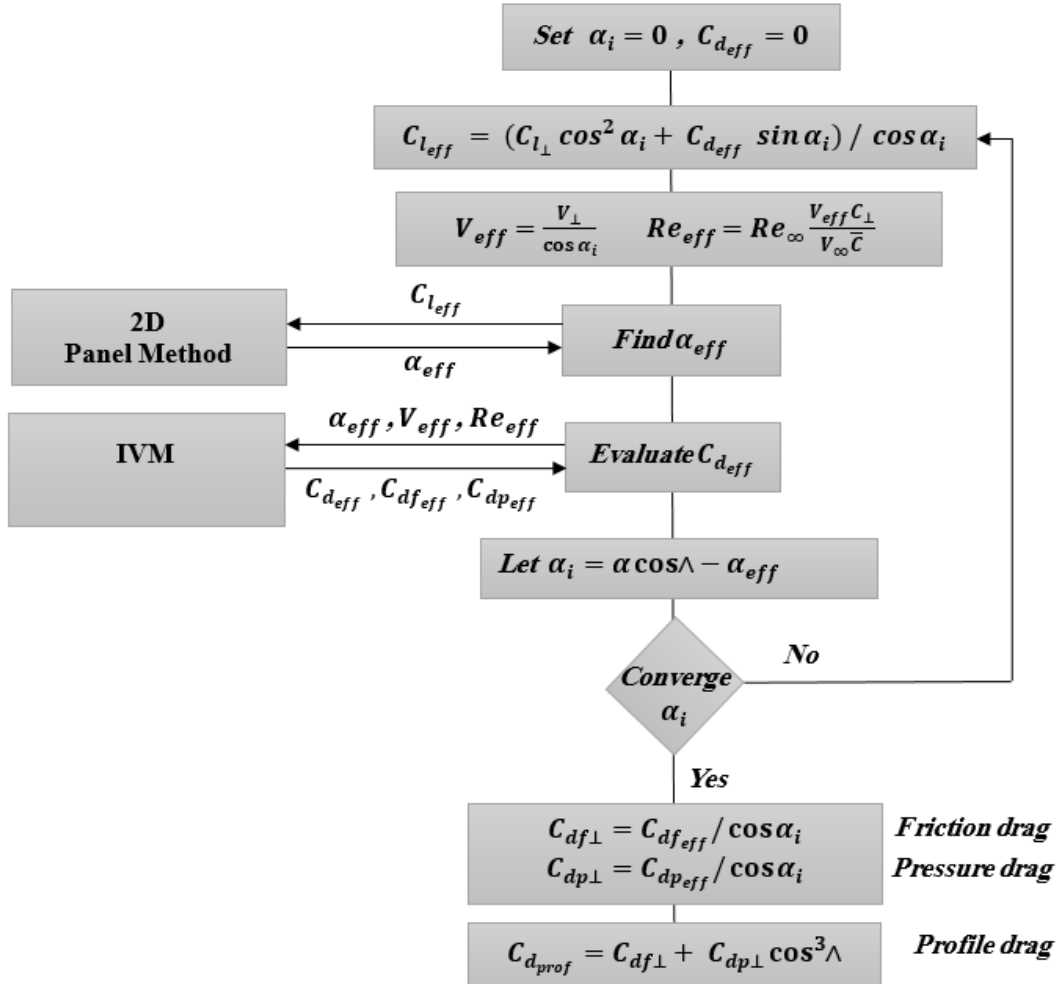


Figure 5-13 Steps to finding the effective angle of attack (α_{eff}) and profile drag

Step Three:

The total profile drag coefficient of the wing ($C_{D_{prof}}$) can be evaluated by integrating the profile drag forces along the wing span

$$C_{D_{prof}} = \frac{2}{S} \int_0^{b/2} C_{d_{prof}} c dy \quad (5.33)$$

The total drag coefficient can now be determined as a sum of the profile drag coefficient and the induced drag coefficient of the wing:

$$C_D = C_{D_{prof}} + C_{D_{in}} \quad (5.34)$$

5.3.1 Validation of the Quasi-Three-Dimensional Aerodynamic Solver

The Quasi-3DM has been validated using experimental data for three different configurations: swept only, tapered only and swept & tapered wings as described in Table 5-2. Figure 5-14 presents the validation results of the three cases. Table 5-3, Table 5-4 and Table 5-5 show the results of the error analysis of the drag calculated by the Quasi-3DM for all three validation cases. The results indicate that the lift coefficient is overestimated because of the Vortex Lattice Method used to evaluate the lift and the induced drag. The drag estimation shows good agreement with the experimental data. The average error for the drag coefficient for the tapered wing (Case 2) is about -5.65% while the average errors for the swept wings (Case 1 & Case 3) are higher at -9.36% and -11.05% respectively due to the neglecting of the three-dimensional nature of the development of the boundary-layer. The time it took to obtain the total drag for each angle of attack, including the time required for the Tornado VLM, was about 10 seconds using a PC with a CORE i5 CPU. This low order model shows a high order quality of predicting the drag for different wing configuration. However, the Quasi-3DM does not work at higher angles of attack when the boundary layer begins to separate.

According to the validation results, the Quasi-3DM can be used in an iterative design process due to its good drag prediction capability and due to its fast computation. Attention should be paid when the optimisation process was searching for the twist and the angle of attack.

Table 5-3 Three Experimental cases for the Quasi-3DM validation

Case No.	1	2	3
Wing dis.	 Swept wing	 Tapered wing	 Swept tapered wing
Sweep [deg.]	45	0	15
AR	5	10	6
Taber ratio	1	1/3	1/2
Re	1.7×10^6	3.1×10^6	3.1×10^6
Root Aerofoil	RAE 101	NACA23018	NACA2415
Tip Aerofoil	RAE 101	NACA23009	NACA2409
References	(Sreher & Wyatt, 1961)	(R. F. Anderson, 1935)	(R. F. Anderson, 1934)

Table 5-4 Error analysis of the Quasi-3DM for the swept wing (45 degree sweep-case 1)

AoA [deg.]	Experimental		Quasi-3DM		ΔC_L %	ΔC_D %
	C_L	C_D	C_L	C_D		
0	0.0000	0.0063	0.0000	0.0070	0	10.45
2	0.1227	0.0079	0.1137	0.0082	-7.38	4.48
4	0.2282	0.0128	0.2271	0.0114	-0.48	-10.74
6	0.3336	0.0196	0.3400	0.0169	1.91	-14.03
8	0.4416	0.0269	0.4521	0.0240	2.39	-10.85
10	0.5400	0.0333	0.5633	0.0327	4.32	-1.85

Table 5-5 Error analysis of the Quasi-3DM for the tapered wing (case 2)

AoA [deg.]	Experimental		Quasi-3DM		ΔC_L %	ΔC_D %
	C_L	C_D	C_L	C_D		
0	0.0985	0.0095	0.0997	0.0087	1.20	-8.55
2	0.2600	0.0120	0.2766	0.0108	6.39	-9.55
4	0.4310	0.0159	0.4536	0.0153	5.23	-4.00
6	0.5950	0.0235	0.6303	0.0215	5.93	-8.78
8	0.7600	0.0318	0.8067	0.0299	6.14	-5.96
10	0.9250	0.0431	0.9826	0.0416	6.22	-3.54
12	1.0950	0.0551	1.1578	0.0555	5.73	0.77

Table 5-6 Error analysis of the Quasi-3DM for the swept tapered wing (case 3)

AoA [deg.]	Experimental		Quasi-3DM		ΔC_L %	ΔC_D %
	C_L	C_D	C_L	C_D		
0	0.1400	0.0096	0.1649	0.0077	17.81	-20.20
2	0.2930	0.0128	0.3173	0.0108	8.29	-15.35
4	0.4420	0.0200	0.4694	0.0171	6.19	-14.58
6	0.5890	0.0294	0.6210	0.0264	5.43	-10.36
8	0.7380	0.0400	0.7718	0.0385	4.58	-3.77
10	0.8900	0.0569	0.9216	0.0525	3.55	-7.77
12	1.0360	0.0727	1.0702	0.0688	3.30	-5.35

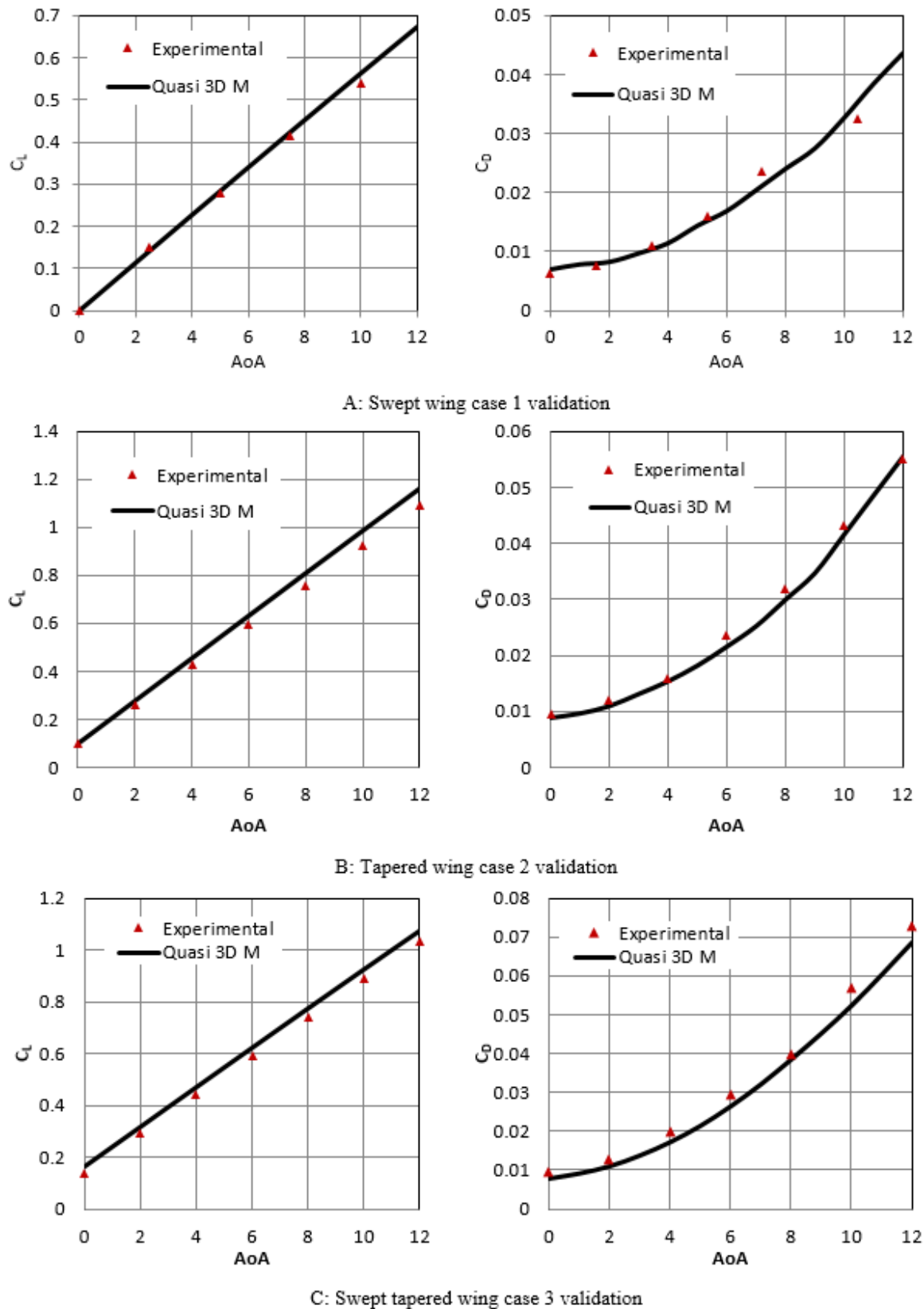


Figure 5-14 Validation results of the Quasi 3DM with the three experimental cases

CHAPTER 6

6 COMPOSITE STRUCTURE MODEL

The physical structure of an aircraft needs to be simplified if the structural design considerations are to be included in the optimisation process. Nowadays, composite materials have been widely used in aircraft structures due to their increased suitability for applications under certain circumstances. These materials are usually based on carbon embedded in a matrix such as Epoxy and Polyester. Such a laminate can be aligned with the major load direction resulting in a more effective design (Megson, 2012).

In this chapter, a composite structure model (CSM) has been developed to design and estimate the wing weight and the mechanical properties of the spar. Also, a linear finite beam elements model has been employed to evaluate the wing deflection.

6.1 Composite wing sizing approach

The wing structure can be broken down into non-spar elements and spar. Non-spar elements can be estimated by using empirical equations while the spars are sized by using a numerical approach, which is introduced in this research. The spars are modeled as a composite rectangular wing-box and assumed to withstand the entire load with no contribution from secondary wing components. The typical wing structure of a high-altitude aircraft is shown in Figure 6-1.

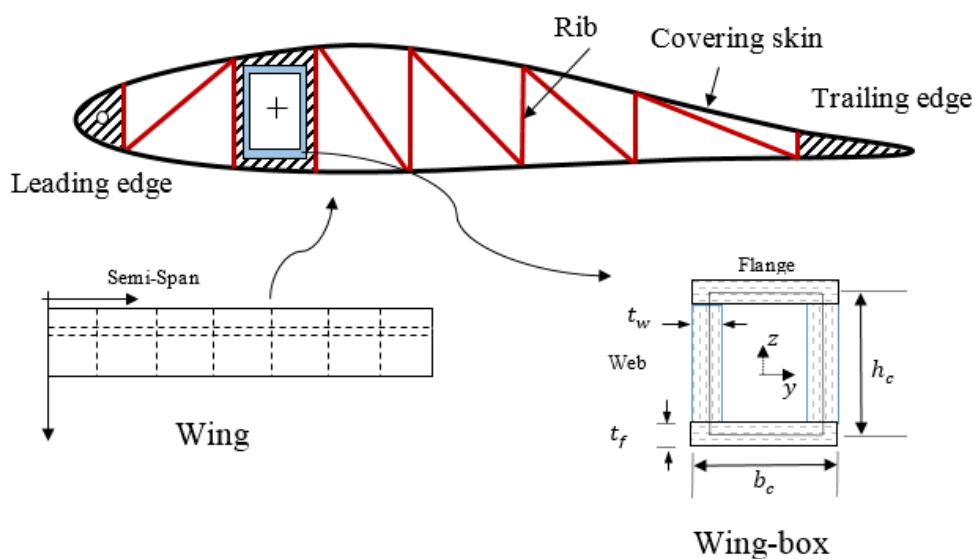


Figure 6-1 Sketch of the Structural Wing Model and Wing-box Idealization

When designing wing structures and investigating its mechanical properties, the weight of the aircraft components must be known from previous knowledge gleaned during the conceptual design stage. The wing configuration and the on-board weight distribution, as well as the maximum wing section and the spar location, are the key parameters that can influence the sizing of the spar.

The following steps summarise the overall weight estimation of the wing structure as detailed in Figure 6-2:

- 1- Set the wing configurations (sweep, dihedral, twist, aerofoil section, span and aspect ratio).
- 2- Suggest a distribution for the on-board weight along the span-wise and chord-wise directions.
- 3- Estimate the weight of the non-spar elements using empirical equations which is detailed in the next section. This weight then can be formulated as a weight density per unit area factor.
- 4- Set the flight state and calculate the critical aerodynamic load using Tornado VLM.
- 5- Suggest the outer dimensions (width and height) of the spar. In this work, the spar height equals 0.8 of the maximum wing thickness whilst the width is represented as a ratio of the spar height.
- 6- Suggest the location of the elastic axis of the spar as an eccentricity ratio of the local wing chord.
- 7- Discretise the spar length into several partitions.
- 8- Find the total load by combining the critical aerodynamic load and the internal weight distribution. The full load can be represented as shear forces, bending moments and torque values about the elastic axes at each station.
- 9- Find the maximum critical load in each spar partition. Neglect the drag force.
- 10- Size each spar partition according to its critical load as will be detailed in section 6.1.2.1. The mechanical properties and the weight of each spar partition can now be found.
- 11- Use the spar weight in accordance with the inertial loads and repeat the sizing process from step 8 above until a convergence is achieved.

The following sections will present the above steps in more details.

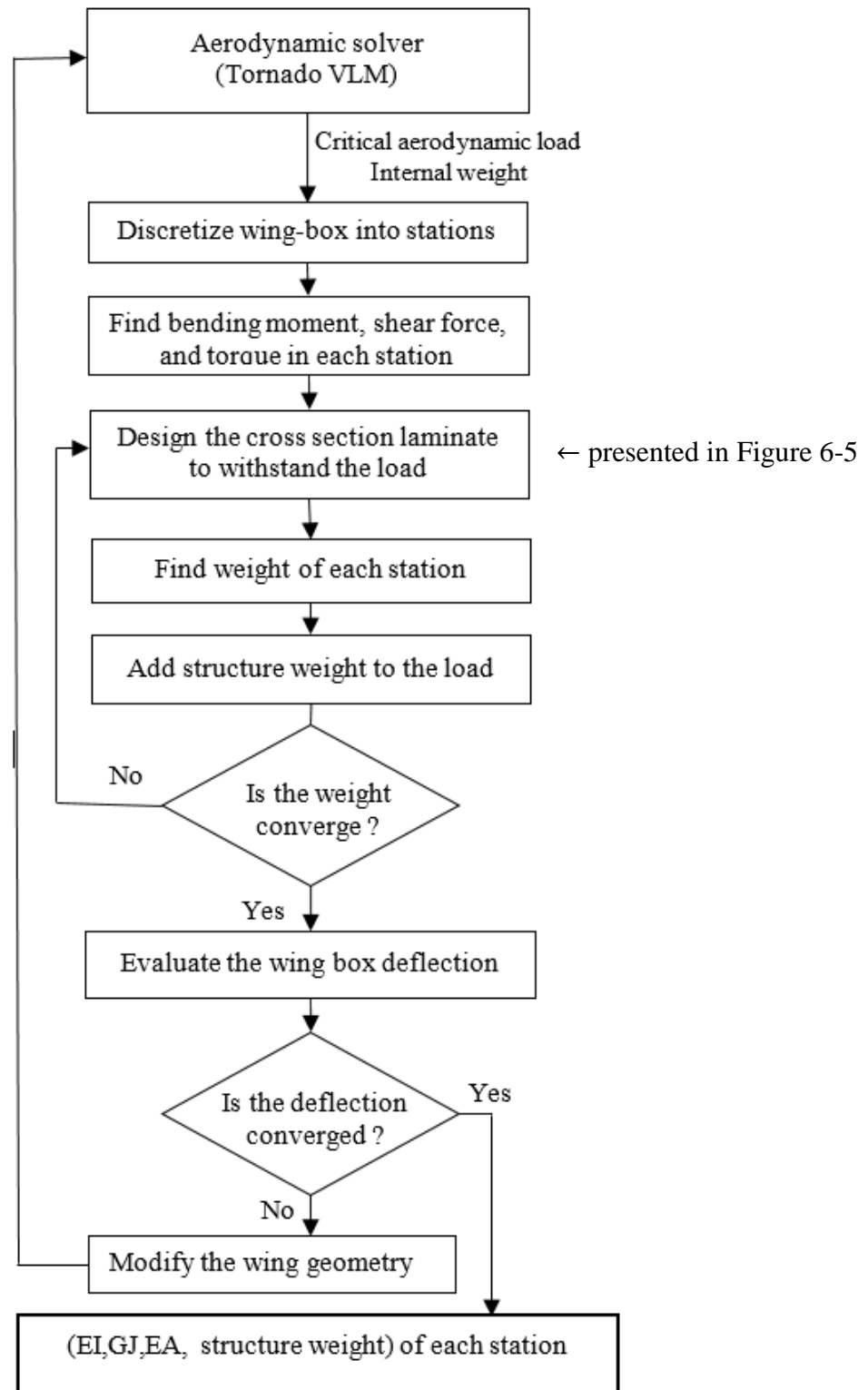


Figure 6-2 Overview of the wing sizing methodology

6.1.1 Non-spar Elements Estimation

The non-spar elements, such as the leading edge, the trailing edge, the skin and the ribs function together to transfer the aerodynamic loads to the spars as well as supporting the wing shape. In the sizing process, particularly at the preliminary design stage, their contribution of reinforcing the wing can be ignored but their weight must be considered. NASA Langley Research Centre and Lockheed Corporation formulated a structural weight estimation model for solar powered planforms (Colozza, 1993). The non-spar elements can be estimated according to the aircraft aspect ratio (AR), the wing wetted area (S_{wet}) and the wing reference area (S) as in the following equations (Colozza, 1993; Hall & Hall, 1984):

Leading edge mass:

$$m_{LE} = 0.9415 S / AR^{0.5} \quad (6.1)$$

Trailing edge mass:

$$m_{TE} = 0.0998 (AR S)^{0.5} \quad (6.2)$$

Covering mass:

$$m_{cov} = (0.2055 + 0.0028 (AR/S)^{0.5}) S_{wet} \quad (6.3)$$

Ribs mass:

$$m_{rip} = 1.033 S^{0.6} \quad (6.4)$$

where the masses are in kg, the planform and wetted areas are in m^2 .

Therefore, the total weight of the non-spar elements (m_{non_sp}) can be given by:

$$m_{non_sp} = m_{LE} + m_{TE} + m_{cov} + m_{rip} \quad (6.5)$$

6.1.2 Spar Sizing Approach

The wing spar which is the primary structure element must be designed to withstand the majority of the loads including the aerodynamic forces and the weight of the systems modules distributed within the wing.

The wingbox is discretised into partitions depending on the design and the manufacturing restrictions. Then, each station will be sized according to the expected maximum bending moment, shear force and torsional moment exerted on the partition. Each partition is sized by finding the required number of layers in each of its sides (flanges and webs) to withstand the critical load with a safety margin. Once the required plies are found, the spar weight can be evaluated and this value, which is effectively inertia relief, will be added to the overall loading condition. The calculations are repeated until a weight convergence is achieved.

The total mass of the spar (m_{spar}) is the sum of weights of the partitions.

$$m_{spar} = \sum m_{spar_par} \quad (6.6)$$

Then the total mass of the structure (m_{af}) will be:

$$m_{af} = m_{spar} + m_{non_sp} \quad (6.7)$$

6.1.2.1 Cross Section Design Procedure

Inspiring from existing methodologies which are adopted for isotropic structural models and from some existing structure design of HALE-UAV, the spar partitions can be represented as rectangular thin-walled beams. Figure 6-3 represents a spar partition where X,Y and Z axes represent the spar element axes whilst x_i, y_i and z_i represent the local axes of each sub element. The height of the spar partition (h_c) equals 0.8 of the maximum wing thickness (Torenbeek, 2013), and its width (w_c) can be assumed as a proportion of its height which is about 0.5 to 2.0 of the spar height. The laminated composite spar section can be divided into four sub-laminates, two webs and two flanges.

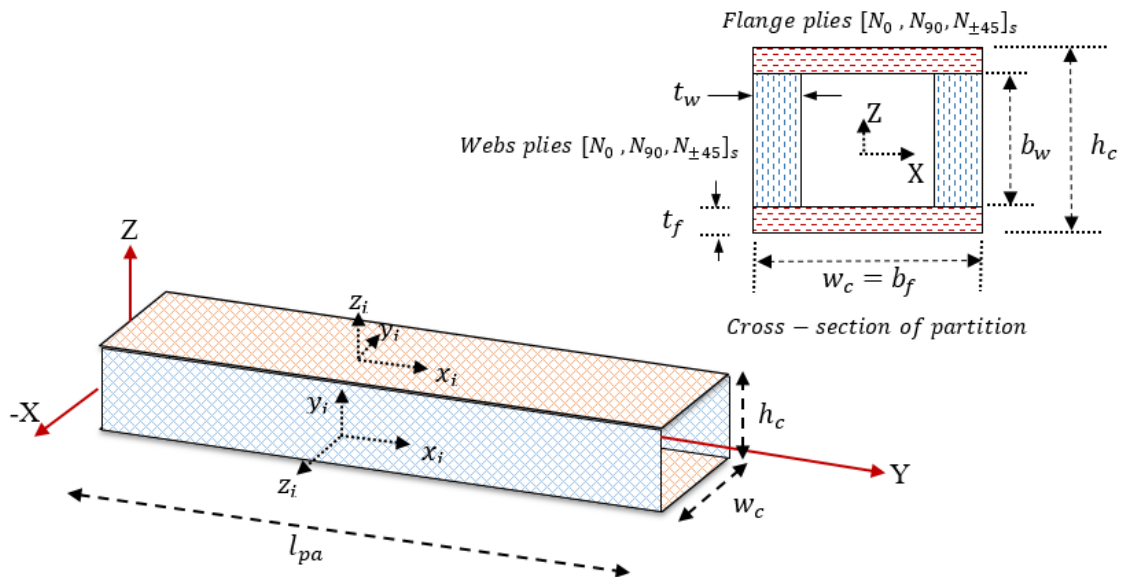


Figure 6-3 Layout of the spar partition (wing box)

Figure 6-4 shows the load distribution within a composite rectangular cross section under three types of loading. In the case of pure shear loading, it can conclude that the maximum shear flow occurs at the midpoint of the webs while the flanges have higher shear flow at its ends. The shear flow under pure torsional load is constant at any position within

the cross-section. The direct stress under pure bending usually differs from ply to ply, depending on its directional stiffness modulus. However, generally, for any ply, the stress distribution is linearly proportional to the distance between a point, which lies on the ply, and the neutral axis (Dato, 2012; Megson, 2012; Vasiliev & Morozov, 2013).

It is concluded that, theoretically, there are three critical zones (in each quarter) where the failure will occur first as indicated in Figure 6-4. Therefore, during the design process, only these zones will be examined against the failure criterions.

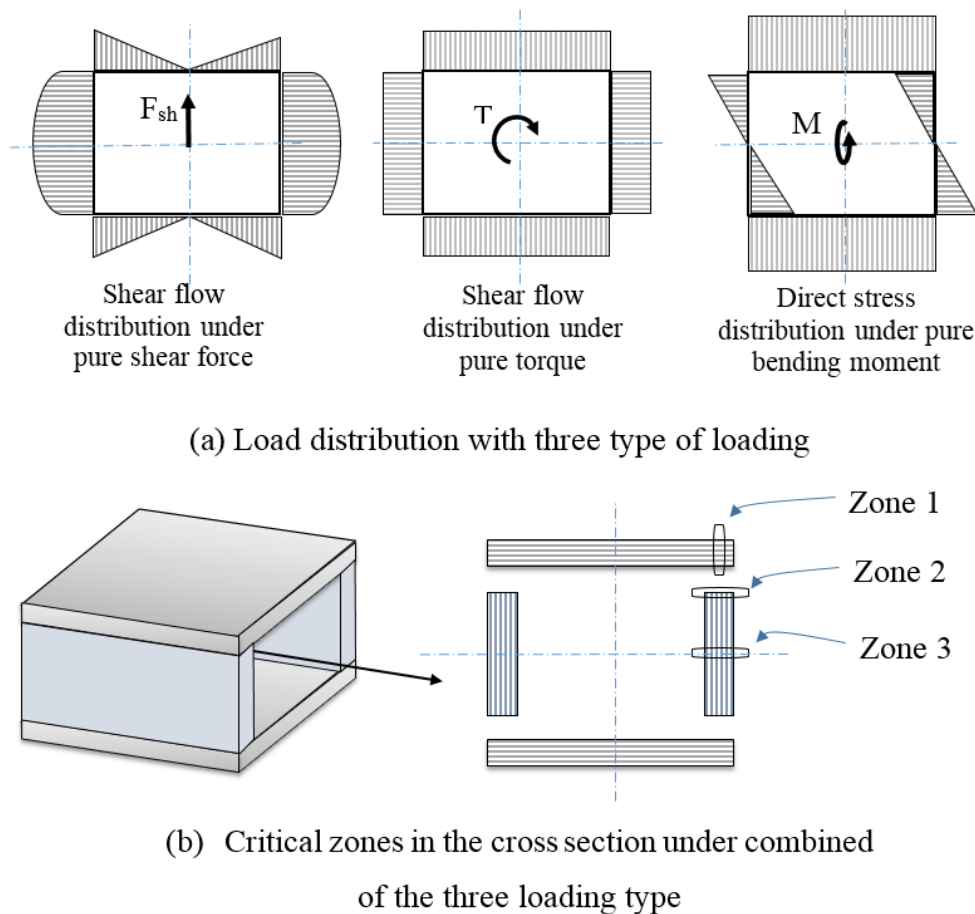


Figure 6-4 Wing-box cross-section loading

Figure 6-5 shows the overall cross-section design procedure and will be detailed in Appendix V. The main concept of the design is suggesting a number of plies for each element in an iterative manner and testing the section till no failure is detected with a safety margin represented by a factor of safety (FoS). The stress analysis within the joints between the composite elements of the spar (web & flanges) is complex and necessitates a high order analysis which is not practical at this early stage of design. The joints between the flanges and webs will be assumed to be fully-bounded as many manufacturer solutions could be

applied aiming to increase the bonding strength. For instance, the common plies between flanges and webs can be folded around the spar to produce more homogeneous structure. Also, splice plates can be used to fasten the spar pieces and transfer the exerted loads (Bureau, 2008; Voyiadjis & Kattan, 2005). Since the designed flanges and webs will represent the major material of the spar section, the weight & failure of the joints will not be considered as critical factors at this design stage.

The stacking pattern of each flange and web in each partition will be suggested under the following constraints:

1. Each web and flange have symmetric laminate about its mid-plane.
2. The webs are identical.
3. The flanges are identical.
4. Each laminate is balanced (containing an equal number of ± 45 degrees).
5. Each laminate must have at least 10 % of plies of the orientations (-45, +45, 90, 0).

This is applied to every subsequent ply up to 10 (Gay, Hoa, & Tsai, 2002; Kennedy & Martins, 2012).

Once the spar section is designed with no-failure detection, its weight is now calculated

$$m_{par} = 2(b_w t_w + b_f t_f) l_{pa} \rho_{ply} \quad (6.8)$$

where l_{pa} is the length of the partition and ρ_{ply} is the ply density.

The stiffness analysis is based on the following assumptions:

- 1- There is no bending-torsion coupling. This implies that the cross-section of the spar must be symmetric.
- 2- The joints between the webs and flanges are fully bounded.
- 3- There is no large displacement within the laminate. The cross-section remains the same under all loading conditions.
- 4- The displacement is within the elastic limit enabling Hooke's law to be applied.
- 5- The principal stresses of each ply are individually evaluated under the three types of loading.

A MATLAB code has been written according to the steps presented in this section to size the wing spar for given exerted loads. The code is detailed in Appendix V.

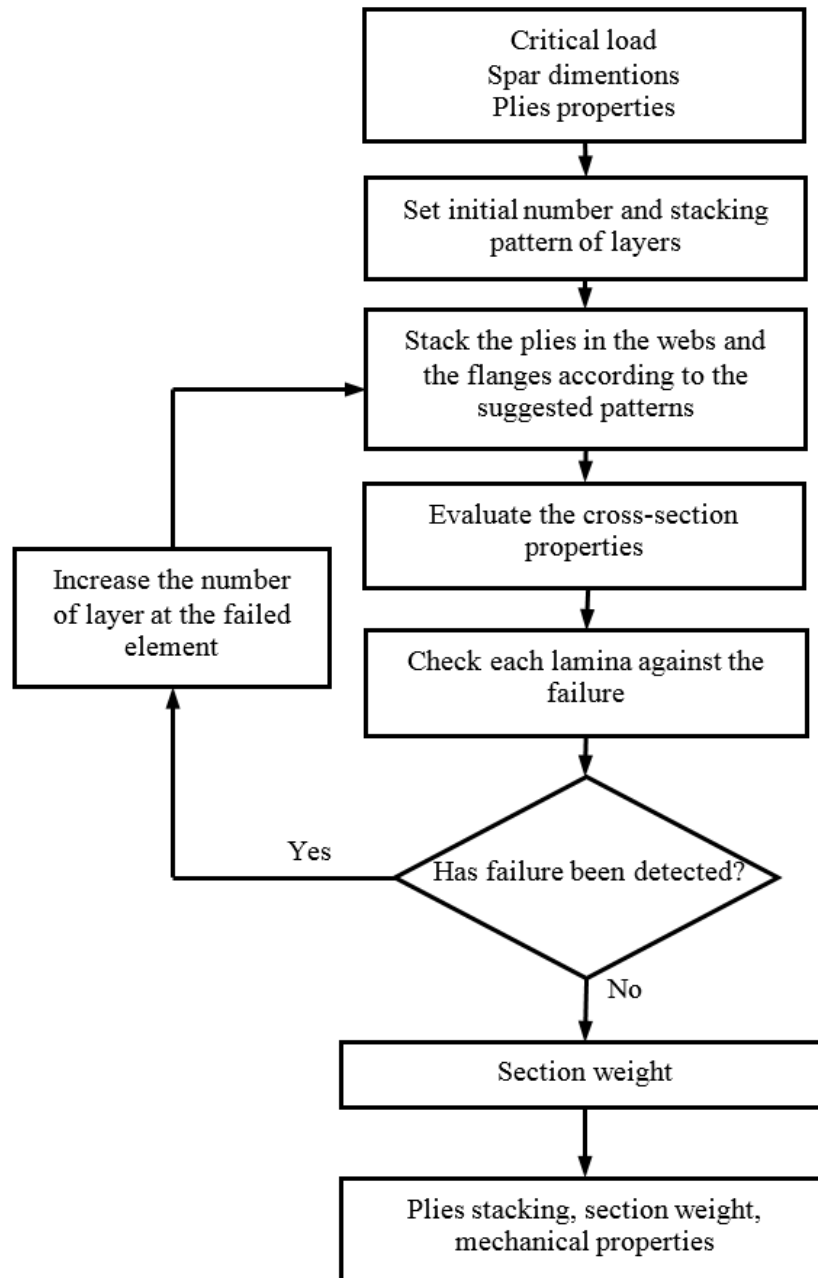


Figure 6-5 Cross-section design methodology

6.2 Finite Beam Element

A linear finite-beam element approach has been used for the structural analysis of the wing to evaluate the elastic deformation. The spar is modelled by means of a three-dimensional finite element beam concentrated in the elastic axis of the wing such as in Figure 6-11. The beam is discretised into elements, each element having two nodes. Each node has six degrees of freedom: three in rectilinear translations and the three associate rotations as showing in Figure 6-12. They are described by local coordinates and then described by their rotation angles (sweep, dihedral and twist) to transfer to the global coordinate system.

The nodal displacement and the nodal load vectors for an element respect to the spar axes (X, Y, Z) are given as:

$$U = [u_{Xa}, u_{Ya}, u_{Za}, \theta_{Xa}, \theta_{Ya}, \theta_{Za}, u_{Xb}, u_{Yb}, u_{Zb}, \theta_{Xb}, \theta_{Yb}, \theta_{Zb}] \quad (6.9)$$

$$F = [F_{Xa}, F_{Ya}, F_{Za}, M_{Xa}, M_{Ya}, M_{Za}, F_{Xb}, F_{Yb}, F_{Zb}, M_{Xb}, M_{Yb}, M_{Zb}] \quad (6.10)$$

A classical stiffness method, using linear finite beam element and torsion theory, was implemented. The linear finite beam equations are derived using the concept of the minimum potential energy. The formulated equations were derived for two-dimensional problem but because the cross-section is symmetric in which there is no coupling between the bending about the X and the Z axes, the method is extended to cover three-dimensional problems. The method is fully detailed in references (Megson, 2012; Seywald, 2011; Vasiliev & Morozov, 2013; Wilson, 2002).

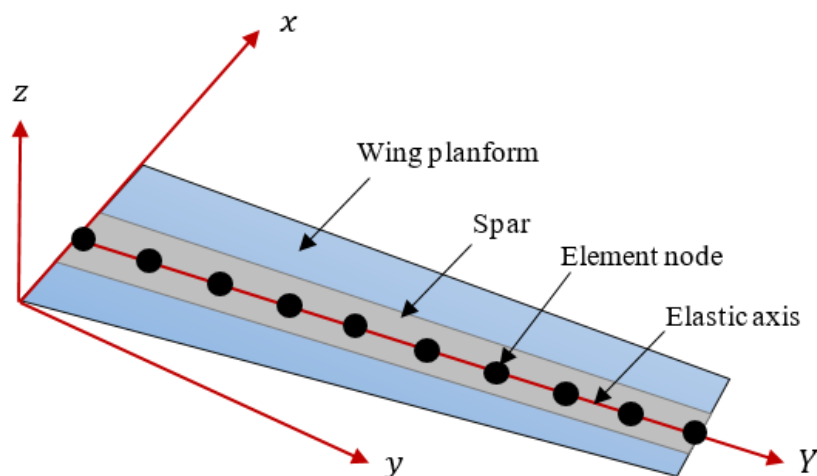


Figure 6-6 Structural wing model

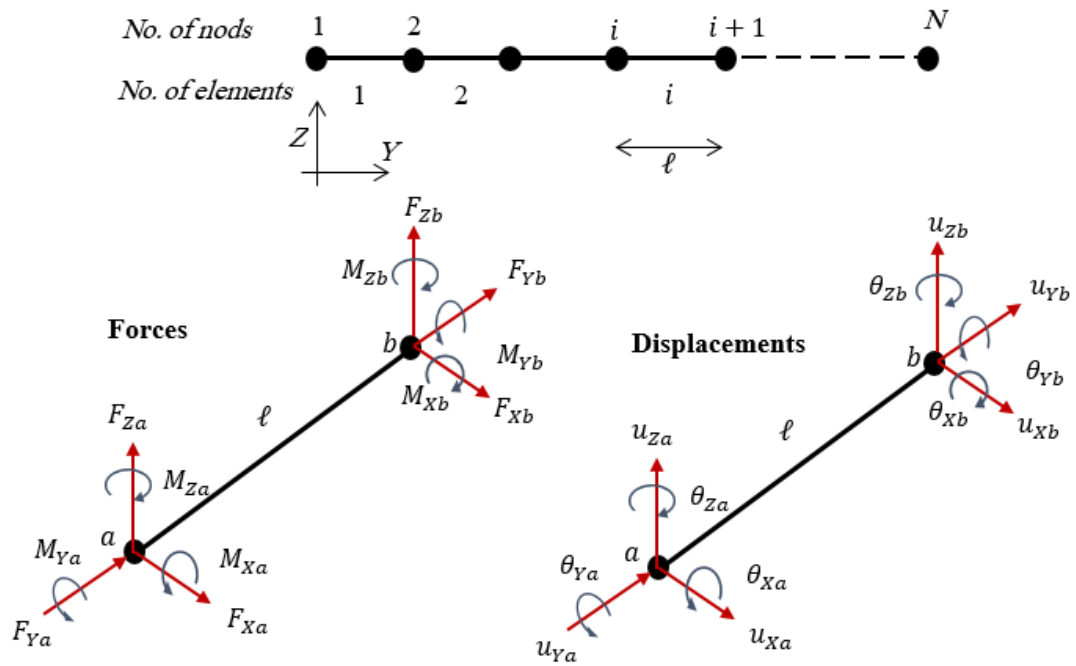


Figure 6-7 Planar beam element and the degrees of freedom

The final relationship between each nodal displacement and the associated nodal load is given by:

$$F = K_{loc} \cdot U \quad (6.11)$$

where K_{loc} is the local stiffness matrix of the beam element which can be determined using the geometric and the mechanical properties of the element:

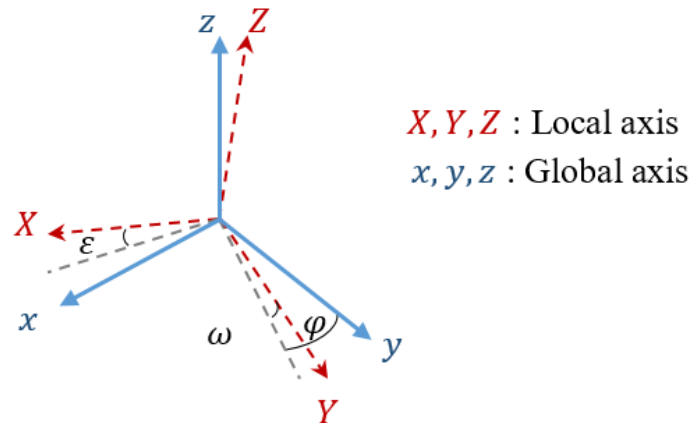


Figure 6-8 Local and global coordinate system

6.3 Critical Design Loads

The aircraft structure is sized to withstand the expected maximum loading conditions (critical loads) which must be defined in advance and classified as either static or dynamic. Usually, different load scenarios can be examined at different flight and manoeuvring conditions such as landing, takeoff, aileron roll, flap deflection and other flight manoeuvres represented by the speed of aircraft combined with the gust conditions. Then, the highest load on each aircraft section can be defined as a ratio of the local load at the critical condition to the local load at the cruise condition (Ajaj et al., 2013; Torenbeek, 2013). These ratios are known as local load factors. Alternatively, a global load factor can be set for all the elements of the aircraft to evaluate the critical loads. The value of the global load factor can be specified from the flight conditions of related aircraft. During the sizing process, along with the critical load limits, a factor of safety (FoS) of the allowable yield stress is also included (Megson, 2012). This factor is employed to ensure that, at the critical loads condition, the wing deformation remains under the elastic limit, and that no permanent deflection will occur.

Only static loads will be considered in the sizing process to hasten the process of iteration convergence in order to produce solution for elastic deformations and weight simultaneously. Techniques from existing design processes and recommendations for sizing the structural elements, the wing structure will be sized with a global load factor of 3 and a factor of safety of 1.5 (Megson, 2012; Noll et al., 2004; Torenbeek, 2013). In each iteration of the optimisation process, the aerodynamic forces will be calculated at the cruise condition. Then, the aerodynamic forces are multiplied by the global load factor to be used in the sizing process (Ajaj et al., 2013).

6.4 Static Aero-elastic Modelling

In general, high altitude aircraft have a large span and ultra-light wings, indicating that the wing will be highly flexible. Therefore, the aerodynamic loads considerably influence the wing shape due to the elastic deformation, and this in return affects the aerodynamic performance.

In this research, only static aeroelasticity properties will be considered in which the inertia forces are neglected. The static aeroelasticity calculations imply a coupling approach between the static aerodynamic loads and the structural forces. This approach starts by calculating the aerodynamic forces and then calculates the structure displacements. The wing geometry is then updated to be used again to evaluate the aerodynamic forces. This process will be iterated until a convergence solution is achieved. The convergence solution means achieving a static equilibrium condition between the internal elastic forces and the external aerodynamic loads.

In the Tornado VLM, the wing can be discretised into partitions; each partition has a dihedral angle in addition to two twist angles for the inner and the outer edges of each partition. The reference axis of these geometric angles is the quarter chord axis of the wing. The deformation results of the finite beam element analysis are about the elastic axis of the spar. The elastic axis can be placed as a ratio of the local chord length along the wing and may not be coincided with the quarter chord axis of the wing. Therefore, in order to modify the wing geometry due to the elastic deformation, a coupling of the aerodynamic mesh and the structural mesh is required. The vertical elastic deformation of the spar can be translated to a dihedral angle (dh_i) and a twist about the quarter chord axis, assuming that the elastic deformation will be linearly distributed within each partition, as shown in Figure 6-14. Similarly, the elastic twist deformation about the elastic axis can be translated to twist, as well as the dihedral for the inner and the outer edges of each partition about its quarter chord axis, assuming that the elastic twist is linearly varied within each partition. It is apparent that an adequate number of partitions is necessary to gain confidence results.

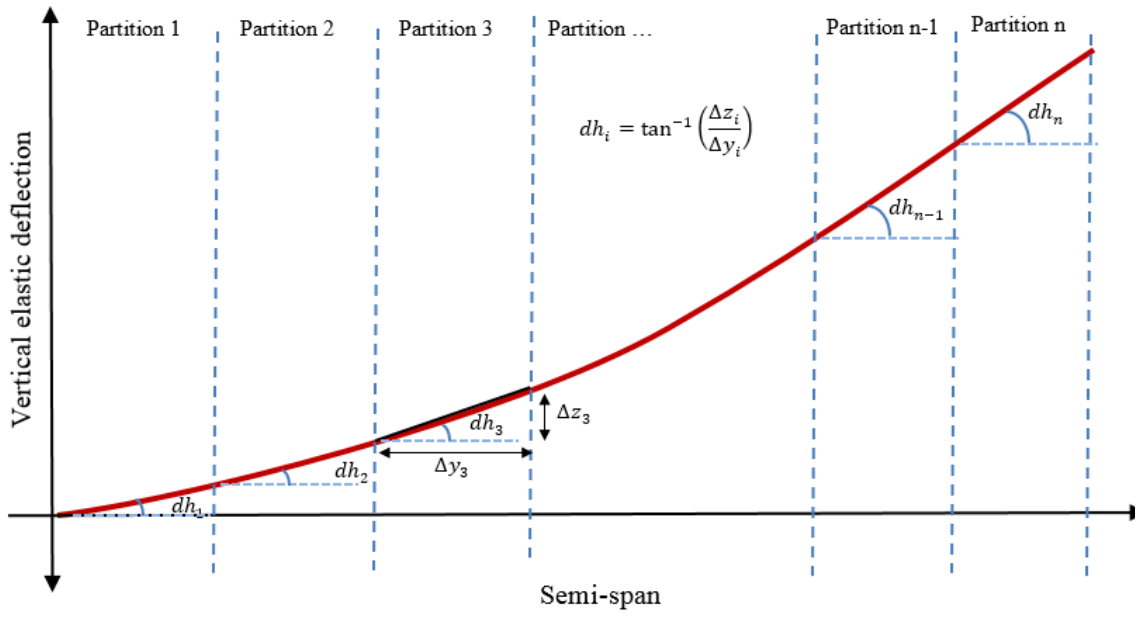


Figure 6-9 Elastic vertical deflection as a function of dihedral angles

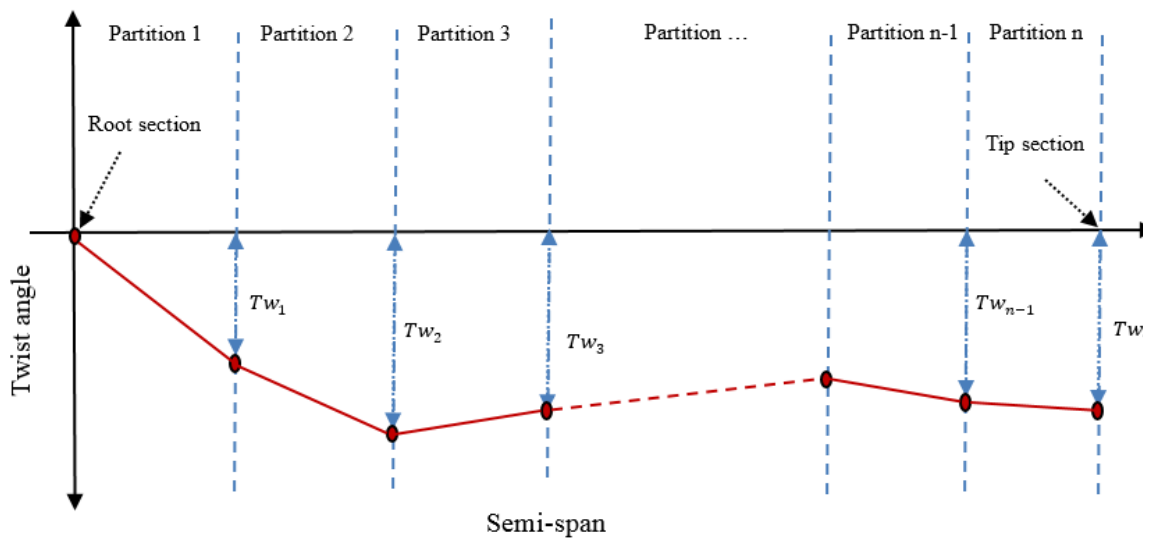


Figure 6-10 Twist distribution pattern in Tornado VLM

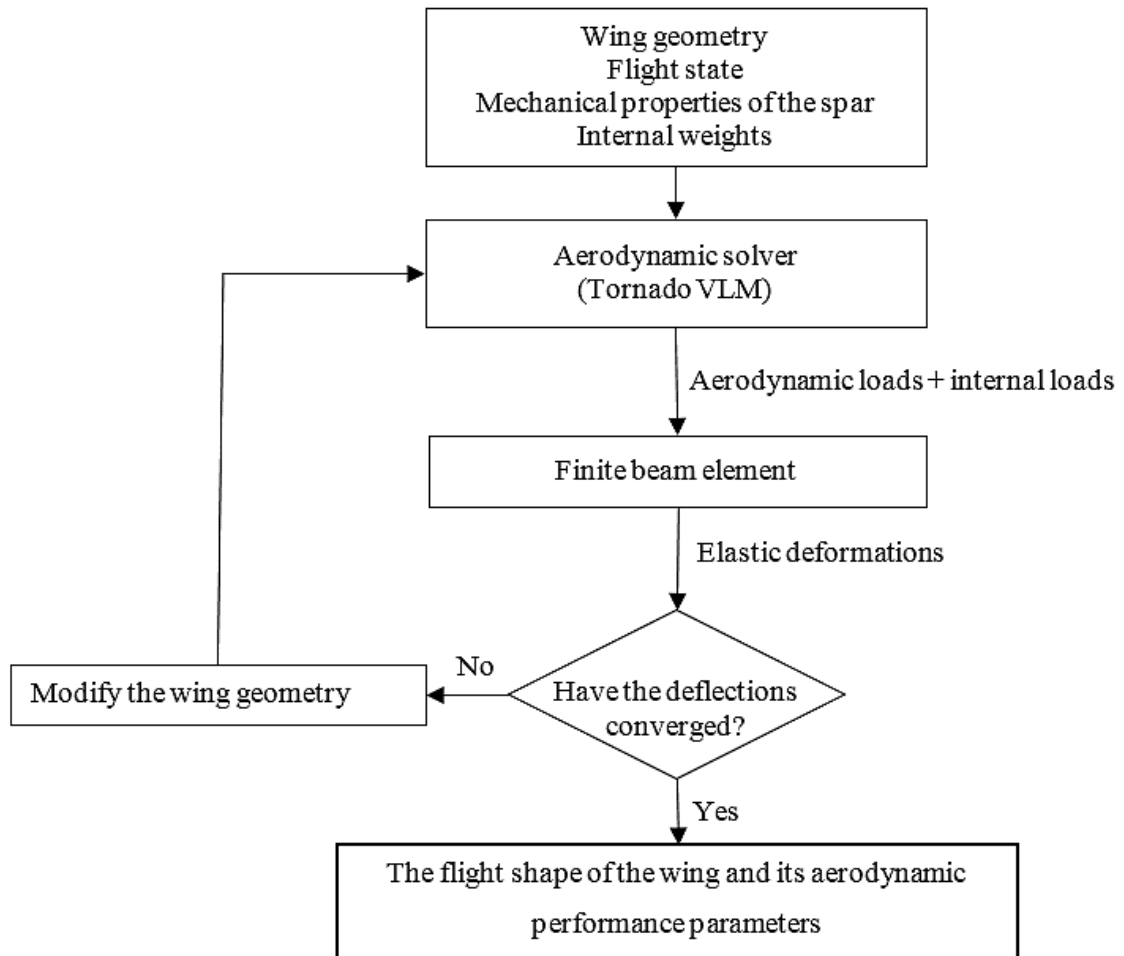


Figure 6-11 Schematic of the aeroelastic coupling adopted in the CSM

6.5 Validating the Stress Analysis and Deformation

The structural model was validated with a high order commercial package (ANSYS). A cantilever beam was used as a rectangular wing-box and fixed at one of its ends. At the other end, it was subjected two types of loads, bending with shear force and pure torsion as shown in Figure 6-17. A symmetric stacking laminate was used on each side of the rectangular cross-section. One mm thick epoxy carbon UD 230GPa Prepreg laminate was used and stacked symmetrically about the mid-plane of each wall as shown in Table 6-1. The objective here is to verify the result of the present structural model represented by the highest stresses, the vertical deflections and the twist angles under the three type of loads by comparing the results with those produced by ANSYS.

Table 6-1 Lamina properties defined by ANSYS

Composite	E1 (GPa)	E2 (GPa)	ν_{12}	G12 (GPa)	Thickness mm
Epoxy Carbon UD 230GPa Prepreg	121	8.6	0.27	4.7	1

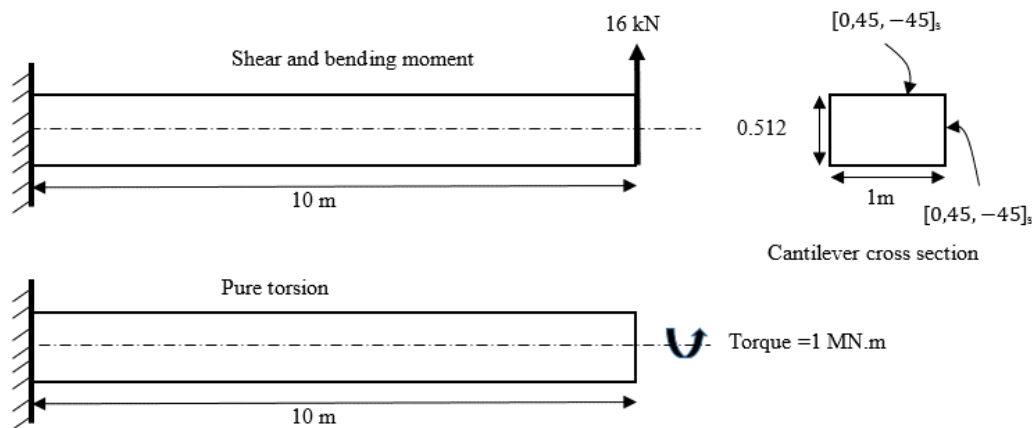


Figure 6-12 Fixed Cantilever wing-box Subjected to Shear-bending and Pure Torsion

There has been a good agreement so far. Table 6-2 shows that the vertical deflection of the beam has been underestimated by 0.17% while the twist has been overestimated by 0.26%. This is a tiny margin of error which concludes that the calculated mechanical properties are very close to those obtained from ANSYS. The stresses at the critical zones also show an acceptable agreement with errors between 1.29% and 4.33%. This is usually expected with low order modeling when several assumptions to simplify the calculation are adopted. In general, composite aircraft structure is designed with a factor of safety of about 1.5 to 3 (Bureau, 2008). Therefore, this margin of error could be accepted in the sizing process.

Table 6-2 Validation results of the composite structural model

Results	Present Model	ANSYS	Error
Shear + Bending			
Vertical Deflection (cm)	11.50	11.52	0.17 %
Maximum Principle Stress (MPa) At corner of flange (0 plies have the higher value)	104.32	102.99	1.29 %
Maximum shear stress (MPa) At top of web (± 45 plies that have the highest value)	5.18	5.3	0.93%
Pure Torsion			
Twist Deflection (degrees)	12.582	12.549	0.26 %
Maximum Principle Stress (MPa) At the flange (45 plies have the highest value)	439.20	459.1	4.33%
Maximum shear stress (MPa) at middle of web (0 plies have the highest value)	34.60	34.06	1.58 %

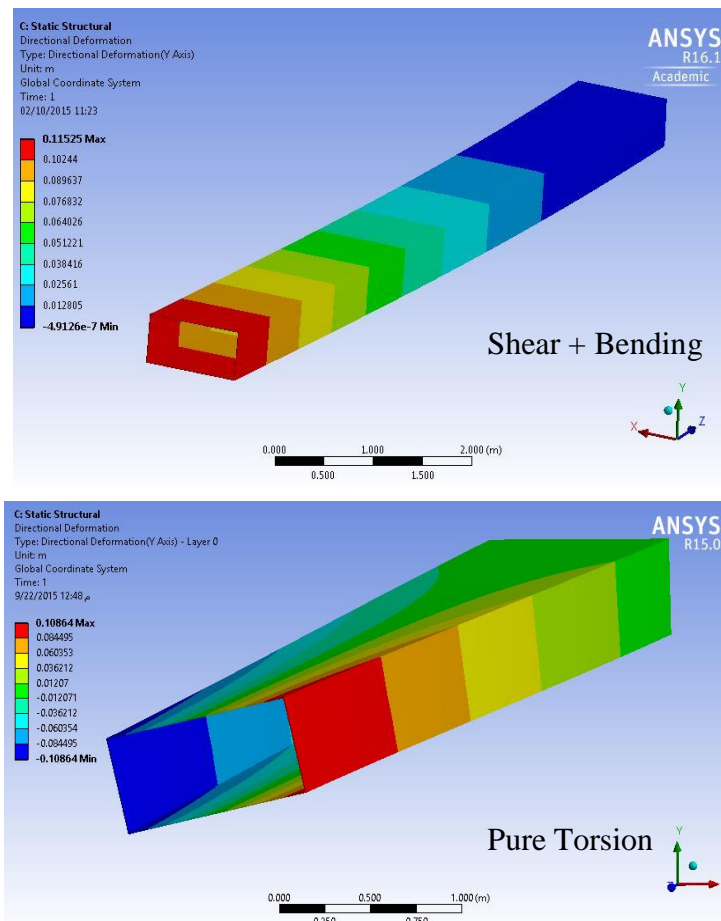


Figure 6-13 Directional deflections under pure torsion and bending-shear force evaluated by ANSYS

6.6 Validating the Weight Estimation Model

In order to verify the modeling of the composite structure, an aircraft baseline configuration is used similar to that of the Helios P03 high altitude UAV. Its structure was constructed mostly from composite materials. Its spar has a circular cross section which is thicker on the top and the bottom to resist the bending moment as shown in Figure 2-23. It is propelled by ten electric motors, each rated at 1.5 kW. Its configuration and known specifications are shown in Figure 6-19 and Table 6-3 as provided in reference (Noll et al., 2004).

Table 6-3 Helios P03 Configurations

Specifications		Specifications	
Length (m)	5	Wing area (m ²)	183.58
Wingspan (m)	75.3	Max. Take-off weight (kg)	1052
Aspect Ratio	30.9	Power for each motor (kW)	1.5
Chord (m)	2.438	Mass of each hydrogen fuel tank (kg)	74.84
Aerofoil name	LA2573A*	Mass of the central pod (kg)	235.86

* The actual aerofoil is similar to LA2573A which was used in Pathfinder UAV

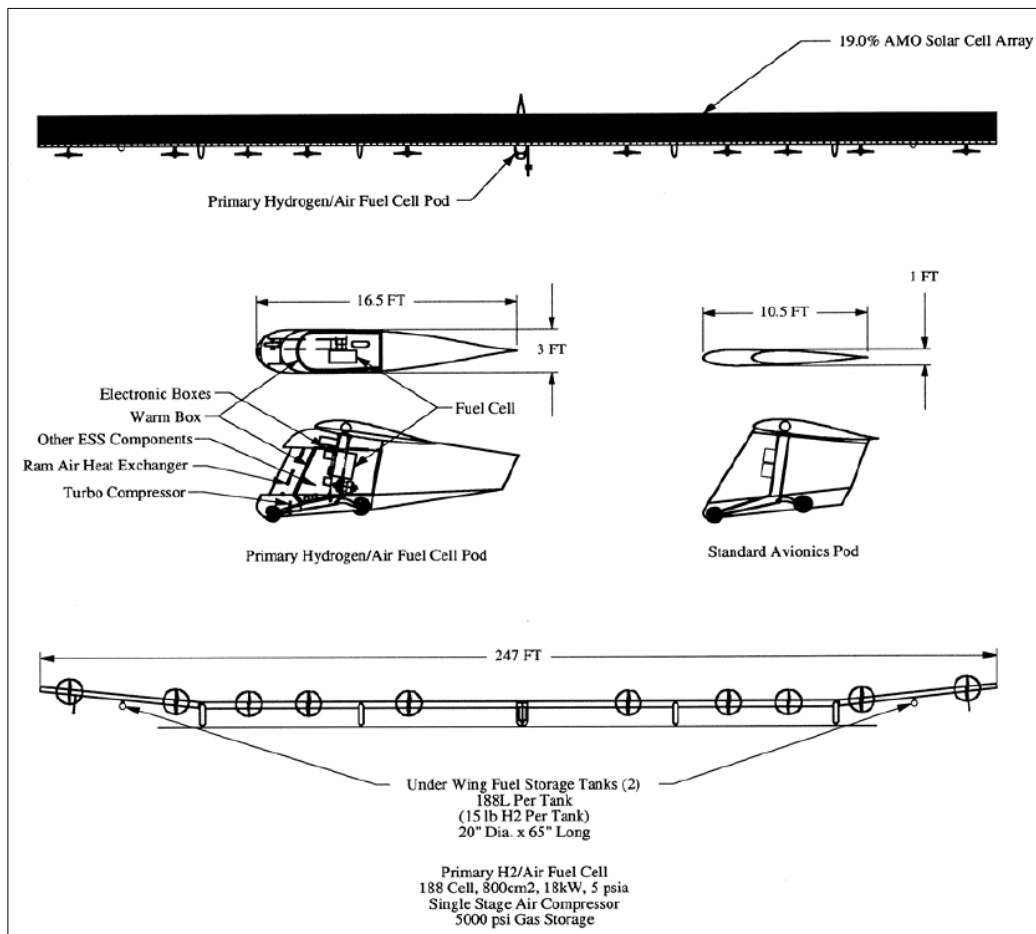


Figure 6-14 NASA Helios P03 HALE UAV (Noll et al., 2004)

To size the spar, all the inboard masses must be known to be employed in the load calculations. There is insufficient detail available for the Helios P03 structure and some of the weights of various elements are unknown. Therefore, the missing data have been estimated according to empirical equations:

1. Determine the structure weight using Rizzo's structure mass estimation model which was obtained by data published for the NASA prototypes (Rizzo & Frediani, 2008):

$$m_{af} = 1.548 b^{1.312} AR^{-0.0046} \quad (6.13)$$

2. Estimate the weight of the non-spar elements using the empirical equations presented in section 6.1.1.
3. Calculate the propulsion system weight by using the following equation:

$$\text{Mass of each motor} = K_{prop} \times \text{Power of each motor}$$

where $K_{prop} = 0.004 \text{ kg/W}$ (Rizzo & Frediani, 2008).

4. Estimate the weight of the battery packs and other inboard elements by subtracting the known weight from the total weight.

It is expected that this weight distribution cannot describe precisely the real model but this could be a possible way to verify that the structural model can give reasonable results. The estimated weights of the missing elements are detailed in Table 6-4.

Table 6-4 Weight estimation for the Helios P03

Elements	Weight [kg]
Structure weight using Rizzo model	441.85
Ribs	23.35
Leading edge	30.60
Trailing edge	7.45
Covering	77.04
Spar weight (Structure weight-non spar weight)	441.85-138.46=303.4
Solar cell weight (if $\rho_{solar \ cell}=0.365 \text{ kg/m}^2$)	52.0
Mass of each motor	6.75
Mass of the central pod and hydrogen fuel tanks	385.54
Mass of other components (the rest weight)	105.1

The objective now is to design a spar which corresponds to the baseline aircraft for the given configuration and flight state. This is done with the following assumptions:

1. The flight condition with a global load factor of three is considered.

2. The span is discretised into six partitions (three in each semi-span) for the sizing process; each partition will be sized according to its maximum loads. The partitions are dimensioned in Figure 6-20.
3. The inboard weights are considered in inertia relief calculations.
4. Other components (mentioned in Table 6-4) are located at the pods numbered 2 and 4.
5. The elastic axis of the spar is the same as the quarter chord axis.
6. The inboard weights distribution along the chord-wise direction is suggested as shown in Figure 6-21.
7. Each lamina in the spar has the same mechanical properties as that of epoxy carbon T800/M18, see Table 6-5.
8. The height of each spar portion (h_c) equals to 0.8 of the maximum wing section. The width (w_c) will be assumed as a ratio of the spar height.
9. The buckling failure is not considered in the sizing process but a minimum number of plies arranged according to a particular sequence have restricted the design process of the spar sides (flanges and webs). The minimum number of plies and their sequence are:

$$[0,0,45,-45]_{symmetric}$$

Table 6-5 The properties of epoxy carbon T800/M18 (Montagnier & Bovet, 2010)

E_1 GPa	E_2 GPa	G_{12} GPa	ν_{12}	X_t MPa	X_c MPa	Y_t MPa	Y_c MPa	S MPa	Thickness mm
162	10	5	0.3	2940	1570	60	290	100	0.125

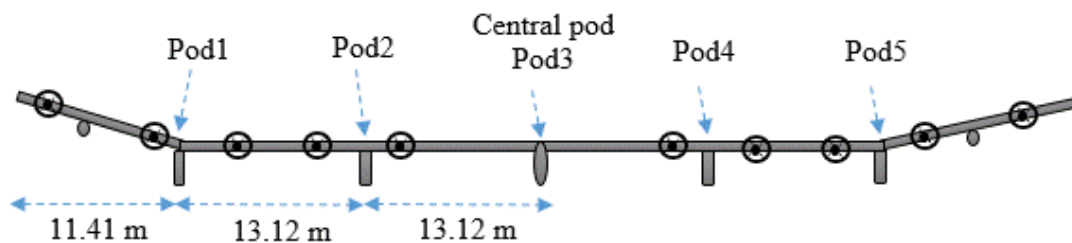


Figure 6-15 The partitions of the spar

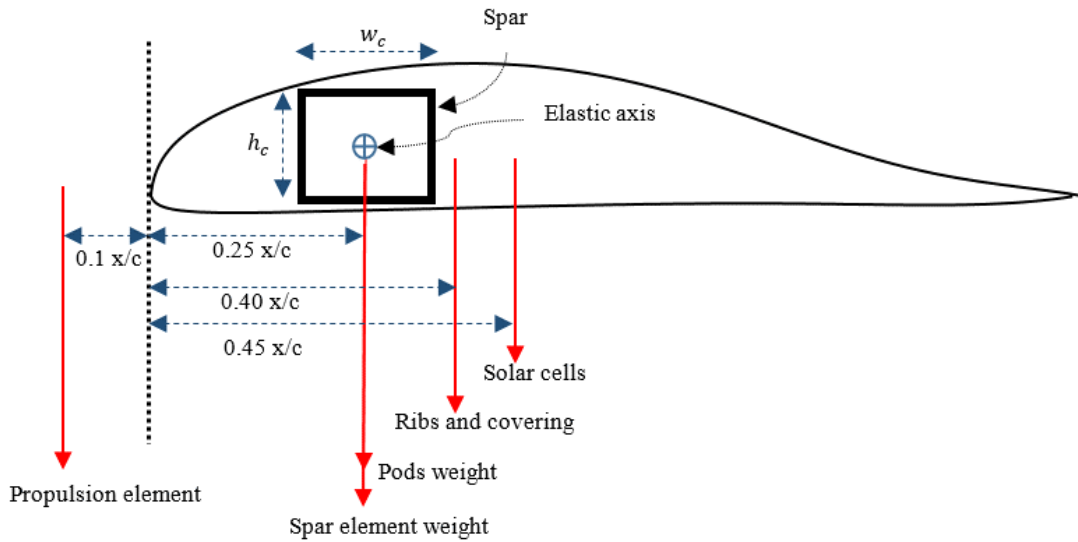


Figure 6-16 Weight distribution along the chord-wise direction

The given wing configurations are programmed in Tornado VLM to evaluate the critical loads. The wing is discretised into 30 span-wise elements for each wing. For each element, the corresponding weight of the non-spar elements and the solar cells, as well as the corresponding lift force, are calculated. Figure 6-22 shows the weight distribution along the semi-span in addition to the local lift forces at steady level flight. Note that the weight of the central pod is not shown in the figure. These loading cases can be represented by the bending moment, the shear force and the torque to be used in the sizing process.

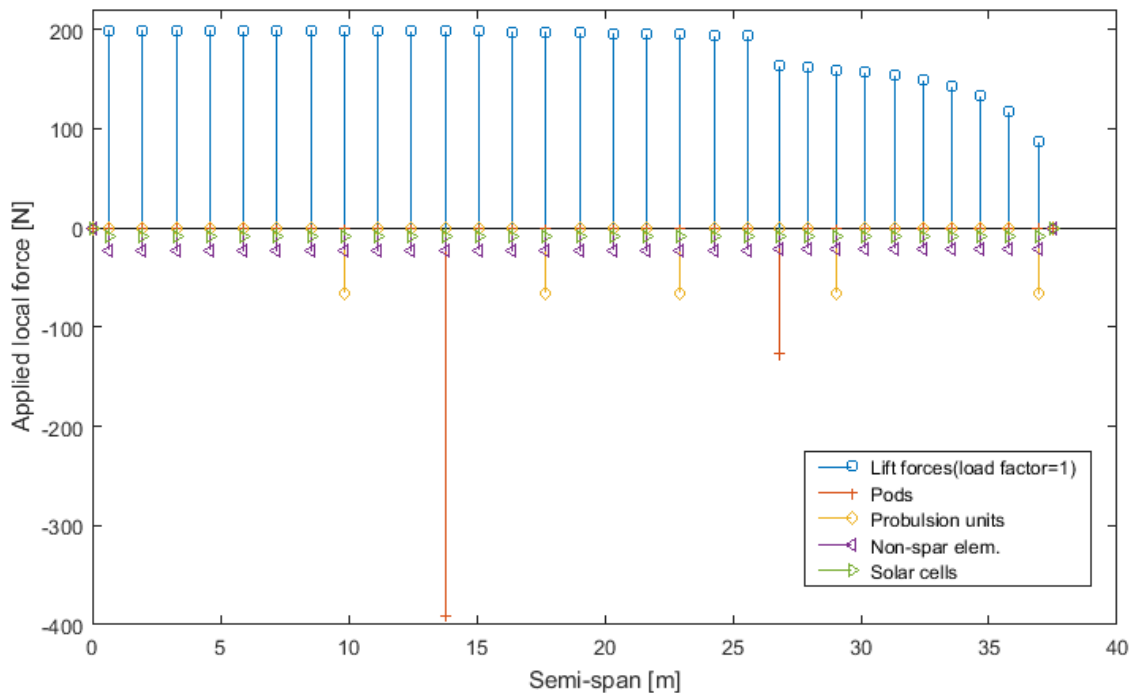


Figure 6-17 The force balance along the semi-span of Helios P03

In order to design the laminate in each spar section, the width of the spar must be set. A brief study has been conducted to investigate the influence of the width of the spar on the weight and the wing deformation. The spar height is fixed at 0.8 of the maximum wing thickness. The width will be represented as a ratio of the spar height, 0.5 to 1.8. In each given ratio, the spar will be designed by finding the required number of plies and their stacking sequence in each partition to withstand the critical load.

Figure 6-23 shows the spar width influence on the weight and the elastic deformation of the spar. For the given wing loading, it is apparent that the minimum spar weight corresponds to the width ratio (w_s/h_c) 1.2. However, under the critical load, the elastic twist shows a reduction with increasing width of the spar whilst the maximum deflection (tip deflection) shows a rise with increasing width ratio of about 0.5 to 1.5. Unfortunately, the maximum wing deflection of the baseline aircraft is not available for comparison. However, in a Mishap Report by NASA, the authors indicate that the wing deflection could reach 12 meters under some critical flight conditions (Noll et al., 2004).

As shown in Table 6-4, the expected spar weight of the Helios P03 is about 303.4 kg. Referring to Figure 6-23, one can conclude that, for a width ratio of about 1.2, the weight of the spar would be about 303.81 kg which is very close to that of the expected weight. Therefore, the width ratio 1.2 is taken the correct figure and again the spar partitions are designed under the critical loads. The final sequences of the spar sides (flanges and webs) for each partition are detailed in Table 6-6. The critical loads, which are presented as bending moment, shear force and torsion, are shown in Figure 6-24. This low order model has proved that it is capable of providing good accuracy relating to weight estimation with the baseline aircraft considered in the case study.

Table 6-6 Plies Stacking in Each Wing-box Station

Station	Stacking at flanges	Stacking at webs
1	$[90, 0_9, 90, 0_9, -45, 45]_s$	$[90, 0_9, 90, 0_9, -45, 45]_s$
2	$[0_6, -45, 45]_s$	$[0_8, -45, 45]_s$
3	$[0, 0, -45, 45]_s$	$[0, 0, -45, 45]_s$

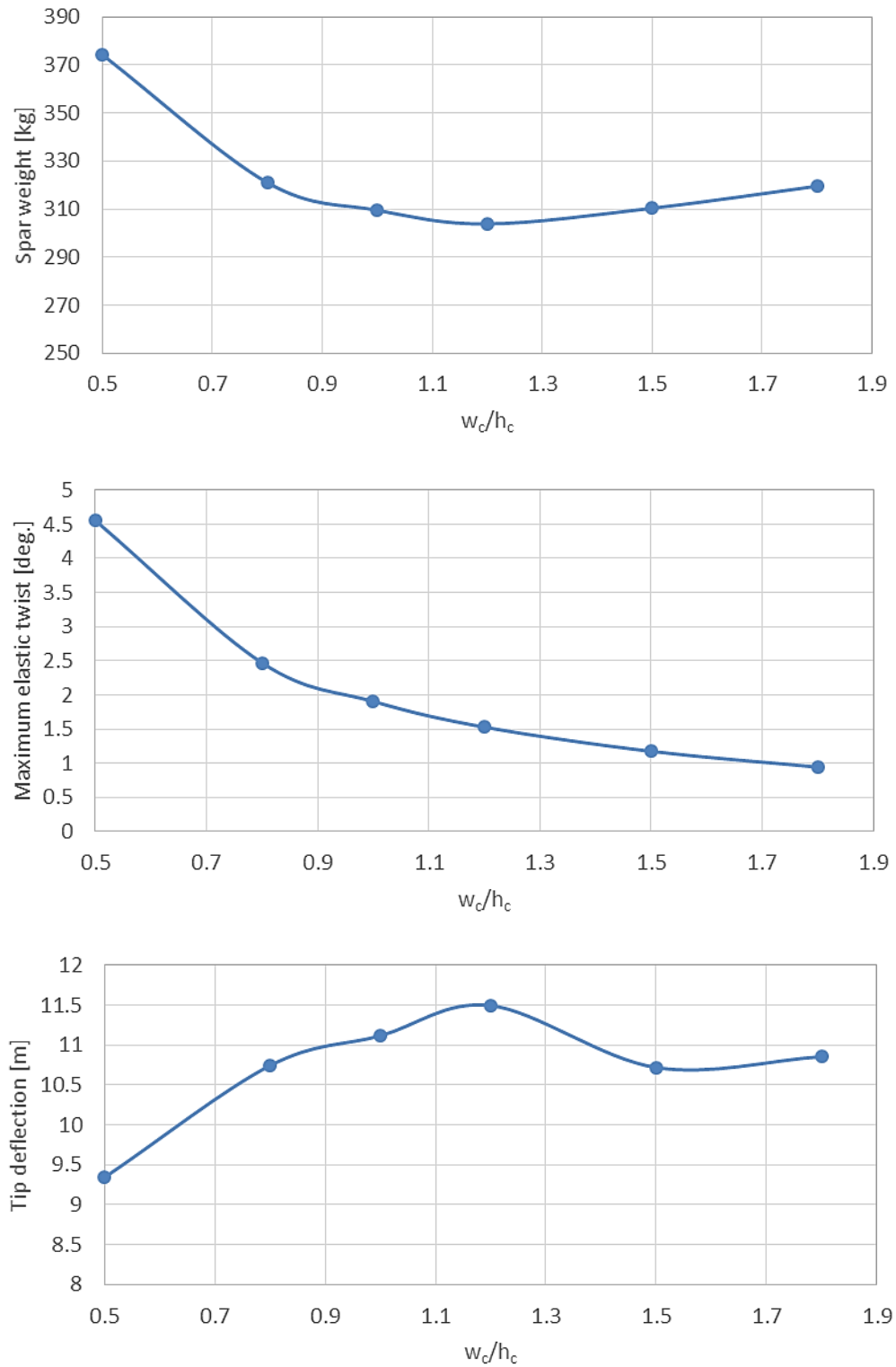


Figure 6-18 The effect of spar height/width ratio on the weight and the elastic deformation under the critical loads at a load factor of 3

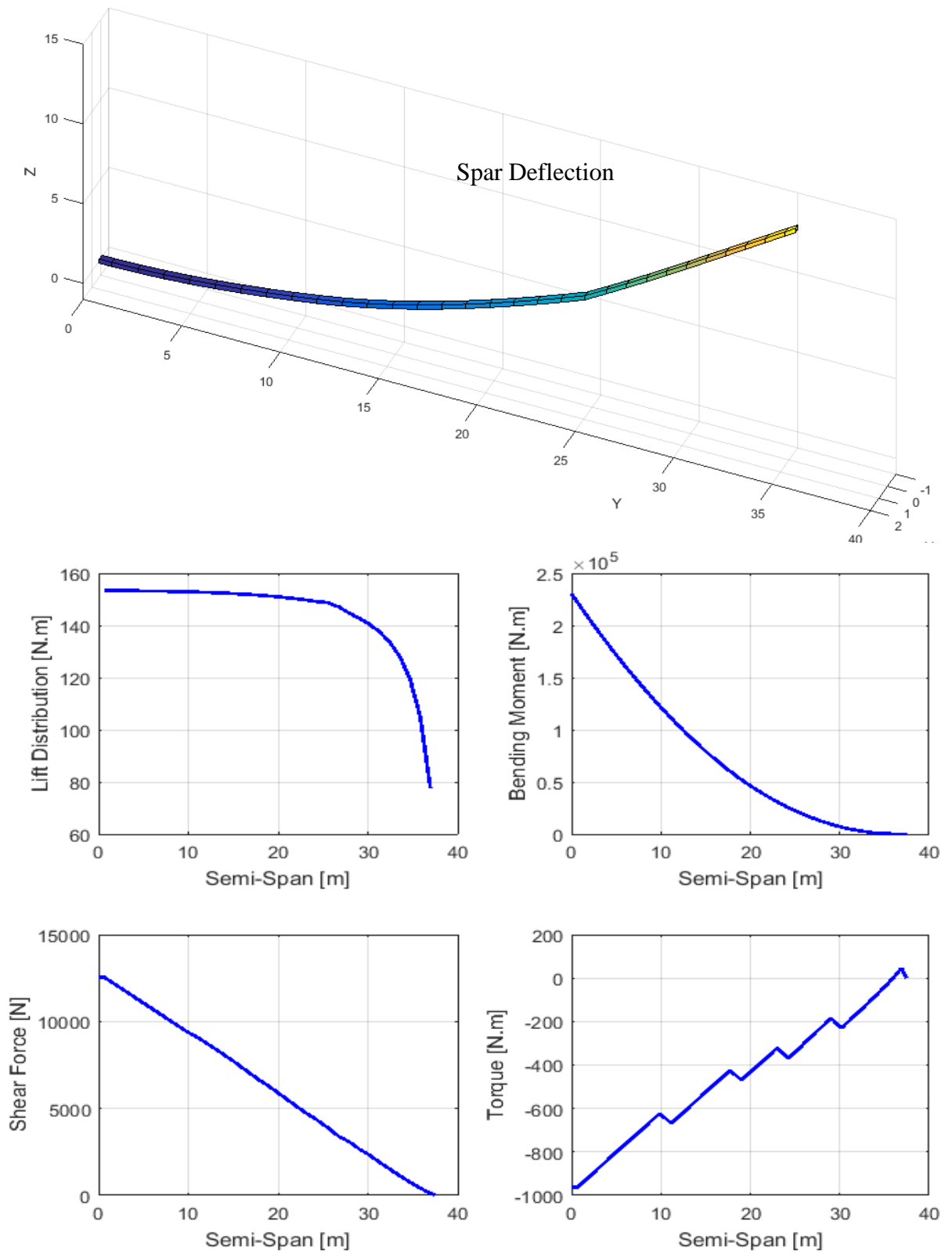


Figure 6-19 The critical load distributions and the spar deflections at a load factor of 3

CHAPTER 7

7 AEROFOIL SELECTION

In this chapter, a number of new aerofoils with varying thicknesses for an aft-swept flying wing UAV have been designed using a MATLAB tool which has been developed in-house. The tool consists of two parts in addition to the aerodynamic solver Xfoil. The first part generates the aerofoil section geometry using a combination of PARSEC and Bezier-curve parameterization functions. The second part contains the optimisation code using a Genetic Algorithm. The primary target is to design a number of aerofoils with low pitching moment, suitable for an aft-swept flying wing configuration operating at low Reynolds number in the region of 0.5×10^6 . In addition, a high order analysis has been conducted to validate the aerodynamic performance of a candidate aerofoil ZMR-17 which will be used in the design of a high altitude long endurance aft-swept flying wing aircraft.

7.1 Existing aerofoils for flying Wing aircraft

In case of using an aft-swept configuration, much attention is paid to the pitching moment of the candidate aerofoil because of the absence of a horizontal stabiliser for stability purposes. Adopting this configuration necessitates the use of an aerofoil with a smaller pitching moment, but not excessively low in order to obtain a high lift coefficient (Nickel & Wohlfahrt, 1994). A number of aerofoils were designed for flying wing aircraft. In this section, existing data for aerofoils at low Reynolds numbers have been gathered to assess the limitations and use for the comparison. Selig et.al, Eppler and Martin Hepperle designed number of aerofoils for low Reynolds numbers operations; some of these are for tailless aircraft configurations (Hepperle, 1988; Michael S. Selig et al., 1995; M. Selig, 2003). Maximising the lift with minimum drag and pitching moment were the design targets for the aerofoils shown in Table 7-1. Although the data in Table 7-1 apply to Reynolds number of 5×10^5 , these aerofoils were not necessarily designed for this particular value.

Table 7-1 Number of flying wing aerofoils, at $Re = 5 \times 10^5$, evaluated by Xfoil

Aerofoil name	At max C_l/C_d					C_{lmax}	C_{lmin}	Stall angle	Thickness t/c %
	C_l/C_d	C_l	C_d	C_m	at $\alpha \approx$				
LA2573A	102	1.247	0.0122	0.0117	10	1.33	-0.6	12	13.7
EPPLER 339	100	1.35	0.0135	-0.045	9	1.50	-0.3	13	13.5
EPPLER 231	95	0.845	0.009	-0.052	5	1.2	-0.35	13	12.33
MH 83	95	1.35	0.0142	-0.064	8	1.9	0.4	15	13.29
EPPLER 344	94	1.41	0.015	-0.032	10	1.55	-0.29	14	14.7
EH 3.0/12	93.9	1.15	0.0123	-0.005	9	1.25	-0.6	12	12
FAUVEL 14	89.3	1.15	0.0128	0.012	9	1.3	-0.74	11	14
EPPLER 342	89.3	1.39	0.0156	0.013	11	1.484	-0.35	13	14.3
EH 2.0/12	89.2	1.01	0.0112	-0.011	8	1.2	-0.8	12	12
S5010	85.85	0.79	0.0092	-0.0022	6	1.316	-0.5	12	9.8
MH 81	85.2	1.4	0.0164	-0.001	11	1.65	-0.5	15	13
MH 61	84.5	0.65	0.0075	-0.006	5	1.03	-0.62	11	10.28
HS 520	84.37	0.78	0.0093	-0.0022	6	1.283	-0.584	13	9.8
MH91	78.9	1.07	0.0136	0.012	9	1.38	-0.87	16	14.98
MH95	63.8	0.826	0.013	-0.007	7	1.34	-0.7	17	15.86

Among these aerofoils, EPPLER 339 and LA2573A have the highest lift/drag ratio and moderate maximum thickness to chord ratio. Their stall angles seem to occur near the region where the lift/drag ratio reaches a maximum. The aerofoil LA2573A has the highest lift/drag ratio among these aerofoils (Woehrle, Costerus, & Lee, 1994). It was used in high altitude straight flying wing aircraft such as the Pathfinder aircraft and Pathfinder Plus (Kroo, 1993). This aerofoil has a positive pitching moment to achieve the stability requirement without the need for either wing sweep or twist. The aerofoils EPPLER-339 also has a high lift/drag ratio and high maximum lift coefficient in addition to a moderate maximum thickness of about 13.5%. Its pitching moment coefficient is small (about -0.045) which suggests it can be used for an aft-swept flying wing configuration.

The symmetric aerofoils generate very low or zero pitching moment about the quarter chord axis but at reduced lift/drag ratio. A NACA 4-digit generator equation has been used to create aerofoils with several thickness ratios to be studied. Figure 7-1 shows the influence of the maximum thickness to chord ratio on the aerofoil performance at low Reynolds number of 0.3×10^6 to 0.8×10^6 conducted by Xfoil. It can be seen that increasing the maximum thickness ratio up to approximately 17% can increase the maximum lift coefficient, the maximum lift/drag ratio and the lift coefficient at the maximum lift/drag ratio. The relationship reverses after a thickness ratio of about 17%. Also, increasing the thickness ratio can increase the drag. Moreover, increasing Reynolds number can enhance the aerodynamic efficiency. However, the best aerodynamic efficiency that can be achieved by the symmetric aerofoils is smaller than asymmetric aerofoils such as the ones tabulated in Table 7-1.

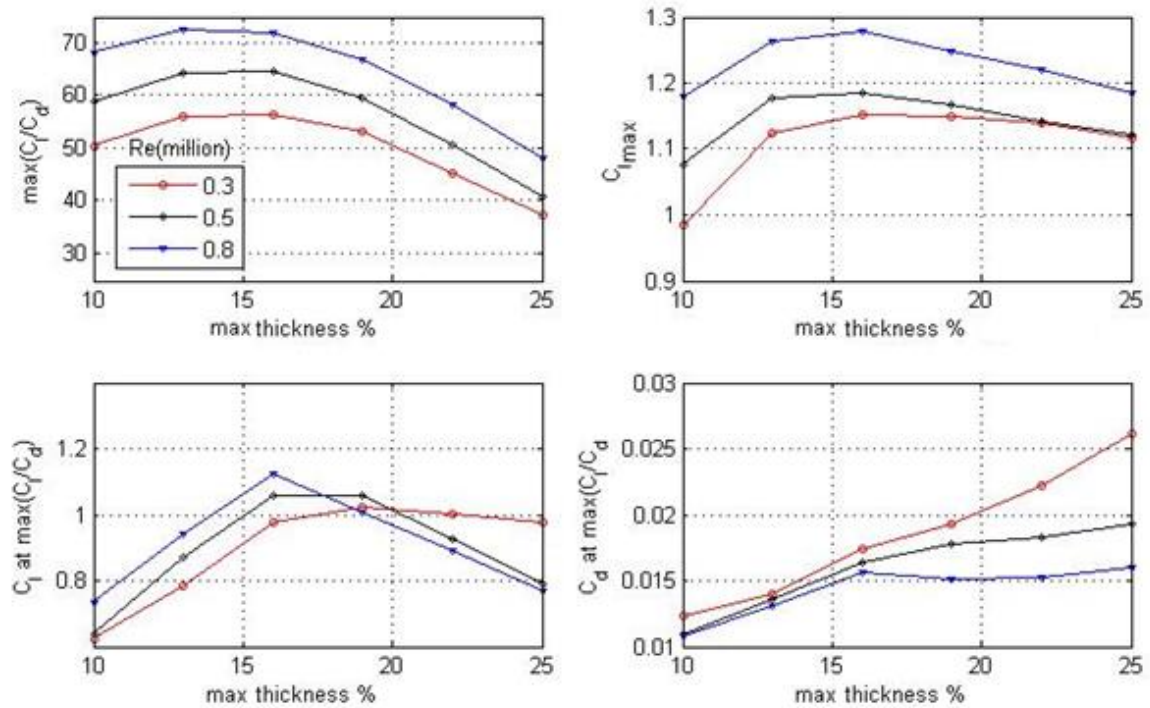


Figure 7-1 Effect of the maximum thickness on the aerodynamic performance for the symmetrical 4-digit NACA aerofoils, obtained by Xfoil.

Therefore, it can be concluded that the aerofoil EPPLER-339 seems to be the best candidate among the existing aerofoils surveyed in this section to be suitable for use in an aft-swept flying wing configuration regarding its high lift/drag ratio and low pitching moment.

Since the aft-swept flying wing configuration has not been adopted in application of high altitude aircraft by the other designers as far as is known, this chapter will investigate and design new aerofoils for three aerodynamic targets as will explained next sections. The aim is to obtain preliminary wing sections that can be used in an aft-swept flying wing configuration at the expected flight conditions. The likely operational Reynolds number that is appropriate to similar aircraft is about 0.5×10^6 .

7.2 Aerofoil Shape Optimisation Tool

Numerous aerofoils with different thicknesses have been designed by a MATLAB tool, which has been coded as a part of this research. This tool consists of two parts in addition to the aerodynamic solver (Xfoil) as shown in Figure 7-2. The first part generates the aerofoil section geometry using a combination of PARSEC and Bezier-curve parameterization developed in this work, involving 9 variables shown in Figure 7-3 and Figure 7-4. PARSEC parametrization is used to represent the camber line while Bezier-curve is used for the thickness distribution. The second part contains the optimisation code using the Canonical Genetic Algorithm while several optimisation algorithms can be utilized within the MATLAB environment.

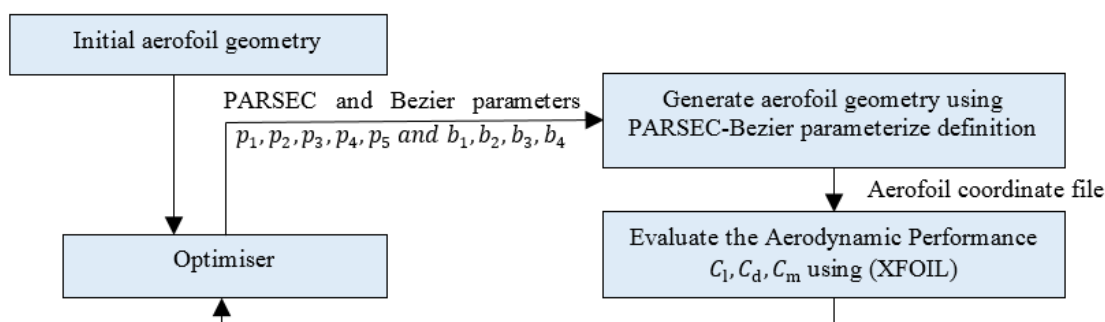


Figure 7-2 Aerofoil shape optimisation flow

7.2.1 Aerofoil Shape Parameterisation

Some of the parameterisation techniques currently in use proved to be advantageous over the others with respect to the rate of convergence, range of aerofoils that could be represented, ... etc (P. Salunke et al., 2014). In order to investigate new aerofoils at different thicknesses for high altitude flying wing, an aerofoil design optimisation tool was written using different parameterisations to represent the aerofoil surface. But convergence problems were experienced during the design process in addition to difficulties concerning the constraining of the resulting aerofoils at a specified thickness. Therefore, a new hybrid parameterisation method is presented using the PARSEC and the Bezier-curve functions. In this parameterisation, the PARSEC function is used to represent the camber line of the aerofoil, while the Bezier-Curve parameterisation is used to represent the thickness distribution. As experience was gathered during this work, this combination was efficient when searching for the optimised setting because of its capability to define a set of proper

design variables leading to rapid convergence. Moreover, Bezier-Curve enables the thickness distribution to be constrained to achieve a positive distribution, in addition to achieving a particular maximum aerofoil thickness.

7.2.1.1 Thickness distribution (Bezier Parameterization)

Bezier-Curve parametrisation has been used to represent the thickness distribution of the section. The curve can be represented by associated control points. The generated curve passes through the first and last control points, but does not need to pass through the other control points (Derksen & Rogalsky, 2010; P. Salunke et al., 2014; Park et al., 2008).

Assume a number of control points (n), with their coordinates as $P(xc_i, b_i)$, where b_i will be denoted as Bezier parameters while xc_i are set as in Figure 7-3. The curve can be discretised into a number of segments; each segment length will be denoted as (t) where $0 \leq t \leq 1$. The blending function of each segment can be evaluated by:

$$B_i^n = \frac{n!}{i!(n-i)!} (1-t)^{n-i} t^i \quad (7.1)$$

The coordinates of each segment of the curve (X_{thick}, Y_{thick}) associated with the given control points are found by:

$$X_{thick}(t) = \sum_{i=1}^n xc_i B_i^n(t) \quad (7.2)$$

$$Y_{thick}(t) = \sum_{i=1}^n b_i B_i^n(t) \quad (7.3)$$

Here Y_{thick} represents the distribution of the half thickness of the aerofoil along x -coordinate. X_{thick} will represent the x -coordinate of the upper and the lower surfaces. So $x = X_{thick}$.

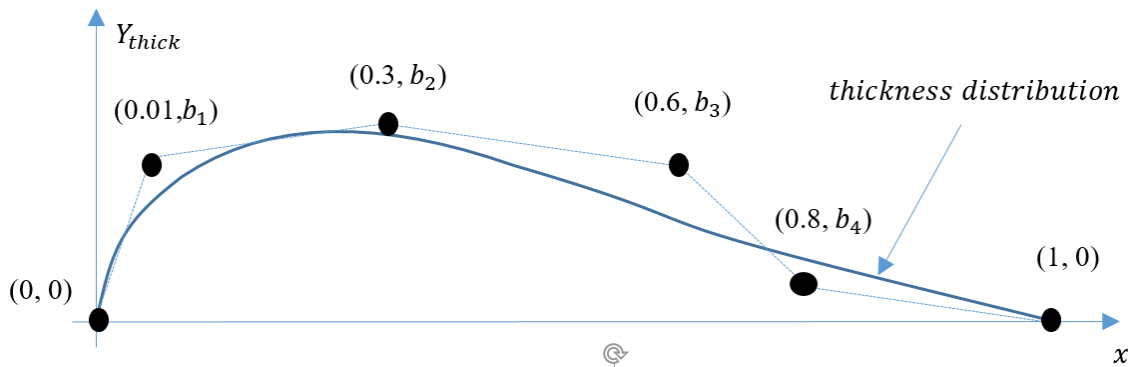


Figure 7-3 Bezier-Curve for Thickness Distribution

7.2.1.2 Camber line (PARSEC Parameterization)

PARSEC parameterisation has been used to represent the camber line of the aerofoil. In this study, only one curve of the PARSEC parametrization is taken. This curve can be represented by associated geometry parameters of the camber line, $(p_1, p_2, p_3, p_4, p_5)$ as defined in Figure 7-4. According to the PARSEC methodology (Sobieczky, 1999), the vertical coordinates of the curve at a given (x) coordinate location is given by:

$$Y_{cam}(x) = \sum_{i=1}^{n=5} a_{pa}^i \cdot x^{i-\frac{1}{2}} \quad (7.4)$$

The coefficients a_{pa} are calculated from the five parameters (p_1, p_2, \dots, p_5) of the aerofoil camber as follows:

$$b_{pa} = a_{pa} \times C_{pa} \quad (7.5)$$

where b_{pa} and C_{pa} are evaluated from the following matrices:

$$C_{pa} = \begin{vmatrix} 1 & 1 & 1 & 1 & 1 & 1 \\ p_2^{\frac{1}{2}} & p_2^{\frac{3}{2}} & p_2^{\frac{5}{2}} & p_2^{\frac{7}{2}} & p_2^{\frac{9}{2}} & p_2^{\frac{11}{2}} \\ \frac{1}{2} & \frac{3}{2} & \frac{5}{2} & \frac{7}{2} & \frac{9}{2} & \frac{11}{2} \\ \frac{1}{2} p_2^{-\frac{1}{2}} & \frac{3}{2} p_2^{\frac{1}{2}} & \frac{5}{2} p_2^{\frac{3}{2}} & \frac{7}{2} p_2^{\frac{5}{2}} & \frac{9}{2} p_2^{\frac{7}{2}} & \frac{11}{2} p_2^{\frac{9}{2}} \\ \frac{-1}{4} p_2^{-\frac{3}{2}} & \frac{3}{4} p_2^{-\frac{1}{2}} & \frac{15}{4} p_2^{\frac{1}{2}} & \frac{15}{4} p_2^{\frac{3}{2}} & \frac{63}{4} p_2^{\frac{5}{2}} & \frac{99}{4} p_2^{\frac{7}{2}} \\ 1 & 0 & 0 & 0 & 0 & 0 \end{vmatrix} \quad b_{pa} = \begin{vmatrix} 0 \\ p_3 \\ \tan(p_5/2) \\ 0 \\ p_4 \\ \sqrt{2p_1} \end{vmatrix}$$

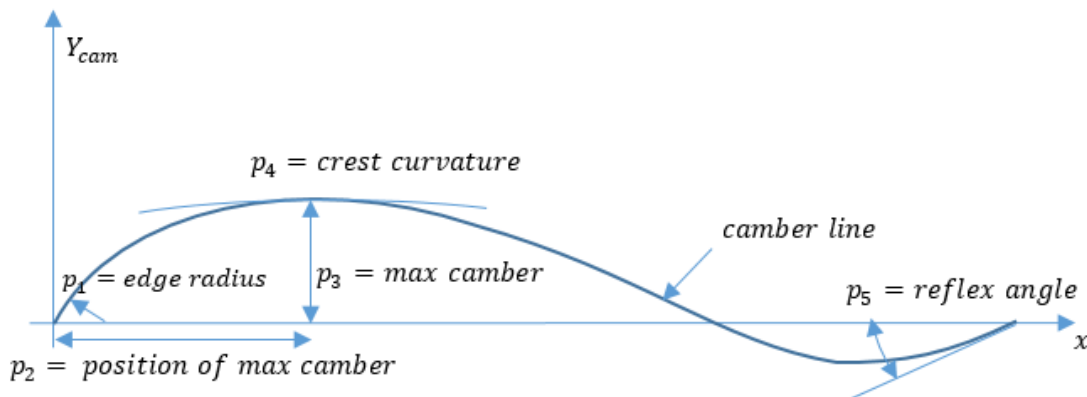


Figure 7-4 PARSEC parametrization for camber line

7.2.1.3 Aerofoil Coordinates

The coordinates of the upper and lower surfaces will be found using the coordinates of the camber line and the thickness distribution. As mentioned before, the x-coordinates of the thickness curve is the same as that of the camber curve. Thus, the y-coordinates of the upper and lower surfaces can be calculated as shown in Figure 7-5 by:

$$y_{up}(x) = Y_{cam}(x) + Y_{thick}(x) \quad (7.6)$$

$$y_{lo}(x) = Y_{cam}(x) - Y_{thick}(x) \quad (7.7)$$

Therefore, the aerofoil surface will be defined regarding the nine PARSEC and Bezier parameters p_1, p_2, p_3, p_4, p_5 and b_1, b_2, b_3, b_4 .

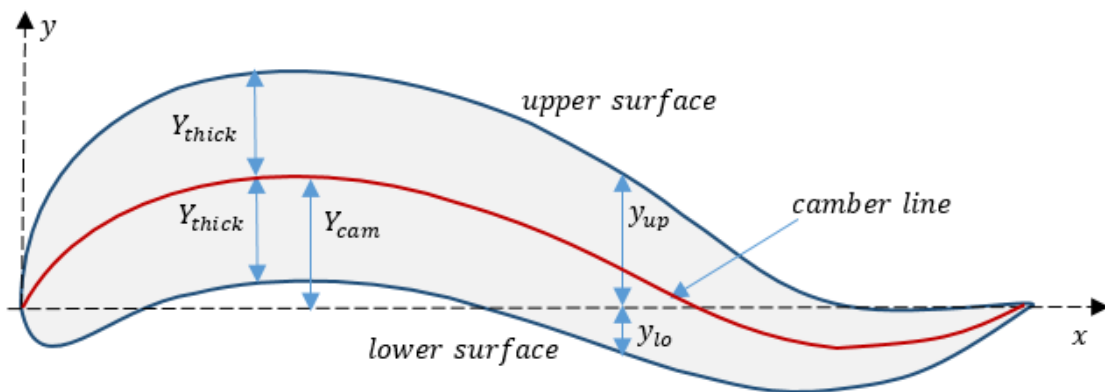


Figure 7-5 Generated aerofoil from the Bezier and PARSEC parameters

7.2.2 The aerodynamic solver

Xfoil has been used as the aerodynamic solver of the optimisation tool. It is a two dimensional aerodynamic solver which is widely used in the design and optimisation of aerofoils due to its ability to produce good and rapid solutions which can be obtained to match experimental data. It is a combination of inviscid-viscous flow analyses where some approximations are assumed (Drela, 1989). The input parameters of this solver are the aerofoil coordinates and the flow conditions such as the angle of attack, the Reynolds number and the amplification factor of the transition “Ncrit”.

7.2.3 Problem formulation

The primary target was to design a number of aerofoils with low pitching moment suitable for an aft-swept flying wing configuration operating at a Reynolds number of about 0.5×10^6 . Three optimisation targets were set to achieve the maximum aerodynamic performance characteristics. Each individual target is run separately to design several aerofoils of different thicknesses that meet the target criteria. The set targets are:

- Achieve maximum lift/drag ratio with no less than a pitching moment coefficient of -0.05:

$$\text{maximise } \left(\frac{C_l}{C_d} \right)$$

$$\text{subject to: } C_m > -0.05$$

- Achieve maximum lift/drag ratio with no less than a pitching moment coefficient of -0.02:

$$\text{maximise } \left(\frac{C_l}{C_d} \right)$$

$$\text{subject to: } C_m > -0.02$$

- Achieve maximum $\left(\frac{C_l^{1.5}}{C_d} \right)$ ratio with no less than a pitching moment coefficient of -0.05:

$$\text{maximise } \left(\frac{C_l^{1.5}}{C_d} \right)$$

$$\text{subject to: } C_m > -0.05$$

The design variables of the optimisation problems are the PARSEC and Bezier parameters:

$$p_1, p_2, p_3, p_4, p_5, b_1, b_2, b_3, b_4$$

In each design target, the thickness of the optimal aerofoil is constrained during the optimisation to offer different aerofoils with different thicknesses. The constraining is done by controlling the upper and the lower bounds of the Bezier parameter values (b_1, b_2, b_3, b_4). The flow condition was set at an angle of attack of 6 degrees and Reynolds number of 0.5×10^6 .

7.3 The Newly Designed Aerofoils

Table 7-2 shows the aerodynamic performance of the newly designed aerofoils at the maximum lift to drag ratio in addition to the maximum & minimum lift coefficients and stall angles. Their names and numbers are temporarily used at this stage of study. The shapes and aerodynamic characteristics of the newly designed aerofoils are shown in Figure 7-6 at Reynolds number 0.5×10^6 .

Table 7-2 Aerodynamic performance of the new aerofoils

Aerofoil name	At max C_l/C_d					$C_{l_{max}}$	$C_{l_{min}}$	Stall angle \approx	Thickness t/c %
	C_l/C_d	C_l	C_d	C_m	at AoA \approx				
max C_l/C_d $C_m > -0.05$									
ZMR-9	117.9	1.081	0.0091	-0.0497	6	1.34	-0.37	15	9.9
ZMR-12	115.4	0.980	0.0085	-0.0497	6	1.25	-0.418	14	12.71
ZMR-13	109.4	0.96	0.0087	-0.0482	6	1.24	-0.52	15	14.44
ZMR-14	111.1	1.051	0.0094	-0.0493	6	1.3	-0.31	15	16.6
ZMR-28	89.88	1.009	0.0112	-0.0466	7	1.136	-0.746	16	20.6
max $C_l^{3/2}/C_d$ $C_m > -0.05$									
ZMR-20	120.8	1.135	0.0094	-0.0496	6	1.448	-0.293	17	9.11
ZMR-17	117.6	1.191	0.0101	-0.049	7	1.446	-0.48	15	12.57
ZMR-19	114.7	1.056	0.0092	-0.0498	6	1.388	-0.34	16	15.02
ZMR-18	114	1.149	0.0093	-0.049	7	1.435	-0.49	16	15.83
ZMR-16	95.51	1.017	0.0106	-0.0443	6	1.296	-0.388	17	20.68
max C_l/C_d $C_m > -0.02$									
ZMR-26	93.91	1.268	0.0139	-0.0181	7	1.495	-1	15	14.91
ZMR-27	80.52	1.234	0.0153	0.0341	10	1.46	-1.152	14	15.57

According to the set of results obtained so far as tabulated in Table 7-2 and Figure 7-6, the overall observations of the optimised aerofoils can be summarised as follows:

1. The lift/drag ratios are higher than the corresponding existing aerofoils tabulated in Table 7-1. This is expected because the pitching moment of the new aerofoils is greater than those in Table 7-1.
2. Increasing the maximum thickness of the aerofoil leads to a decrease in the maximum lift/drag ratio.
3. For thicker aerofoils such as ZMR-16, ZMR-18 and ZMR-19, the lift/drag ratio per the angle of attack slope drops sharply after the maximum value.
4. The variation of the pitching moment with the angle of attack is not smooth in some of the optimised aerofoils.
5. The stall angles are not close to the angles in which the maximum lift/drag ratio is reached.

6. Reducing the pitching moment results in the reduction of the maximum lift/drag ratio and increased drag (see ZMR-26 AND ZMR-27 in Table 7-2).

It is worth mentioning that the maximum lift coefficient was not employed in the optimisation target and the focus was at an angle of attack of 6 degrees for maximum lift to drag ratio away from the stall angle. Therefore, most of the newly designed aerofoils would have stalled at about 8 degrees from the angle corresponding to the maximum lift/drag ratio.

ZMR-17 is the most interesting one among the newly designed aerofoils and will be a candidate for an aft-swept aircraft due to its moderate thicknesses and high maximum lift to drag ratio. Its maximum thickness is 12.57% located at 32% of the chord. It will be validated by a high order analysis solver in the next section. The author is aware that using an aerofoil necessitates conducting experimental tests to verify its performance and instill confidence and that there is no unexpected behaviour which is not indicated by the computational fluid dynamic (CFD) packages. This should be kept in mind when one of these aerofoils is used in an actual model. Therefore, five different algorithms will be used to investigate and verify the aerodynamic performance of the aerofoil ZMR-17.

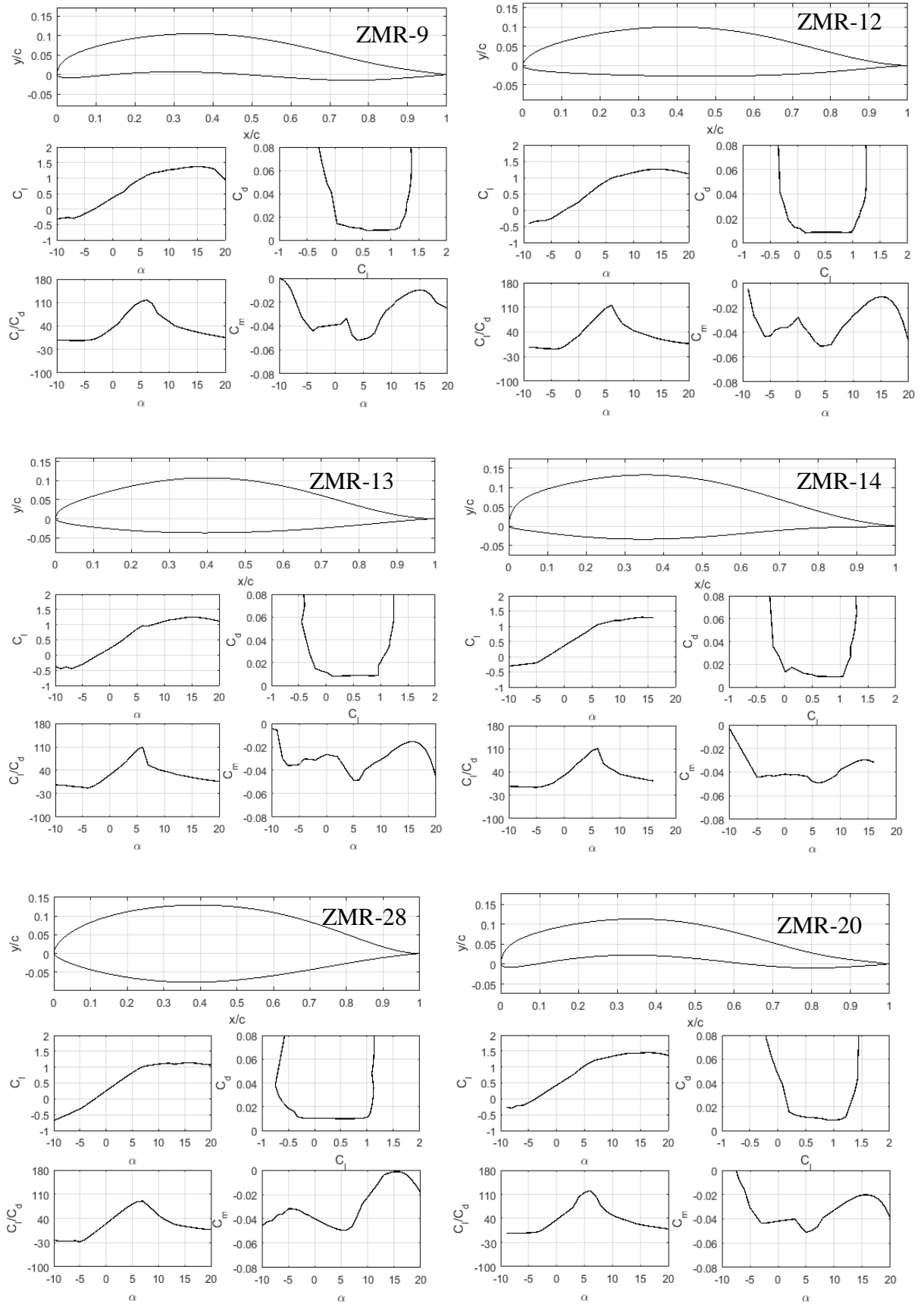


Figure 7-6 Aerodynamic performance of the newly designed aerofoils, $Re = 0.5 \times 10^6$

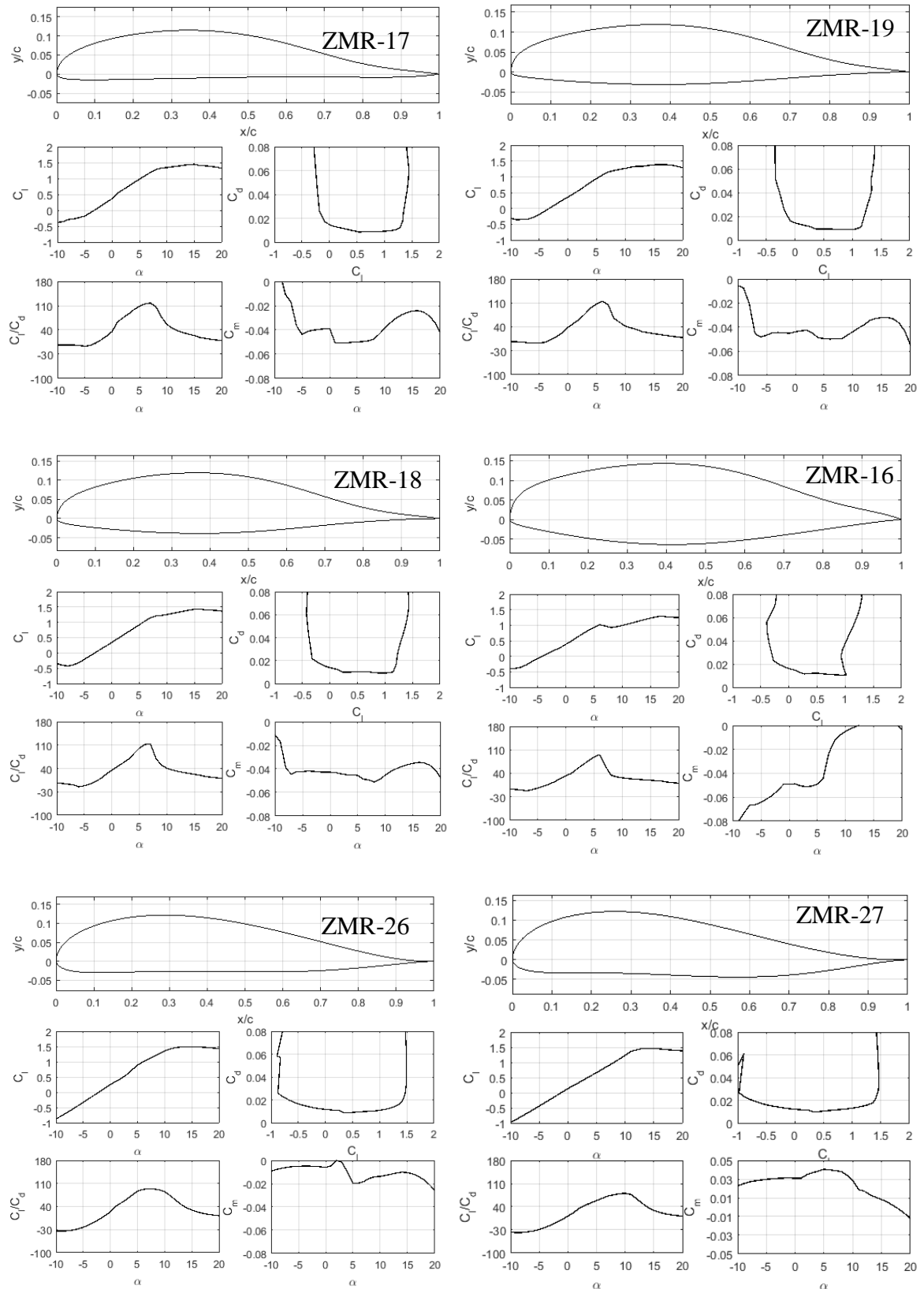


Figure 7-7 Aerodynamic performance of the newly designed aerofoils, $Re = 0.5 \times 10^6$

7.4 CFD Models

High-order CFD analysis has been conducted to validate one of the newly designed aerofoils using ANSYS Fluent. The results of the high order CFD are compared with the results obtained by Xfoil and the recently developed model Inviscid/Viscous 2D aerodynamic model (IVM). For the CFD analysis, a C-type mesh is adopted with a proper mesh density to ensure that Y^+ of the first row of cells adjacent to the aerofoil surface is less than one with a cell aspect ratio less than 100 as recommended by the guide of CFD models (Ansys, 2013). The boundary conditions are the upper and the lower flow domain boundary as a function of the velocity-inlet boundary whilst the downstream is considered as a pressure-outlet boundary. Also, the aerofoil surface is considered as a wall.

Two transition models, $k\text{-}kl\text{-}\omega$ and SST- $k\text{-}\omega$ (4eq), have been used due to their accuracy for a wide class of flows which can predict laminar-to-turbulent transition. Moreover, a fully turbulent model Spalart-Allmaras also has been used. These models are based on the Reynolds-averaged approach and the Reynolds stresses are related to the mean velocity gradients. Full details of these models can be found in reference (Ansys, 2013). They will be briefly described next.

Transition SST- $k\text{-}\omega$ (4eq)

This is a transition model based on the coupling of the turbulent model SST- $k\text{-}\omega$ with two transport equations for the intermittency and the transition onset criteria. The turbulence model SST- $k\text{-}\omega$ is one of the popular turbulent models which contains two equations eddy-viscosity. These are the transport equation for the turbulent kinetic energy (k) and the inverse turbulent time scale (ω) for the inner parts of the boundary layer. The model is switched to a $k\text{-}\epsilon$ behaviour for those cells at the free stream because the $k\text{-}\omega$ is too sensitive for the turbulence properties of the inlet free-stream. The intermittency and transition onset criteria are functions of the momentum-thickness Reynolds number. In ANSYS Fluent, the transition SST- $k\text{-}\omega$ (4eq) model is supported by an empirical correlation to cover flows and standard bypass transition in low freestream turbulence environments.

Transition $k\text{-}kl\text{-}\omega$ (3eq)

This is a transition model which can predict the boundary layer development and the transition onset. In this model, the eddy viscosity is represented by three equations; transport equations for the laminar and turbulent kinetic energy (kl and k respectively) in addition to the inverse turbulent time scale (ω).

Spalart-Allmaras (1eq)

It is a turbulent model in which one transport equation represents the kinematic eddy (turbulent) viscosity. The Spalart-Allmaras model was designed for aeronautical applications and has proved to give good results. It was formulated to model a viscosity-affected region of the boundary layer at low Reynolds number.

7.4.1 The Aerodynamic Performance of ZMR-17

The aerofoil ZMR-17 has been selected to be adopted for a high altitude aft-swept flying wing configuration. The CFD analysis was conducted with a proper mesh density as the schematic of a partial domain as shown in Figure 7-8. Three models have been used in the Fluent ANSYS as described in the previous section. In addition, the results have been compared with those obtained by Xfoil and IVM codes. The aerodynamic analysis is conducted at two different operational Reynolds number; 0.5×10^6 and 0.9×10^6 .

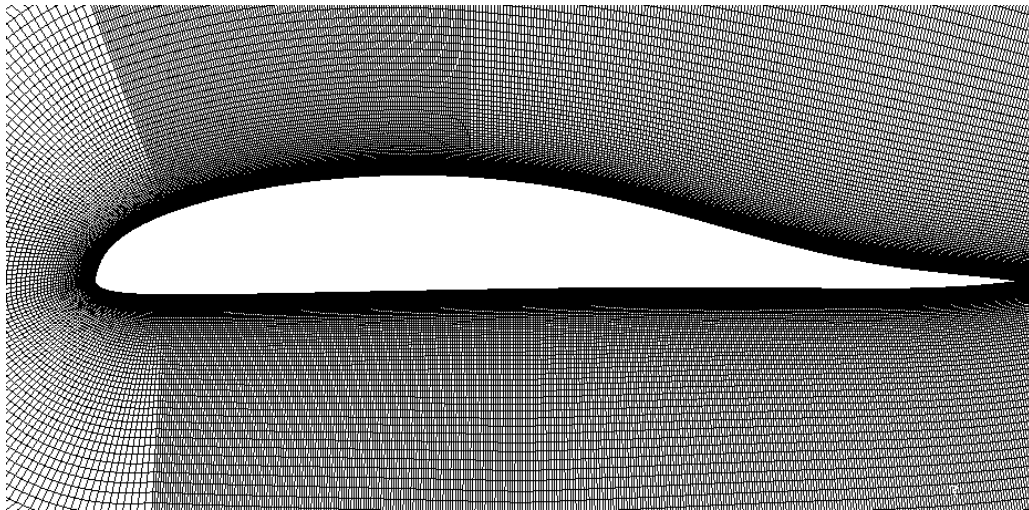


Figure 7-8 The schematic of a partial domain of ZMR-17

7.4.1.1 The Aerodynamic Performance at $Re=0.5 \times 10^6$

Figure 7-9 shows the results of the lift, drag and pitching moment coefficients at Reynolds number of about 0.5×10^6 . The aspect of these results can be summarised in the following:

- **For angle of attack in the range -5 to +10 degrees**
 1. The prediction of lift coefficients of all models shows a good agreement with each other. However, the Xfoil prediction was slightly overestimated.

2. The prediction of drag coefficients also was in good agreement, but as expected, the turbulent model (Spalart-Allmaras) results in higher drag prediction than the transition models.
 3. The pitching moment coefficient obtained by the Xfoil and the high order transition models behave similarly with the angle of attack. The result from the Spalart-Allmaras model indicates that the pitching moment almost remains constant from about 0 to 10 degrees and it is closer to the IVM prediction (inviscid pitching moment).
- **For angle of attack in the range +10 degrees to the stall angle**
 1. Under this range of angles of attack, the separation begins to appear, and the solution of the transition models became hardly convergent at higher angles of attack.
 2. The Spalart-Allmaras model provided the lowest estimates and relatively good agreement with Xfoil. The transition models k-kl- ω and SST-k- ω give similar lift coefficient results. The stall angle for all the models except the IVM is about 15 degrees.
 3. The drag results obtained by all models at stall area also differ. However, the drag calculated by the k-kl- ω and SST-k- ω models have the highest values. As expected, the results of the IVM are not accurate in the stall region.
 4. The result obtained by the high order transition models looks similar and differ from that obtained by Xfoil and Spalart-Allmaras. This indicates that the separation bubbles predicted by the transition models considerably influenced the pressure distribution and hence the pitching moment. It can be clearly noticed in Figure 7-13 and Figure 7-14 which show the separation bubbles obtained by the transition models at higher angles of attack, appeared and then the flow reattached to the aerofoil at the trailing edge. The separation bubble predicted by Spalart-Allmaras is located closer to the trailing edge than that predicted by the transition models as shown in Figure 7-15.
 - **For angle of attack less than -5 degrees**
 1. In this range of large negative angles of attack, the separation begins on the lower skin.
 2. The lift coefficients of the Xfoil, Spalart-Allmaras and SST-k- ω are in good agreement and differ from those obtained by the k-kl- ω model and the IVM.

3. The IVM considerably underestimated the drag coefficient when compared to any of the other methods due to separation encountered the flow.

7.4.1.2 The Aerodynamic Performance at $Re=0.9 \times 10^6$

The aerodynamic performance also has been conducted at Reynolds number of 0.9×10^6 as indicated in Figure 7-10. The results show the same behaviour that was discussed above but with the following differences:

- 1- At higher angles of attack, results of the lift and drag coefficients obtained by the SST-k- ω , Xfoil and Spalart-Allmaras models differ from those calculated by the k1-k- ω model.
- 2- At higher angles of attack, the pitching moment coefficients obtained by all the models except the IVM were less scattered. The size of the separation bubbles predicted by the transition models, see Figure 7-13 and Figure 7-14, is small which means less disturbance is present in the pressure distribution. This explains why the pitching moment predicted by the transition models become closer to that obtained by Spalart-Allmaras models if compared to the low Reynolds prediction.

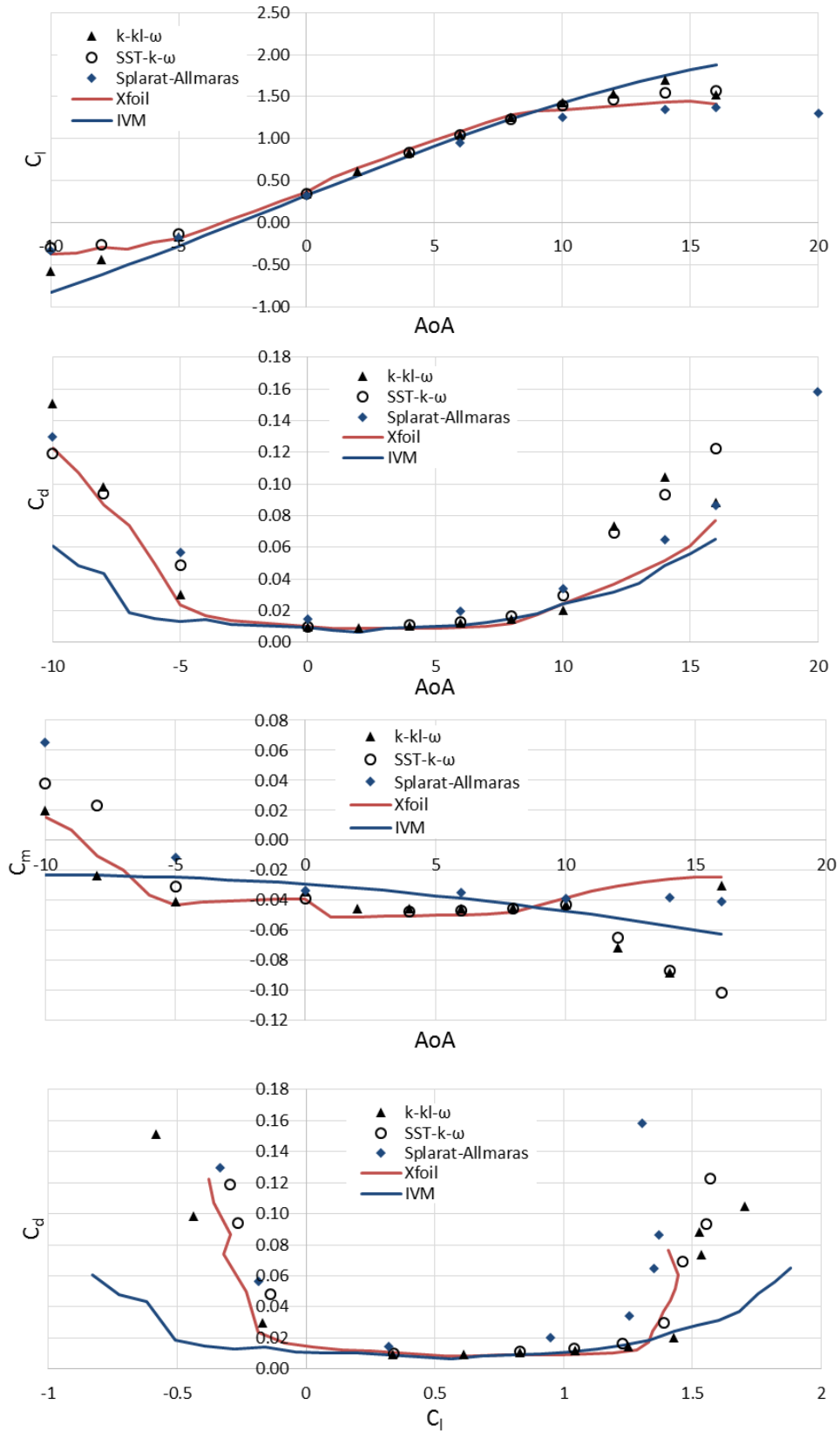


Figure 7-9 The aerodynamic performance of ZMR-17 at $Re=0.5 \times 10^6$

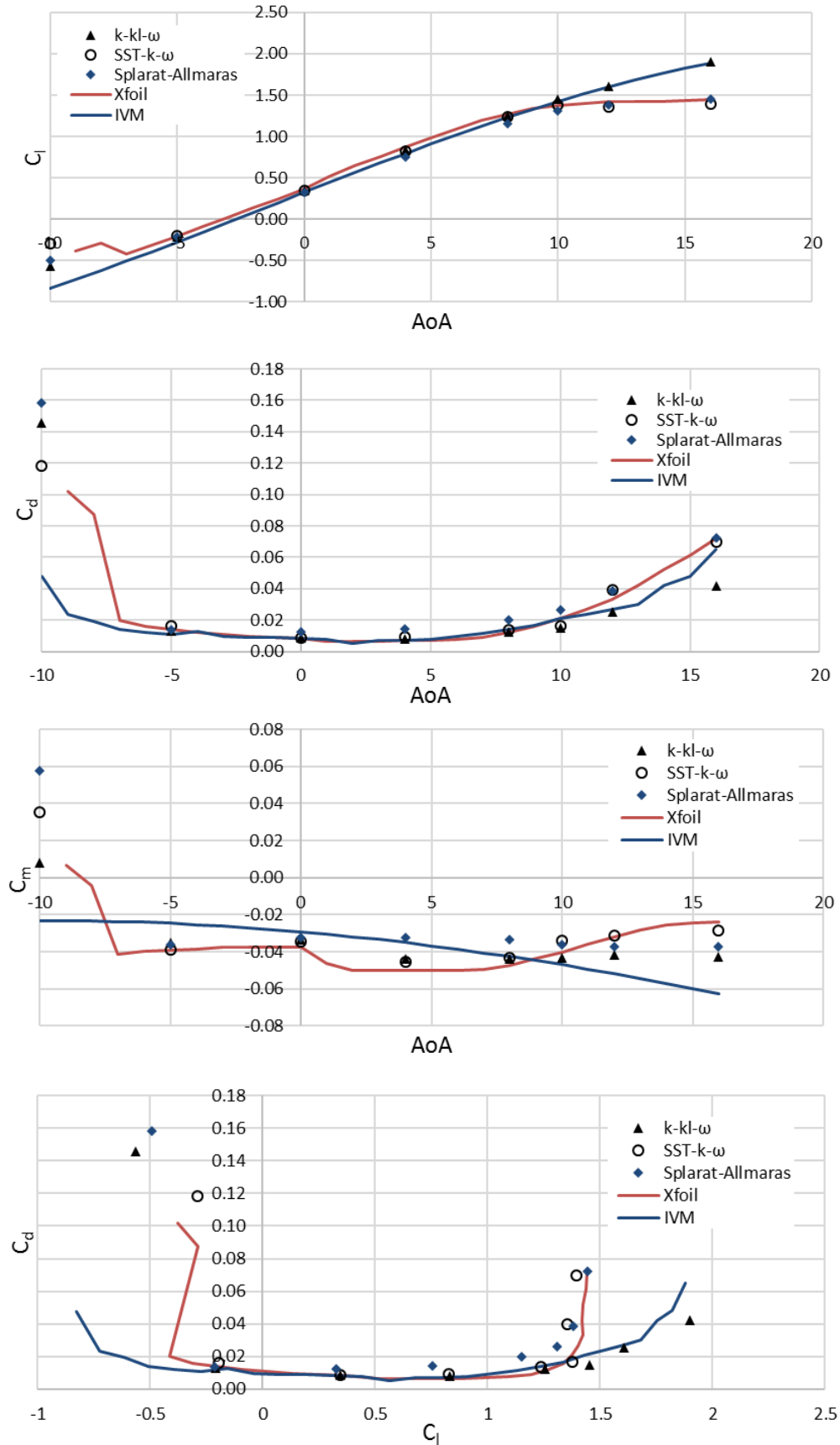


Figure 7-10 The aerodynamic performance of ZMR-17 at $Re=0.9 \times 10^6$.

7.4.2 Laminar Bubbles

The velocity contour and vectors of the transition models used in the high order CFD analysis are indicated in Figure 7-11 and Figure 7-12 at Reynolds number of 0.5×10^6 and 0.9×10^6 respectively. The results calculated at both Reynolds numbers show that laminar bubbles (LB) can be observed at the upper surface of the aerofoils. Downstream of the location of these bubbles, the flow reattaches to the surface. However, the size of the bubbles is too small and hence the magnitudes of the velocity vectors within the bubble in the figures are scaled to 5. With increasing angle of attack, the laminar bubble at the upper surface has migrated forwards and become smaller. The results also indicate that there is no turbulent separation occurring in the range of angle of attacks from -4 to +10 degrees. Outside this range, turbulent separation begins and becomes larger with increasing angle of attack.

7.4.3 Flow Aspect at Stall Areas

The flow streamlines at high positive and negative angles of attack (stall areas) obtained by the transition models (SST-k- ω and k-kl- ω) and the Spalart-Allmaras model at the two Reynolds numbers are shown in Figure 7-13, Figure 7-14 and Figure 7-15. As indicated in the aerodynamic performance results obtained by the models, the results in the stall areas differ and the high order CFD analyses experienced difficulty in converging. Also, this difference can obviously be seen in the graphs of flow streamlines at varying angles of attack. The aspects of the flow at the positive and the negative stall areas can be summarised as follows:

1. The size of the turbulence separation predicted by the k-kl- ω model is smaller than that predicted by the other models. It also makes more pronounced the improvement in the aerodynamic performance at increased Reynolds number.
2. At -5 degrees and Reynolds number of 0.5×10^6 , all the models predict a separation bubble at the lower surface. However, it vanishes at higher Reynolds number. The transition model predicts a small bubble close to the leading edge while the Spalart-Allmaras predicts a large region of separation along the lower surface of the aerofoil.

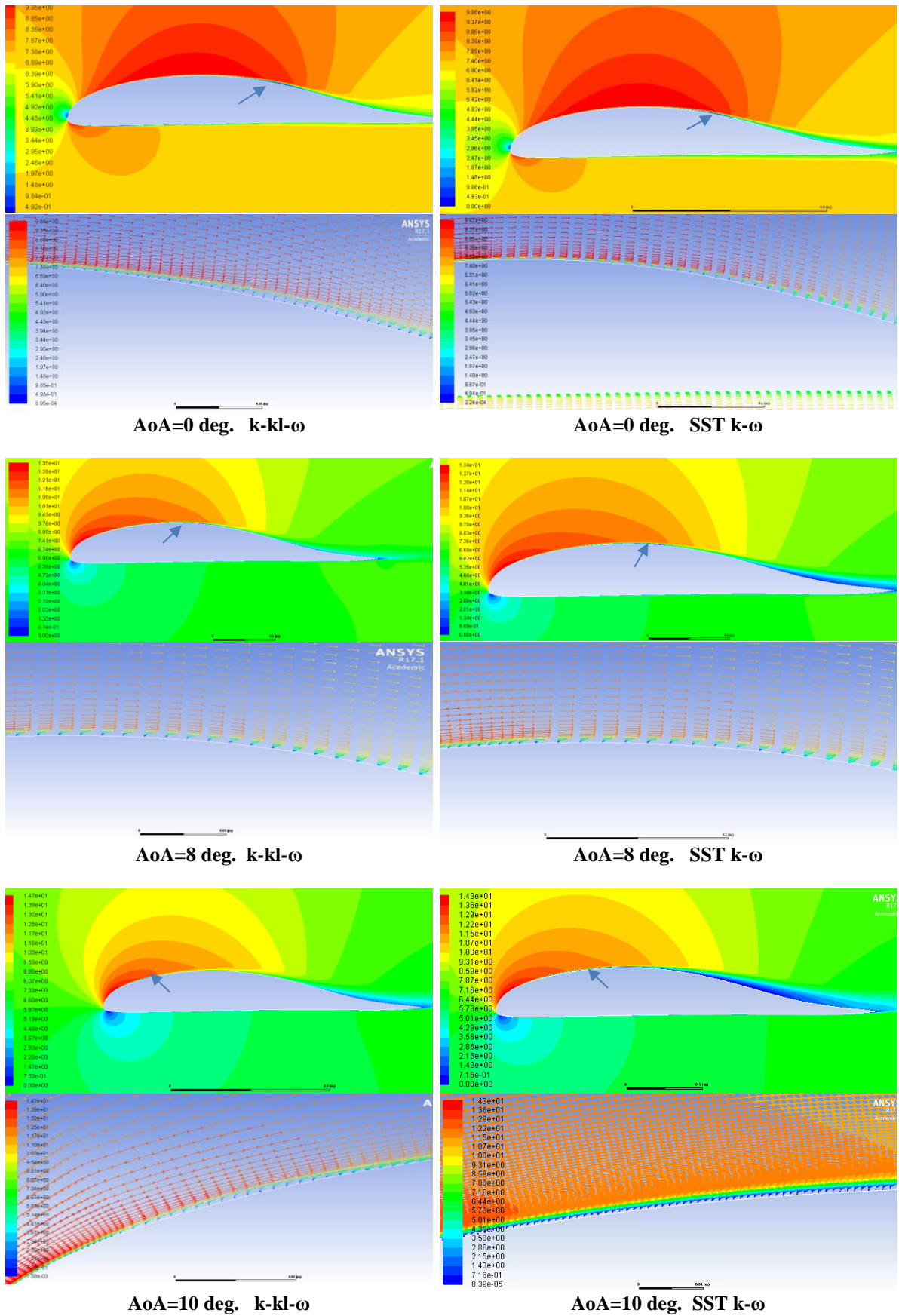


Figure 7-11 Velocity contour and vector obtained by the transition models for ZMR-17, $Re=0.5 \times 10^6$.

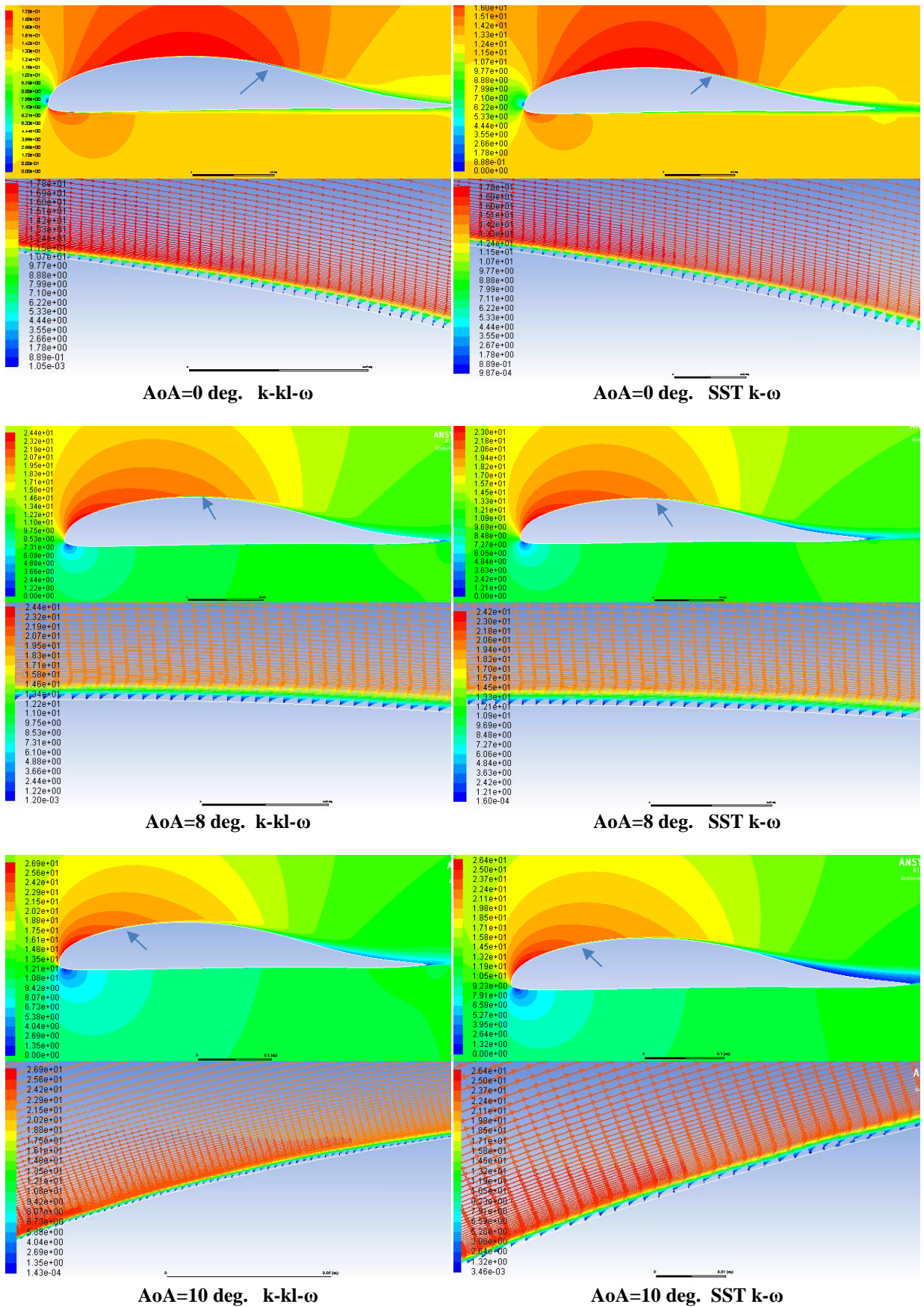
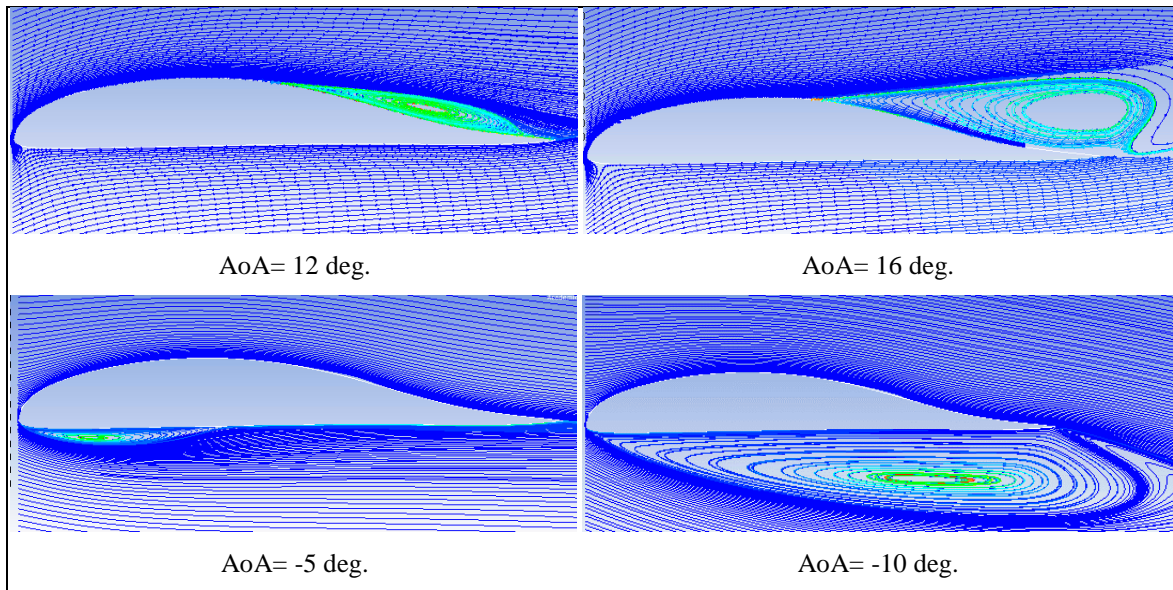
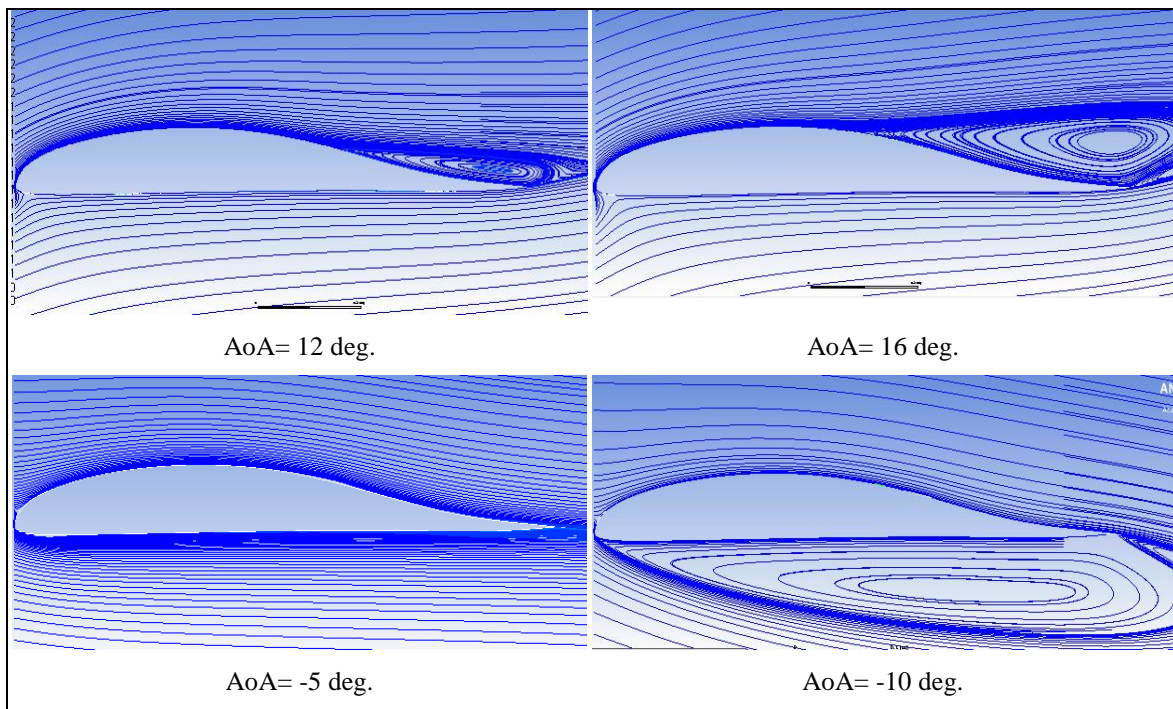


Figure 7-12 Velocity contour and vector obtained by the transition models for ZMR-17, $Re=0.9 \times 10^6$.



SST $k-\omega$, $Re = 0.5 \times 10^6$



SST $k-\omega$, $Re = 0.9 \times 10^6$

Figure 7-13 Stream lines around ZMR-17 at different angles of attack using transition SST $k-\omega$ model

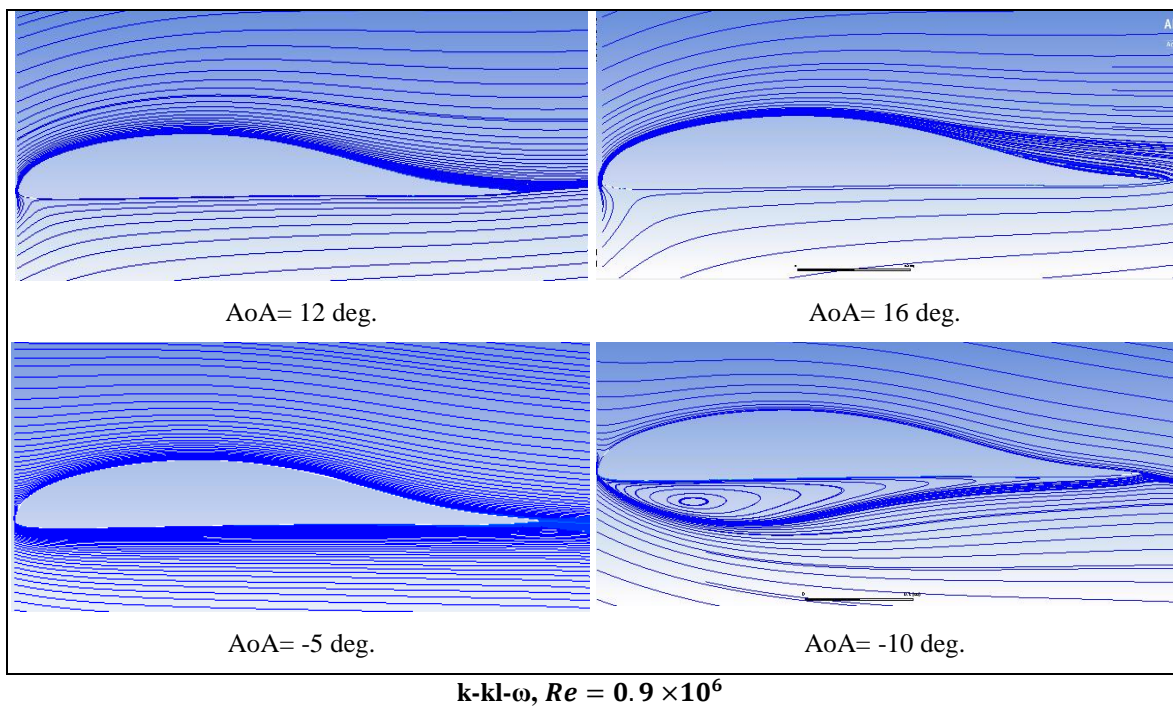
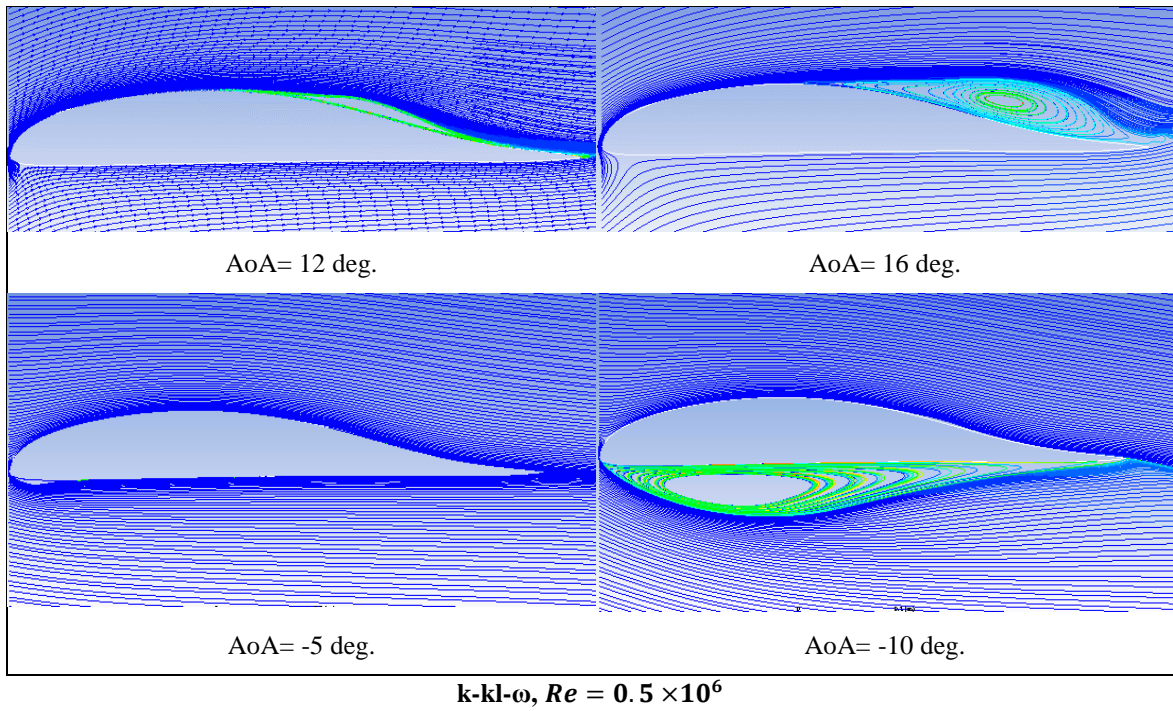


Figure 7-14 Stream lines around ZMR-17 at different angles of attack using transition k-kl- ω model.

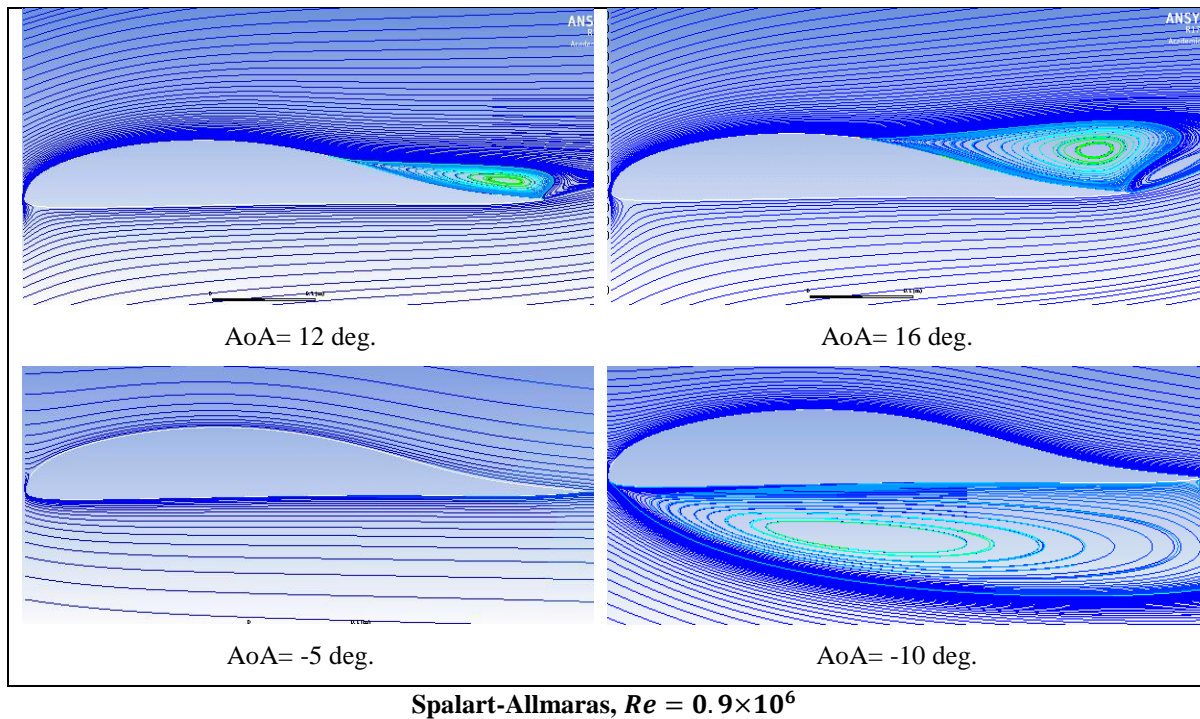
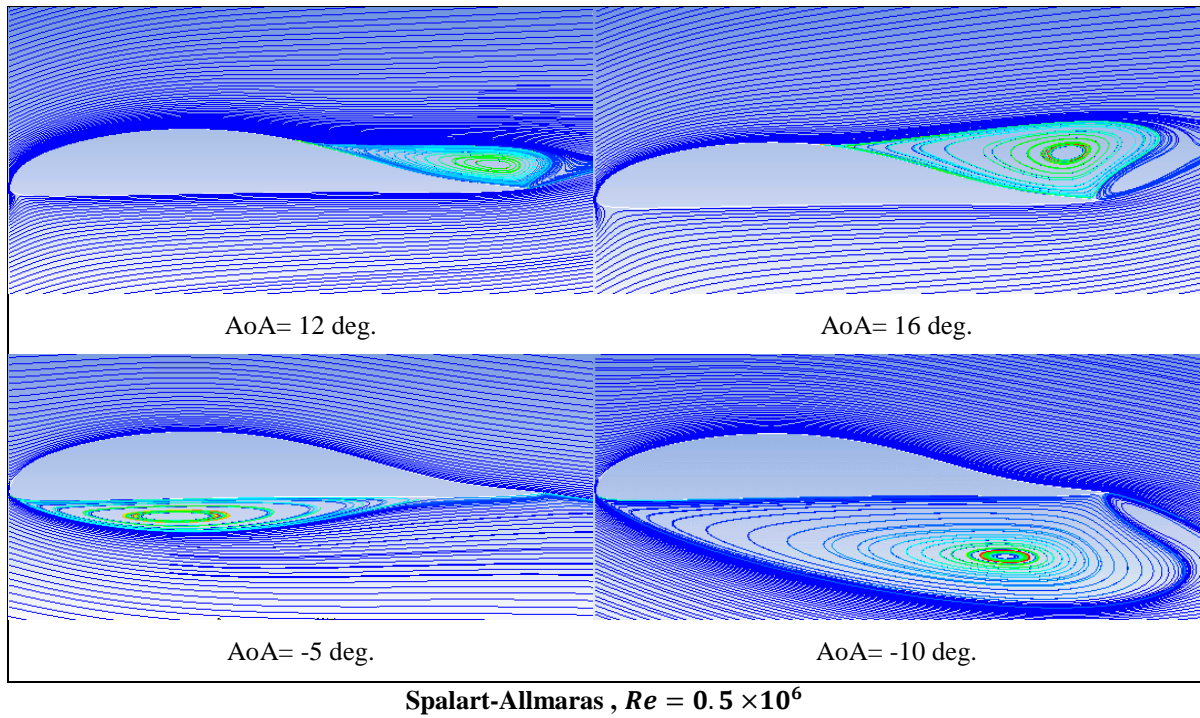


Figure 7-15 Stream lines around ZMR-17 at different angles of attack using Spalart-Allmaras model.

CHAPTER 8

8 CONCEPTUAL AND PRELIMINARY DESIGN OF SUMER UAV

A procedure for the design of a high altitude long endurance solar powered aft-swept aircraft called ‘SUMER’ is presented in this chapter. The total weight in addition to the component weight and power factor for all the aircraft elements such as the fuel cells, solar panels, propulsion system, avionics and the other electronics were estimated. The wing area in addition to its span length and aspect ratio were also found. A preliminary design approach including the optimisation process is then presented and used to design the wing geometry of SUMER to meet the mission requirements using the main characteristics obtained from the conceptual design. Also, the effects of the wing sweep, static stability margin and the location of the spar on the aerodynamic performance were studied with and without the structural influences.

8.1 Conceptual Design of SUMER

As a case study, a new conceptual design of a high altitude, long endurance, solar powered UAV was designed using the conceptual design model presented in Chapter 4. A simple mission is adopted to operate the aircraft in southern Iraq, particularly above the marshlands close to the ancient city of Sumer for surveillance purposes whilst carrying a 100 kg camera rated at 1.25 kW between 1st April and 10th September at an altitude of about 17 km. The minimum available solar energy and its corresponding daytime hours were evaluated using the solar irradiance model (presented in section 4.5) at 17 km altitude and 31.01° N latitude for the given duration as shown in Figure 8-1.

As indicated in Chapter 4, the aerofoil intended to be used in the design should be selected prior conducting the conceptual design in order to have a better estimate for the aerodynamic performance of the aircraft. The aerofoil ZMR-17 designed in Chapter 7, will be adopted due to its high flight endurance factor and maximum lift coefficient coupled with low pitching moment. Adopting different aerofoils along the wing is not a preferable choice especially for large aspect ratio wing due to the compounding of the analytical complications

arising from characteristics such as laminar bucket and maximum aerofoil lift coefficient (Nickel & Wohlfahrt, 1994). Therefore, aerofoil ZMR-17 whose aerodynamic performance studied at different Reynolds number in section 7.4, will be adopted for the entire wing. As indicated in section 4.3.8.1, the cruise lift coefficient can be estimated using the minimum allowable speed concept with a safety margin for air turbulence and gust. It was represented as a function of the maximum lift coefficient. This indicates that the aircraft might fly at a lift coefficient lower than the one corresponding to the minimum power flight. However, an approximation has been made to consider the maximum lift coefficient of the wing which is assumed to be the same regardless of the twist required for the washout at the outer sections of the wing for stability reasons. Aerofoil ZMR-17 has a maximum lift coefficient of about $C_{l_{max}} \approx 1.38 \sim 1.4$. Therefore, using equation (4.30), the cruise lift coefficient (reference lift coefficient) will be $C_{L_{ref}} \approx 0.8$. The associated mission requirements and the aerodynamic characteristics such as the reference lift coefficient and the span efficiency, are assumed constant during the sizing process. The fixed parameter that were assumed constant are detailed in Table 8-1. The weight and power fractions used in the conceptual design tool are detailed in Table 4-2.

Applying the conceptual design methodology to the given mission had led to the design space for the aircraft as shown in Figure 8-2. From this figure, particularly the gross weight-span curves, one can conclude that the gross weight 932.27 kg represents the minimum weight in the design space at a wingspan of 58 m and a wing aspect ratio of 19. Hence, this choice can be used to determine the weight and power of all the corresponding aircraft elements as can be concluded from Figure 8-2. These optimal characteristics are tabulated in Table 8-2.

Figure 8-3 shows the weight fraction of the aircraft components in which the weight of the fuel cells represents 40.27 % of the gross weight followed by the airframe weight fraction of about 33.76%. The optimal flight state indicates that the aircraft will need to be flown at 0.907×10^6 Reynolds number where the drag coefficient would be 0.019153.

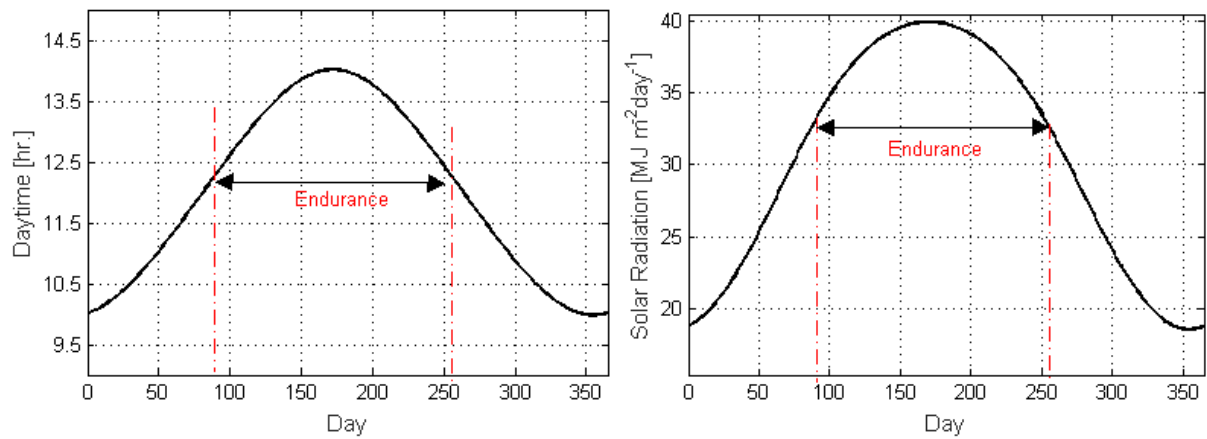


Figure 8-1 Solar irradiance per unit area and daytime hours versus days, for 31.01° latitude at 17 km altitude

Table 8-1 The mission requirement of the case study SUMER

Parameter	Value	Units	Description
C_{Lref}	0.80	-	Aeroplane lift coefficient at cruise
e	0.95	-	Span efficiency of the wing
E_{day}	33.37	MJ/m ² /day	Solar radiation between 1 st April and 10 th September) at latitude 31.01° southern Iraq at 17km altitude
I_{max}	1182	W/m ²	Maximum irradiance
T_{day}	12.32	hr	Daytime duration
$m_{payload}$	100	kg	Payload
P_{pld}	1250	W	Payload power consumption
ρ	0.1382	kg/m ³	ISA air density at an altitude of 17 km

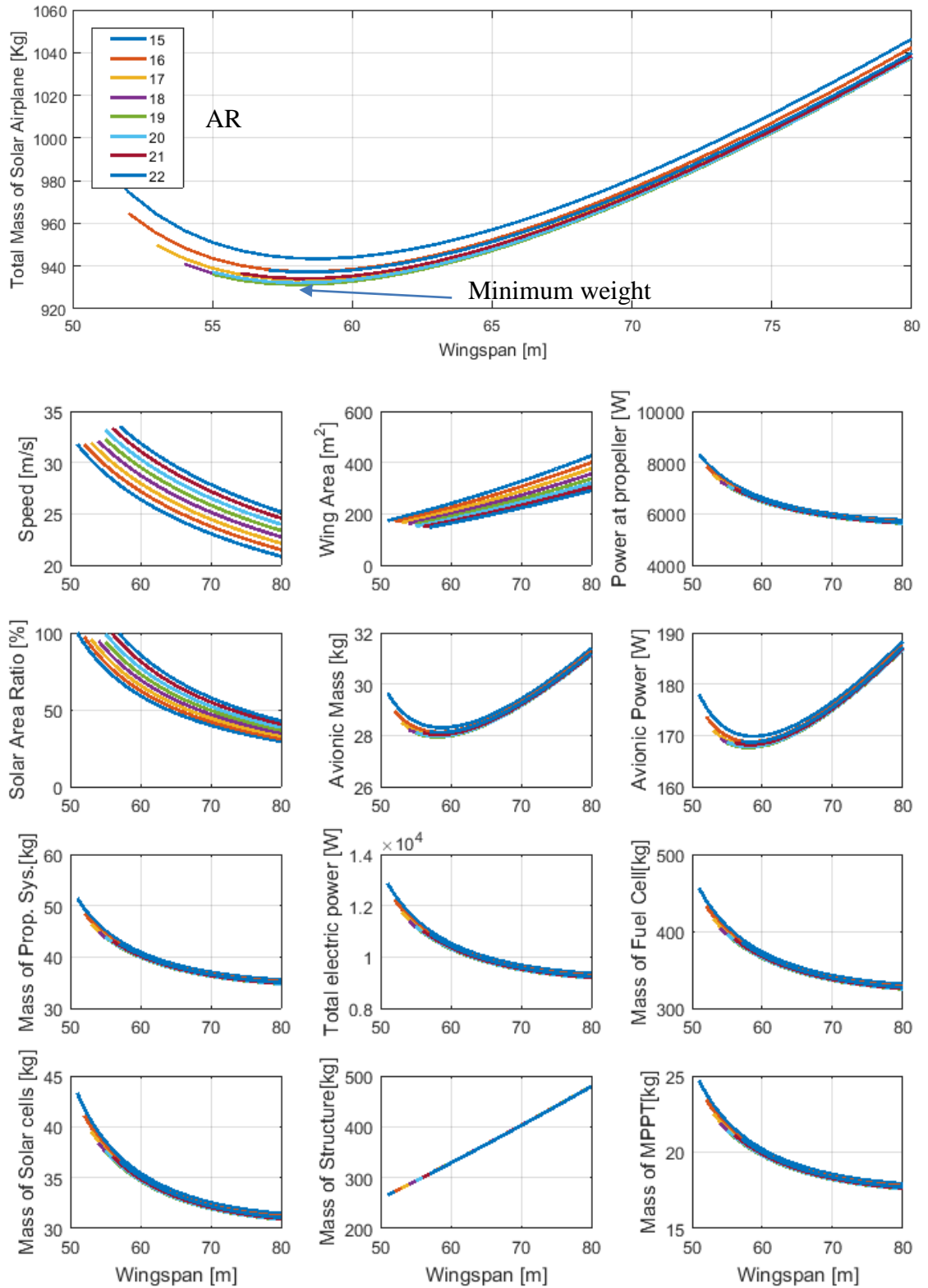


Figure 8-2 The design space for the given mission requirements of the SUMER

Table 8-2 The main characteristics of the SUMER

Parameter	Value	Unit	Description
AR	19	-	Aspect ratio
b	58	m	Wingspan
m	931.27	kg	Total mass
m_{af}	314.41	kg	Airframe mass
m_{fc}	375.01	kg	Mass of fuel cells
m_{sc}	35.63	kg	Mass of solar panels
m_{mppt}	20.307	kg	Mass of maximum power point tracker
m_{prop}	41.203	kg	Mass of Propulsion system
m_{av}	27.94	kg	Mass of Avionics
m_{lg}	16.763	kg	Landing gear mass
S	177.053	m ²	Planform Area
A_{sc}	142.527	m ²	Area of the solar cells
C_{av}	3.052	m	Mean geometric chord
V_{∞}	30.538	m/s	True airspeed at level flight
$P_{elec\ tot}$	10.595	kW	Total electric power consumption in level flight
Re	0.907×10^6	-	Reynolds number at level flight
C_D	0.019153	-	Total drag coefficient at level flight

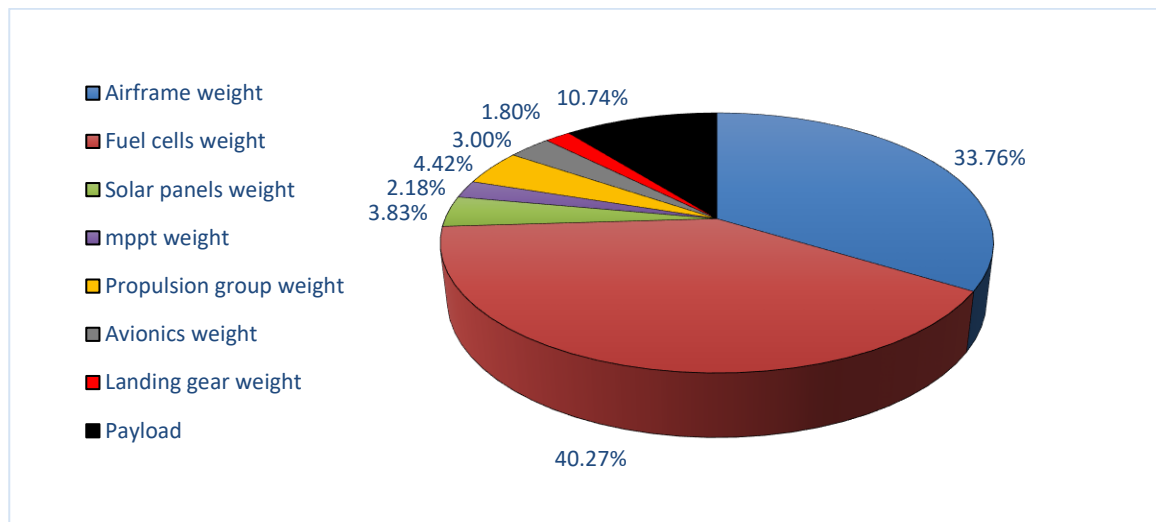


Figure 8-3 The weight distribution of SUMER

8.2 Preliminary Design of SUMER

The wing geometry will now be designed using data obtained from the conceptual design to meet the mission requirements. Accordingly, the wing will be optimised for the specified flight condition and no other operational requirement will be considered. Therefore, the aircraft will be designed to generate a trimmed lift coefficient of 0.8 with an overall drag coefficient no greater than 0.019153 at an airspeed of 30.53 m/s at 17 km altitude. The wing spar will be designed according to the critical loads at the cruise condition as detailed in the Chapter 6. Moreover, the gross weight of the aircraft must not exceed the expected weight of 931.27 kg.

The following steps represent the overall procedure for the preliminary design:

- Suggest an aircraft geometry based on the outcome of the main characteristics resulting from the conceptual design.
- Define the aircraft elements and their weights such as the number of electrical motors, fuel cells and landing gear. These weights must meet the allocated values generated from the conceptual design.
- Suggest a reasonable distribution of the aircraft system elements in the spanwise and chordwise directions.
- Find the required sweep angle to achieve the static stability requirements and a trimming condition at the reference lift coefficient of about 0.8. An optimisation tool will be used to conduct this study.
- Use the optimisation tool individually to study the influence of the sweep, static margin and the location of the spar on the aerodynamic performance and structural behaviour. This will lead to better understanding of the design challenges relating to a flexible aft-swept flying wing for high altitude aircraft.
- Compare the final design solutions to the mission requirements and assess the effectiveness of the design process.

8.2.1 Aircraft layout and its Components

An aft-swept, untapered flying wing which has the same area, aspect ratio and span obtained from the conceptual design as shown in Figure 8-4 was adopted at the start. The outer portion of the wing was given 10-degree dihedral to promote roll and indeed directional stability characteristics. The weight of the wing itself including the weight of the aircraft systems can modify the distribution of load along the wing and significantly influence the sizing process along with the elastic behaviour of the wing (Torenbeek, 2013).

At this stage of the design process, the weights of the aircraft elements are known and only the spar needs to be sized according to the ultimate loads. Therefore, the location of aircraft elements must be defined prior to the spar sizing process. Moreover, the number of the spar segments along the spanwise direction and the location of the spar along the chord wise direction must be known. The location of the spar is defined as a factor of the chord length and will be investigated in accordance with the design cases presented in section 8.3.2.1.

The weights of aircraft elements are sized and laid out distributed as follows:

1. The span is discretised into 28 segments (14 in each semi-span). The length of each segment is 2.1 m except the last four segments at each wing tip which are 2.03 m long. A square cross section is adopted for the spar where its height and width are equal to 0.8 of the maximum thickness of the wing section. Each span segment will be sized according to the maximum bending moment, shear force and torque exerted on the spar segment.
2. Propulsion unit similar to that used in the Helios aircraft will be adopted here. Each motor weighs about 6.75 kg including the gear box and the propeller (Noll et al., 2004). Using the allocated weight and power for the propulsion system indicated in Table 8-2, six electric motors will be considered for the propulsion system. The motors are spread out along the span, three in each wing as shown in Figure 8-5. The centre of mass of each unit is assumed to lie at 0.1 of the local chord in front of the leading edge as shown in Figure 8-6.
3. The allocated weight for the fuel cells and the Maximum Power Point Trackers are about 396 kg as indicated in Table 8-2. A decision was made to use four fuel cells, each of mass of about 99 kg including the Maximum Power Point Tracker (MPPT). These cells are distributed along the span to reduce the bending moments, especially

- at the root section. The centre of mass of each fuel cell is assumed to coincide with the elastic axis of the spar to reduce local wing twist.
4. The payload and the avionics are located at the root section while the location of their mass centre in the chord wise direction (X_{pay}) will be selected later to adjust the static margin.
 5. The weight of the landing gears is discretised into five units of equal weight located under the excessively loaded points which are under the fuel cells and the payload as shown in Figure 8-5.
 6. The non-spar elements are also discretised into segments, the mass centre of each is assumed to coincide with the centroid of the shaded area of the wing section which is at about $0.4x/c$ as calculated by the AutoCAD software package.
 7. The solar panels are discretised into strips in the spanwise direction such that their mass centres coincide with the $0.45x/c$ axis as measured from the wing leading edge.

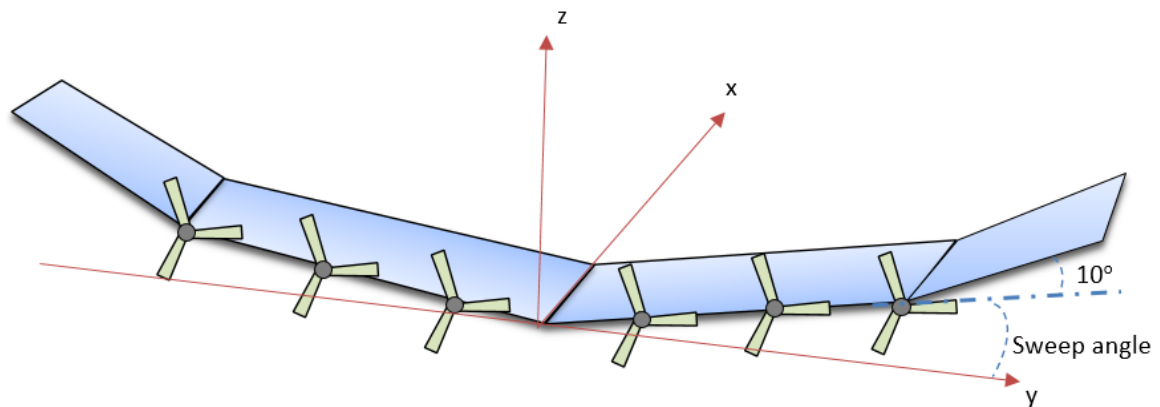


Figure 8-4 Initial layout of the SUMER

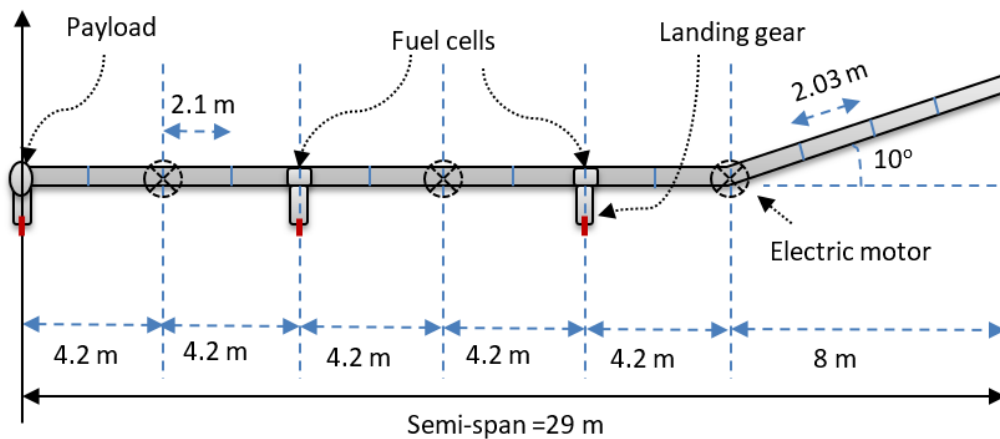


Figure 8-5 The front-side view of half wing of the SUMER and its weight distribution along the semi-spanwise direction

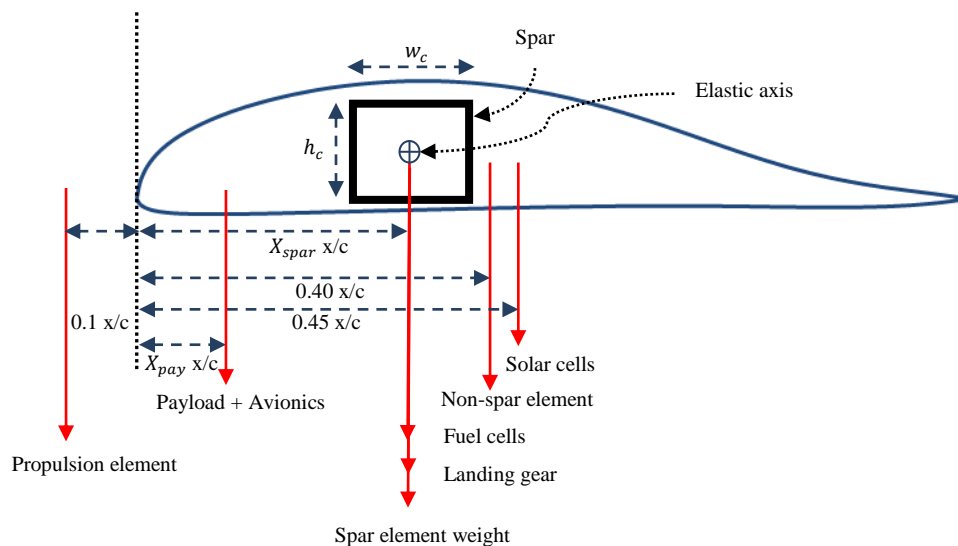


Figure 8-6 The weight distribution along the chordwise direction of the SUMER

8.2.2 The Static Stability Parameters

In this section, different parameters are defined in addition to introducing some techniques which will be adopted to facilitate the analysis of static stability. The concept of static stability refers to the tendency of the aircraft to return to equilibrium immediately after encountering a disturbance at the steady flight condition. The static equilibrium of aircraft occurs when there is no acceleration at the trim condition. It means that the summations of

the forces and the moments applied on the aeroplane are zero. In this study, only the static stability will be considered during the optimisation process. The aircraft case study will aim for continuous flight over 5 months and therefore only the cruise condition will be focussed on during the optimisation process. Trimming the aircraft at a specific lift coefficient will be addressed while other constraints such as stability during the climb and descent will not be considered. The outer portion of the wing is bent upwards by 10 degrees (dihedral) to aid roll and to a limited extent, weathercock stability. The sweepback of the wing also can help to achieve the static stability about all three axes (Nickel & Wohlfahrt, 1994). A combination of sweep and twist distribution of the wing can be utilised to achieve the requirements for the longitudinal static stability. To do that, there are three factors that will need to be considered:

1. The centre of gravity must be located ahead of the aerodynamic centre. This can be represented by the well-known ratio, static margin (Sm). It is a dimensionless factor which represents the distance between the centre of gravity (\bar{X}) and the aerodynamic centre (\bar{X}) divided by the mean aerodynamic chord (\bar{C}) (Cook, 2013).

$$Sm = \frac{\bar{X} - \bar{X}}{\bar{C}} \quad (8.1)$$

The location of the CG can be controlled by the sweep and the weight distribution inside the wing (location of fuel cells, propulsion systems, payload ...etc.).

2. The slope of the pitching moment coefficient about the centre of gravity versus the lift coefficient must be negative:

$$\frac{\partial C_M}{\partial C_L} < 0 \quad (8.2)$$

3. The zero-lift pitching moment coefficient ($C_{M_{L=0}}$) about the centre of gravity must be positive:

$$C_{M_{L=0}} > 0 \quad (8.3)$$

In the following sections, the location of the aerodynamic centre and the centre of gravity are discussed in addition to presenting the trim condition analysis.

8.2.2.1 Centre of Gravity

The location of the centre of gravity (CG) of aircraft is important when calculating the aerodynamics moments about all three axes. In addition, the CG is used as a reference point to calculate the mass moments of inertia needed to conduct stability analyses.

Therefore, it is necessary to have a reasonably accurate CG location to obtain design optimisation results.

The CG has \bar{X} , \bar{Y} and \bar{Z} coordinates whose origin is located at the front of the nose. At this point, the location and weight of all aircraft elements are known and the weight distribution about the xz plane is assumed to be symmetrical. Therefore, the mass moment about the y-coordinate will be zero. The moment arms of each aircraft element, denoted by X_i and Z_i , can be calculated regarding to the distance between the mass centre of element and the origin. Therefore, \bar{X} and \bar{Z} coordinates of the CG can be found by:

$$\begin{aligned}\bar{X} &= \frac{\sum_{i=1}^n m_i X_i}{\sum_{i=1}^n m_i} \\ \bar{Z} &= \frac{\sum_{i=1}^n m_i Z_i}{\sum_{i=1}^n m_i}\end{aligned}\tag{8.4}$$

where m_i is the element mass, n is the total number of aircraft elements, X_i and Z_i are the moment arms of each element regarding to the x and y axes respectively.

During the optimisation, the centre of gravity will be calculated for the unloaded wing shape and will not be influenced by the elastic deformations.

8.2.2.2 Aerodynamic Centre

The location of the aerodynamic centre can be obtained using the thin aerofoil theory which implies that the aerodynamic centre of each wing section along the spanwise direction is located at local quarter chord point. This means that the quarter chord point of the geometric mean chord coincides with the quarter chord point of the aerodynamic mean chord. The geometric mean chord is usually used as a reference length of calculating the non-dimensional moment coefficients. As indicated in ESDU-76003, for a straight-tapered wing (no crank), the geometric mean chord C_{av} and its quarter chord location \bar{X} can be found by (ESDU76003, 2012):

$$C_{av} = C_r \frac{1 + TR}{2}\tag{8.5}$$

$$\bar{X} = C_r \left(\frac{1 + 2TR}{12} AR \tan \Lambda + \frac{1}{4} \right)\tag{8.6}$$

where C_r is the root chord, TR is the wing taper ratio, AR is the wing aspect ratio, Λ is the sweep angle of the quarter chord axis.

8.2.2.3 Trim Condition

The aircraft can be in a trim condition when the summation of the forces and moments is zero. This means, at the cruise condition, the weight of the aircraft must equal the lift while the drag equals the thrust with zero pitching moment about the centre of gravity.

During the optimisation, which is an iterative search process, it is important to find the trim condition as well as the derivative of the lift-pitching moment curve at reduced computational cost. Therefore, a mathematical technique was suggested to find the angle of attack at which the trim condition is achieved. Since the aircraft structure is flexible, the pitching moment and lift coefficient might be nonlinearly varied with the angle of attack. Therefore, the relationship of each curve of $[C_L - \alpha]$ and $[C_M - C_L]$ will be represented by a second-degree polynomial equation as in the following equations:

$$C_L = \beta_1 \alpha^2 + \beta_2 \alpha + \beta_3 \quad (8.7)$$

$$C_M = \gamma_1 C_L^2 + \gamma_2 C_L + \gamma_3 \quad (8.8)$$

where β_i and γ_i are constants.

Three points are required to determine the constants of each polynomial equation. Here, the aerodynamic parameters at three different angles of attack will be used, as illustrated in Figure 8-7.

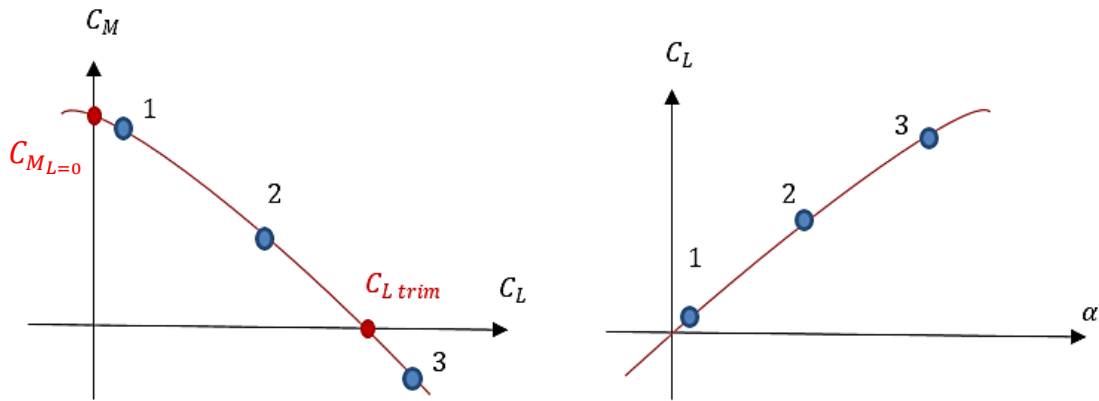


Figure 8-7 Representations of aerodynamic parameters

Once the constants are calculated, the zero-lift pitching moment C_{M_0} , the lift coefficient at the trim condition $C_{L_{trim}}$ and its corresponding $[C_M - C_L]$ slope and angle of attack α_{trim} can be found from the following equations:

$$C_{L_{trim}} = \max \left(\frac{-\gamma_2 \pm \sqrt{\gamma_2^2 - 4\gamma_1 \gamma_3}}{2\gamma_1} \right) \quad (8.9)$$

$$C_{M_{L=0}} = \gamma_3$$

$$\frac{\partial C_M}{\partial C_L}_{trim} = 2\gamma_1 C_{Ltrim} + \gamma_2$$

$$\alpha_{trim} = \max \left(\frac{-\beta_2 \pm \sqrt{\beta_2^2 - 4\beta_1(\beta_3 - C_{Ltrim})}}{2\beta_1} \right)$$

8.2.3 Optimisation Tool

A design optimisation framework was developed within a MATLAB environment combining the quasi-3D aerodynamic model and the composite structure model. The built-in Interior Point Algorithm (IPA) in the MATLAB environment was used in the optimiser code. The IPA is a derivative-based algorithm which uses a polynomial time programming procedure and an interior point method. In this method, the values of the upper and lower bounds of the design variables can be defined whilst the stopping criterion can be set to either reach a maximum number of iterations or achieve a minimum tolerance of the objective function or the value of the variable.

Figure 3-5 shows an overview of the communication shape among the disciplinary models of the optimisation tool in which, for each iteration, three main steps are conducted:

- 1. Evaluate the critical aerodynamic loads and size the spar.**

An angle of attack was chosen to evaluate the aerodynamic loads at the cruise condition for sizing purposes. The design cases performed prior this study indicated that the trim condition will occur at an angle of attack of around 7 or 8 degrees. Therefore, 8 degrees angle of attack was selected to evaluate the aerodynamic loads that will be used for sizing of structural elements. The calculated aerodynamic loads will be multiplied by a factor to equalise the lift force with the aircraft weight. Then, the aerodynamic load will be multiplied by a global load factor to evaluate the critical aerodynamic load. Subsequently, using the composite structure model, the spar will be sized. In this step, only one flow solution is needed while the sizing process will be repeated to employ the inertial relief of the spar weight until a solution that converges is achieved. The effects of static aeroelasticity are ignored at this stage.

- 2. Find the trim condition and its corresponding angle of attack**

As indicated in the section 8.2.2.3, the aerodynamic performance parameters will be calculated at three angles of attack: 1, 6 and 9 degrees. At each angle of attack, the coupling of the aerodynamic and the structural influences will be considered until achieving a solution which converges for elastic deformations. Then, the

aerodynamic parameters at the three angles of attack will be used to calculate the angle of attack corresponding to the trim condition assuming that the curves $[C_L \text{ versus } \alpha]$ and $[C_M \text{ versus } C_L]$ are represented as polynomial equations. Moreover, the static longitudinal stability parameters $\frac{\partial C_M}{\partial C_L}$ and $C_{M_{L=0}}$ are then found. A number of flow solutions and structural analyses are required for each angle of attack.

3. Evaluate the aerodynamic performance parameters at the trim condition

The aerodynamic performance parameters of the flight shape at the trim condition are then calculated using the trimmed angle of attack (α_{trim}) obtained from the previous procedure.

The concept of the optimisation problem is to achieve the best possible result within the design space variables. Here, the design variables are the manufactured twist distribution (Tw_i) as will be discussed next section. The objective of the optimisation is to achieve the minimum drag coefficient of the aircraft at the flight condition. It is necessary to enable the objective function to drive the optimisation process to achieve trim condition at the reference lift coefficient (C_{Lref}) of 0.8 whilst maintaining the drag coefficient at the minimum value. Therefore, the objective function was modified to minimise the trimmed drag coefficient ($C_{D trim}$) in addition to reducing the difference between the achieved trimmed lift coefficient ($C_{L trim}$) and the reference lift coefficient (C_{Lref}). The optimisation problem can be formulated as:

Objective:

$$\text{minimise } (|C_{Lref} - C_{L trim}| + C_{D trim})$$

Subject to:

$$C_{M trim} = 0$$

$$\frac{\partial C_M}{\partial C_L} < 0$$

$$C_{M_{L=0}} > 0$$

Design variables:

$$Tw_1, Tw_2, Tw_3 \dots \dots \dots Tw_{14}$$

where Tw_i are the manufactured twist distribution (as will be described next section)

$$1^\circ > Tw_i > -5^\circ$$

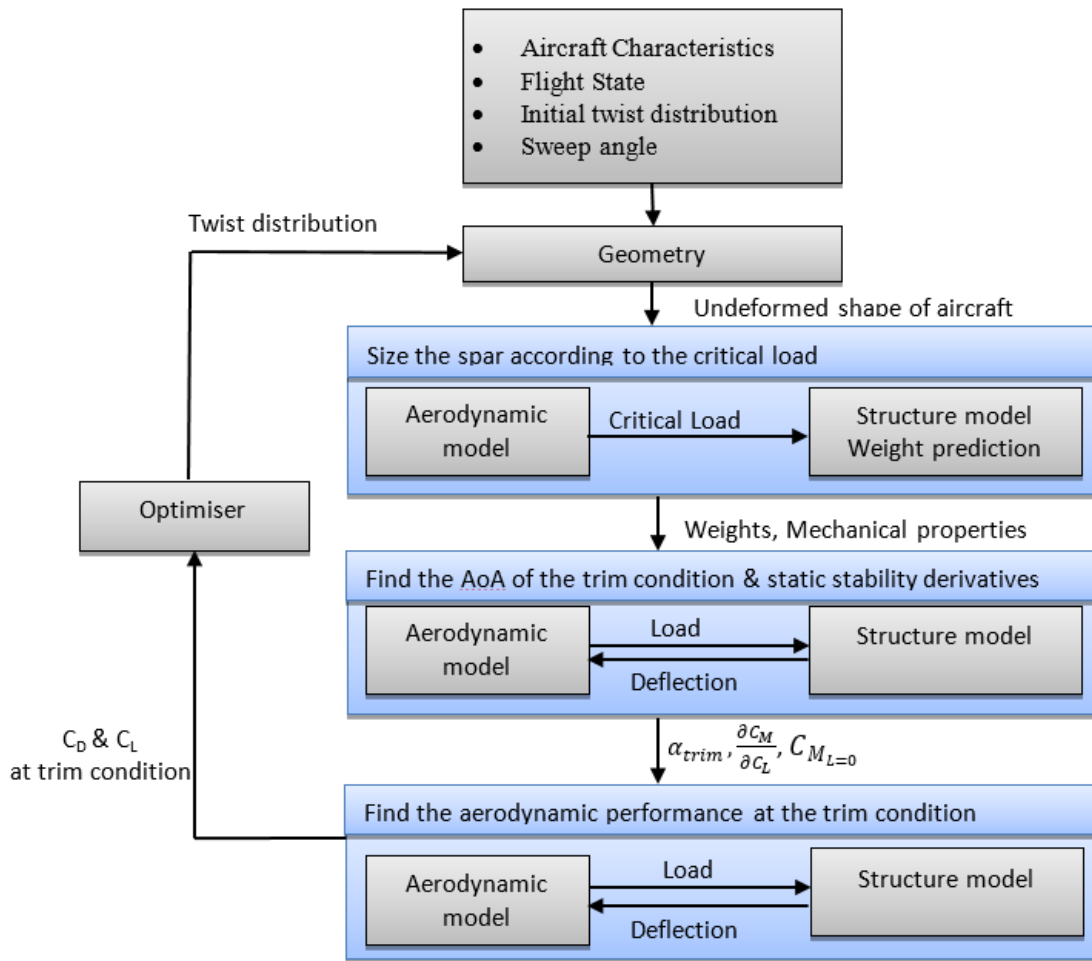


Figure 8-8 Optimisation flow

8.2.3.1 Design Variables-Twist Distribution

In this research, during the optimisation process, only the manufactured twist distribution parameters will be the design variables. The reason for optimising the twist is to achieve the static stability requirement in addition to increasing the aerodynamic efficiency of the wing at the trim condition. Therefore, it is necessary to suggest indicative points at which the twist will be set. Between each two points, the twist distribution is linearly interpolated. Also, this process must be applicable when defining the geometry to the aerodynamic solver. In Tornado VLM, the wing can be discretised into partitions; each partition has a dihedral angle in addition to two twist angles for the inner and the outer edges.

Here the wing is discretised into 28 partitions, 14 in each semi-span. The twist angle of an outboard edge of a partition will be the inboard twist angle of its neighbouring partition. The root section will not be employed in the manufactured twisting since the aircraft angle

of attack will be based on the root section. Therefore, only 14 twist angles are required to define the manufactured twist distribution for the semi-wing. The twist of the panels within each partition will be linearly twisted according to the inboard and the outboard twist angles as shown in Figure 6-15.

It is worth mentioning that when the wing is elastically deformed, its geometry gets modified until a quasi-static equilibrium is achieved as indicated in the structural model. So, the twist distribution, represented by the manufactured twist, will be amended as a result of static aeroelastic moments and forces assuming that the elastic twist within each partition will be linear. Therefore, there are three twist angles values which must be determined for each inboard and outboard edge of the panels within the wing:

1. The manufactured twist angles (Tw_i): the twist angles of the wing at off-load condition. These values will be the design variables during the optimisation.
2. Elastic twist angles: the resulted twist due the elastic deformations under the aerodynamic loads respect to the flow direction. They are calculated using finite beam element.
3. Total twist: the summation of the manufactured twist and the elastic twist. These values represent the effective twist of the wing at the flight condition.

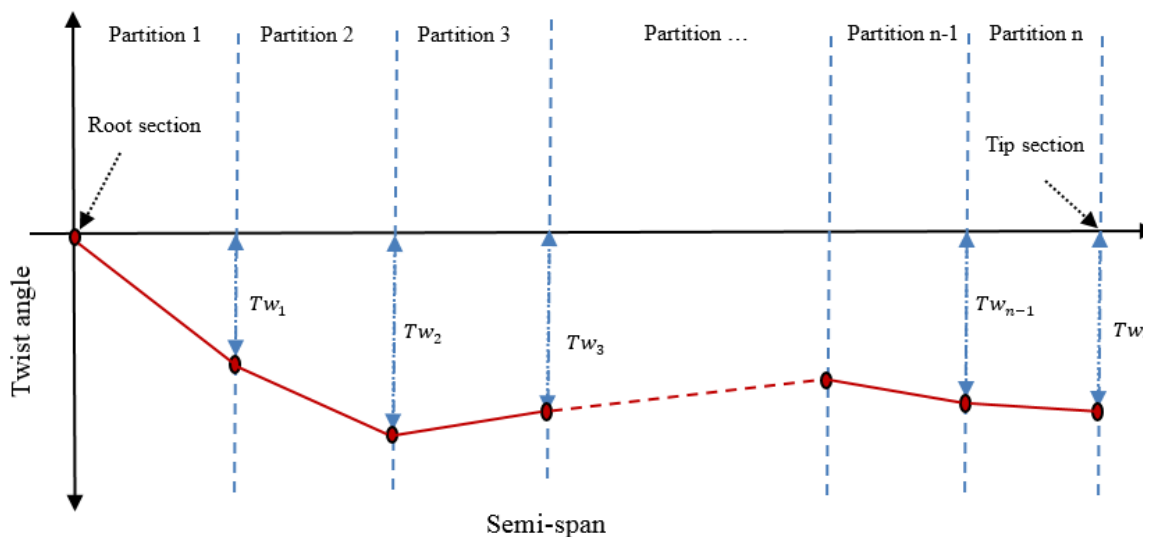


Figure 8-9 Manufactured twist distribution pattern

8.2.3.2 Panel Density and Number of Strips

In Tornado vortex lattice method, the wing is modelled as a lifting surface following the camber lines of the wing sections. The lifting surface is divided into a number of panels (horseshoe vortices) in the chordwise and spanwise directions. The number of these panels in both the directions has a significant effect on the accuracy of the results. However, increasing the number of panels is accompanied with a significant increase in the computational time and the memory usage. An initial wing geometry with 8 degree sweep and 8 degree angle of attack is selected to find a practical number of panels in the chordwise and spanwise directions needed for reasonable accuracy. Figure 8-10 shows the effect of the number of panels on the aerodynamic coefficients; lift, induced drag and pitching moment. The figure indicates that the lift coefficients are highly affected by the number of panels in the semi-spanwise direction whilst the pitching moment and drag coefficients are clearly influenced by the number of panels in both directions. However, a grid size will be selected to be 42 panels in the semi-spanwise direction and 15 panels in the chordwise direction indicated by the arrow. This selection yields a deviation of the lift coefficient by about 0.4%, on the induced drag coefficient by about 0.2% and on the pitching moment coefficient by about 7.5 % with respect to the convergence point (100 panels in the semi-spanwise direction and 25 panels in the chordwise direction).

For the strip method, 42 strips are selected and placed in a way similar to the distribution of the panels in the spanwise direction in order to prevent several coding steps to interpolate the aerodynamic forces on each strip.

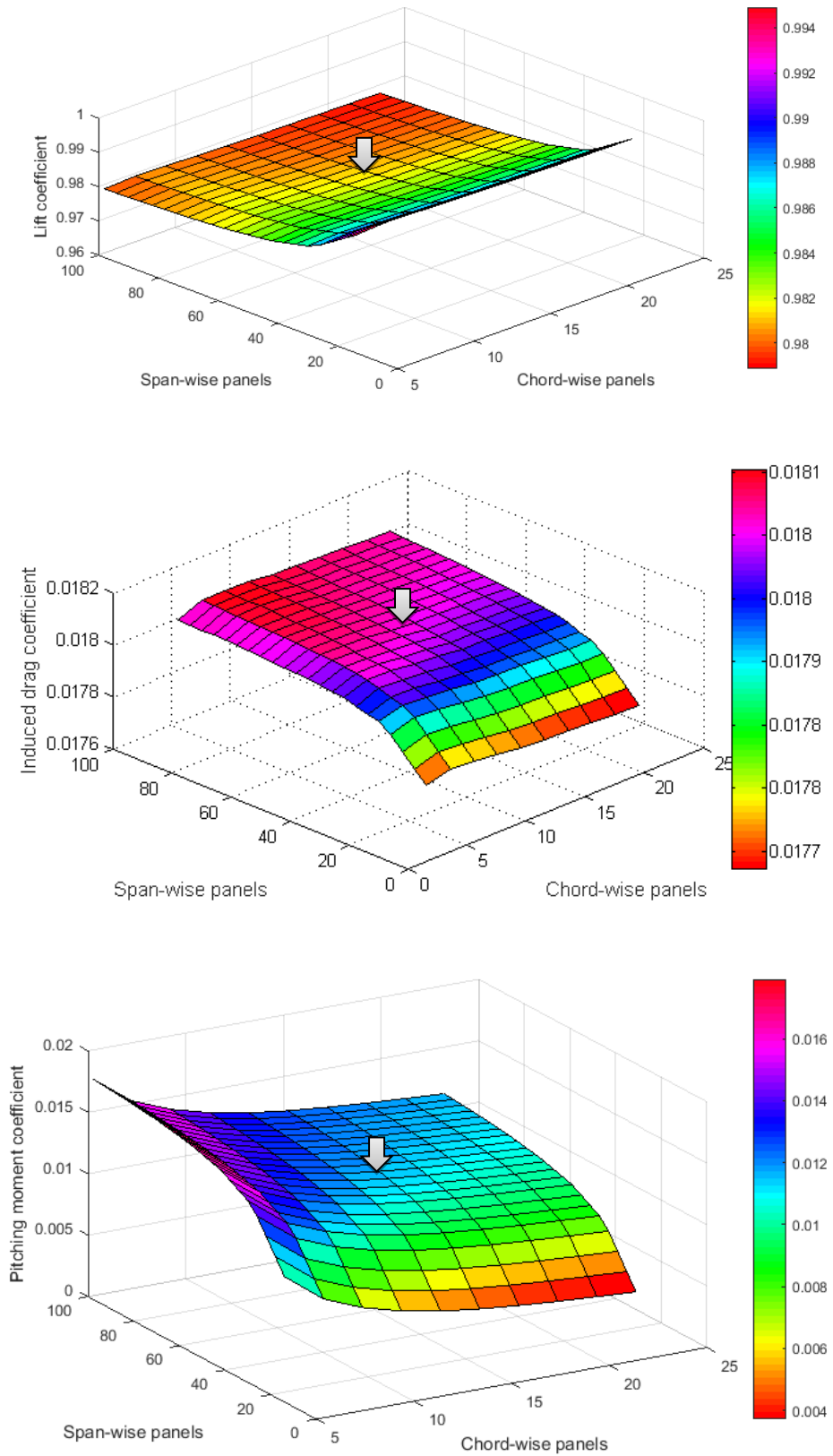


Figure 8-10 Effect of number of spanwise and chordwise panels on the coefficients of lift, induced drag and pitching moment about the $0.25x/c$ root axis

8.2.4 Required Sweep

As mentioned in the prior section, the centre of gravity and the aerodynamic centre can be influenced by sweeping the wing. In this study, the demand of sweeping the wing is to achieve a specific static margin (Sm) required to satisfy one of the stability criterions. The amount of sweep must incorporate an appropriate twist distribution to achieve a statically stable aircraft which is capable of trimming at a specific lift coefficient. So, the two questions that arise are:

1. How much sweep is required to achieve a certain static margin?
2. Is that calculated sweep adequate to trim the aircraft at the reference lift coefficient?

To answer the above questions, it is necessary to define a feasible value for the static margin in addition to specifying the limit for the wash-out twist angles. In general, tailless aircraft has a small static margin (Blot, 1945; Nickel & Wohlfahrt, 1994). Accordingly, 0.05 will be used as a reference value for the static margin. The aerodynamic performance study of the aerofoil ZMR-17 indicates that the aerofoil will be at negative stall when the angle of attack drops below -5 degrees (see Chapter 7). Therefore, at this design point, to prevent tip stall at lower angles of attack, the maximum and minimum manufactured twist will be between +1 and -5 degrees.

8.2.4.1 Minimum Required Sweep to Achieve 0.05 Static Margin

The weight distribution of the aircraft elements influences the location of centre of gravity (CG) and thus the static margin. If the sweep angle was small, the weight distribution along the span-wise direction could slightly influence the CG while the distribution along the chord-wise direction will also have a considerable effect. The payload location along root-chordwise direction can play a significant role in adjusting the location of the CG. One can assume that the ultimate location of the payload can be between 0 to 0.5 x/c of the root chord. Accordingly, it is expected that the minimum required sweep can be found when the payload is placed at the aircraft nose at 0 x/c of the root chord.

The minimum required sweep angle can be calculated using an iterative scenario such as in the following steps:

- 1- Assume the payload is placed at the aircraft nose
- 2- Assume an initial twist distribution for the wing
- 3- Assume an initial sweep angle for the wing
- 4- Size the wing and find the centre of gravity.
- 5- Calculate the static margin

- 6- Check whether the static margin is equal to 0.05; if not, increase the sweep angle and repeat the above steps from 4.

This scenario has been conducted and the results show that the wing needs at least 5 degrees of sweep to achieve a static margin of about 0.05.

8.2.4.2 Minimum Required Sweep to Trim the Aircraft at 0.8 Lift Coefficient

The first attempt to optimise failed because five degrees sweep and the wash-out twist distribution limit of +1 to -5 degrees were not enough to trim the aircraft at 0.8 lift coefficient. Hence, the sweep angle had to exceed five degrees. In this step, the static margin will be assumed to be constant and can be used to locate the centre of gravity in relation to the aerodynamic centre. Then the sweep can be obtained to find the maximum trimmed lift coefficient using the optimisation tool. This can be achieved as following:

- 1- Suggest an initial sweep (more than 5 degrees)
- 2- Calculate the centre of gravity using the aerodynamic centre and the assumed static margin (0.05)
- 3- Use the optimisation tool to maximise the trimmed lift coefficient until achieving a value more than 0.8 ($C_{L Ref}$) regardless of the drag coefficient. Here, the optimisation problem can be formulated as:

Objective :

$$\text{maximise } (C_{L trim})$$

Subject to :

$$C_{M trim} = 0, \quad \frac{\partial C_M}{\partial C_L} < 0$$

Design variables :

$$Tw_1, Tw_2, Tw_3 \dots \dots \dots Tw_{14}, \text{ where: } 1^\circ > Tw_i > -5^\circ$$

- 4- If the optimisation process got terminated without reaching the target, increase the sweep angle and repeat the above steps from 2.

The results show that the minimum required sweep to trim the aircraft at 0.8 lift coefficient is about 6.5 degrees. The optimisation was conducted to maximise the lift coefficient at the trim condition regardless other factors such as the drag coefficient.

8.3 The Design Cases

The minimum required sweep to achieve the stability requirements at the reference lift coefficient was investigated in the previous section. In order to get some freedom of twisting the wing to achieve minimum drag for the subsequent optimisation process, the minimum sweep will be considered as 7 degrees. Several design cases will be introduced to study the influence of the sweep angle, the static margin and the spar location on the aircraft characteristics such as the aerodynamic performance, the longitudinal static stability, the gross weight and the elastic deformations. The study was performed in two stages for two sets of cases. The first set was analysed considering aerodynamic effects only with the elastic deformation disregarded; these were abbreviated as ‘‘AerO’’ series. Static aeroelastic effects were included in the second set; these were abbreviated as ‘‘AerEl’’ series. In each design case, the optimisation tool was applied to find the optimal twist distribution (manufactured twist distribution) for minimum drag at the trim condition at 0.8 lift coefficient.

❖ Aerodynamic-Only Cases (AerO series)

Five design cases at different sweep angles and static margin values were designed when the elastic deformations of the wing were neglected. The name of each case is designated by the group name followed by the sweep angle and the static margin as listed in Table 8-3.

For example, AerO 07-05 represents

$$\begin{array}{ccc} \text{AerO} & & \text{07} \quad - \quad \text{05} \\ \textit{The case is resulted when the elastic} & & \textit{Sweep angle=7} \quad \textit{Static margin} \\ \textit{deformation is neglected} & & \textit{Sm=0.05} \end{array}$$

Table 8-3 Design cases when only aerodynamic performance factors are considered

Cases	Sweep [deg.]	Static Margin
AerO 07-05	7	0.05
AerO 09-05	9	0.05
AerO 11-05	11	0.05
AerO 09-08	9	0.08
AerO 09-02	9	0.02

For these design cases, the optimisation tool is the same as that described in Figure 8-8 except that the weight estimation and structural analyses were not accounted as indicated in Figure 8-11.

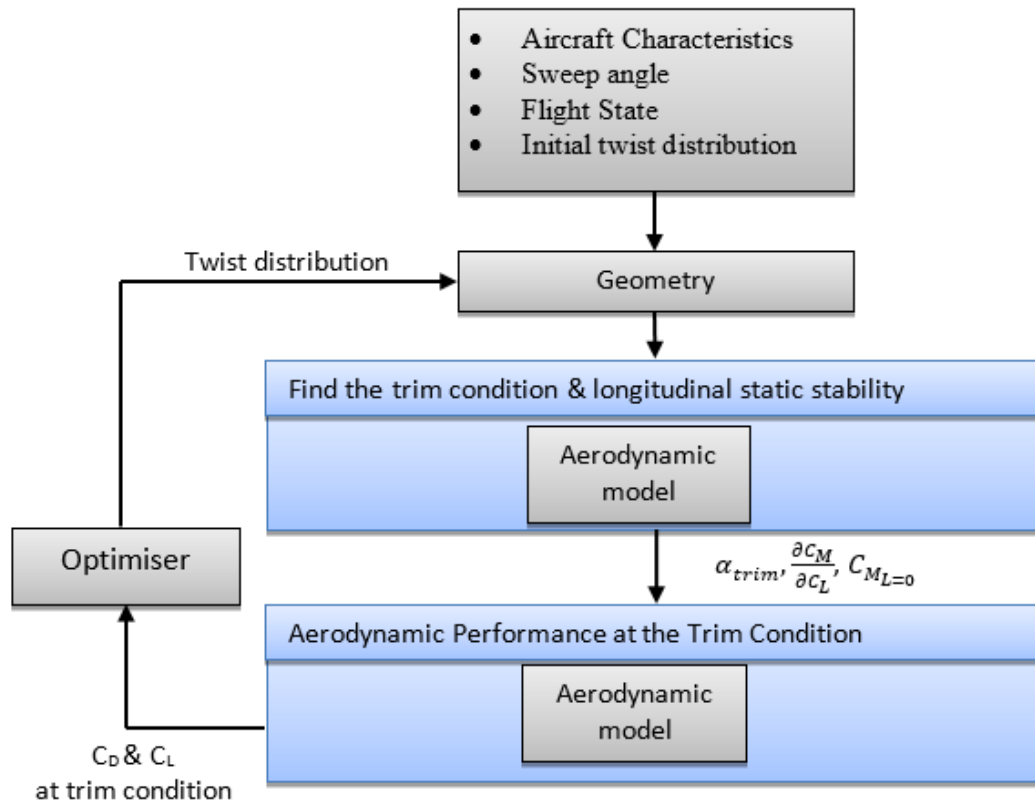


Figure 8-11 Optimisation flow for the AerO cases

❖ Static Aeroelasticity Cases (AerEl series)

A number of cases including static aeroelastic effects was considered. In these cases, the influence of the spar location in addition to the static margin and the sweep angle were studied. The name of each case was represented by the group name followed by the sweep angle, the static margin value and the location of the spar as listed in Table 8-4.

For instance, AerEl 09-08-25 represents

AerEl
The case is resulted when the elastic deformation is considered
09
Sweep angle=9
—
05
Static margin Sm=0.05
—
25
The spar location coincide with the quarter chord axis (X_{spar}=25%x/c)

Table 8-4 Design cases when aeroelastic effects are considered

Cases	Sweep [deg.]	Static Margin	Spar Location
AerEl 09-05-25	9	0.05	0.25 x/c
AerEl 09-05-30	9	0.05	0.30 x/c
AerEl 09-05-35	9	0.05	0.35 x/c
AerEl 09-05-40	9	0.05	0.40 x/c
AerEl 09-02-35	9	0.02	0.35 x/c
AerEl 09-08-35	9	0.08	0.35 x/c
AerEl 07-05-35	7	0.05	0.35 x/c
AerEl 11-05-35	11	0.05	0.35 x/c

8.3.1 Optimisation Results – Aerodynamic Only (AerO series)

8.3.1.1 Sweep Influence

Three different optimisations cases were examined in which the influences of the elastic deformations were ignored. The only difference between these cases is the sweep angle of the wing. The static margin was set at 0.05 by assigning the centre of gravity correspond to the theoretical aerodynamic centre. In each design case, the optimisation tool was set to find the optimal manufactured twist distribution to achieve minimum drag coefficient at the trim condition. The final manufactured twist distribution in addition to the aerodynamic performance of each resulting case are presented in Figure 8-12. It is apparent from the results that all the design cases ended up with statically stable aircraft capable of being trimmed at a lift coefficient of 0.8. As expected, the required washout twist reduces with increasing sweep angle. It seems that the requirement to trim the aircraft at 0.8 lift coefficient has driven the optimisation process to twist the wing in the spanwise direction in a way which slightly shifted the location of the aerodynamic centre and hence the degree of stability (the static margin is represented by $-\frac{\partial C_M}{\partial C_L}$) as shown in Table 8-5. However, the aircraft with less sweep demonstrated greater longitudinal static stability due to the static margin being assumed constant regardless of the sweep. Table 8-5 tabulates the aerodynamic performance parameters at the trim condition. The results indicate that, within the range of the sweep angles, there is a slight overall increase in the total drag coefficient as the sweep increases. The difference in the washout twist distribution slightly reduces the trimmed angle of attack (α_{trim}).

Table 8-5 Aerodynamic performance at trim condition for varying wing sweep angles for AerO cases

Cases	Sweep [deg.]	Aerodynamic performance at trim condition ($C_L = 0.8$)					α_{trim} [deg.]	$C_{M_{L=0}}$
		$C_{D_{prof}}$	$C_{D_{in}}$	C_D	$\frac{C_L}{C_D}$	$\frac{\partial C_M}{\partial C_L}$		
AerO 07-05	7	0.00823	0.01063	0.01886	42.395	-0.0317	8.172	0.0200
AerO 09-05	9	0.00842	0.01073	0.01915	41.782	-0.0250	8.156	0.0142
AerO 11-05	11	0.00806	0.0111	0.01916	41.746	-0.0178	7.923	0.0081

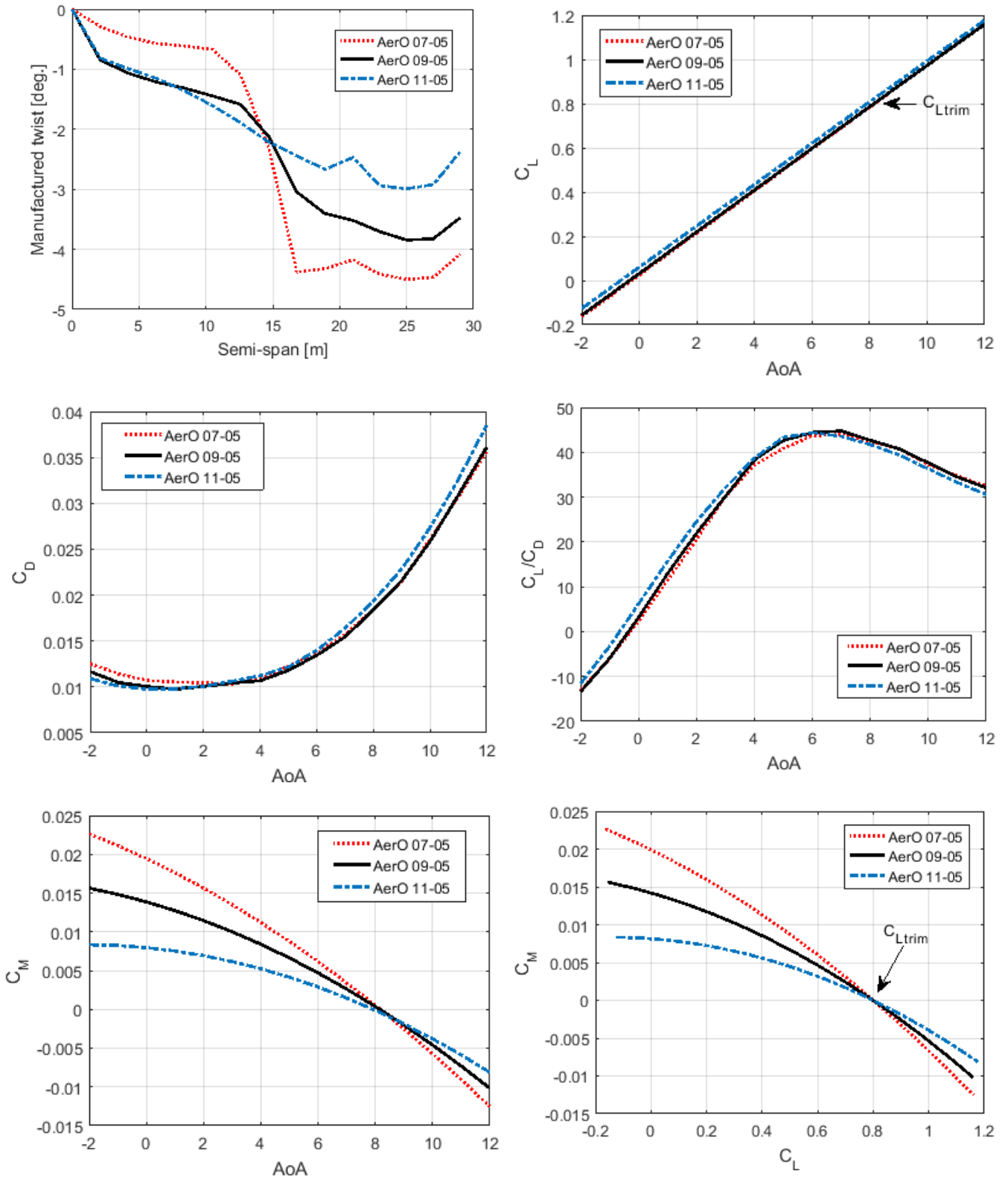


Figure 8-12 Optimal manufactured twist distribution and aerodynamic performance parameters for the cases AerO at varying wing sweep angles: static margin=0.05

8.3.1.2 Static Margin influence

The influence of the static margin was investigated for the nine degree sweep angle cases. Three different values for the static margin were considered; 0.02, 0.05 and 0.08 based on specifying the centre of gravity with respect to the theoretical aerodynamic centre. The optimisation process for the case AerO 09-02 with 0.02 static margin failed to achieve 0.8 lift coefficient at the trim condition because the sweep was too high. The results of the other cases (AerO 09-05 and AerO 09-08) indicate that the longitudinal static stability improved with increasing static margin as indicated in Figure 8-13 (C_L - C_M graph). However, the required twist is considerably increased with higher longitudinal stability. This in turn slightly influenced the aerodynamic performance at the trim condition as shown in Table 8-6.

Table 8-6 Aerodynamic performance at trim condition for varying static margin for AerO cases

Cases	Static Margin	Aerodynamic performance at trim condition ($C_L = 0.8$)					α_{trim} [deg.]	$C_{M_{L=0}}$
		$C_{D_{prof}}$	$C_{D_{in}}$	C_D	$\frac{C_L}{C_D}$	$\frac{\partial C_M}{\partial C_L}$		
AerO 09-02	0.02	-	-	-	-	-	-	-
AerO 09-05	0.05	0.00842	0.01073	0.01915	41.782	-0.0250	8.1560	0.0142
AerO 09-08	0.08	0.00871	0.01055	0.01927	41.51	-0.0559	8.0542	0.0389

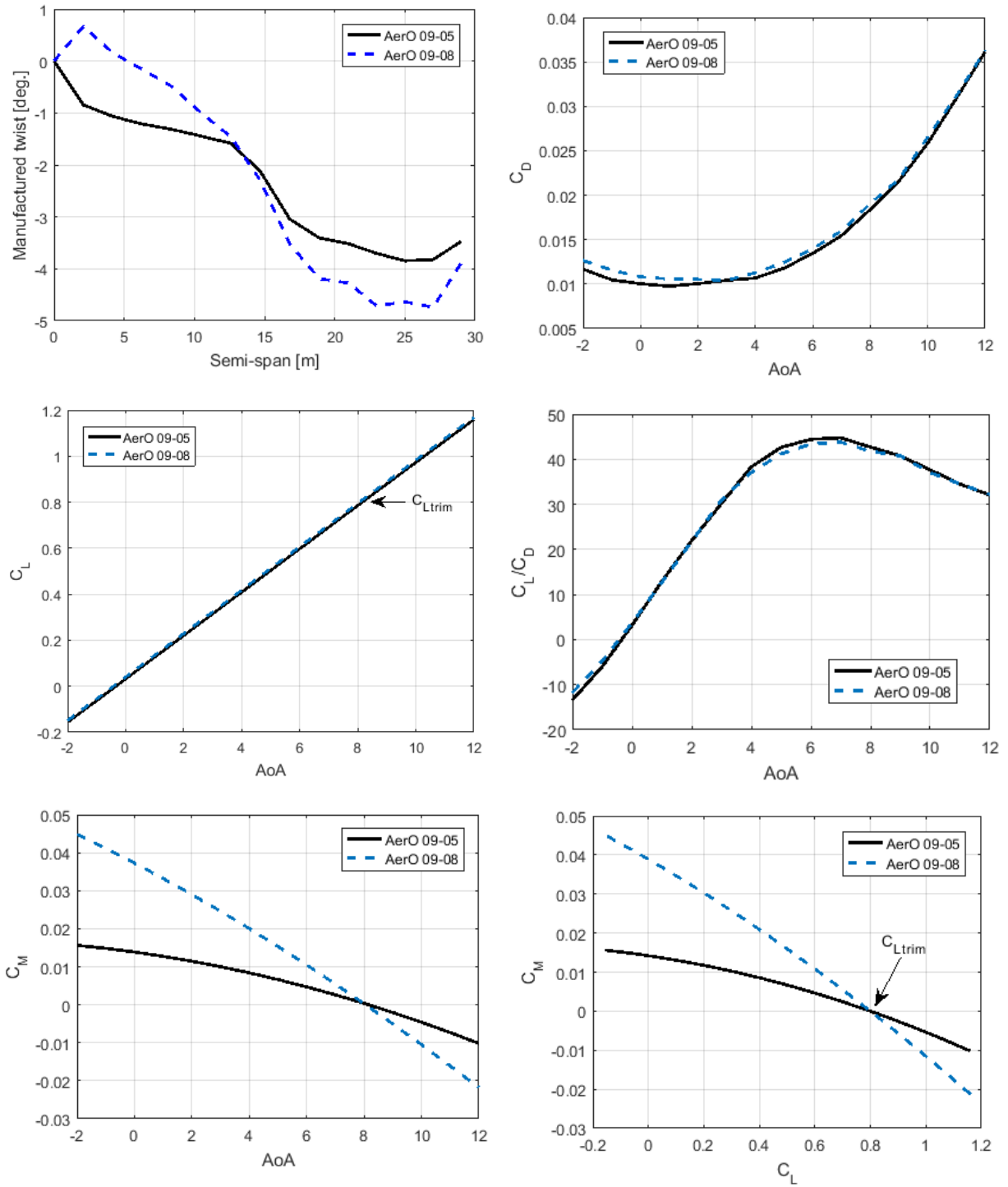


Figure 8-13 Optimal manufactured twist distribution and aerodynamic performance parameters for the cases AerO at varying static margin values: sweep angle=9°

8.3.2 Optimisation results - Static Aeroelasticity (AerEl series)

8.3.2.1 Spar Locus Effects

Four design cases have been introduced with the spar located at $0.25x/c$, $0.30x/c$, $0.35x/c$ and $0.4x/c$. In each case, the optimisation tool was used to select the manufactured twist distribution for achieving minimum drag coefficient at a trimmed lift coefficient of 0.8. Care was taken to ensure that the fuel cells were always placed on the elastic axis of the spar to prevent local twist deformations. Moreover, the payload location was adjusted in every design case to achieve a specific static margin of about 0.05.

The optimisation process was conducted at each design case. The optimal manufactured twist distribution and the aerodynamic performance of the resulting cases are presented in Figure 8-14. The results indicate that the spar location has an enormous impact on the structural behaviour and hence the aerodynamic performance and stability. A significant influence can be seen in the lift slopes and the trimmed angle of attack. All the resulting cases were statically stable at the trim condition at the lift coefficient of 0.8. However, for cases where the spar was located at $0.25x/c$ and $0.3x/c$, the system became unstable at lower angles of attack due to elastic deformations encountered as presented in Figure 8-15 and Figure 8-16.

The elastic twist distribution shown in Figure 8-15 was with respect to the flow direction indicating that this elastic twist was part of the total incidence change due to the local torque, and a part of the bending deflection due to the wing sweep. In order to better understand how the spar location can influence the wing, the essentials of the swept wing theory need to be invoked. For an aft-swept wing, in the case of up-bending load, the incidence angles will be reduced due to the bending of the spar. At the down-bending load, this behaviour will be reversed leading to an increase in the incidence angles. The aerodynamic torques (local pitching moments) about the elastic axis can worsen or reduce the change in the incidence.

For the case AerEl 09-05-25 with $0.25x/c$ spar location, the elastic axis was located in front of the local aerodynamic centre which resulted in negative pitching moments about the elastic axis which tends to reduce the incidence at higher wing loading (higher angle of attack). At lower angles of attack, the negative lift will result in positive pitching moments which tend to increase the incidence angle. This will be more pronounced at the wing tips where the wash-out in the manufactured twist is exploited. It can be concluded that the vertical deflections will work in cooperation with the aerodynamic torque to worsen the

elastic behaviour when the spar was located in front of the local aerodynamic centre. In the second case in which the spar was located at $0.30x/c$, the elastic twist is reduced due to reducing the aerodynamic torsions (pitching moments) about the elastic axis.

In case AerEl 09-05-40 with the spar located at $0.40x/c$, the behaviour of the elastic twist is reversed due to the elastic axis situated behind the local aerodynamic centre. At higher angles of attack, the aerodynamic torques tend to increase the incidence angles while the bending up of the wing tends to reduce it. The behaviour is reversed at the lower angles of attack. However, the local aerodynamic torques are increased which in turn necessitates a stiffer structure leading to increasing structural weight as indicated in Table 8-7. Accordingly, the stiffer structure led to reduced vertical deflection. This case produced the best aerodynamic performance and static stability compared with the other cases but at a heavier structural weight.

In the case AerEl 09-05-35, with the spar located at $0.35x/c$, a compromise solution was reached at which the aerodynamic loads could mitigate the twist due to the bending deformation. This choice led to a reduction in the change of the elastic twist with increasing wing loading. Also, the spar was located adjacent to the line of the maximum thickness of the wing sections. Moreover, the aerodynamic performance of this design looks similar to AerO 09-05, the one which was designed disregarding the elastic deformation.

Table 8-7 Aerodynamic performance at trim condition for varying spar locations for AerEl cases

Cases	Spar Locus x/c	Aerodynamic performance at trim condition ($C_L = 0.8$)					α_{trim} [deg.]	$C_{M_{L=0}}$	Gross Weight [kg]
		$C_{D_{prof}}$	$C_{D_{in}}$	C_D	$\frac{C_L}{C_D}$	$\frac{\partial C_M}{\partial C_L}$			
AerEl 09-05-25	0.25	0.008140	0.010757	0.01889	42.33	-0.0522	7.2626	-0.0001	874.23
AerEl 09-05-30	0.30	0.008132	0.010657	0.01879	42.58	-0.0558	7.1478	0.0076	872.28
AerEl 09-05-35	0.35	0.008115	0.010580	0.01870	42.77	-0.0524	8.1376	0.0158	900.04
AerEl 09-05-40	0.40	0.007816	0.010704	0.01852	43.19	-0.0479	6.4874	0.0204	977.42

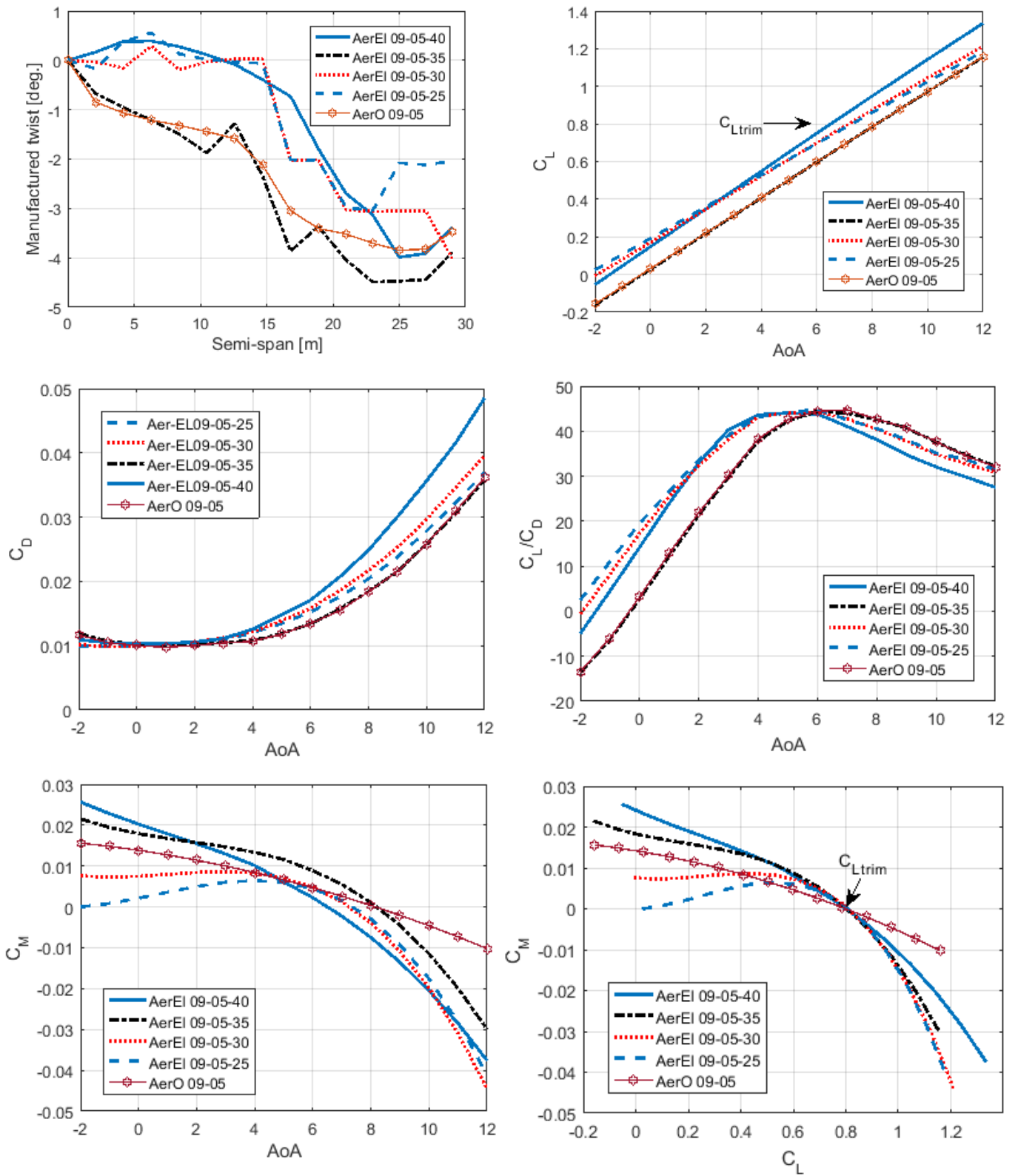


Figure 8-14 Optimal manufactured twist distribution and aerodynamic performance parameters for the cases AerEI at varying spar locations: sweep angle=9°, static margin=0.05

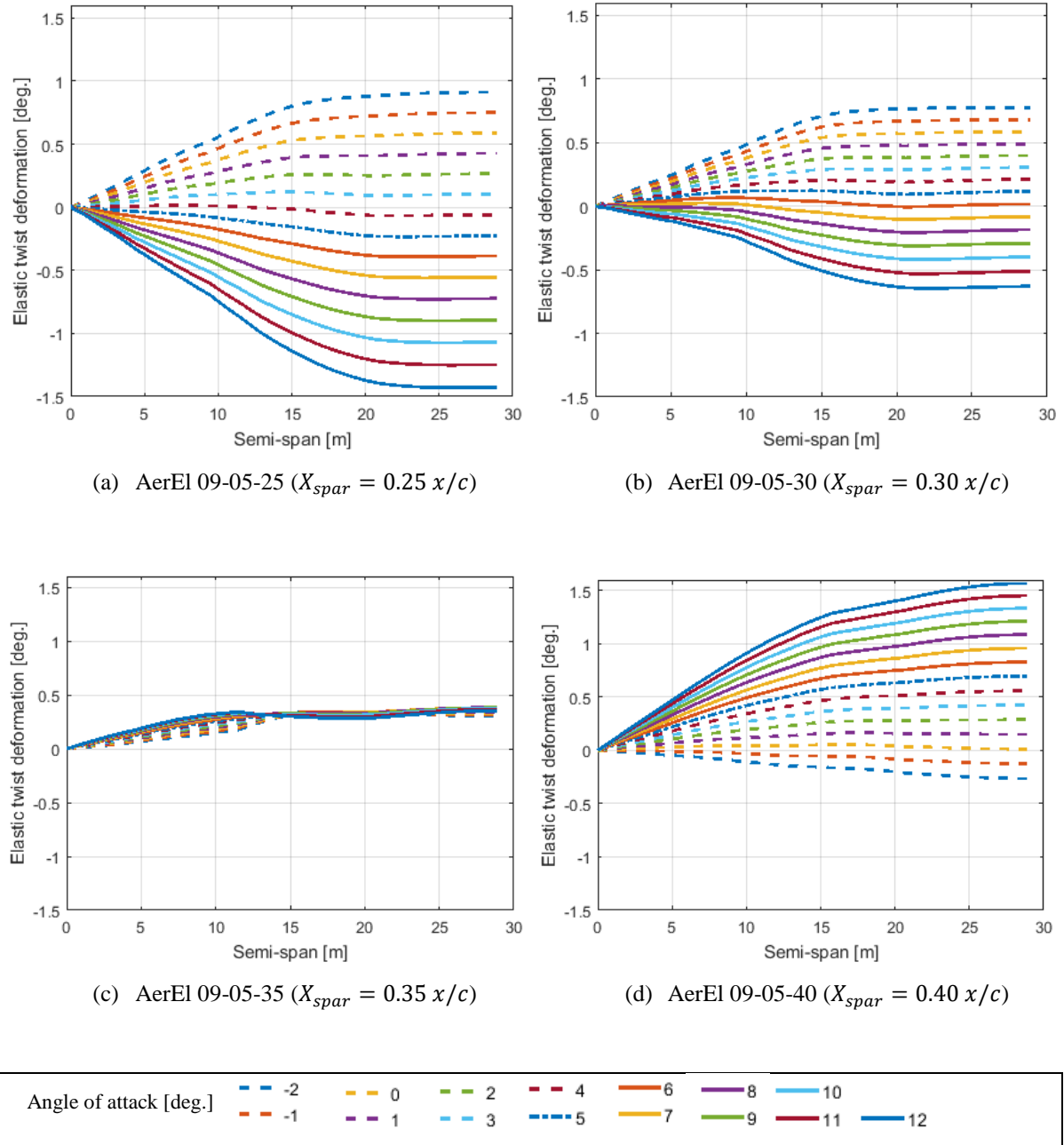


Figure 8-15 Elastic twist deformation, respect to the flow direction, for the cases AerEl at varying spar locations: sweep angle=9°, Static margin=0.05

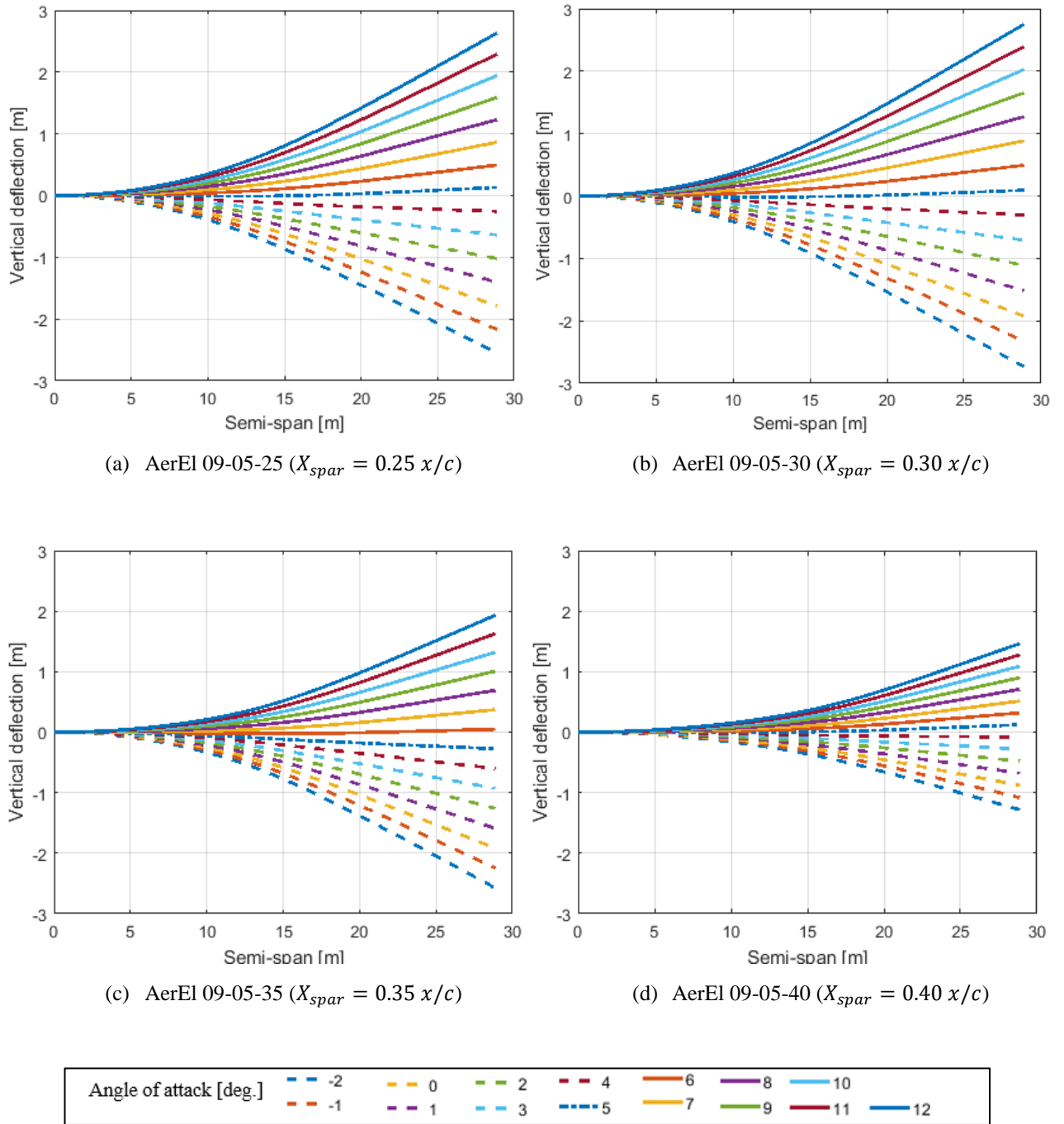


Figure 8-16 Elastic vertical deflections for the cases AerEI at varying spar locations: sweep angle=9°, static margin =0.05

8.3.2.2 Static Margin Influence

The effect of the static margin was investigated here. A wing configuration with a nine degree sweep and the spar located at $0.35x/c$ was considered to design three cases at static margins of 0.02, 0.05 and 0.08. Figure 8-17 shows the optimal manufactured twist distribution and the aerodynamic performance parameters for these cases. In addition, the elastic twist and the vertical deflection for different angles of attack are illustrated in Figure 8-18.

The results indicate that the three cases are statically stable at the trim condition and 0.8 lift coefficient. However, the case AerEl 09-02-35, which has a 0.02 static margin, reveals instability at lower angles of attack. The results of the cases AerEl 09-05-35 and AerEl 09-08-35 demonstrated that a high static margin required more twist to achieve 0.8 trimmed lift coefficient. However, a high twist will lead to reducing the aerodynamic efficiency as indicated for the case of 0.08 static margin in Table 8-8. Moreover, the elastic twist and the vertical deflection for the cases with 0.05 and 0.08 static margin are slightly influenced due to the increased static margin as shown in Figure 8-18.

Table 8-8 Aerodynamic performance at trim condition for varying static margin for AerEl cases

Cases	Static margin	Aerodynamic performance at trim condition ($C_L = 0.8$)					α_{trim} [deg.]	$C_{M_{L=0}}$	Gross Weight [kg]
		$C_{D_{prof}}$	$C_{D_{in}}$	C_D	$\frac{C_L}{C_D}$	$\frac{\partial C_M}{\partial C_L}$			
AerEl 09-02-35	0.02	0.007929	0.01134	0.01927	41.50	-0.0210	7.6283	-0.0091	912.95
AerEl 09-05-35	0.05	0.008115	0.01058	0.01870	42.77	-0.0524	8.1376	0.0158	900.04
AerEl 09-08-35	0.08	0.008460	0.01062	0.01907	41.93	-0.0828	7.8498	0.0381	898.09

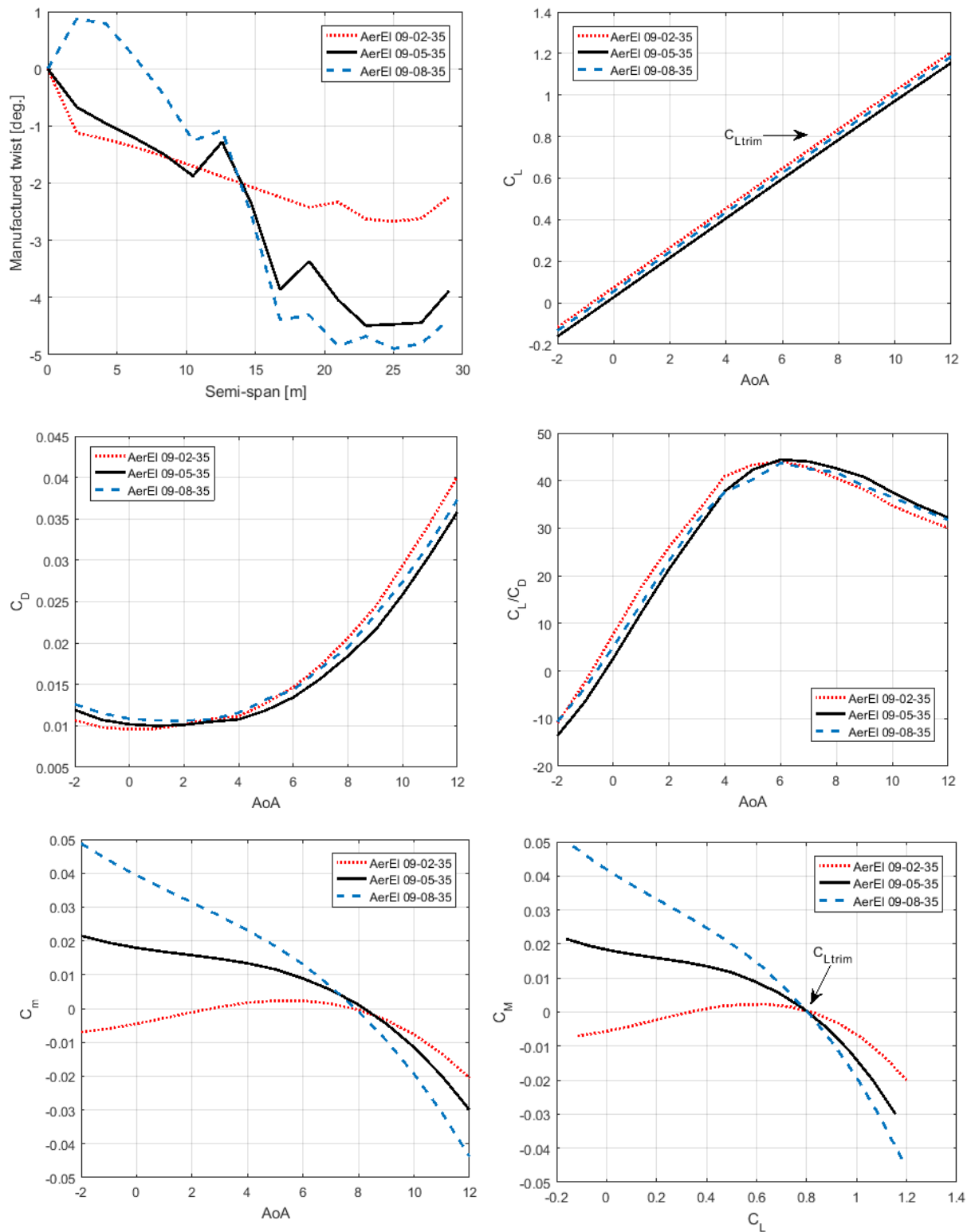
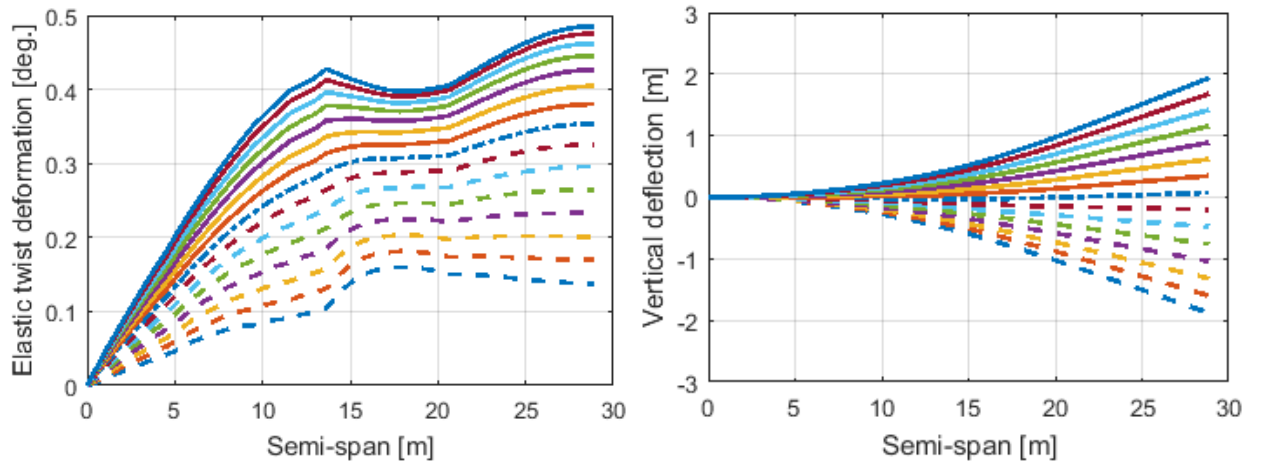
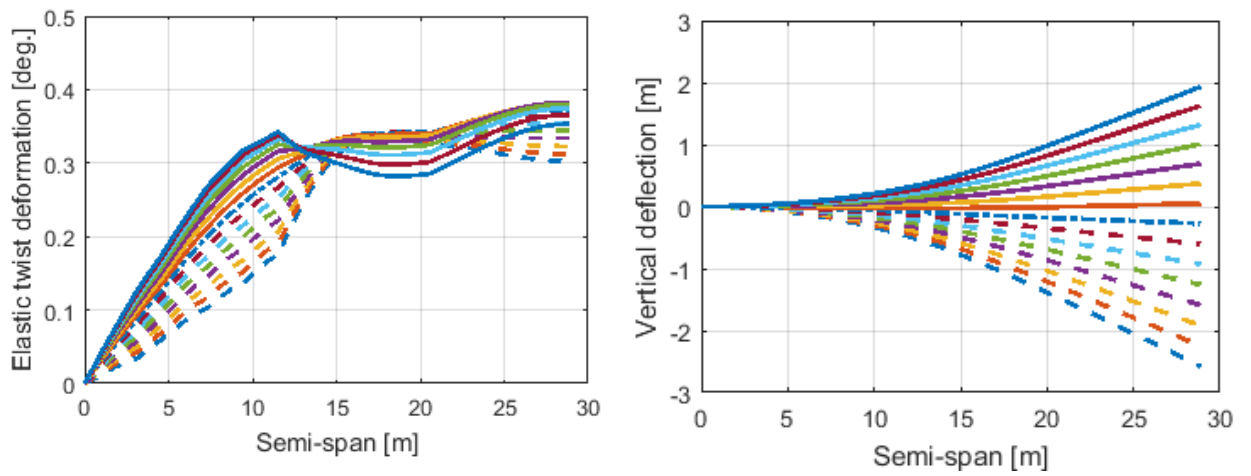


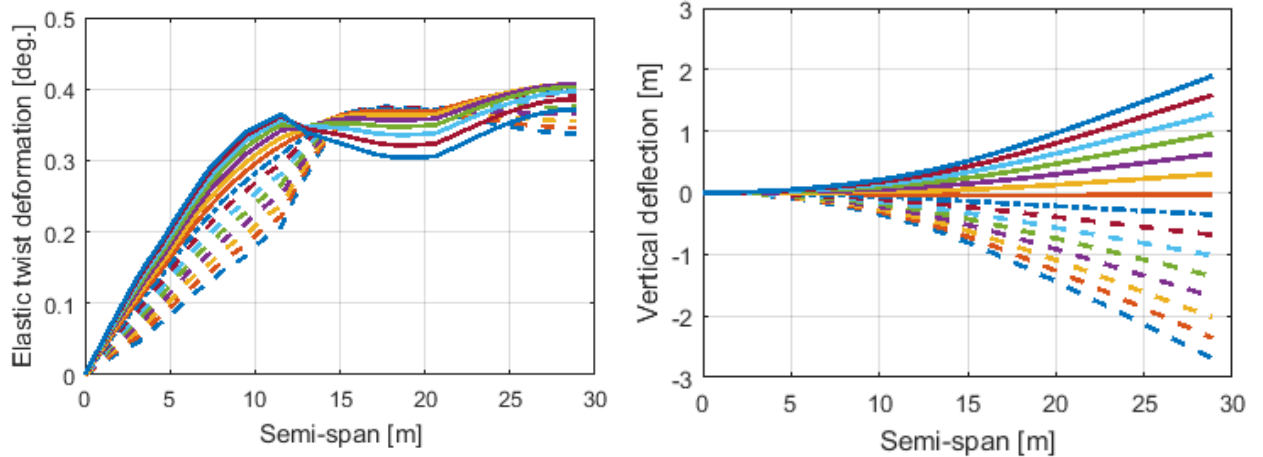
Figure 8-17 Optimal manufactured twist distribution and aerodynamic performance parameters for the cases AerEI at varying static margin values: sweep angle=9°, spar locus= 0.35 x/c



(a) AerEl 09-02-35 ($Sm = 0.02$)



(b) AerEl 09-05-35 ($Sm = 0.05$)



(c) AerEl 09-08-35 ($Sm = 0.08$)

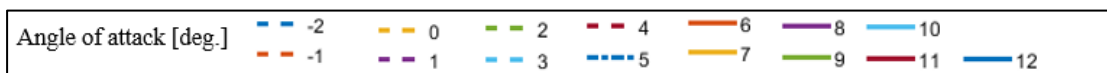


Figure 8-18 Elastic deformations, respect to the flow direction, for the cases AerEl at varying static margin study:

sweep angle=9°, spar locus =35% x/c

8.3.2.3 Sweep Influence

The influence of the sweep angle on the design was investigated here. A wing configuration with 0.35x/c spar location and 0.05 static margin was considered to design three cases at sweep angles of 7, 9 and 11 degrees. The final manufactured twist distribution in addition to the aerodynamic performance of each resulting case are presented in Figure 8-19. In general, the influence of the sweep angle is similar to that studied without the aeroelastic considerations as discussed in section 8.3.1.1. The results indicate that the need for the required washout twist is raised at lower sweep angles. In addition, at lower angles of attack, the static stability is reduced with increasing the sweep angle whilst keeping the static margin constant. The gross weight shows a slight sensitivity at increased sweep within the study range. The elastic twist respect to the flow direction showed an increase in the case AerEl 07-05-35 (7-degree sweep) while the behaviour is reversed in the case AerEl 11-05-35 (11-degree sweep).

It can be concluded that in the case with the 11-degree sweep, the majority of the change in incidence was due to the wing bending effect. However, the change of incidence can be mitigated by using the aerodynamic torque by adjusting the location of the spar as explained in the section 8.3.2.1.

Table 8-9 Aerodynamic performance at trim condition for varying wing sweep angles for AerEl cases

Cases	Sweep [deg.]	Aerodynamic performance at trim condition ($C_L = 0.8$)					α_{trim} [deg.]	$C_{M_{L=0}}$	Gross Weight [kg]
		$C_{D_{prof}}$	$C_{D_{in}}$	C_D	$\frac{C_L}{C_D}$	$\frac{\partial C_M}{\partial C_L}$			
AerEl 07-05-35	7	0.00833	0.01069	0.01902	42.04	-0.0627	7.8716	0.0223	897.40
AerEl 09-05-35	9	0.00811	0.01058	0.01870	42.77	-0.0524	8.1376	0.0158	900.04
AerEl 11-05-35	11	0.00804	0.01082	0.01887	42.39	-0.0434	8.2457	0.0087	904.91

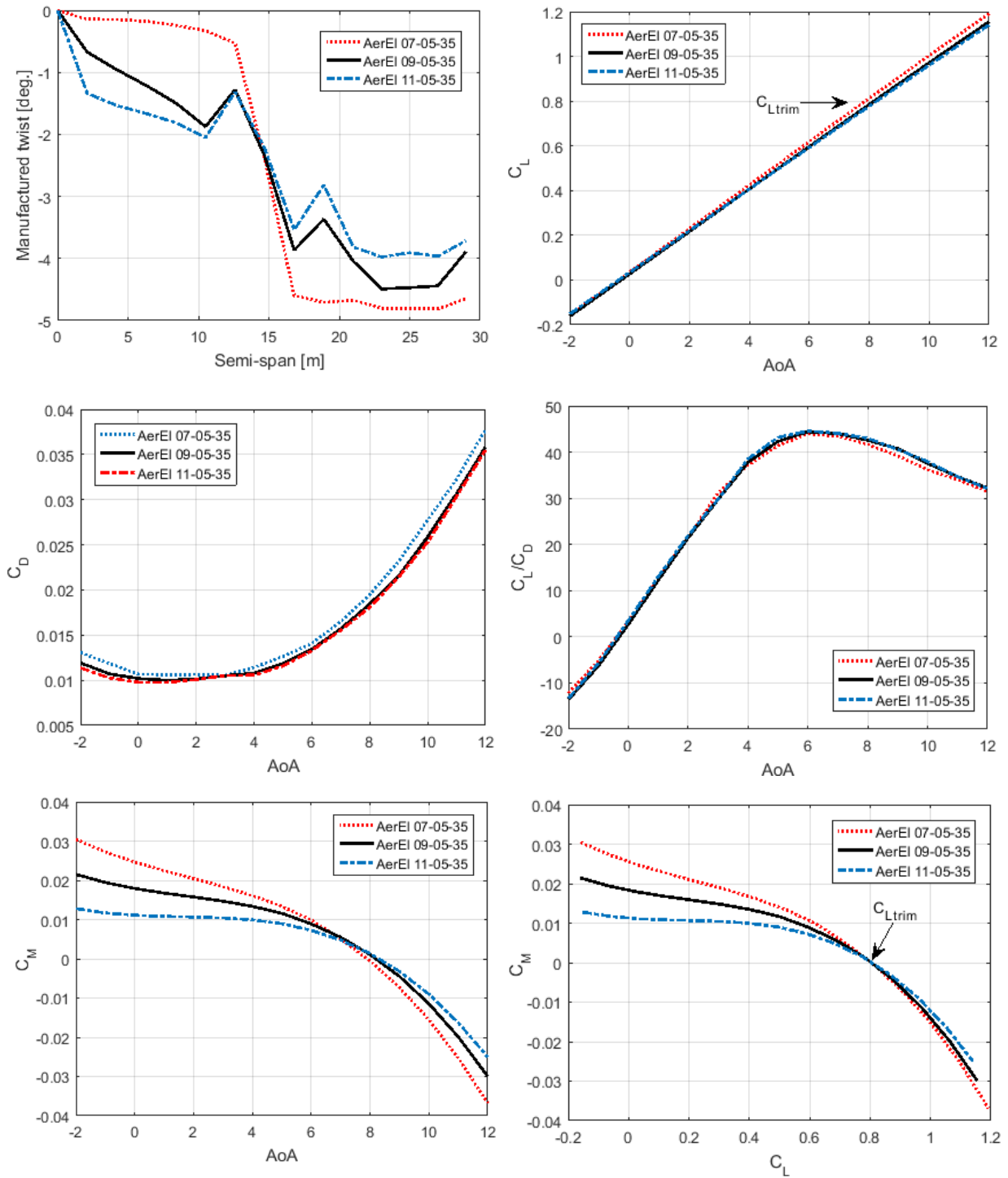
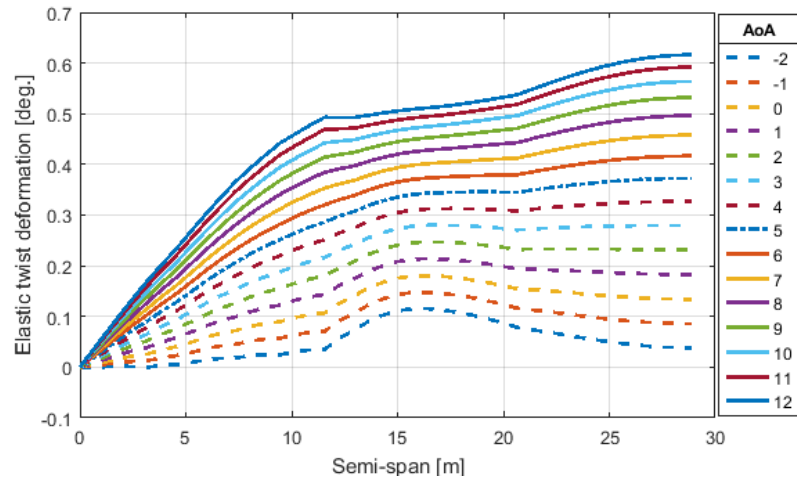
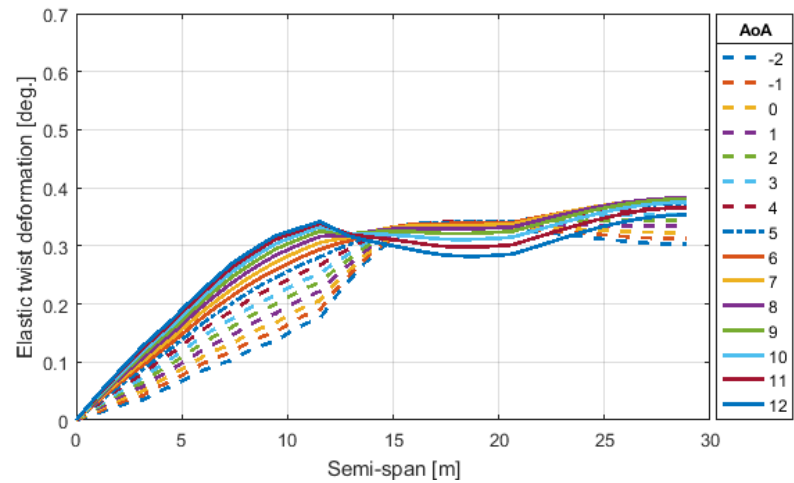


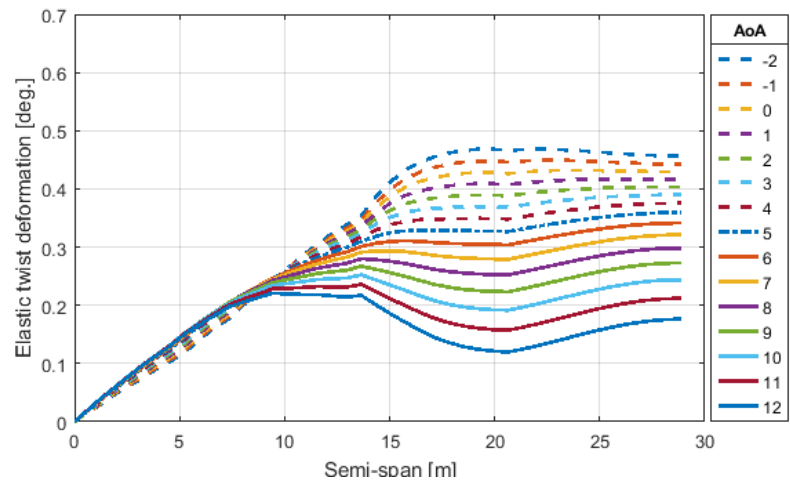
Figure 8-19 Optimal manufactured twist distribution and aerodynamic performance parameters for the cases AerEI at varying wing sweep angles: static margin=0.05, spar locus= 0.35 x/c



(a) AerEl 07-05-35 (Sweep=7°)

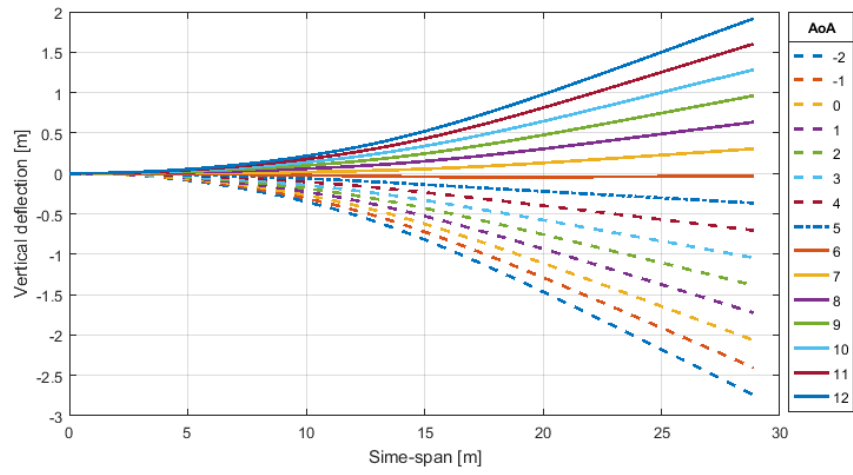


(b) AerEl 09-05-35 (Sweep=9°)

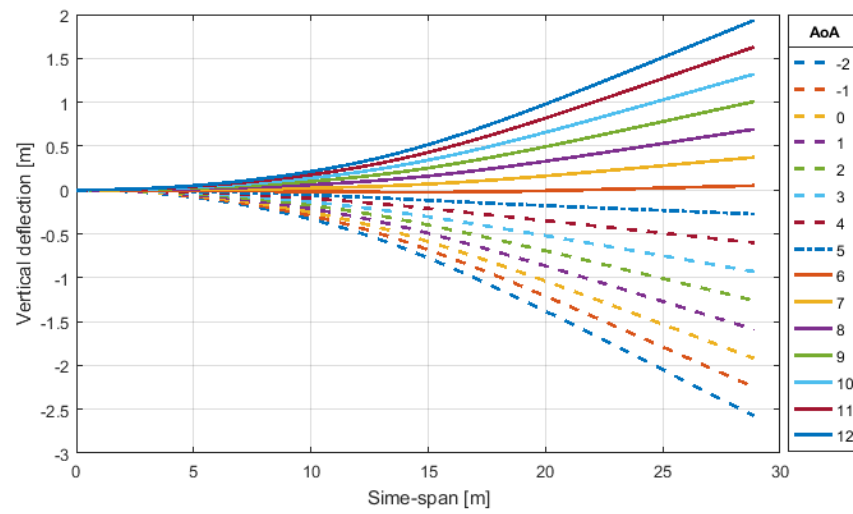


(c) AerEl 11-05-35 (Sweep=11°)

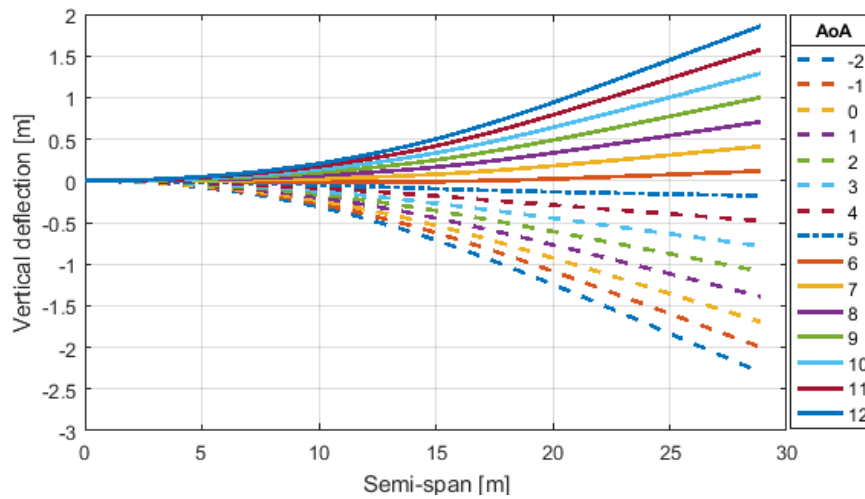
Figure 8-20 Elastic twist deformation, respect to the flow direction, for the cases AerEl at varying sweep angles: spar locus= 0.35 x/c, static margin=0.05



(a) AerEl 07-05-35 (Sweep=7°)



(b) AerEl 09-05-35 (Sweep=9°)



(c) AerEl 11-05-35 (Sweep=11°)

Figure 8-21 Elastic vertical deflection for the cases AerEl at varying sweep angles: spar locus= 0.35 x/c, static margin=0.05

8.3.3 Concluding Remarks from the Design Cases

The results achieved so far presented some interesting aspects which can be summarised as follows:

1. The elastic deformations of the wing have a considerable effect on the aerodynamic and stability performance parameters, and hence must be taken in account to achieve an optimal flight shape of the wing at the cruise condition. The elastic deformation can destabilise the wing and this indicates the need to study the wing performance depending on the wing loading at different flight conditions. The influence of the elastic deformation could worsen the stability at low aerodynamic loading due to the wash-out twist and the weight of the wing itself.
2. The aerodynamic loads can enhance the stability by mitigating the elastic deformations. Such a suitable location for the spar behind the local aerodynamic centre will enable the aerodynamic loads to effect a change in the incidence due the bending deflections of an aft-swept wing. The optimal spar location depends on the sweep angle which in return has a direct influence on the amount of elastic twist deformation with respect to direction of the airflow due to the bending of the wing. Also, the wing sections may have an influence due to the location of the aerodynamic centre. Moreover, the weight distribution within the wing can have a balancing effect which reduces the aerodynamic loads acting on the structure.
3. The location of the spar demonstrates an influence on its sizing. If the distance between the elastic axis of the spar and the axis of the local aerodynamic centre increases, the accompanying increase in the wing torque will need to increased torsional stiffness making the structure heavier.
4. The static margin has an influence on the required sweep and twist of the wing. Lower longitudinal stability will necessitate less sweep and washout twist to achieve a specific trimmed lift coefficient.
5. It can be concluded that the required sweep angle and the amount of washout twist are associated with the required trimmed lift coefficient and the reference static margin.
6. Some cases showed instability or less stability at lower angles of attack due to elastic influences. This could be avoided by adding more optimisation constraints including the slope criterion for the $[C_M - C_L]$ curve at lower angles of attack.

8.4 Final Design

The results of the design cases showed an overview about the aerodynamic and structural performances for a number of design cases. In order to decide on the best solution, a static margin of 0.05 will be selected in accordance with the typical value recommended by the previous designers of conventional flying wing aircraft (Kroo, 1993; Nickel & Wohlfahrt, 1994). According to the results obtained earlier, the sweep angle would need to be between 7 and 9 degrees.

Case AerEl 07-05-35 (with sweep=7°) shows good static stability but at high drag because of the excessive twist needed to achieve the trimmed lift coefficient of 0.8. Case AerEl 09-05-35 (with sweep=9°) shows less static stability with a static margin of 0.05 but with lower drag. Therefore, an eight degree sweep angle layout would have to be selected for the optimum. Based on this wing sweep angle, the location of the spar can be determined.

Optimisation studies were then conducted at spar locations 0.33, 0.34 and 0.35 x/c. The optimal manufactured twist distribution and the aerodynamic performance parameters are shown in Figure 8-19. The variation in the aerodynamic performances is relatively small. The best solution turned out to be for the case where the spar was located at 0.34x/c as shown in Table 8-10. Moreover, this case shows a lower variation in the twisting of the wing due to the aerodynamic loads over the range of angles of attack -2 to +12 degrees as shown in Figure 8-23. Therefore, case AerEl 08-05-34 was chosen as the final and definitive solution as it generated the lowest drag with acceptable longitudinal static stability in addition to meeting the main characteristics of the conceptual design results and the mission requirements. This design was christened SUMER and this name will refer to AerEl 08-05-34 in the rest of this thesis.

Table 8-10 Aerodynamic performance at trim condition for varying spar locations for AerEl cases

Cases	Spar Locus %x/c	Aerodynamic performance at trim condition ($C_L = 0.8$)					α_{trim} [deg.]	$C_{M_{L=0}}$	Gross mass [kg]
		$C_{D_{prof}}$	$C_{D_{in}}$	C_D	$\frac{C_L}{C_D}$	$\frac{\partial C_M}{\partial C_L}$			
AerEl 08-05-33	33	0.0083547	0.0105435	0.0188982	42.33	-0.05519	6.7846	0.01760	889.78
AerEl 08-05-34	34	0.0082321	0.0105788	0.0188110	42.52	-0.05340	6.91047	0.01895	899.67
AerEl 08-05-35	35	0.0083381	0.0106459	0.0189840	42.14	-0.05255	6.5960	0.02053	909.57

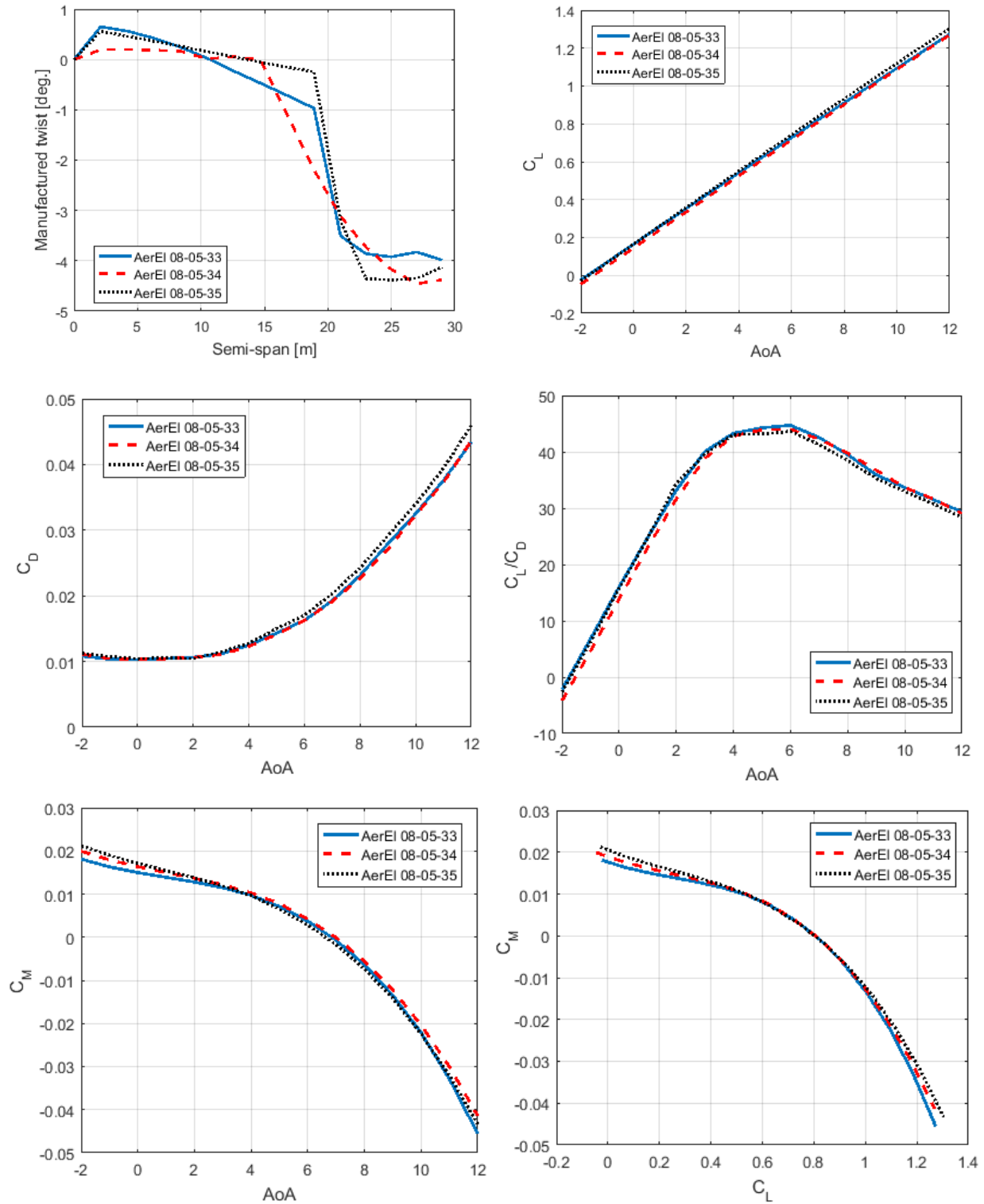


Figure 8-22 Optimal manufactured twist distribution and aerodynamic performance parameters for the cases AerEI at varying spar locations: static margin=0.05, sweep=8°

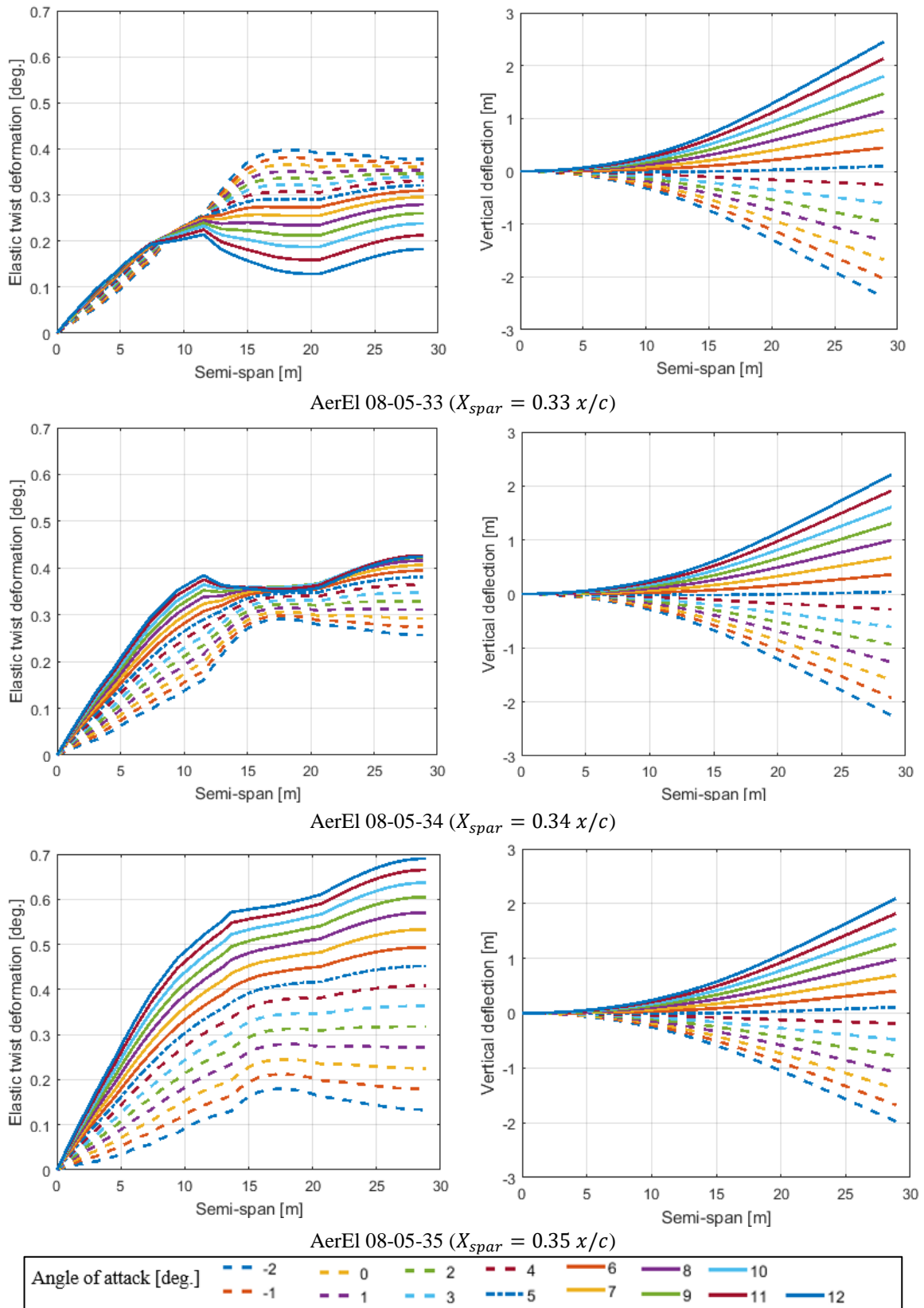


Figure 8-23 Elastic deformation for the cases at varying spar locations: sweep angle=8°, static margin=0.05

8.4.1 Final Design of SUMER

The conceptual shape of SUMER is shown in Figure 8-25. This aircraft has the same characteristics shown in Table 8-1 and Table 8-2 which were concluded at the conceptual design stage and used in the preliminary design process. The weight distributions along the chordwise and spanwise directions are detailed in Figure 8-5 and Figure 8-6 respectively. In the optimisation process, the centre of gravity was located to achieve a longitudinal static stability margin of 0.05. Therefore, for the given weight distribution, the centre of mass of the payload and the avionics has to be located at 29.6% x/c .

The optimal manufactured twist and its aerodynamic and structure performances are presented in Figure 8-22 and Figure 8-23. Moreover, the distribution of the lift coefficient along the semi span at different angles of attack is presented in Figure 8-24. At the cruise condition of 17 km altitude and 30.52 m/s air speed, the aircraft achieves trimmed lift coefficient of 0.8 when the angle of attack reaches the value of 6.91°. As indicated in Table 8-10, the induced drag accounts for 56% of the total drag at a lift/drag ratio of 42.52. The weight of the non-spar and spar elements estimated by the composite structure model are detailed in Table 6-4. Also, the stacking of the flanges and the webs of each spar partition and their mechanical properties are shown in Table 6-6.

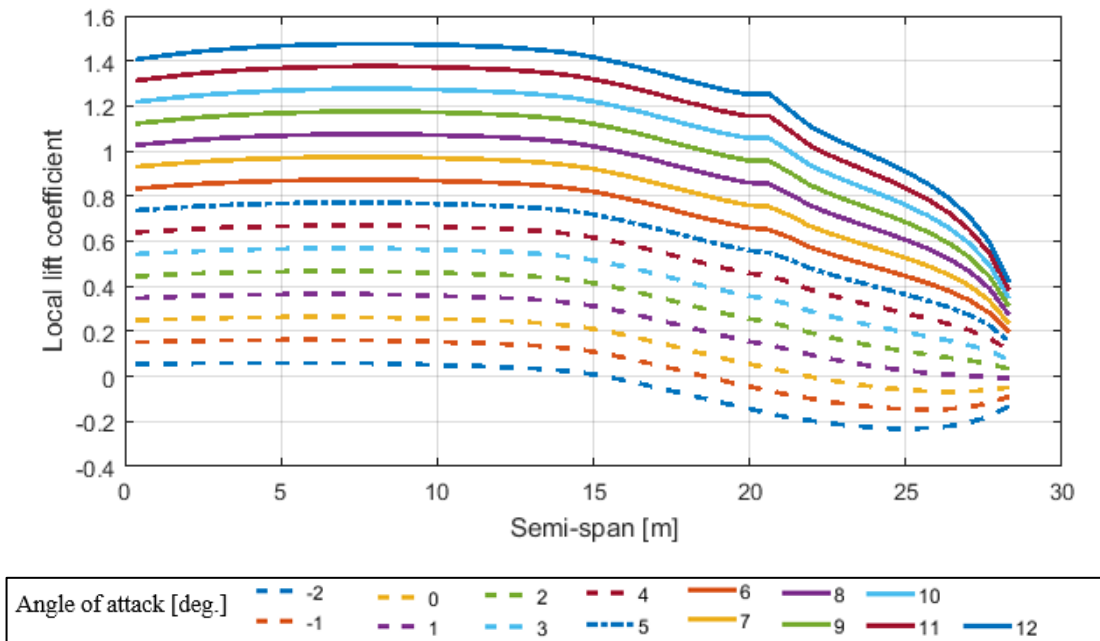


Figure 8-24 Local lift distribution along spanwise direction at varying angles of attack

Table 8-11 The weight of the spar and non-spar elements of the SUMER

Elements	mass [kg]
Ribs	23.07
Leading edge	38.24
Trailing edge	5.79
Covering	75.39
Total non-spar elements	142.49
Spar	140.38
Total Structure	282.87

Table 8-12 Plies stacking at each spar section in the semi-span of SUMER

Spar Seg.	Stacking at flanges	Stacking at webs	Length [m]	EI_x [MPa.m ⁴]	EI_z [MPa.m ⁴]	GJ [MPa.m ⁴]	EA_y [MPa.m ²]
1	[0 ₆ , 90, 0 ₉ - 45 45] _s	[0 ₈ , -45, 45] _s	2.1	10.3	7.67	1.00	292.95
2	[0 ₄ , 90, 0 ₉ - 45 45] _s	[0 ₈ , -45, 45] _s	2.1	9.21	7.29	0.97	268.42
3	[90, 0 ₉ - 45 45] _s	[0 ₆ - 45 45] _s	2.1	6.62	5.42	0.87	194.86
4	[0 ₈ - 45 45] _s	[0 ₆ - 45 45] _s	2.1	5.94	5.19	0.84	179.87
5	[0 ₆ - 45 45] _s	[0 ₄ - 45 45] _s	2.1	4.43	3.67	0.77	130.42
6	[0 ₄ - 45 45] _s	[0 ₄ - 45 45] _s	2.1	3.28	3.28	0.74	105.56
7	[0, 0, -45 45] _s	[0, 0, -45 45] _s	2.1	1.74	1.74	0.67	55.71
8	[0, 0, -45 45] _s	[0, 0, -45 45] _s	2.1	1.74	1.74	0.67	55.71
9	[0, 0, -45 45] _s	[0, 0, -45 45] _s	2.1	1.74	1.74	0.67	55.71
10	[0, 0, -45 45] _s	[0, 0, -45 45] _s	2.1	1.74	1.74	0.67	55.71
11	[0, 0, -45 45] _s	[0, 0, -45 45] _s	2.05	1.74	1.74	0.67	55.71
12	[0, 0, -45 45] _s	[0, 0, -45 45] _s	2.05	1.74	1.74	0.67	55.71
13	[0, 0, -45 45] _s	[0, 0, -45 45] _s	2.05	1.74	1.74	0.67	55.71
14	[0, 0, -45 45] _s	[0, 0, -45 45] _s	2.05	1.74	1.74	0.67	55.71

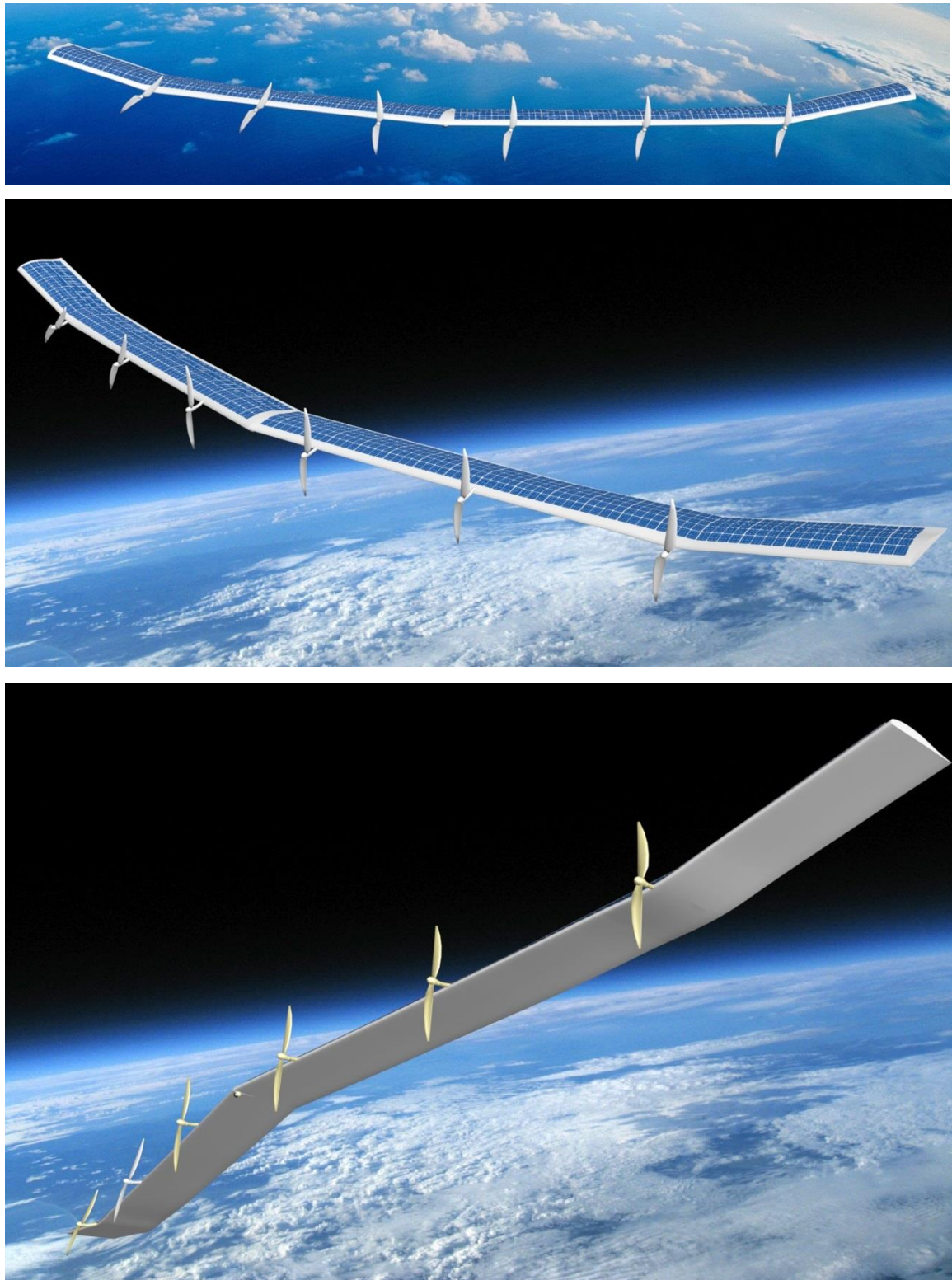


Figure 8-25 Computerised rendering of the SUMER in cruise condition

8.4.2 Performance at Different Flight Speeds

Since the mission of the SUMER UAV is to operate for about six months at a somewhat constant altitude, no operational matters apart from the critical load factor for sizing purposes were considered. The aerodynamic performance of the shape of the aircraft in flight was targeted only during the optimisation process at the trim condition. It is expected that the shape will change if the wing loading was altered. In this section, the aerodynamic and the structural performance parameters at varying flight speeds and at a constant flight altitude of 17 km will be studied.

Figure 8-26 shows the aerodynamic performance of SUMER at flight speeds of 20, 30.53 (design speed) and 40 m/s. The results indicate a significant effect on the pitching moment due the elastic deformations. It seems that the location of the aerodynamic centre is affected by the elastic deformations which in turns has an influence on the static longitudinal stability. The trimmed angle of attack reduced at higher speed and vice-versa as one would expect. This behaviour is preferable because it will reduce the requirement for control surfaces deflections in the future as the design matures. The curve $[C_M-C_L]$ indicates an increase in the static stability margin at higher speeds. Also, the local wing incidence due to elastic deformations were reduced at high speed as illustrated in Figure 8-27. The slope of the curve $[C_L-AoA]$ is slightly influenced by the range of speeds. However, the coefficients of lift and pitching moment were calculated using the Vortex Lattice Method and are not affected by the operational Reynolds number. The drag however was affected by changes in the air speed due to variations in the Reynolds number in addition to the changes in the shape of the wing.

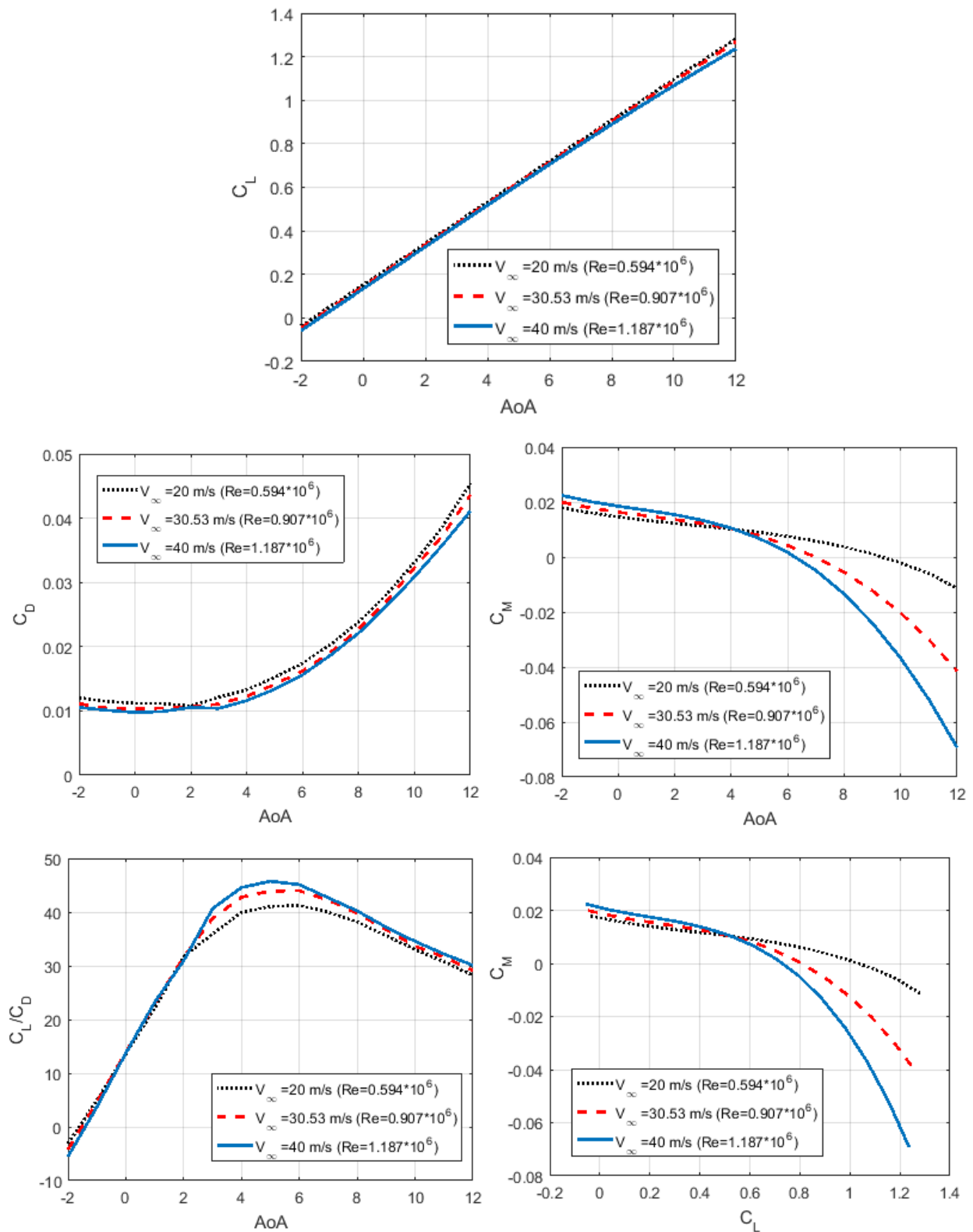
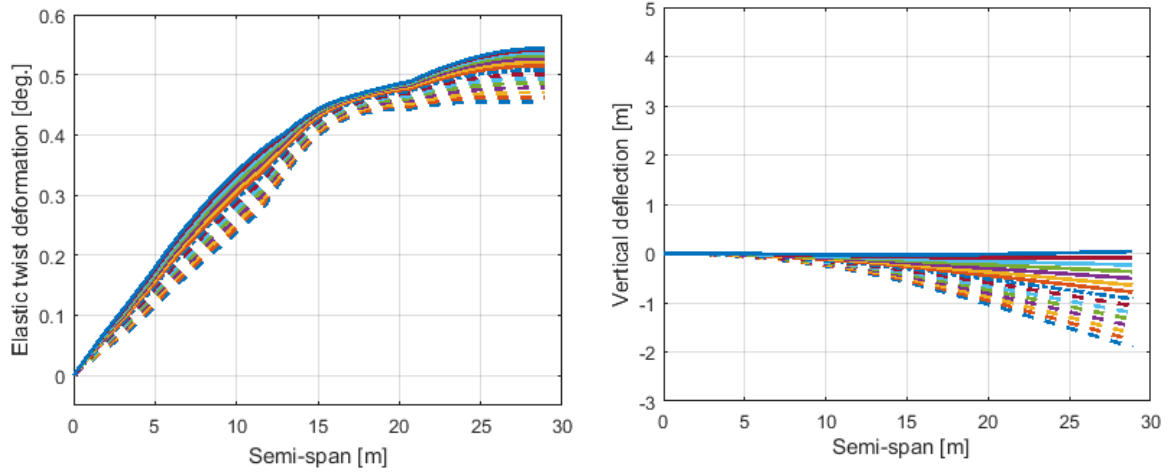
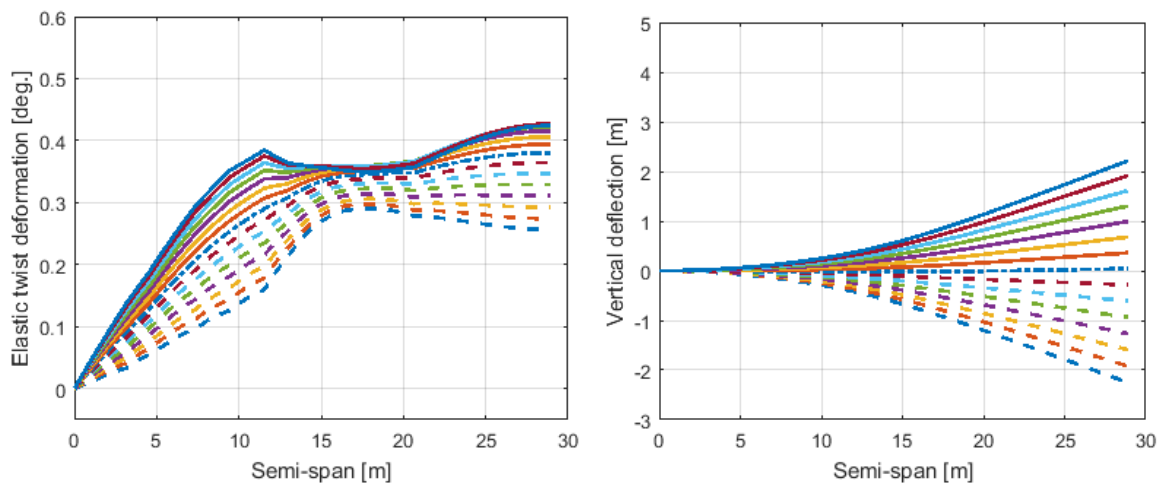


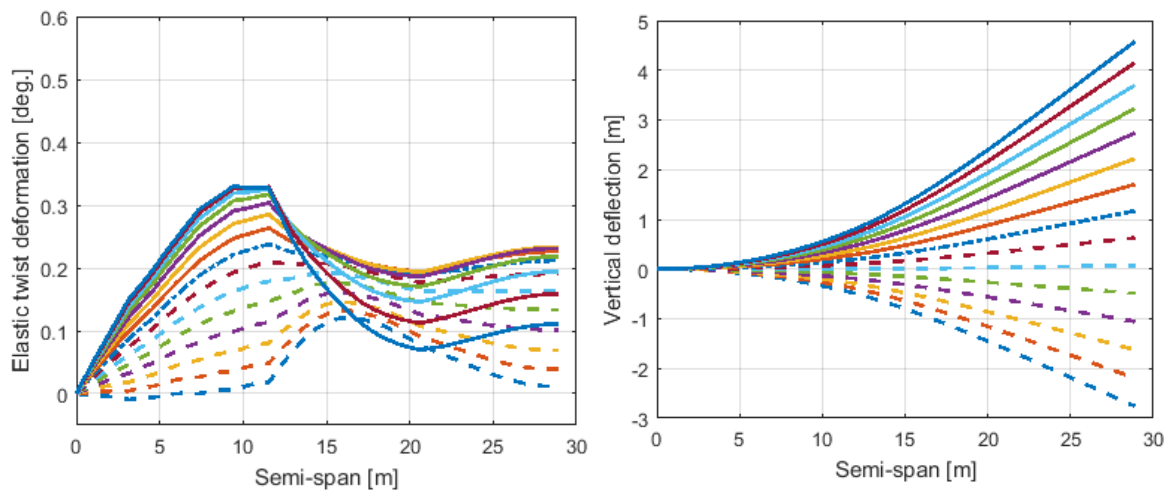
Figure 8-26 Aerodynamic performance parameters for the final case (AerEl 08-05-34) at varying airspeeds:
 Altitude=17 km, static margin=0.05, spar locus at $0.34x/c$, sweep= 8° , altitude=17km



$V_\infty = 20 \text{ m/s}$ ($Re = 0.594 \times 10^6$)



$V_\infty = 30.53 \text{ m/s}$ ($Re = 0.907 \times 10^6$)



$V_\infty = 40 \text{ m/s}$ ($Re = 1.187 \times 10^6$)

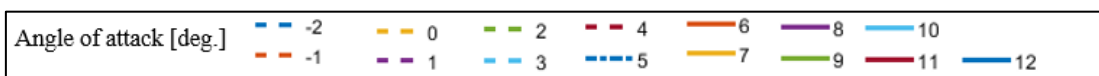


Figure 8-27 Elastic deformation for the final case at varying flight speeds

8.4.3 Assessment of the performance of SUMER

The adopted preliminary design procedure is based on the outcome of the conceptual design process and the mission requirements. At the initial stage, the reference aerodynamic parameters had to be estimated as the power required was strongly associated with these values, and enabled prediction of the main characteristics of the aircraft. The lift coefficient was estimated for minimum speed which was represented as a function of the maximum lift coefficient with a safety margin for wind gusts. The maximum lift coefficient of the wing is assumed to be the same of that of the aerofoil. The span efficiency (inviscid theory) was assumed constant as demonstrated by aircraft such as the Helios P03, and the early studies published by the author (Alsahlani, Johnston, & Atcliffe, 2017; Alsahlani & Rahulan, 2016, 2017). The profile drag was estimated using the value for the aerofoil drag at the maximum lift/drag ratio. These assumptions have to be matched to the preliminary design output. Except for the structural weight, the main aircraft characteristics such as the weight of aircraft system elements and the area & span of the wing were assumed constant from the conceptual to the preliminary design phases. During the preliminary design stage, only the lift coefficient at the trim condition was driven to be equal to the reference lift coefficient (0.8) whilst the total drag was targeted for minimum value during the optimisation process. Therefore, it is necessary to assess the validity of the assumptions that were made and the design procedure that followed.

A comparison between the results of the conceptual and preliminary design stages is presented in Table 8-13. The results of the final design indicate that the span efficiency of the SUMER is greater than unity which is higher than that suggested at the conceptual design stage. The reason for that might be due the limitation in Tornado VLM to predict an accurate induced drag coefficient for a cambered twisted wing as noted in reference (Pomeroy & Visser, 2010). Moreover, the dihedral part in the wing might work as a winglet and had reduced the vorticity at the wing tips. However, the total drag coefficient obtained by the preliminary design stage is less than the ultimate value (0.019153) which was obtained from the conceptual design tool. The structural mass is about 10% less than that estimated by Rizzo's model (indicated in section 4.3.1). This has led to a total saving of about 31 kg.

Table 8-13 Results achieved by the design stages

Parameters	Conceptual design Stage	Preliminary design Stage	Differences %
C_{Lref}	0.8	0.800	0.00
Span efficiency (e)	0.95	1.013	+6.68
C_{Din}	0.011280	0.0105788	-6.21
C_{Dprof}	0.007873	0.0082321	+4.56
C_D	0.019153	0.0188110	-1.78
Structural mass [kg]	314.41	282.87	-10.03
Total mass [kg]	931.27	899.67	-3.39

The aerodynamic efficiencies versus angle of attack for the final design are presented in Figure 8-28. It can be seen in Figure 8-28 (a) that the cruise condition of the aircraft is beyond the maximum lift to drag ratio. However, it is at a flight condition which is very close to that for maximum endurance as indicated in Figure 8-28 (b). The consideration that was adopted in selecting the reference lift coefficient was constrained by the minimum speed to avoid stall as discussed in section 4.3.8.1. However, the maximum lift coefficient for the final design cannot be determined because of the limitation in the Quasi 3DM which does not cater for evaluating the aerodynamic performance in the stall region.

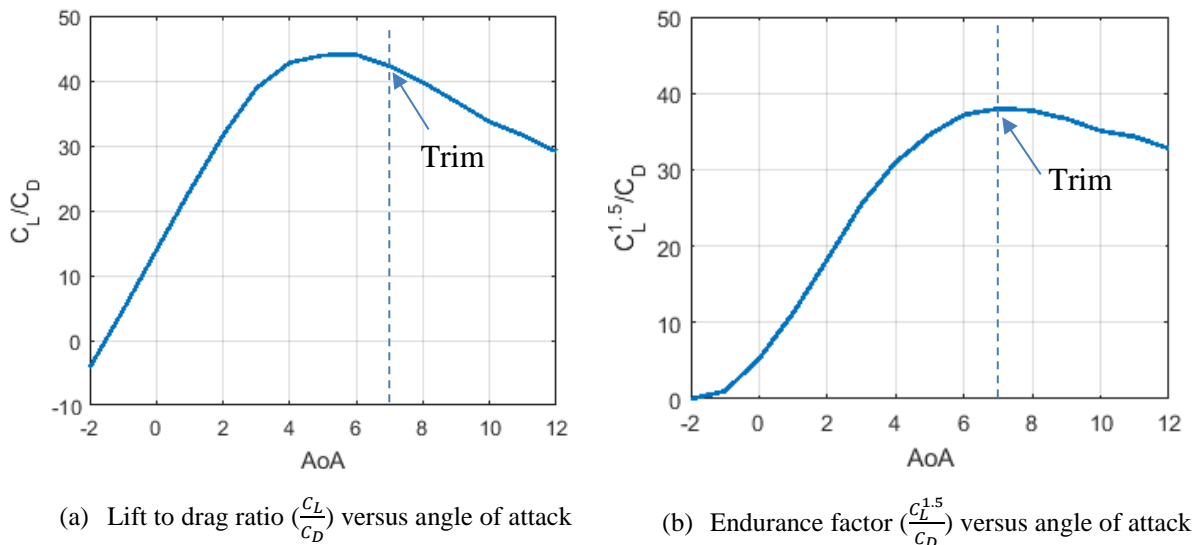


Figure 8-28 The aerodynamic efficiencies of the SUMER at different angles of attack, airspeed=30.53 m/s, altitude 17km

From this comparison, one can deduce that the outcome of the preliminary design stage has met the conceptual design constraints with an adequate safety margin. However, both design processes were conducted using low fidelity analyses in which it would have been preferable to have imposed tolerance levels for the results.

From these assessments one can conclude that:

1. The profile drag estimated by the conceptual design tool was a good estimate to forward to the preliminary design stage. However, it may be wise to have a safety margin.
2. The value of the span efficiency which was assumed at the conceptual design stage was lower than that obtained during the preliminary design stage. However, the reduction in the induced drag was substituted by an increase in the profile drag.
3. The structural mass estimated at the conceptual design stage proved to be acceptable when compared with the preliminary design results. However, this might not be the case if the spar dimensions or the load factor were to be modified.
4. According to equation (4.5) and the aerodynamic performance at cruise condition along with the final iteration for the aircraft mass, the mechanical power required for level flight (P_{lev}) turned out to be about 6.73 % less than that estimated during the conceptual design stage. This means that the final design should be capable of flying at the required mission altitude throughout the specified flight endurance.

8.4.4 CFD Validation of the Design of SUMER

A high order fidelity CFD analysis was conducted for the final design of SUMER. The shape of the wing in flight was found using the Quasi-3DM and the composite structure models (CSM) at different angles of attack. The resulting geometries were then modelled using the ANSYS's Design Modeller using the dihedral & the sweep of the quarter chord axis as well as the wing twist. For example, Figure 8-28 shows the wing shapes in flight at different angles of attack. The wing section at each wing partition (ZMR-17) was assumed parallel to the z-axis of the aircraft and was not influenced by the elastic deflection as was assumed in the Quasi-3DM. The flow field and the grid used for the CFD analysis of the semi-span are presented in Figure 8-29. A structured tetrahedral grid type was used for all studies in the fluid domain and was refined at the wing surface with boundary layer of 12-ply up. The flow field is sized as 20 times the chord width, 40 times the chord length and 20 times the chord height. The transition model $k-k\ell-\omega$ (3eq) has been used to model the flow. The boundary condition was fixed as all the flow field sides, except the plane of symmetry, were set as a pressure far field. The flow state was set to achieve 0.907×10^6 Reynolds number. Moreover, the reference point (not the origin of the axes set) for calculating the pitching moment was set at the centre of gravity of the aircraft.

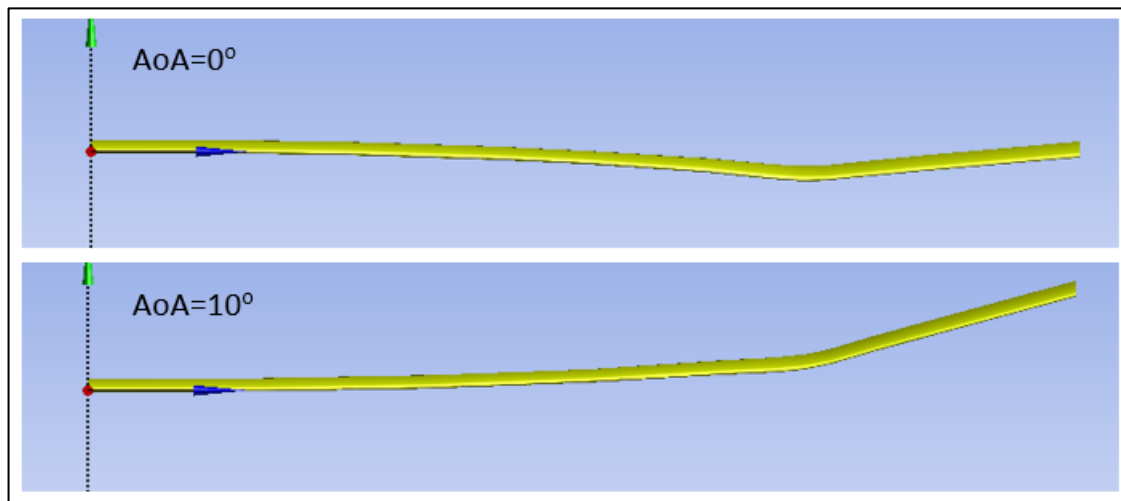


Figure 8-29 Front-side of the wing shapes in flight at angles of attack 0 and 10 degrees

8.4.4.1 Validation of Aerodynamic Performance

Figure 8-30 shows the aerodynamic performance parameters of the SUMER obtained by the CFD package compared with that obtained by the Quasi-3DM. In addition, the pressure contours of the upper and the lower wing surfaces are presented in Figure 8-31.

At lower angles of attack, the lift coefficients are in good agreement. At higher angles of attack, the slope of lift coefficient obtained by CFD is lower due to viscous effects. This was expected because of the inviscid flow approach used by the Vortex Lattice Method.

The drag coefficients obtained from the CFD analyses were higher than those obtained from the Quasi-3DM computations. However, the trend displayed by both curves of the drag coefficient versus the angle of attack are quite similar. The reasons for the difference in the value of the slopes are as follows:

1. Error associated within the Quasi-3DM:

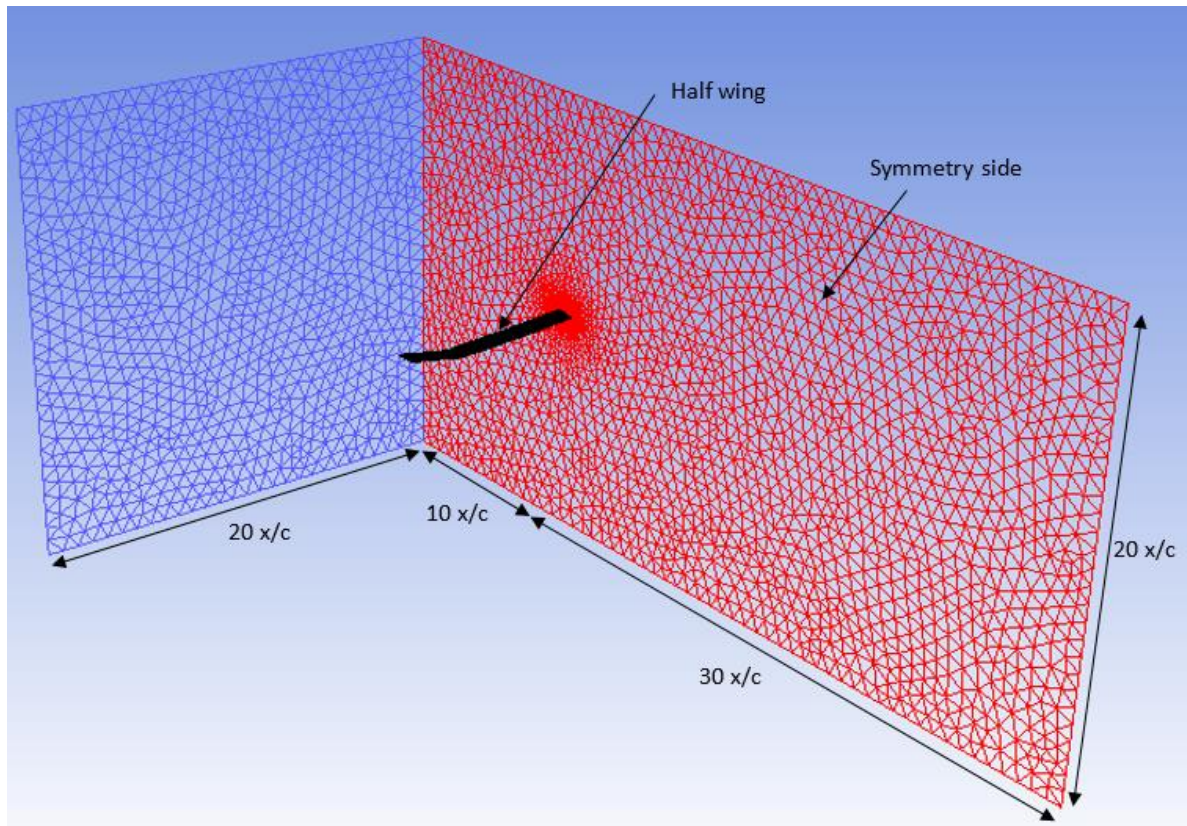
The analysis is based on the strip theory in which the effect of the development of the boundary layer in the three-dimensions is approximated. Moreover, there is a margin of error in the calculations of the effective angles of attack that were calculated using the local lift forces obtained by the vortex lattice method (inviscid analysis). Another reason that can affect the total drag estimate is the accuracy of evaluating the induced drag coefficient as indicated in (8.4.3).

2. Errors associated with high order CFD modelling.

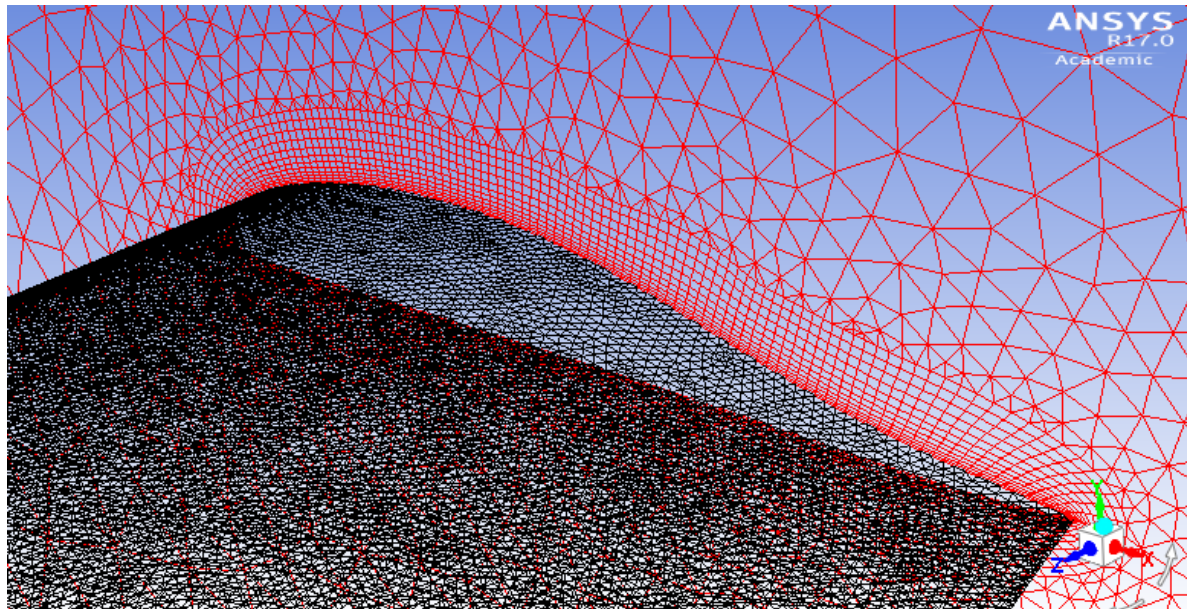
The used mesh density could be the reason for overestimating the drag force component. In general, the mesh quality has a considerable influence on the accuracy which in turn required more computational time and the need for high speed data processing. Low Reynolds number operation necessitates a dense mesh to capture the boundary layer developments around the wing. Moreover, the high aspect ratio of the wing induces a larger fluid domain necessary to model the flow wake behind the wing. The computational facility that was available struggled somewhat with the relatively dense mesh needed to handle the large fluid domain.

The pitching moment coefficient obtained by the Quasi-3DM is inviscid indicating that the viscous effects on the pitching moment were neglected. The trend of the curves [C_M -AoA] at lower angles of attack obtained by both aerodynamic solvers look similar but at exhibit different values. In the optimisation tool, the proper location of the centre of gravity with respect to the mean aerodynamic centre to achieve a specific static margin was assumed. The aerodynamic centre was found according to the thin aerofoil theory which was employed in the Quasi-3DM (see section 8.2.2.2) in which its location is only dependent on the planform shape of the wing. However, for viscous flow over a cambered aerofoil, this location could be different. Moreover, the mean aerodynamic centre was calculated for the rigid wing.

The pressure contours shown in Figure 8-31 are what one would expect and do not show any abnormalities.



(a) Orthogonal view of the fluid domain



(b) Wing grid at the root section attached to the symmetry side

Figure 8-30 Orthogonal view fluid domain and wing grid

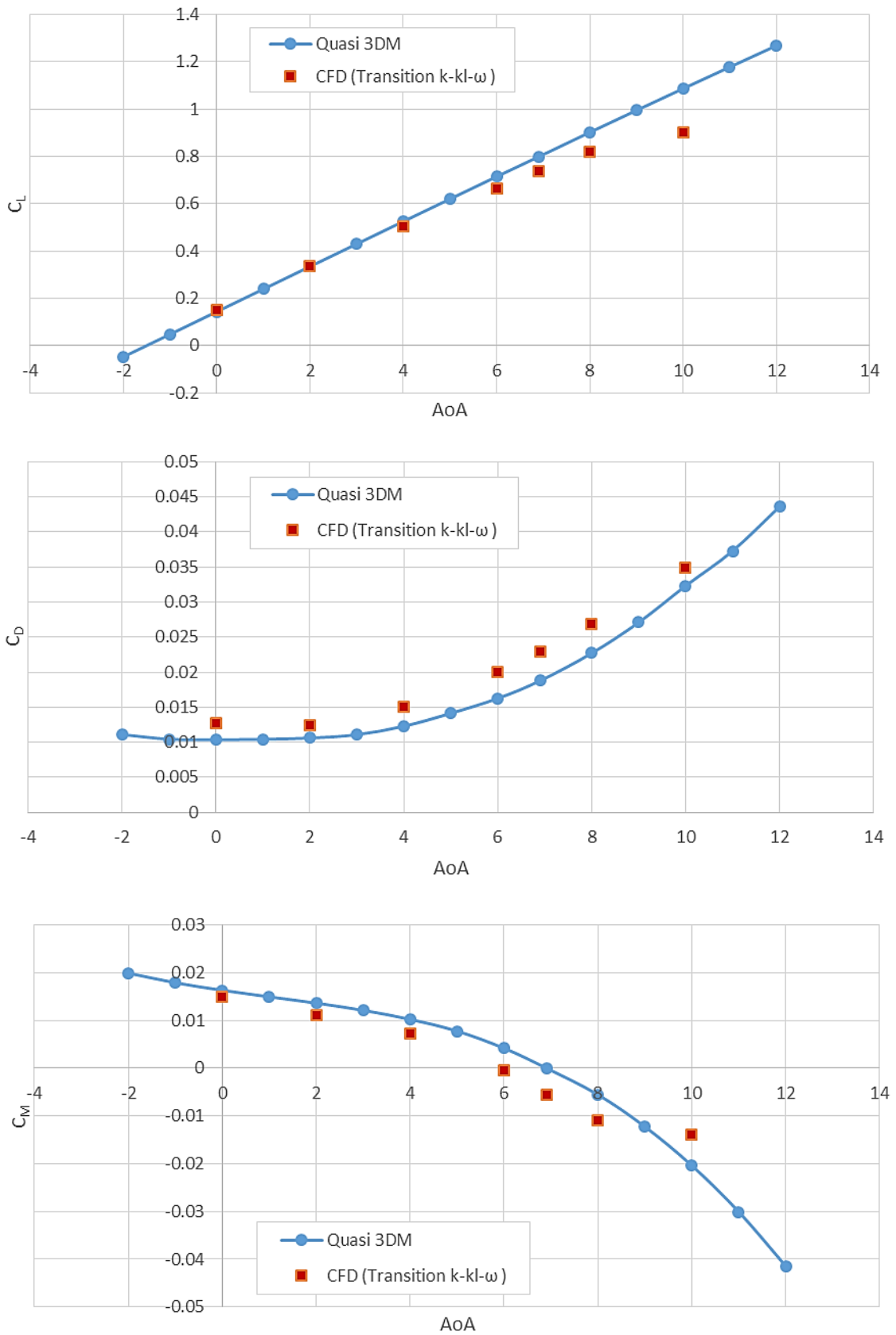


Figure 8-31 Comparison of the aerodynamic performance obtained from Quasi-3DM and CFD

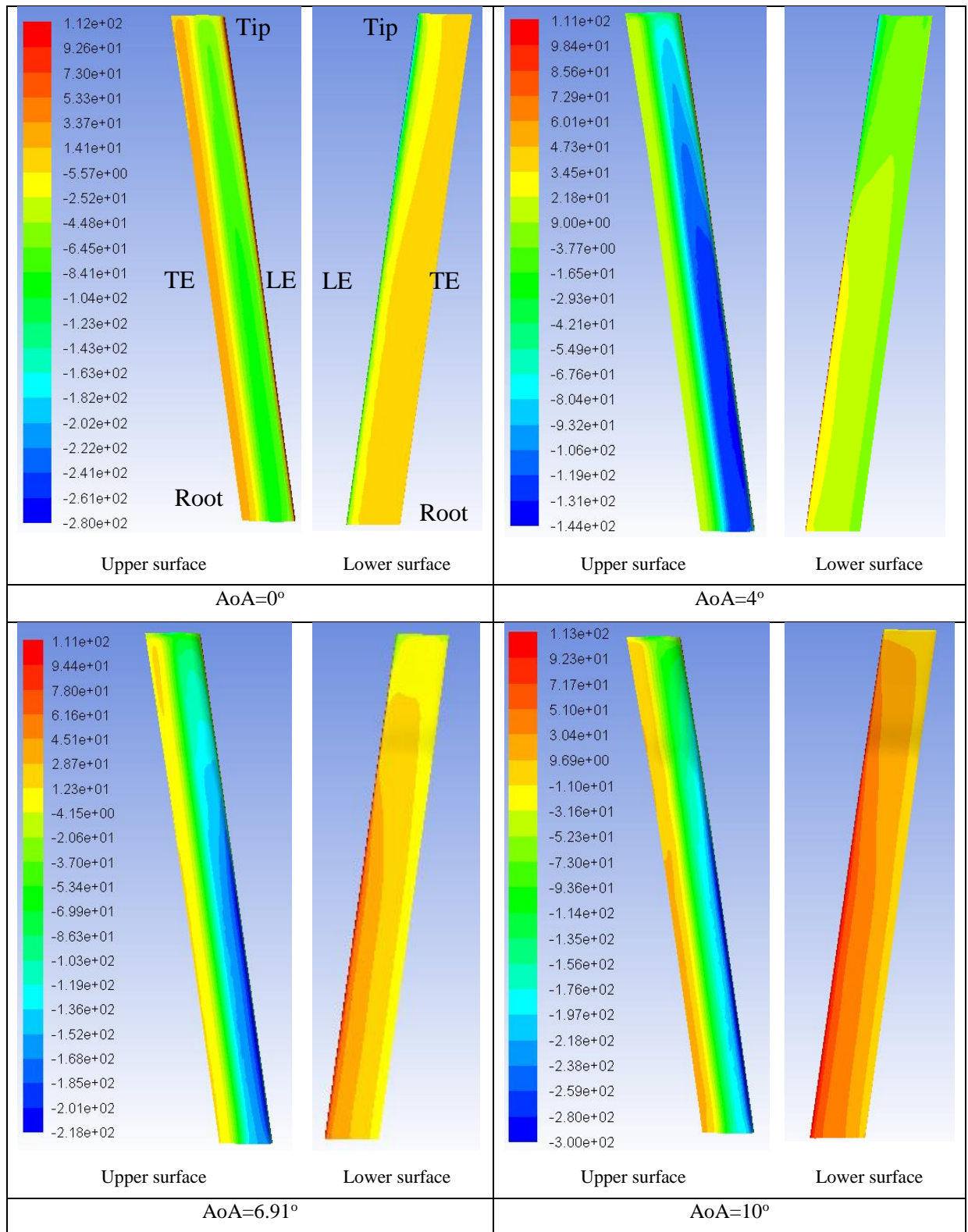


Figure 8-32 Pressure contours of the upper and lower surfaces of SUMER at varying angles of attack

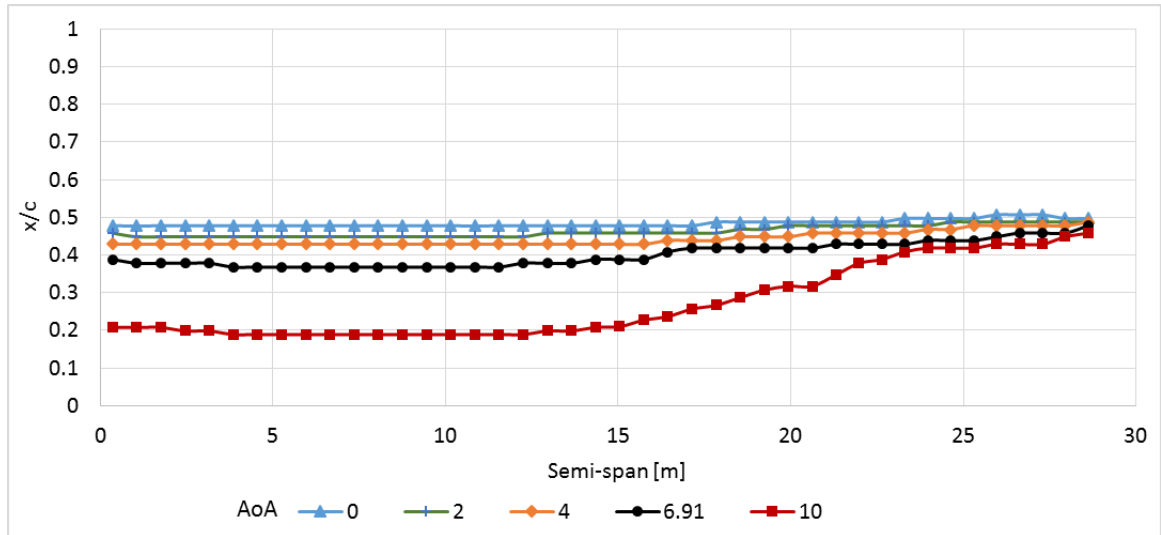
8.4.4.2 Validation of Flow Turbulence

In the Quasi-3DM, the flow transition from the laminar to turbulent was predicted using Michel's criterion which was implemented in the 2D inviscid-viscous model (IVM) as detailed in Chapter 5. Beyond this point or the laminar bubbles, the flow is considered turbulent. For the entire wing, the transition points of the two-dimensional sections will highlight the regions of the laminar and the turbulent flows. Figure 8-32 shows the transition line on the upper and the lower surfaces of the wing predicted by the Quasi-3DM at different angles of attack. The intensity of the turbulence at different angles of attack obtained by the CFD is presented in Figure 8-34. In this region, the blue colour represents laminar flow.

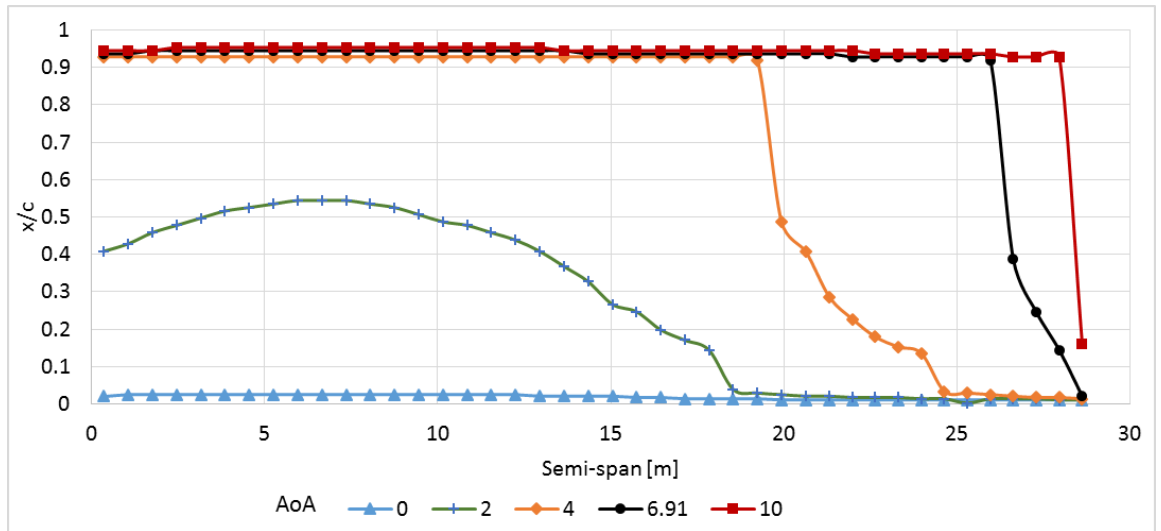
At zero AoA, the onset of turbulent boundary layer starts at $0.49 x/c$ of the upper surface of the wing as predicted by both aerodynamic solvers. Moreover, the majority of the lower surface experiences turbulent flow. However, the CFD results show that the intensity of the turbulence zigzags spanwise along the lower surface of the wing.

With increasing angles of attack, the flow under the wing becomes laminar as shown at angles of attack 4-10 degrees as shown in Figure 8-34. The prediction of the Quasi-3DM is slightly diverted from that obtained from the CFD at the wing tip region due to not taken into account 3D flow.

For the upper surface, both sets of results indicate the forward migration of the transition line with increasing angle of attack. Figure 8-33 compares the transition line estimated by both aerodynamic solvers at angle of attack of 6.91° . They show good agreement throughout the span except at the wing tip.



(a) At the upper surface



(b) At the lower surface

Figure 8-33 Transition points predicted by the Quasi-3DM at varying angles of attack

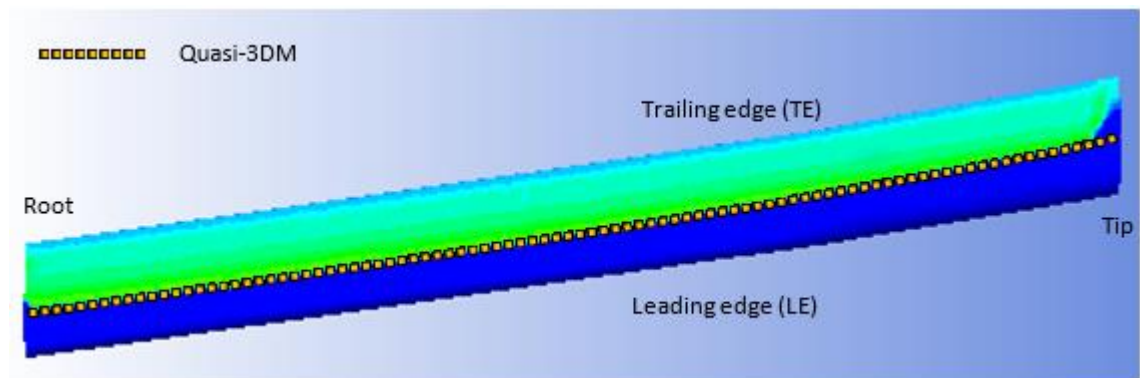


Figure 8-34 Upper surface transition line obtained by Quasi-3DM and CFD at AoA= 6.91°

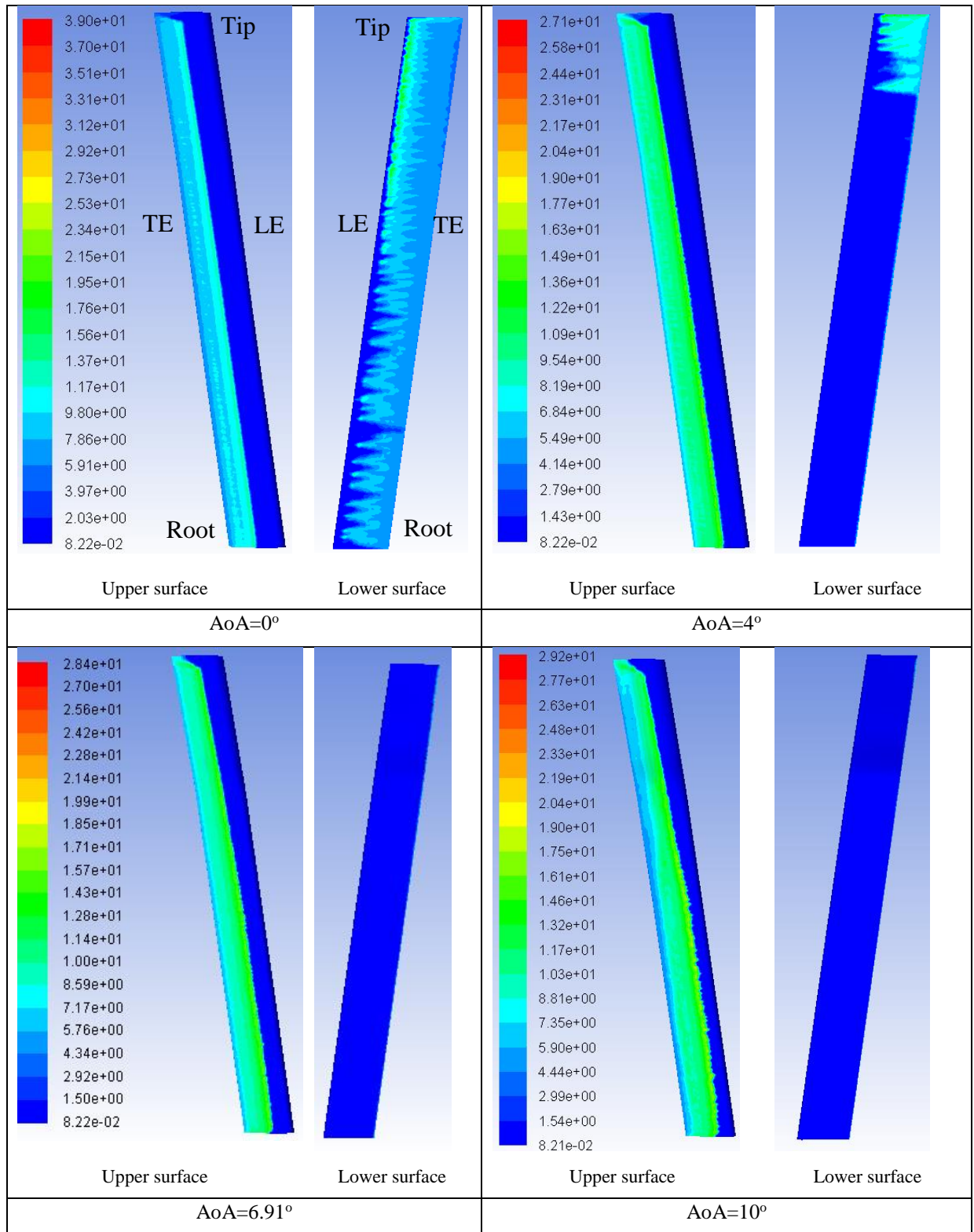


Figure 8-35 Turbulent intensity contours of the upper and lower surfaces of SUMER at varying angles of attack

CHAPTER 9

9 OVERALL DISCUSSION

This chapter presents the overall discussion for the tools developed in this research and the results obtained.

9.1 Conceptual Design Tool

A mathematical model has been developed to size a solar powered high altitude aircraft for given mission requirements. In this model, the equation for the total mass was derived by representing all the mass or/and power of the aircraft elements as fractions of the main characteristics of the aircraft. These fractions were interpolated from set of empirical data relating to similar aircraft. However, these fractions were gathered from different sources and so particular attention was paid towards the application for the aircraft considered in this study. Improper use of the estimation procedure can result incorrect mass and power predictions. This particularly the case for component weight breakdown analysis relating to the mass of the structure and fuel cells. The structural weight will be revisited during the preliminary design stage in order to validate the values obtained during the conceptual design stage.

A MATLAB tool was coded according to this methodology to numerically solve the final equation and present the design space in order to conclude the optimal size. The enhancement in representing the drag coefficients at the conceptual design stage was quite useful as observed when comparing the results with those obtained by the preliminary design stage. The tool has been validated by redesigning a related aircraft called SHAMPO using its mission requirements. The accuracy of the results gave confidence when predicting the sizing of the aircraft elements.

The tool was used to study how the mission requirements can influence the main characteristics of the resulted design. These requirements were the start and end dates of the mission in addition to the operational location and flight level of the mission. In addition, the reference lift coefficient, the span efficiency and the payload were examined. The results show that increasing the reference altitude of the design can lead to a heavier aircraft. This was accompanied by a proportional increase in the wingspan and aspect ratio of the wing. Also, the results indicated that the wing area needed for the solar cells was less than that

required for the aerodynamic performance at higher altitudes. Moreover, designing the aircraft with a high lift coefficient can lead to less required airspeed and thus lower operational Reynolds number. Increasing the span efficiency will lead to reduced gross weight, wingspan, aspect ratio and the ratio of the solar cells area. Nevertheless, the daytime period besides the available solar energy showed a noticeable influence in the achievement of the design aims.

9.2 Aerofoil shape Optimisation

A low order aerofoil shape optimisation tool has been developed using the 2D aerodynamic solver Xfoil. A new hybrid parametrisation method using the PARSEC and the Bezier-curve parameterisation functions was presented. This combination enabled the optimisation tool to achieve reasonable aerofoil geometries and mitigate the un-convergence problem presents within the aerodynamic solver leading to increased convergence stability and reduced computation time. Moreover, the Bezier-Curve enabled the thickness distribution to be constrained to achieve a positive distribution whilst ensuring a limit on its maximum value.

A number of new aerofoils with varying thicknesses for an aft-swept flying wing UAV have been designed. The primary target was to design a number of aerofoils with low pitching moment, suitable for such an aft-swept flying wing configuration operating at low Reynolds number in the region of 0.5×10^6 . The performances of the resulting aerofoils indicated that increasing the maximum thickness will lead to a decrease in the maximum lift/drag ratio. Moreover, reducing the pitching moment results in the reduction of the maximum lift/drag ratio and increased drag. The newly designed aerofoils have stall angles not close to the angles in which the maximum lift/drag ratio is reached.

An aerofoil was chosen among the newly designed aerofoils for the aircraft for moderate thickness and high maximum lift to drag ratio. A high order CFD analysis has been conducted to validate the aerodynamic performance using different transition and turbulent models in addition to the Xfoil and the newly developed aerodynamic model (IVM). In general, the validations indicated good agreements at lower angles of attack while the results were diverted at stall regions.

9.3 Preliminary Design Tools

A multi-disciplinary optimisation tool has been developed to size the aircraft and optimise the wing geometry. This tool consists of two major models - aerodynamic and structure in addition to the optimiser code.

(A) The Aerodynamic Solver (Quasi-3DM)

A quasi three-dimensional aerodynamic solver (Quasi-3DM) was built using the Vortex Lattice Method coupled with a two-dimensional inviscid-viscous aerodynamic solver (IVM). The coefficients of the induced drag, lift and pitching moment were calculated using the Vortex Lattice Method. While the profile drag of the wing was calculated using that of the two-dimensional wing sections obtained by a one-way coupling Panel Method and the boundary layer equations. The validation of the IVM results indicated an acceptable level of accuracy compared with experimental data. The Quasi-3DM was also validated with experimental results and demonstrated to be acceptable for prediction with reasonable accuracy of the profile drag. However, this model did not work when turbulent separation appeared. Therefore, the analysis of the flow at stall region will not be applicable with this solver.

(B) The Structure Model (CSM)

A new composite structure model (CSM) and methodology were developed to size the wing structure by evaluating the elastic deflection using linear finite beam element method and to size the spar section according to the critical loads respectively. The stacking of the plies within the spar sections was inspired by existing designs of high altitude aircraft. Empirical equations were then used to evaluate the non-spar element weights as a function of the wing geometry. The weight estimation and the elastic deformations have been validated individually. Structural detail of existing related aircraft was used to validate the developed model. The results proved that it is capable of predicting the weight with reasonable accuracy within a short time period (few seconds). The elastic deformations and the stress analysis of the CSM were also validated using the high order fidelity commercial package ANSYS. The estimation of the elastic deflections was in excellent agreement with the ANSYS results whereas the estimate of the stresses was less accurate.

(C) Multi-Disciplinary Optimisation

The Quasi-3DM and the CSM were used to build a multi-disciplinary optimisation tool. A quasi-static aeroelasticity was adopted to predict the wing shape at the flight condition. Additional models have been added to find the centre of gravity, the mean aerodynamic

centre, static stability parameters and the trim condition of the aircraft. A mathematical technique was suggested to calculate the angle of attack corresponding to the trim condition by representing the lift-pitching moment coefficient curve by a polynomial representation. This reduced the number of evaluation points to determine the aerodynamic performance for each iteration within the optimisation process. All the tools were coded in the MATLAB environment in addition to modify an existing Vortex Lattice code (Tornado VLM) to be applicable for coupling with the 2D aerodynamic solver and the composite structure model.

9.4 Design an Aft-Swept Flying Wing (HALE UAV)

Procedures were presented in the conceptual and preliminary design stages using newly developed tools. A conceptual design for a solar-powered high altitude long endurance aircraft was studied using the conceptual design tool for a surveillance mission over southern Iraq. The mission specifications included the payload, the endurance and the flight level. Then, the reference power available from solar energy and the daylight hours were estimated for the given mission using a solar model. The basic aerofoil characteristics used during the conceptual design stage, enabled estimation of the reference aerodynamic performance parameters as functions of Reynolds number and the main wing geometry. The conceptual design was then used to find the main optimised characteristics of the aircraft to be used to initiate the preliminary design stage.

An aft-swept aircraft layout was adopted for the design. The aircraft elements were then distributed inside the wing in a way to reduce the bending stress at the root section. The final wing geometry has been optimised to achieve the operational wing shape by finding the optimal twist and sweep of the wing. The design variables were for the unloaded wing shape while the optimisation target was towards the performance of the wing shape in flight. The procedure of the preliminary design began by finding the minimum required sweep to achieve a stability margin of about 0.05. This was done by increasing the sweep until the targeted static margin was reached. However, the resulting sweep was inadequate to reach the reference trimmed lift coefficient of 0.8. Then, the sweep angle was investigated to find the minimum sweep required to achieve 0.8 trimmed lift coefficient by using the optimisation tool.

Number of design cases have been optimised to investigate how the sweep angle, spar location and static margin can influence the aerodynamic and structural performances. The conclusion of this study indicated that the elastic deformation has a considerable effect on the performance. The elastic deformation can destabilise the wing and could worsen the

stability at low aerodynamic loading due to the wash-out twist and the weight of the wing itself. However, the spar location can be utilised to mitigate the elastic deformation and hence the stability. But this may have an influence on the spar weight due to additional wing torsions. The static margin study indicated that a small static margin value necessitates less sweep and washout twist to achieve a specific trimmed lift coefficient. Moreover, the results showed that the required sweep angle and amount of geometric washout are associated with the required trimmed lift coefficient and reference static margin.

The final design, called the SUMER, has been selected from the presented design cases. It has 8 degree sweep, $0.34x/c$ spar location and 0.05 static margin. This case was selected among the design cases because of its low drag coefficient and acceptable longitudinal static stability. The aerodynamic and structure of SUMER have been studied at different flight speeds. The study showed that the aerodynamic centre was affected by the elastic deformations and hence the static longitudinal stability. Moreover, for the final design (SUMER), the results indicated that increasing the wing loading will enhance the longitudinal stability. This was due to the appropriate spar location that was selected in a way the elastic twist deformations due to bending will overcome the elastic twist due to the aerodynamic torsion at higher wing loading.

An assessment has been conducted by comparing the results achieved by the preliminary design stage with those results concluded by the conceptual design stage and the mission requirements. The finding was that the design process proved to be very good in matching the weight, lift coefficient and total drag coefficient. This indicates that the final design had met the mission requirements. Moreover, the design procedure and the developed tools in this thesis proved its capability of predicting and designing the aircraft characteristics using low order methods enabling the designer to reach a feasible design with low computational time and a good level of accuracy.

As expected, when using high order CFD analysis, the results will be different from those obtained by lower order CFD analysis. The flight shape of the wing at different angles of attack have been modelled in ANSYS-FLUENT. The results indicated good lift coefficient estimates at lower angles of attack. The drag counts were overestimated when compared with the results of the Quasi-3DM. Moreover, the pitching moment was underestimated but at the same time, the trend was similar to that obtained at the preliminary design stage.

CHAPTER 10

10 CONCLUSIONS AND RECOMMENDATIONS

The main goal of this thesis was the analyses of solar powered unmanned aerial vehicles designed for extended flight operations at high altitudes. The main interest of the study was the focus on utilising an aft-swept flying wing for high altitude applications. This chapter presents the main concluding remarks in addition to recommendations for further work

10.1 Conclusions

The main conclusions can be summarised as follows:

- 1 Employing the individual weight of all the aircraft elements and the power losses in the conceptual design tool led to more realistic estimations for the total weight and the power of the aircraft. Moreover, formulating the total drag as a function of Reynolds number and the aerofoil performance produced more accurate estimate for the drag of the final design at the preliminary design stage. Several design parameters were studied using the conceptual design model. The significant conclusion was the sensitivity of the total weight when operating at high altitudes.
- 2 The newly developed composite structure model using low order stress analysis proved its ability in estimating the structural weight in addition to evaluating the elastic deformations. The computation time was quite low (a few seconds) which indicated its suitability for employment in a multidisciplinary optimisation process. Moreover, the structural weight estimated by the composite structural model showed good agreement with that obtained by an empirical equation (Rizzo's model) which was used in the conceptual design stage.
- 3 A design procedure has been presented, which was initiated by a conceptual design stage followed by a more detailed design phase using a multidisciplinary optimisation process. The design procedure and the developed tools in this thesis proved its capability of predicting and designing the aircraft characteristics using low order methods enabling the designer to reach a feasible design with low computational time and a good level of accuracy.

- 4 An aft-swept aircraft layout was adopted for the design case study to fly for a specific mission over southern Iraq. The study showed the possibility of using this configuration at high altitudes. However, the elastic deformations greatly influenced the aerodynamic performance and stability. Such issues could be dealt with by easily adjusting the spar location by utilising the aerodynamic torsion such a manner to balance the loads. This mitigated the reduction in incidence angle induced by the bending deformation at the cost of a slightly heavier structure.

10.2 Recommendations

The design of solar powered high altitude long endurance UAVs represents a substantial challenge since numerous inter-related engineering disciplines are needed for analysis. However, this study investigated some of the main challenges of the design using low order analyses. The developed tools have a number of limitations and also some of the assumptions that were made can be improved. These can be summarised as follows:

10.2.1 Recommendations for the Developed Tools

(A) Conceptual Design Tool

1. Develop an empirical equation to predict the Oswald factor for the wing based on more realistic data and employ it in the mass equation. The available empirical equations were evaluated for a set of conventional aircraft considering the parasite drag of fuselage and the interference drag.
2. Enhance the prediction of the profile drag equation with a safety factor.
3. Support the representation of aircraft elements by additional requirements such as the wing shape effects on the efficiency of the solar cells, additional energy backup and financial constraints.
4. Evolve the model to design aircraft for multi-payload systems and different altitude and latitude defined in mission requirements.
5. Track the development of evolving technologies for new generation aircraft systems to modify the fractions that are used to represent the mass and power of the aircraft elements.

(B) The Quasi 3DM

- 1- Support the Strip Theory by pre-calculated results for the aerofoil performance at different operational Reynolds numbers. These results can be achieved using experiment data or by conducting high order CFD analysis. This can replace the

need for a 2D aerodynamic solver and reduce the time consumption and increase the accuracy during the optimisation process.

- 2- Employ viscous evaluation for the pitching moment coefficient in the Strip Method. This will replace the need for the pitching moment coefficient obtained by the Vortex Lattice Method.

(C) The Composite Structured Model (CSM)

- 1- Employ aeroelasticity influences during spar design stage.
- 2- Employ non-linear finite beam element to evaluate the elastic deformations. This will be beneficial especially at higher wing loadings.
- 3- Use the local load factor instead of global one in the spar sizing process. This necessitates investigating the critical loads at each part of the wing at expected flight conditions.
- 4- Add additional failure criteria such as the flutter, buckling and reversal problems in the sizing process.
- 5- Develop the empirical equations that were adopted to estimate the weight of the non-spar elements using more recent design data.

(D) Optimisation Tool

- 1- Use multi objective optimisation algorithm for different targets such as the drag, static stability, weight, maximum deflections and dynamic stability.
- 2- Try other optimisation algorithms.

10.2.2 Recommendations for the Design Procedure

- 1- Use more design iterations between the conceptual design and the preliminary design stages to achieve optimal solutions. For example, the zero-lift drag coefficient, the span efficiency and the reference lift coefficient can be amended and used again in the conceptual design stage. Further analysis in the preliminary design stage can be conducted until the solution converges.
- 2- Enhance the prediction of the mean aerodynamic centre location. It can be located by using the local aerodynamic centre of the aerofoil and hence the mean aerodynamic centre of the wing. Higher order CFD analysis may be used instead.
- 3- Increase the number of variables that represent the wing twisting during the optimisation process. This may lead to an optimal wing which generates less drag.

- 4- Introduce additional design constraints during the optimisation such as the aircraft performance at different flight conditions. The stability of aircraft at lower angles of attack could be one of these constraints.
- 5- Employ other variables in the optimisation process such as the sweep, dihedral and taper ratio of the wing. However, these may require more design constraints and must be offered within the optimisation process.
- 6- Investigate in more detail the resulting aeroelastic effects. However, this will require more sophisticated aerodynamic and structural analyses.
- 7- Design the control surfaces for the wing and investigate the dynamic stability of the aircraft.

11 APPENDICES

Appendix I: Optimiser Code (Canonical Genetic Algorithm)

An optimiser code has been written within MATLAB environment by using the Canonical Genetic Algorithm.

I-1 Canonical Genetic Algorithm (CGA)

The CGA is based on the principle of genetic evolutionary processes (Holland John, 1992) with the help of work published in references (Cao & Wu, 1999; Coley, 1999; Khan, 2010; Mitchell, 1999). This algorithm has a standard procedure, consists of four main steps; initialization, selection, crossover and mutation, which are repeated until finding a certain optimal value or until reaching a maximum number of iterations.

However, before describing the method, some terms used with the Genetic Algorithm must be known. For example, assume that the objective function is (f), which is a function of three variables x, y and z . For giving optimisation variables x_i, y_i, z_i denoted “chromosome”, the value of (f_i) will be called “fitness”. The possible values of the variables can be generated using the upper and the lower bounds defined by the user. The generated values of the variables are called design variable pool or population. In this method, the real values of the variables will be used instead of converting their values to the binary form as used in the classical Genetic Algorithm.

1- Initialisation

In this step, the initial chromosomes (the initial parents) will be selected. These chromosomes will be selected randomly from the populations. Moreover, every value of any variable has an equal chance to form the parents without repeating the same value for more than one parent. The number of these parents should be more than the number of variables to ensure that the best parents will remain during the optimisation process as will see in the next steps.

2- Selection

The fitness values of the selected parents from the previous step will be evaluated using the given fitness function. The fitness values are then re-arranged from the best to the worse parents. Each parent will follow its fitness during the arrangement. If the best fitness value has met the target, the process will be stopped. If not, the process will continue to the next step.

3- Crossover

In this step, 50 % of the bad parents will be replaced by the best parents. The best parents are called the elite.

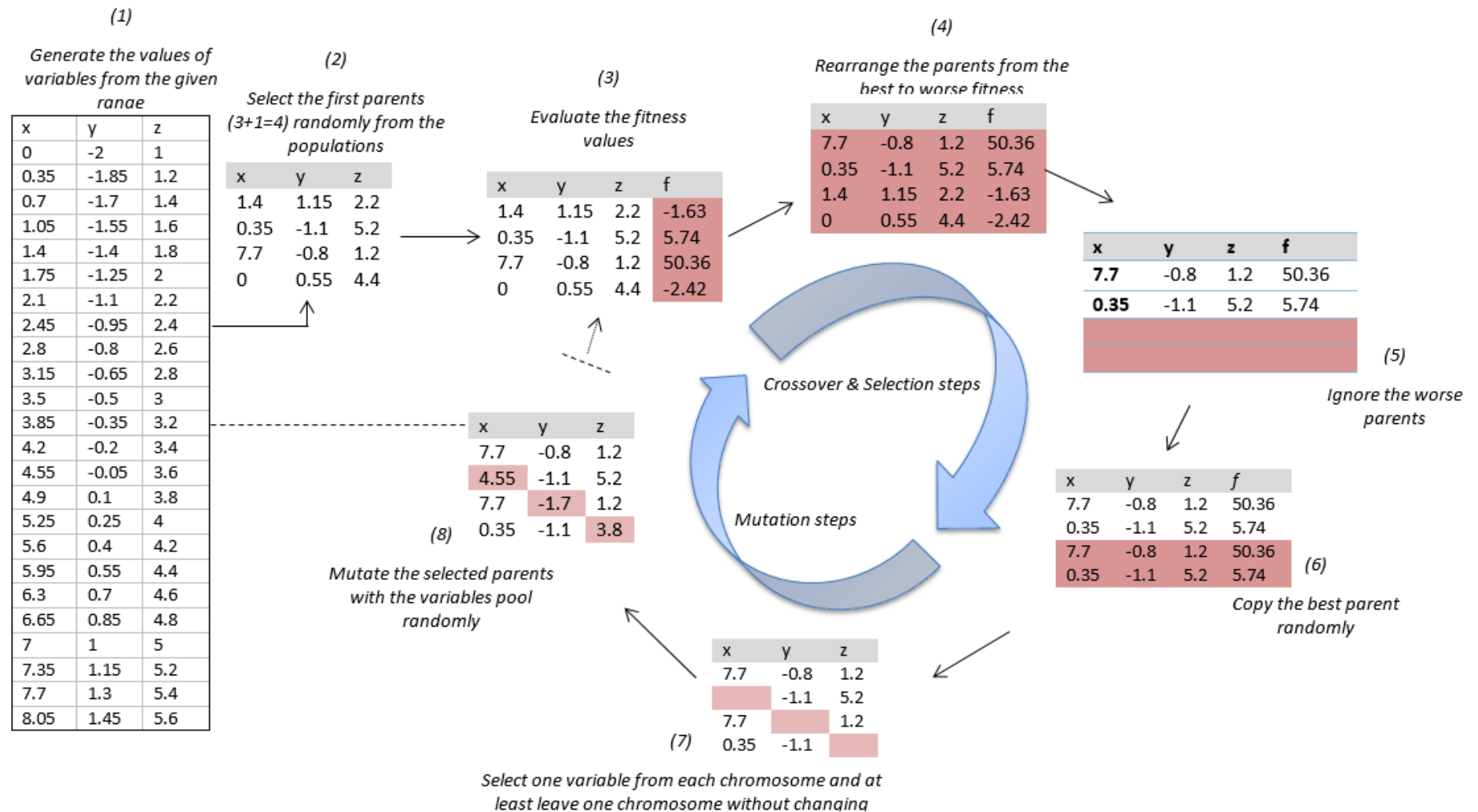
4- Mutation

The parents (chromosomes) from the previous step are then mutated by new variables that are selected randomly from the populations. Each chromosome will change in one variable of its structure. At least one of these chromosomes will not be mutated to ensure that the best parent will remain for the comparison purpose in the next iteration. The new chromosomes, which are called “children”, will be “parents” for the next generation.

The step 2-4 will be repeated again until a designated iteration number is completed or the target is satisfied. When the optimisation is stopped, the first chromosome of the last set of parents will contain the best the optimal values for the variables. In the next page, a simple example is presented to show the procedure. The next section presents the code which were written according to this algorithm.

Canonical Genetic Algorithm Procedure with an example

The object is to find maximum $f = \frac{x^2}{z} - zy$, if the variables x,y,z , are vared as the following: $0 < x < 8.05$; $-2 < y < 1.45$; $1 < z < 5.6$



I-2 The Optimiser Code

Optimiser.m

```
% This Code contain the setting of the Canonical Genetic Algorithm
% this code calls CGA.m which contains the optimisation code
% the setting hear is just an example for problem for 6 variables
clear
Lb=[-5 -5 -5 -5 -5 -5]; % lower bound
Ub=[ 1 1 1 1 1 1 ]; % upper bound
Pin=[0.5 0.5 1 1 0 0 ]; % initial value of the variables
nvars=6; % No. of variable
div=40; % number of divisions of the variables
Max_Itre=100; % maximum iteration
job=1; % job =2 to maximise, job=1 to minimise
[Prt,Fitness]=CGA(Ub,Lb,Pin,nvars,div,Max_Itre,job);
P=Prt(1,:); % Optimal variables
%===== END Optimiser.m =====
```

CGA.m

```
function [Prt,Fitness]=CGA(Ub,Lb,Pin,nvars,div,Max_Itre,job)
% this code contains the optimisation code according to the Canonical
Genetic Algorithm
% See the Optimiser.m for defining the optimisation variables and their
ranges
% this code calls the fitness function TheObjective.m
% Prt: is the best variables set accumulated during the optimisation
process
% Fitness: is the best fitness value

extra=1; % add extra parent
% Generate the variable pool
=====
for i=1:nvars
    p(i,1:div)=Lb(i):abs((Ub(i)-Lb(i))/(div-1)):Ub(i);
end
p=p';
% Generate the first parents
np=nvars+extra;
for i=1:np
    for n=1:nvars
        R_o=round(randperm(div));
        Prt(i,n)=p(R_o(i),n);
        R_o=round(randperm(div));
    end
end
% apply the initial parents
Prt(1,1:nvars)=Pin;
for i=1:extra
    [f(i)]= TheObjective(Prt(i,:));
end
%===== Optimization process =====
for glob=1:Max_Itre
    glob
    % Evaluate the fitnesses value
    for i=extra+1:np
        [f(i)]= TheObjective(Prt(i,:));
    end
```

```

% Cross over and apply conditions
switch job % set the conditions of the minimum lift and Drag
case 1 % this done if we need minimum induced drag
    [B,IX]=sort(f,'ascend');
%-----
case 2 %this done if we need maximum Lift
    [B,IX]=sort(f,'descend');
otherwise
end % end switch

for i=1:np
    for n=1:nvars
        Prt1(i,n)=Prt (IX(i),n);
        f1(i)=f (IX(i));
    end
end
Prt=Prt1; f=f1;
Prt(1,:)
% copy the best instead the bad
bad=round(np/2);
q=1;
for i=bad:np
    Prt(i,:)=Prt(q,:);
    q=q+1;
end
% Mutation process
n=nvars;
for i=np:-1:extra+1
    pp=randperm(div);
    Prt(i,n)=p(pp(1),n);
    n=n-1;
end
Fitness(glob)=B(1);
Prt(1,:)
Fitness(glob)
Iter(glob)=glob;
%Draw the fitness value =====
plot(Iter(glob),Fitness(glob),'Marker','*');
drawnow;
hold on;

end
%=====END CGA.m =====

```

Appendix II: Conceptual Design Tool

```

% This code is to design a solar powered high altitude long endurance UAV
% for given mission requirements

clear
%== Aerodynamics =====
CL= 0.80;           % Aircraft lift coefficient
e= 0.95 ;          % span efficiency factor
Ppayload= 1250;    % [W] Payload power consumption
Mpayload= 100;     % [kg] Payload mass
%===== Irradiance conditions=====
alt=17000;         % [m] Altitude
Itot=33.37e6;      % [J/m2/day] Solar Radiation
Tday=12.32*3600;   % [s] Daytime duration
%===== Solar Irradiance =====
Imax=Itot*(pi/2)/(Tday); % [] Maximum Irradiance
Ksolmargin= 1;     % - Irradiance margin factor
Tnight=24*3600-Tday; % [s] Night time
%===== Wing & fuselage Structure =====
Kstruct= 1.548;    % [kg/m3] Structural mass constant W=k b^x1 AR^x2
x1= 1.312;        % - Structural mass area exponent
x2= -0.0046;      % - Structural mass aspect ratio exponent
g=9.8;
%===== Propulsion group =====
Kprop= 0.0045;    % [kg/W] Mass to power ratio of propulsion unit
Qprop= 0.85;      % - Efficiency of propeller
Qgrbox= 0.95;     % - Efficiency of gearbox
Qmot= 0.95;       % - Efficiency of motor
Qctrlr= 0.95;     % - Efficiency of motor controller
%===== Battery and Stepdown converter =====
Qchrg= 0.99;     % - Efficiency of battery charge
Qdischrg= 0.60;  % - Efficiency of battery discharge
Kbatt= 550*3600; % [J/kg] Energy density of battery or fuel cell
Qbec= 0.985;     % - Efficiency of step-down converter
%===== Solar cells =====
KSC= 0.25 ;      % [kg/m2] Mass density of solar cells
Kencaps= 0.0;    % [kg/m2] Mass density of encapsulation
Kmppt= 0.00047; % [kg/W] Mass to power ratio of mppt
Qcells= 0.30;   % - Efficiency of solar cells
Qcbr=0.9;       % - Efficiency of cambered configuration
Qmppt= 0.95;    % - Efficiency of mppt
%===== Avionics =====
Kav=0.03;        % - avionic Mass to structure mass ratio
Klg=0.018;       % landing gear weight fraction
Kpav=6;          % [kg/W] avionic Mass to power ratio

% Find Density at given altitude =====
alt_array=[0, 1000, 2000, 4000, 6000, 10000, 15000, 20000, 25000, 30000];
vis_array=[1.789, 1.758, 1.726, 1.661, 1.595, 1.458, 1.422, 1.422, 1.448,
1.475]*1e-5;
rho_array=[1.224,1.11,1.006,0.819, 0.659, 0.413,0.192,0.087,0.039,0.017];
dens =spline(alt_array,rho_array,alt); % Air density at given altitude
Viscosity=spline(alt_array,vis_array,alt); % Air viscosity at given
% altitude [kg/m^3]
%=====
ARi=15; ARE=33; ARs=1; % the range of aspect ratio and increment
InitSol=800; % initial solution
jj=0;joj=1;

```

```

for AR =ARi:ARs:ARE
    CD_ind = CL^2 / (e*pi*AR);
    i=1;
for b=30:1:180
    Q1=(Tday+Tnight/(Qchrg*Qdischrg))/
        (Qcells*Qcbr*Qmppt*Ksolmargin*Imax*Tday*2/pi);
    Q2=(KSC+Kencaps+Kmppt*Imax*Qcbr*Qcells*Qmppt);
    K2=Q1*Q2;
    Qlos=Qctrlr*Qmot*Qgrbox*Qprop;
    x3=0.471;Kfr=5.0322;
    AA=(1/Viscosity*sqrt(2*g*dens/(CL*AR)))^(-x3)*Kfr/(CL^1.5*b)
        *sqrt(2*AR*g^3/dens)*(Tnight/(Qdischrg*Kbatt*Qlos)
            +Kprop/Qlos+K2/Qlos);
    BB=CL^0.5/(e*pi*b)*sqrt(2*g^3/(AR*dens))
        *(Tnight/(Qdischrg*Kbatt*Qlos)+Kprop/Qlos+K2/Qlos);
    CC=Kav+Klg+((Tnight/(Qdischrg*Kbatt))*Kpav*Kav+Kpav*Kav*K2)/Qbec-1;
    DD=Tnight*Ppayload/(Qdischrg*Kbatt*Qbec)+Mpayload
        +Kstruct*b^x1*AR^x2+K2*Ppayload/Qbec;
    clear fun x
    fun = @(x)(AA*x^(1.5-(0.5*x3))+BB*x^1.5+CC*x+DD);
    m(i) = fzero(fun,InitSol);
    vell=sqrt(2*m(i)*g/(CL*b^2/AR*dens));
    Re=dens*vell*b/AR/Viscosity;
    CDa=Kfr/Re^(x3);
    CD=CDa+CD_ind;

if (isnan(m(i))==0)
    P_level(i)      = CD/CL^1.5*sqrt(2*AR*g^3/dens)*m(i)^1.5/b; % level
                                                            % flight power
    m_af(i)         = Kstruct*AR^x2*b^x1;                    % airframe mass
    m_av(i)         = Kav*m(i);                              % avionic mass
    p_av(i)         = m_av(i)*Kpav;                          % avionic power
    P_elec_tot(i)   = P_level(i)/Qlos+(p_av(i)+Ppayload)/Qbec; % total
                                                            % electric power
    m_bat(i)        = P_elec_tot(i)*Tnight/(Qdischrg*Kbatt); % battery mass
    A_sc(i)         = Q1*P_elec_tot(i);                      % solar panels area
    m_sc(i)         = (KSC+Kencaps)*A_sc(i);                 % solar panels mass
    m_mppt(i)       = (Kmppt*Imax*Qcells*Qcbr*Qmppt)*A_sc(i); % mppt mass
    P_sc(i)         = (Imax*Qcells*Qcbr*Qmppt)*A_sc(i); % solar electrical
                                                            % power max
    m_prop(i)       = Kprop*P_level(i)/Qlos;                 % propulsion group mass
    v(i)            = sqrt(2*m(i)*g/(CL*dens*b*b/AR)); % level flight speed
    D(i)            = m(i)*g/CL*CD;                          % total drag
    A(i)            = b^2/AR;                                 % wing surface
    m_lg(i)         = Klg*m(i);                              % landing gear mass
    CDo(i)          = CDa;                                    % aerofoil drag coeff.
    CDin(i)         = CD_ind;                                 % induced drag coeff.
    RE(i)           = Re;                                     % Reynolds number
    SCratio(i)     = A_sc(i)/A(i)*100; % ratio of the solar panels area
end

if (isnan(m(i))==1) || (A_sc(i) > b*b/AR)
    m(i)            = NaN;
    P_level(i)      = NaN;
    m_af(i)         = NaN;
    P_elec_tot(i)   = NaN;
    m_bat(i)        = NaN;
    A_sc(i)         = NaN;
    m_sc(i)         = NaN;
    m_mppt(i)       = NaN;
    P_sc(i)         = NaN;

```

```

        m_prop(i)      = NaN;
        v(i)          = NaN;
        D(i)          = NaN;
        A(i)          = NaN;
        m_av(i)       = NaN;
        p_av(i)       = NaN;
        m_lg(i)       = NaN;
        SCratio(i)    = NaN;
    end
    Span(i)=b;
    i=i+1;
end % End b

if max(m)>0
% Find the min m and its location for each AR -----
minM=min(m); % minimum weight
LminM=find(m==minM); % location of the min weight within the matrix
OPatAR(joj,:)= [m(LminM), P_level(LminM), m_af(LminM), P_elec_tot(LminM)
, m_bat(LminM), A_sc(LminM), m_sc(LminM), m_mppt(LminM), P_sc(LminM),
m_prop(LminM), v(LminM), D(LminM),
A(LminM), m_av(LminM), p_av(LminM), m_lg(LminM), Span(LminM), AR, CDo(LminM), CD
in(LminM), RE(LminM)/1000000, SCratio(LminM)];
joj=joj+1;
% Draw the design space. Here the function DragSolar will be called
jj=jj+1;
DrawSolar(m, P_level, m_af, P_elec_tot, m_bat, A_sc, m_sc, m_mppt, P_sc, m_prop, v,
D, A, AR, Span, jj, ARe, ARi, ARs, m_av, p_av)
AArr(jj)=AR; M(jj,:)=m;
end
end % End AR
%== The Final Optimal -----
MinOptARs=min(OPatAR(:,1));
MinOptLo=find(OPatAR==MinOptARs);
TheOptimal=OPatAR(MinOptLo,:); % create the vector contain the minimum
% mass and its corresponding characteristics
%===== END =====

```

Appendix III: Panel Method

It is a technique for solving incompressible, irrotational potential flow governed by the Laplace equation around the aerofoil geometry. According to the panel method, the aerofoil surface can be represented by straight-line panels as shown in Figure 10-1. In this model, distribution of sources and vortices are assumed around the geometry surface. Along the panels, the vortex distribution γ is the same on each panel, while the source strength distribution (σ_i) is constant on each panel and differs from panel to panel. The tangential velocity in each panel can be evaluated by applying the boundary condition whereby the transpiration velocity (normal velocity) is zero in each collecting point of each panel. Once the tangential velocities are found, the pressure is then calculated using the Bernoulli equation. The lift and pitching moment coefficients are then calculated by integrating the pressure around the aerofoil. The method adopted here is detailed in (Houghton & Carpenter, 2003; Moran, 2003; Wauquiez, 2009). However, the main equations are given below.

The total potential function ϕ is given by:

$$\phi = \phi_\infty + \phi_s + \phi_v \tag{11.1}$$

where ϕ_∞ denotes potentials corresponding to the free stream, ϕ_s is potentials corresponding to the source distribution, ϕ_v is potentials corresponding to the vortex distribution.

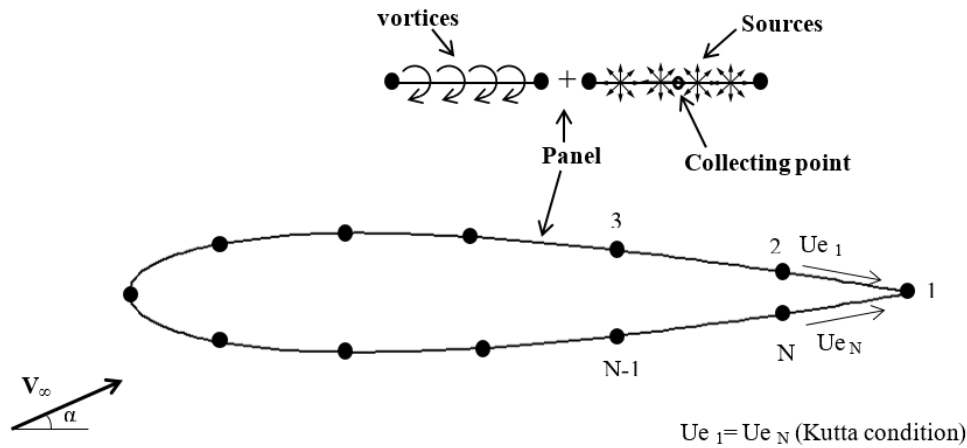


Figure 11-1 Discretization of an aerofoil contour into panels

Resolving this system results in two equations which are the tangential and transpiration velocities at the collecting points.

$$Ue_i = \bar{V}_\infty \hat{t}_i + \sum_{j=1}^N \sigma_j T_{i,j} + \gamma T_{i,N+1} \quad (11.2)$$

$$Vn_i = \bar{V}_\infty \hat{n}_i + \sum_{j=1}^N \sigma_j N_{i,j} + \gamma N_{i,N+1} \quad (11.3)$$

1- Ue_i and Vn_i are the tangential and transpiration velocities at the midpoint of panel (i), α is the angle of attack, V_∞ is the freestream velocity and N is the total number of panels

2- \hat{t}_i and \hat{n}_i are the tangential and normal vectors of the panel i . They are given by:

$$\hat{t}_i = \cos\theta_i \hat{I} + \sin\theta_i \hat{J} \quad (11.4)$$

$$\hat{n}_i = -\sin\theta_i \hat{I} + \cos\theta_i \hat{J} \quad (11.5)$$

where θ_i is the orientation of the panel respect to the x axis.

3- $T_{i,j}$ and $N_{i,j}$ are coefficients representing the tangential and perpendicular velocities induced at the collecting point of the panel (i) by the source of unit strength distribution of the panel (j).

$$N_{i,j} = v_{PQ} \hat{n}_i = v_{xQ} \hat{n}_i \cdot \hat{t}_j + v_{yQ} \hat{n}_i \cdot \hat{n}_j \quad (11.6)$$

$$T_{i,j} = v_{PQ} \hat{t}_i = v_{xQ} \hat{t}_i \cdot \hat{t}_j + v_{yQ} \hat{t}_i \cdot \hat{n}_j \quad (11.7)$$

where v_{xQ} , v_{yQ} are the velocity components induced at point P due to the sources on a panel centred at point Q as in Figure 11-2. They are calculated by:

$$v_{xQ} = -\frac{1}{2} \ln \left[\frac{\left(x_Q + \frac{\Delta s}{2}\right)^2 + y_Q^2}{\left(x_Q - \frac{\Delta s}{2}\right)^2 + y_Q^2} \right] \quad (11.8)$$

$$v_{yQ} = - \left[\tan^{-1} \left(\frac{x_Q + \frac{\Delta s}{2}}{y_Q} \right) - \tan^{-1} \left(\frac{x_Q - \frac{\Delta s}{2}}{y_Q} \right) \right] \quad (11.9)$$

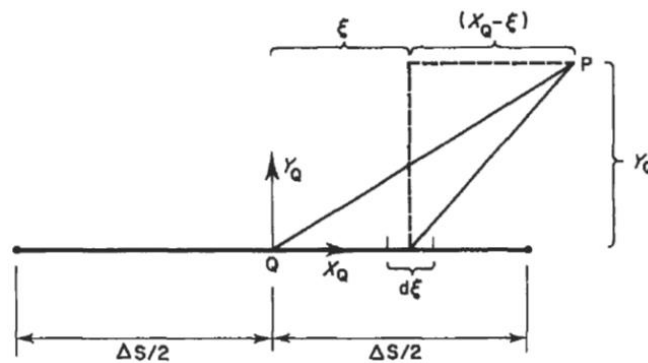


Figure 11-2 The components of the velocity induced at a point due to the sources (Houghton & Carpenter, 2003)

- 4- $T_{i,N+1}$ and $N_{i,N+1}$ are the tangential and perpendicular velocities induced at the collecting point of the panel (i) by the vortices of the panel (j).

$$T_{i,N+1} = \sum_{j=1}^N \hat{T}_{i,j} \quad (11.10)$$

$$N_{i,N+1} = \sum_{j=1}^N \hat{N}_{i,j} \quad (11.11)$$

And

$$\hat{N}_{i,j} = \hat{v}_{PQ} \hat{n}_i = \hat{v}_{xQ} \hat{n}_i \cdot \hat{t}_j + \hat{v}_{yQ} \hat{n}_i \cdot \hat{n}_j \quad (11.12)$$

$$\hat{T}_{i,j} = \hat{v}_{PQ} \hat{t}_i = \hat{v}_{xQ} \hat{t}_i \cdot \hat{t}_j + \hat{v}_{yQ} \hat{t}_i \cdot \hat{n}_j \quad (11.13)$$

where \hat{v}_{xQ} and \hat{v}_{yQ} are the components of the velocity induced at point P due to the vortices on a panel centred at point Q as shown in Figure 11-3:

$$\hat{v}_{xQ} = \gamma \left[\tan^{-1} \left(\frac{x_Q + \frac{\Delta s}{2}}{y_Q} \right) - \tan^{-1} \left(\frac{x_Q - \frac{\Delta s}{2}}{y_Q} \right) \right] \quad (11.14)$$

$$\hat{v}_{yQ} = -\frac{\gamma}{2} \ln \left[\frac{\left(x_Q + \frac{\Delta s}{2} \right)^2 + y_Q^2}{\left(x_Q - \frac{\Delta s}{2} \right)^2 + y_Q^2} \right] \quad (11.15)$$

where Δs is the length of the panel, x_Q & y_Q are coordinates of the collocating point.

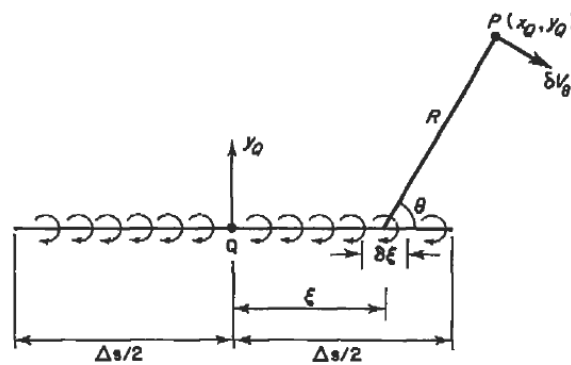


Figure 11-3 The components of the velocity induced at a point due to the vortices (Houghton & Carpenter, 2003)

The boundary conditions are:

- 1) No flow can penetrate the panel. So, the transpiration velocity (V_n) is set to zero
Accordingly, equation (11.3) can be written as:

$$\bar{V}_\infty \hat{n}_i + \sum_{j=1}^N \sigma_j N_{i,j} + \gamma N_{i,N+1} = V_n = 0 \quad (11.16)$$

- 2) There is no circulation at the trailing edge and the flow leaves the trailing edge smoothly. The Kutta condition was used to ensure that the tangential velocities of the panels at the trailing edge are equal as shown in Figure 11-1. Therefore, applying this condition to equation (10.2) for those two panels at the trailing edge will lead to:

$$\bar{V}_\infty \hat{t}_1 + \sum_{j=1}^N \sigma_j T_{1,j} + \gamma T_{1,N+1} = - \left(\bar{V}_\infty \hat{t}_N + \sum_{j=1}^N \sigma_j T_{N,j} + \gamma T_{N,N+1} \right) \quad (11.17)$$

where 1 and N refer to the two panels at the trailing edge.

The System of equations:

From the two equations of the boundary layer condition, the system of equations can be written as:

$$M a = b \quad (11.18)$$

where M is $(N + 1 \times N + 1)$ matrix and a & b are $(N+1)$ vectors.

$$\begin{aligned} M_{i,j} &= N_{i,j} \\ b_i &= -V_\infty \hat{n}_i \\ a_i &= \sigma_i \end{aligned} \quad (11.19)$$

where: $i=1,2,3,\dots,N$ and $j=1,2,3,\dots,N+1$.

The boundary condition equation (10.16) can be used to evaluate the $N+1$ coefficients:

$$\begin{aligned} M_{N+1,j} &= T_{1,j} + T_{N,j} \\ a_{N+1} &= \gamma \\ b_{N+1} &= -\bar{V}_\infty \cdot (\hat{t}_1 + \hat{t}_N) \end{aligned} \quad (11.20)$$

This system of linear equations are functions of the unknowns σ_i and γ which can be solved numerically. Once σ_i and γ are found, the tangential velocity can be calculated using equation (11.2).

Appendix IV: The 2D inviscid-viscous Aerodynamic model (IVM)

```

function[cl_inv,cd_press,cd_vis,XtrU,XspU,XtrL,XspL]=IVM(alpha,Re,XP,YP,N
,ne,density)
% Input:=====
% Re: Reynold Number
% alpha: angle of attack
% N: Number of panels
% XP,YP: the aerofoil coordinates
% ne: Kinematic viscosity
% density: air density
% Output:=====
% cl_inv: the lift coefficient obtained by the Panel method
% cd_press,cd_vis: coefficients of pressure and profile drag respectively
% XtrU, XtrL: locations of transition point at the upper and lower
surfaces respectively
% XspU,XspL: locations of separation at the upper and lower surfaces
%-----
% functions of the Panel Method [InfCoeff, SolvSys]
% functions of the boundary layer equations model [BoundLayer, DVe]
U=1; trans=0; j=0;
%== PANEL METHOD -----
% Influence coefficient -----
[AN,AT,NHAT,THAT,XC,YC]=InfCoeff(XP,YP,N);
%== Solve the system of equations -----
vn(1:N)=0;
[Ue,cp,cl_inv,cd_inv]=SolvSys(AN,AT,XP,YP,U,N,NHAT,THAT,alpha,vn);
%=====

%== Boundary layer development -----

%== find stagnation point -----
% regarding to Hiss and smith results in this code Ue is minus along the
% upper surface
for i=1:N;
    if Ue(i)<0
        j=j+1;
    end
end

% for lower surface
uel(2:j+1)=Ue(j:-1:1);
xcl(2:j+1)=XC(j:-1:1);
ycl(2:j+1)=YC(j:-1:1);
Nl=j+1;
% for upper surface
ueu(2:N-j+1)=Ue(j+1:N);
xcu(2:N-j+1)=XC(j+1:N);
ycu(2:N-j+1)=YC(j+1:N);
Nu=N-j+1;

Istag=j;
xcstag=(xcu(2)+xcl(2))/2; % stagnation coordinate
ycstag=(ycu(2)+ycl(2))/2; % stagnation coordinate

ueu(1)=0; xcu(1)=xcstag; ycu(1)=ycstag;
uel(1)=0; xcl(1)=xcstag; ycl(1)=ycstag;
ix98U=min(find(xcu>0.98));
ix98L=min(find(xcl>0.98));

```

```

% Create the S distance for the upper and the lower surfaces -----
Xu(1:Nu)=0; Xl(1:Nl)=0 ;
for i=2:Nu
    Xu(i)=Xu(i-1)+sqrt((xcu(i)-xcu(i-1))^2+(ycu(i)-ycu(i-1))^2);
End

for i=2:Nl
    Xl(i)=Xl(i-1)+sqrt((xcl(i)-xcl(i-1))^2+(ycl(i)-ycl(i-1))^2);
end
% Increase the mesh density to double -----
XU(1)=Xu(1); XL(1)=Xl(1);
UeU(1)=ueu(1); UeL(1)=uel(1);
p=2;
for i=2:Nu
    XU(p)=(Xu(i-1)+Xu(i))/2;
    UeU(p)=(ueu(i-1)+ueu(i))/2;
    XU(p+1)=Xu(i);
    UeU(p+1)=ueu(i);
    p=p+2;
end
UeU(p-1)=ueu(Nu);
XU(p-1)=Xu(Nu);
Nu=p-1;
p=2;
for i=2:Nl
    XL(p)=(Xl(i-1)+Xl(i))/2;
    UeL(p)=(uel(i-1)+uel(i))/2;
    XL(p+1)=Xl(i);
    UeL(p+1)=uel(i);
    p=p+2;
end
UeL(p-1)=uel(Nl);
XL(p-1)=Xl(Nl);
Nl=p-1;

ix98U=ix98U*2-1;
ix98L=ix98L*2-1;

% Boundary layers for the upper surface -----
[cfu,tawu,cdu,itransu,isperu,Hu,thu,lau,Lu,duEU,UJU,xnewu,NU]=BoundLayer(
UeU,XU,Nu,Re,U,ne,density,ix98U);

if itransu==0
    XtrU=1;
else
    XtrU=xcu(min(find(Xu>XU(itransu))));
end
if isparu==0
    XspU=1;
else
    XspU=xcu(min(find(Xu>XU(isparu))));
end

% Boundary layers for the lower surface -----
uel=-uel;
UeL=-UeL;
[cfl,tawl,cdl,itransl,ispersl,Hl,thl,lal,Ll,duEL,UJL,xnewl,NL]=
BoundLayer(UeL,XL,Nl,Re,U,ne,density,ix98L);

if itransl==0
    XtrL=1;

```

```

else
XtrL=xcl(min(find(Xl>XL(itransl))));% because No of panel was increased
if isparl==0
    XspL=1;
else
XspL=xcl(min(find(Xl>XL(isparl)))); % because No of panel was increased
end

% Normal velocity -----
dodo=Nu;
if isparu>5 ; dodo=isparu; end

if isparu<5
    airfoil=[XP; YP];
end
cdfu=trapz(XU(3:dodo),real(cfu(3:dodo)));
%-----
dodo=Nl;
if isparl>5 ; dodo=isparl; end

cdfl=trapz(XL(3:dodo),real(cfl(3:dodo)));
%== Ploting -----
cd_fr=cdf+cdfu;
cd_vis=real(cdu+cdl); % it is right if no separation is occurred
cd_press=cd_vis-cd_fr;
%===== END of the IVM.m =====

```

SolvSys.m

```

function [vs, cp, cl, cd, Cm]=SolvSys(AN, AT, xp, yp, U, N, NHAT, THAT, alpha, vn)
% This function solves the equations system of the Panel Method
% cl,cd and cm: inviscid lift, drag and pitching moment coefficients
% vs: tangential velocity
% cp: pressure coefficient

NP=N+1;
for j=1:NP
    AN(NP,j)=AT(1,j)+AT(N,j);
    AT(NP,j)=AN(1,j)+AN(N,j);
end

for i=1:N
b(i)=-U*(NHAT(i,1)*cos(alpha)+NHAT(i,2)*sin(alpha))+vn(i);
end
b(NP)=-
U*((THAT(1,1)+THAT(N,1))*cos(alpha)+(THAT(1,2)+THAT(N,2))*sin(alpha));
q=AN\b';
for i=1:N
    qt=0; qtn=0;
    for j=1:N
        qt=qt+q(j)*AT(i,j);
        qtn=qtn+q(j)*AN(i,j);
    end

vs(i)=qt+U*(THAT(i,1)*cos(alpha)+THAT(i,2)*sin(alpha))+q(NP)*AT(i,NP);
cp(i)=1-(vs(i)/U)^2;
end

%Calculate Lift and Drag coefficient -----

```

```

cy = 0.0;
cx = 0.0;
Cm=0;
for i=1:N
    if i==1
        dx=xp(N)-xp(1);
        dy=yp(N)-yp(1);
        xmid=0.5*(xp(N)+xp(1));
        ymid=0.5*(yp(N)+yp(1));
    else
        dx = xp(i-1)-xp(i) ;
        dy = yp(i-1)-yp(i) ;
        xmid=0.5*(xp(i-1)+xp(i));
        ymid=0.5*(yp(i-1)+yp(i));
    end
    cx = cx + cp(i) * dy;
    cy = cy + cp(i) * dx;
    Cm=Cm-cp(i)*(dx*(xmid-0.25)+dy*ymid);
end

cd = cx * cos(alpha) + cy * sin(alpha);
cl = cy * cos(alpha) - cx * sin(alpha);
%===== END of the SolvSys.m =====

```

InfCoeff.m

```

function [AN,AT,NHAT,THAT,XC,YC]=InfCoeff(xp,yp,N)
NP=N+1; U=1;
for i=1:N
    if i==1
        xpl=xp(N);
        ypl=yp(N);
    else
        xpl=xp(i-1);
        ypl=yp(i-1);
    end
    XC(i)=0.5*(xp(i)+xpl);
    YC(i)=0.5*(yp(i)+ypl); % co-ordinates of collocation points.
    S(i)=sqrt((xp(i)-xpl)^2+(yp(i)-ypl)^2);%Calculating panel length.
    THAT(i,1)=(xp(i)-xpl)/S(i); % x coordinate of unit tangent vector.
    THAT(i,2)=(yp(i)-ypl)/S(i); % y co-ordinate of unit tangent vector.
    NHAT(i,1)=-THAT(i,2); % x co-ordinate of unit normal vector.
    NHAT(i,2)=THAT(i,1); % y co-ordinate of unit normal vector.
end

% calculating the influence coefficients-----
AN(1:N,NP)=0.0;
AT(1:N,NP)=pi;

for I=1:N
for J=1:N
    if I==J
        AN(I,J) =pi;
        AT(I,J) =0.0;
    else

        DX=XC(I)-XC(J);
        DY=YC(I)-YC(J);

        XQ=DX*THAT(J,1)+DY*THAT(J,2);
        YQ=DX*NHAT(J,1)+DY*NHAT(J,2);
    end
end

```

```

VX=0.5*log( ((XQ+0.5*S(J))^2+YQ^2 ) / ((XQ-0.5*S(J))^2+YQ^2) );
VY=(atan( (XQ+0.5*S(J))/YQ)-atan( (XQ-0.5*S(J))/YQ) );

NTIJ =0.0;
NNIJ=0.0;
TTIJ =0.0;
TNIJ= 0.0;

for K=1:2
    NTIJ = NHAT(I,K)*THAT(J,K)+NTIJ;
    NNIJ = NHAT(I,K)*NHAT(J,K)+NNIJ;
    TTIJ = THAT(I,K)*THAT(J,K)+TTIJ;
    TNIJ = THAT(I,K)*NHAT(J,K)+TNIJ;
end

AN(I,J) =VX*NTIJ+VY*NNIJ;
AT(I,J) =VX*TTIJ+VY*TNIJ;
AN(I,NP) =AN(I,N+1)+VY*NTIJ-VX*NNIJ;
AT(I,NP) =AT(I,N+1)+VY*TTIJ-VX*TNIJ;
end
end
end
%===== END of the InfCoeff.m =====

```

BoundLayer.m

```

function[cf,taw,cdb,itrans,ispar,H,th,la,L,du,UJ,x,nu]=BoundLayer(ue,xx,
nu,Re,U,ne,density,ix98)
trans=0; ispar=0; itrans=0; taw=0;

%find dUe/dx f1 f2 f3 numerically
[UJ,x,nu]=DVe(ue,xx,nu);

due(1:nu)=UJ(1:nu,2); % dUe/dx

% Laminar flow field [Thwaites Method] =====
% find theta and lambda
th(1) = sqrt(0.075/(Re*due(1))); % momentum thickness
la(1)=th(1)^2*due(1)*Re ; % lambda
rex= x(1)*ue(1)*Re ; % Rex at x
ret= th(1)*ue(1)*Re ; % Reth at th
retmax= 1.174*(rex^0.46+22400*rex^(-0.54));
if ret>retmax
    itrans = 1;
end

if la(1)>0
    L(1)=0.22+ 1.57*la(1)-1.8*la(1)^2;
    H(1)=2.61-3.75*la(1)+5.24*la(1)^2;
end

if la(1)<0
    if la(1)==-0.107
        la(1)=-0.106;
    end;
    L(1)=0.22+ 1.402*la(1)+0.018*la(1)/(la(1)+0.107);
    H(1)=2.088+0.0731/(la(1)+0.14);
end

```

```

for i=2:nu
K = 0.45/Re;
dx = (x(i)-x(i-1));
f1 = UJ (i,3); f2 = UJ (i,4); f3 = UJ (i,5);
dth2ue6 = K*dx/18*(5*f1^5+8*f2^5+5*f3^5);
thsq = ((th(i-1)^2*ue(i-1)^6 + dth2ue6)/ue(i)^6);
th(i)=sqrt(thsq);
la(i)=th(i)^2*due(i)*Re ;

% Calculate Cf and shear force
if la(i)>=0
    L(i)=0.22+ 1.57*la(i)-1.8*la(i)^2;
    H(i)=2.61-3.75*la(i)+5.24*la(i)^2;
end
if la(i)<0
    if la(i)==-0.14
        la(i)=-0.139;
        disp('H(lambda) : Lambda = -0.14 -> Lambda = -0.139');
    end;
    if la(i)==-0.107
        la(i)=-0.106;
        disp('l(lambda) : Lambda = -0.107 -> Lambda = -0.106');
    end;
    L(i)=0.22+ 1.402*la(i)+0.018*la(i)/(la(i)+0.107);
    H(i)=2.088+0.0731/(la(i)+0.14);
end

    if la(i)<-0.09
        trans = 1; itrans = i;
        LaminarSaparation=la(i);
        break;
    end

    cf(i)=2*L(i)/(Re*ue(i)*th(i));
    tauw(i)=density*ne*ue(i)/th(i)*(la(i)+.009)^0.62;
% find Transition point [Michel's Transition Criterion] -----
    rex = x(i)*ue(i)*Re ;
    ret = th(i)*ue(i)*Re ;
    retmax= 1.174*(rex^0.46+22400*rex^(-0.54));
    if ret>retmax
        trans = 1; itrans = i;
        break;
    end
end

%==== Turbulent flow field [Head's Method] =====
if trans==1
    if H(itrans)<1.2
        H(itrans)=1.2;
    end
    if H(itrans)>2
        H(itrans)=1.6;
    end
%==== H1 from H at separation point -----
    if H(itrans) <1.1
        H1(itrans) = 16;
    end
    if H(itrans) <= 1.6
        H1(itrans) = 3.3 + 0.8234*(H(itrans)-1.1)^(-1.287);
    end
    if H(itrans) > 1.6

```


DVe.m

```

function [UJ,x,n]=DVe (u,x,n)
% this code calculates the matrix UJ which contain
% UJ(ue,du/dx,f1,f2,f3)
% f1 f2 f3 are used in the integration for the Thwaites Method
% see code BoundLayer

du1=(u(2)-u(1))/(x(2)-x(1));
if du1<0
    ue1=u(1); s1=x(1);
    ue2=(u(1)+u(2))/2; s2=(x(1)+x(2))/2;
    du1=(ue2-ue1)/(s2-s1)
    if du1<0
        ue1=u(1); s1=x(1);
        ue2=(u(1)+ue2)/2; s2=(x(1)+s2)/2;
        du1=(ue2-ue1)/(s2-s1);
    end
end
coeff = sqrt(3/5);
UJ(1:n,1)=u;  UJ(1,2)=du1;
for i=2:n-1
    u1=u(i-1); x1=x(i-1);
    u2=u(i);   x2=x(i);
    u3=u(i+1); x3=x(i+1);
    X=[1 x1 x1^2; 1 x2 x2^2; 1 x3 x3^2];
    U=[u1 u2 u3];
    A=X\U';
    du=A(2)+2*A(3)*x2;
    xm = (x(i)+x(i-1))/2;
    dx = (x(i)-x(i-1));
    xf1 = xm-coeff*dx/2;
    xf2 = xm;
    xf3 = xm+coeff*dx/2;
    f1=A(1)+A(2)*xf1+A(3)*xf1^2;
    f2=A(1)+A(2)*xf2+A(3)*xf2^2;
    f3=A(1)+A(2)*xf3+A(3)*xf3^2;
    UJ(i,2)=du;    UJ(i,3)=f1;    UJ(i,4)=f2;    UJ(i,5)=f3;
    if i==n-1 ;
        UJ(n,2)=A(2)+2*A(3)*x3;
        xm = (x(n)+x(n-1))/2;
        dx = (x(n)-x(n-1));
        xf1 = xm-coeff*dx/2;
        xf2 = xm;
        xf3 = xm+coeff*dx/2;
        f1=A(1)+A(2)*xf1+A(3)*xf1^2;
        f2=A(1)+A(2)*xf2+A(3)*xf2^2;
        f3=A(1)+A(2)*xf3+A(3)*xf3^2;
        UJ(n,3)=f1;    UJ(n,4)=f2;    UJ(n,5)=f3;
    end
end

%===== END of the DVe.m =====

```

Appendix V Spar Sizing

The following steps represent the design procedure of the cross section of a single spar partition for given dimensions (height (h_c), width (w_c) and length (l_{pa})) and given load (shear force (F_{sh}), bending moment (M_X) and torsion (T)):

- 1- Assume symmetrical plies stacking in each spar side.
- 2- Evaluate the dimensions of each flange and web as shown in Figure 11-4:

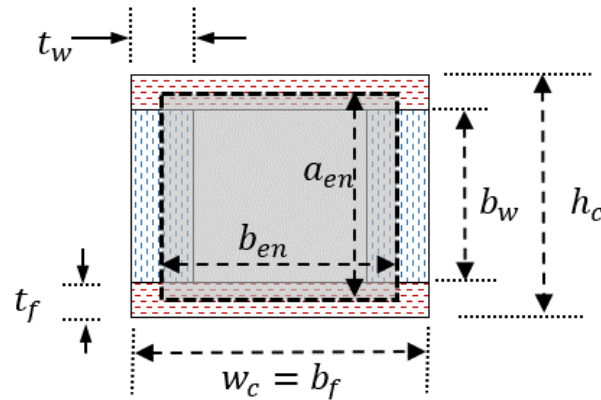


Figure 11-4 Enclosed area of the cross-section contour

- The thickness of each flange and web (t_f and t_w , respectively) can be evaluated by:

$$t_f = \text{no. of plies in each flange} \times \text{ply thickness} \quad (11.21)$$

$$t_w = \text{no. of plies in each web} \times \text{ply thickness}$$

- Height of the web (b_w) is found by:

$$b_w = h_c - 2 t_f \quad (11.22)$$

- The flange width equals the spar width

$$b_f = w_c \quad (11.23)$$

- 3- Evaluate the mechanical properties of each play respect to the x-y coordinate:

- Evaluate the lamina stiffness matrix Q_{ij} for each ply in the cross section respect to the ply's axis 1-2 (Gibson, 2011).

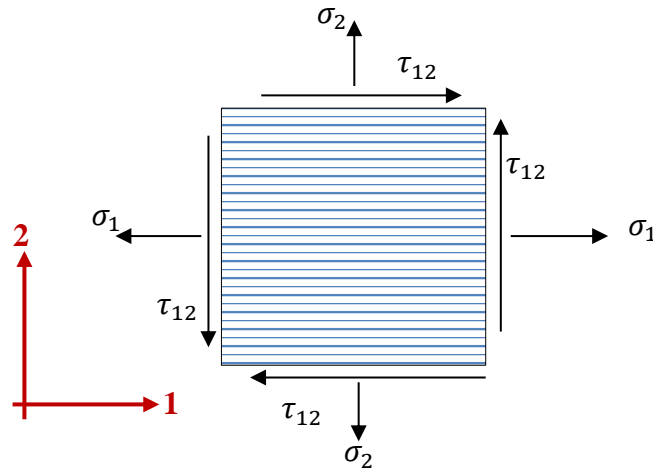


Figure 11-5 Stress system of a ply respect to the 1-2 axis

The stress system matrix is given by (Gay et al., 2002)

$$\begin{bmatrix} \sigma_1 \\ \sigma_2 \\ \tau_{12} \end{bmatrix} = \begin{bmatrix} Q_{11} & Q_{12} & 0 \\ Q_{21} & Q_{22} & 0 \\ 0 & 0 & 2Q_{66} \end{bmatrix} \begin{bmatrix} \epsilon_1 \\ \epsilon_2 \\ \frac{\gamma_{12}}{2} \end{bmatrix} \quad (11.24)$$

where

$$\begin{aligned} Q_{11} &= \frac{E_1}{1 - \nu_{12}\nu_{21}} \\ Q_{12} = Q_{21} &= \frac{\nu_{12}E_2}{1 - \nu_{12}\nu_{21}} \\ Q_{22} &= \frac{E_2}{1 - \nu_{12}\nu_{21}} \\ Q_{66} &= G_{12} \end{aligned} \quad (11.25)$$

(E_1, E_2) and (ϵ_1, ϵ_2) are the elastic constants and the elastic strains in the axis 1-2 of the ply, respectively. ν_{12}, ν_{21} are the corresponding Poisson's ratios. G_{12}, γ_{12} are the shear modulus and the shear strain of the ply in the 1-2 plane.

- Transform the lamina stiffness matrix Q_{ij} to the x - y coordinate system as follows:

$$\begin{bmatrix} \sigma_x \\ \sigma_y \\ \tau_{xy} \end{bmatrix} = [T_r]^{-1} \begin{bmatrix} Q_{11} & Q_{12} & 0 \\ Q_{21} & Q_{22} & 0 \\ 0 & 0 & 2Q_{66} \end{bmatrix} [T_r] \begin{bmatrix} \epsilon_x \\ \epsilon_y \\ \frac{\gamma_{xy}}{2} \end{bmatrix} \quad (11.26)$$

$[T_r]$ is the transformation matrix which is given by:

$$[T_r] = \begin{bmatrix} (\cos \theta)^2 & (\sin \theta)^2 & 2(\cos \theta \sin \theta) \\ (\sin \theta)^2 & (\cos \theta)^2 & -2(\cos \theta \sin \theta) \\ -(\cos \theta \sin \theta) & (\cos \theta \sin \theta) & (\cos \theta)^2 - (\sin \theta)^2 \end{bmatrix} \quad (11.27)$$

where θ is the ply orientation regarding the coordinate system as shown in Figure 11-6.

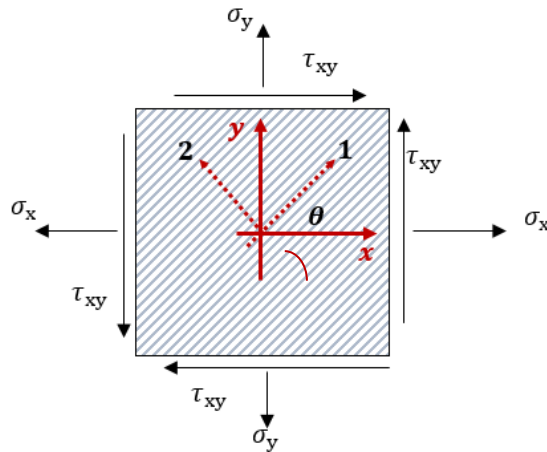


Figure 11-6 Stress system of a ply respect to the coordinate system

The resultant of the transformation is:

$$\begin{bmatrix} \sigma_x \\ \sigma_y \\ \tau_{xy} \end{bmatrix} = \begin{bmatrix} \bar{Q}_{11} & \bar{Q}_{12} & \bar{Q}_{16} \\ \bar{Q}_{12} & \bar{Q}_{22} & \bar{Q}_{26} \\ \bar{Q}_{16} & \bar{Q}_{26} & \bar{Q}_{66} \end{bmatrix} \begin{bmatrix} \epsilon_x \\ \epsilon_y \\ \gamma_{xy} \end{bmatrix} \quad (11.28)$$

- Evaluate young's modulus of each ply ($E_{x_{ply}}$ and $E_{y_{ply}}$) by (Gay et al., 2002; Harris, 1999):

$$E_{x_{ply}} = \frac{1}{\frac{(\cos \theta)^4}{E_1} + \left[\frac{-2\nu_{12}}{E_1} + \frac{1}{G_{12}} \right] (\cos \theta)^2 (\sin \theta)^2 + \frac{(\sin \theta)^4}{E_2}} \quad (11.29)$$

$$E_{y_{ply}} = \frac{1}{\frac{(\cos \theta)^4}{E_2} + \left[\frac{-2\nu_{12}}{E_1} + \frac{1}{G_{12}} \right] (\cos \theta)^2 (\sin \theta)^2 + \frac{(\sin \theta)^4}{E_1}} \quad (11.30)$$

4- Evaluate the mechanical properties of each spar side (flanges and webs)

- Evaluate the stiffness matrices $(ABD)_{web}$ and $(ABD)_{flange}$ as well as their inverses $(abd)_{web}$ and $(abd)_{flange}$ at each mid-plane side (flanges and webs) considering each side is as a laminated plate as in Figure 11-7:

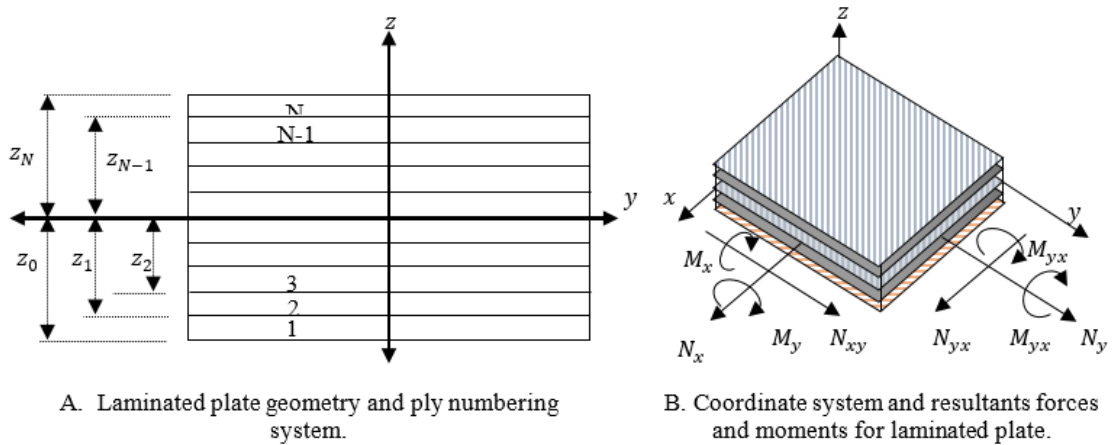


Figure 11-7 Laminate plate geometry

The laminate extensional stiffness element A_{ij} , the laminate coupling stiffness element B_{ij} and the laminate bending stiffness element D_{ij} are given by (Harris, 1999):

$$A_{ij} = \sum_{k=1}^N (\bar{Q}_{ij})_k (z_k - z_{k-1}) \quad (11.31)$$

$$B_{ij} = \frac{1}{2} \sum_{k=1}^N (\bar{Q}_{ij})_k (z_k^2 - z_{k-1}^2) \quad (11.32)$$

$$D_{ij} = \frac{1}{3} \sum_{k=1}^N (\bar{Q}_{ij})_k (z_k^3 - z_{k-1}^3) \quad (11.33)$$

where z_k is the distance between the ply and the mid-plane of the element as shown in Figure 11-8 and N is the total number of plies on each side.

Hence the resultant forces and moments on the laminated plate can be written as:

$$\begin{pmatrix} N_x \\ N_y \\ N_{xy} \\ M_x \\ M_y \\ M_{xy} \end{pmatrix} = \begin{pmatrix} A_{11} & A_{12} & A_{16} & B_{11} & B_{12} & B_{16} \\ A_{12} & A_{22} & A_{26} & B_{12} & B_{22} & B_{26} \\ A_{16} & A_{26} & A_{66} & B_{16} & B_{26} & B_{66} \\ B_{11} & B_{12} & B_{16} & D_{11} & D_{12} & D_{16} \\ B_{12} & B_{22} & B_{26} & D_{12} & D_{22} & D_{26} \\ B_{16} & B_{26} & B_{66} & D_{16} & D_{26} & D_{66} \end{pmatrix} \begin{pmatrix} \epsilon_x^0 \\ \epsilon_y^0 \\ \gamma_{xy}^0 \\ k_x \\ k_y \\ k_{xy} \end{pmatrix} \quad (11.34)$$

where (ϵ) and (k) are the mid-plane strains and curvatures of the laminate. Also, the latter matrix can be written as a compliance system:

$$\begin{Bmatrix} \epsilon_x^0 \\ \epsilon_y^0 \\ \gamma_{xy}^0 \\ k_x \\ k_y \\ k_{xy} \end{Bmatrix} = \begin{bmatrix} a_{11} & a_{12} & a_{16} & b_{11} & b_{12} & b_{16} \\ a_{12} & a_{22} & a_{26} & b_{12} & b_{22} & b_{26} \\ a_{16} & a_{26} & a_{66} & b_{16} & b_{26} & b_{66} \\ b_{11} & b_{12} & b_{16} & d_{11} & d_{12} & d_{16} \\ b_{12} & b_{22} & b_{26} & d_{12} & d_{22} & d_{26} \\ b_{16} & b_{26} & b_{66} & d_{16} & d_{26} & d_{66} \end{bmatrix} \begin{Bmatrix} N_x \\ N_y \\ N_{xy} \\ M_x \\ M_y \\ M_{xy} \end{Bmatrix} \quad (11.35)$$

- Evaluate the equivalent membrane elastic constant for each element (webs and flanges) assuming that only a longitudinal load is applied using the following equations (Dato, 2012):

$$E_{x\ flange} = 1/(t_f a_{11})_{flange} \quad (11.36)$$

$$E_{y\ flange} = 1/(t_f a_{22})_{flange} \quad (11.37)$$

$$E_{x\ web} = 1/(t_w a_{11})_{web} \quad (11.38)$$

$$E_{y\ web} = 1/(t_w a_{22})_{web} \quad (11.39)$$

where t_f and t_w are the thicknesses of the flange and the web respectively.

5- Evaluate the mechanical properties of the cross section with respect to the spar coordinate system (X, Y, Z).

- Evaluate the bending equivalent EI_X and EI_Z of the cross-section (known as the overall section second moments because the value of the Young's modulus is varied from element to element depending on the layout configuration of the laminate) (Dato, 2012; Gibson, 2011).

$$EI_X = 2(E_x I_{XX})_{web} + 2(E_x I_{XX})_{flange}$$

$$EI_Z = 2(E_y I_{ZZ})_{web} + 2(E_y I_{ZZ})_{flange}$$

where I_{XX} and I_{ZZ} are the element second moment of area about the X and the Z axes respectively.

- Evaluate the cross-section torsional stiffness GJ about the Y axis by using the following equation (Canale, 2010; Dato, 2012):

$$GJ = \frac{2 A_{en}^2}{(b_{en} + a_{en})^2} \left[\left[b_{en} \left(A_{66} - \frac{A_{26}^2}{A_{22}} \right) \right]_{web} + \left[a_{en} \left(A_{66} - \frac{A_{26}^2}{A_{22}} \right) \right]_{flange} \right] \quad (11.40)$$

where A_{en} is given by the equation

$$A_{en} = b_{en} \times a_{en} \quad (11.41)$$

where b_{en} and a_{en} are the height and the width of the enclosed area as shown in Figure 11-4.

$$b_{en} = b_f - t_w \quad (11.42)$$

$$a_{en} = b_w + t_f \quad (11.43)$$

- Evaluate the axial stiffness of the section in the Y direction (EA_Y). This can be evaluated by (Gibson, 2011):

$$EA_Y = 2(E_x A_{el})_{web} + 2(E_x A_{el})_{flange} \quad (11.44)$$

where A_{el} is the area of element section.

$$A_{el_{web}} = b_w \times t_w \quad (11.45)$$

$$A_{el_{flange}} = b_f \times t_f \quad (11.46)$$

6- Evaluate the principal stresses of each ply in the critical zones.

The stresses are evaluated under pure bending and pure torsion individually.

- Find the bending stress in each ply of each flange and in the top/bottom plies at the webs using the following equation (Gibson, 2011):

$$\sigma_{x_{ply}} = M_x z_p \frac{E_{x_{ply}}}{EI_x} \quad (11.47)$$

where (z_p) is the distance between the neutral axis of the cross section (X-axis) and the point at the ply as shown in Figure 11-8.

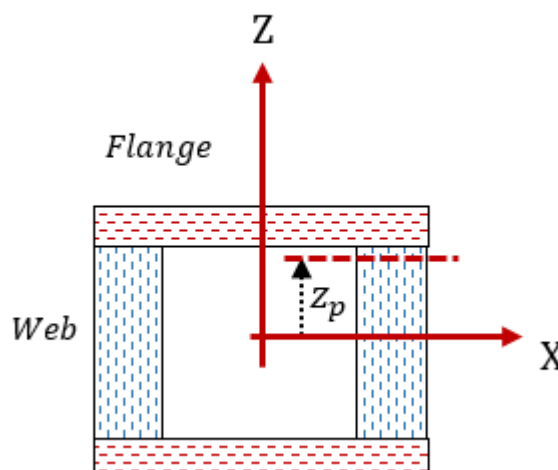


Figure 11-8 The distance (z_p) between the neutral axis and the point on the ply

- Evaluate the principal stresses in each ply of each flange and, the top & the bottom of each web due to the bending load as indicated below:

$$\sigma_1 = \sigma_{x_{ply}} \cos^2 \theta \quad (11.48)$$

$$\sigma_2 = \sigma_{x_{ply}} \sin^2 \theta \quad (11.49)$$

$$\tau_{12} = -\sigma_{x_{ply}} \cos \theta \sin \theta \quad (11.50)$$

- Evaluate the shear flow (q_t) produced from the torsion load (T). This is assumed to be the same on each side using the Bredt–Batho formula (Vasiliev & Morozov, 2013):

$$q_t = T/(2 A_{en}) \quad (11.51)$$

- Evaluate the shear flow (q_s) due to the shear load (F_{sh}) at middle of the web and at the corners of the cross section:

$$(q_s)_{at\ middle\ of\ wep} = \frac{F_{sh}}{8 EI_X} \left[2E_{x_{flange}} t_f b_{en} a_{en} + E_{x_{web}} t_w a_{en}^2 \right] \quad (11.52)$$

$$(q_s)_{at\ corners} = \frac{F_{sh}}{4 EI_X} \left[E_{x_{flange}} t_f b_{en} a_{en} \right] \quad (11.53)$$

Note that the shear flow at the corner is common between the web and flange at the joint (Vasiliev & Morozov, 2013).

- Evaluate the shear stress due to the shear load in the critical zones as shown below:

$$(\tau_{xy})_{at\ middle\ of\ wep} = (q_s)_{at\ middle\ of\ wep}/t_w \quad (11.54)$$

$$(\tau_{xy})_{at\ top/bottom\ of\ wep} = (q_s)_{at\ corners}/t_w \quad (11.55)$$

$$(\tau_{xy})_{at\ corners\ of\ flange} = (q_s)_{at\ corners}/t_f \quad (11.56)$$

- Evaluate the shear stress due to the torsional load in each ply assuming that the load is restricted to pure torsion and that there is no bend-twist coupling:

$$(\tau_{xy})_{at\ middle\ of\ wep} = (q_t)_{at\ middle\ of\ wep}/t_w \quad (11.57)$$

$$(\tau_{xy})_{at\ top/bottom\ of\ wep} = (q_t)_{at\ corners}/t_w \quad (11.58)$$

$$(\tau_{xy})_{at\ corners\ of\ flange} = (q_t)_{at\ corners}/t_f \quad (11.59)$$

- Evaluate the principal stresses in each ply of the flanges at each corner and the top/bottom/middle of the webs due to the shear force and due to the torsional load using the following equations:

$$\sigma_1 = 2\tau_{xy} \cos \theta \sin \theta \quad (11.60)$$

$$\sigma_2 = -2\tau_{xy} \cos \theta \sin \theta \quad (11.61)$$

$$\tau_{12} = \tau_{xy} (\cos^2 \theta - \sin^2 \theta) \quad (11.62)$$

- Sum the effects of bending, shear and torque for those plies located in the critical zones.

7- **Check whether failure has been detected in each ply.** If yes, add an extra number of plies on the sides that failed and repeat the calculation above (from step 2). The maximum failure criterion has been used as the following inequalities (Dattoo, 2012):

$$\begin{aligned} \sigma_1 &\leq X_t / FoS \\ \sigma_2 &\leq Y_t / FoS \\ |\sigma_1| &\leq |X_c| / FoS \\ |\sigma_2| &\leq |Y_c| / FoS \\ \tau_{12} &\leq S_e / FoS \end{aligned} \quad (11.63)$$

where FoS is the factor of safety,

X_t, Y_t, X_c, Y_c and S_e are the maximal strength properties in the longitudinal tension, transverse tension, longitudinal compression, transverse compression and in-plane shear respectively.

If the principal stresses of a ply were not satisfied in any of the above inequalities, the ply will be considered as a failure case. Flanges or webs which contain failed ply will need to be strengthened as mentioned earlier.

Cross-section Design Code

```

Function[EIx,GJ,EA,Weight_el,fW,fF,EIym]=SizeComp(Q_shear,M,T,height,width
h,L)
% this function can size the spar segment for given loads
% Input-----
% Q_shear: Shear force
% M: Bending moment
% T: Torsion
% height: height of spar
% width: width of spar
% L: spar length
% output-----
% EIx,GJ,EA,EIym: mechanical properties of the spar section
% Weight_el: weight of the spar segment
% fW,fF: plies orientation of the web and flange

%=== Initial plies=====
FlP=[0,0,0,0,0,0,0,0,0,90];
WeP=[0,0,0,0,0,0,0,0,0,90];
failureW=1; failureW_top=1; failureF=1;
%stacking pattern for flanges
FP=[45 -45 FlP FlP];
%stacking pattern for webs
WP=[45 -45 WeP WeP];
%=== Ply properties (Carbon fibre) =====
E1=162e9; % Young's Modulus 1-direction
E2=10e9; % Young's Modulus 2-direction
NU12=0.30; % Poisson's ratio 12-plane
G12=5e9; % Shear Modulus 12-plane
NU21 = NU12*E2/E1; % Poisson's ratio 21-plane
t=1.25e-4 ; % Ply thickness (assumed the same for each layer)
FOS=1.5; % factor of safety
Xt=2940e6/FOS; % Tensile X direction Pa
Xc=1570e6/FOS; % compressive X direction Pa
Xmin=Xc;
Yt=60e6/FOS; % Tensile Y direction Pa
Yc=290e6/FOS; % Tensile Y direction Pa
Ymin=Yt;
S_Shear=100e6/FOS; % Shear XY Pa
density=1530; % ply density kg/m^3
%=====
Q = ReducedStiffness(E1,E2,NU12,G12);
%=====
ddw=4; ddf=4;
clear fWs fFs
for JJ=1:50
if max([failureW, failureW_top])>1
ddw=ddw+1;
end
if max(failureF)>1
ddf=ddf+1;
end
fWs=WP(1:ddw); % plies orientation of web
fFs=FP(1:ddf); % plies orientation of Flange
clear failureF failureW failureW_top LaW LaF fW fF
fW=[fWs(end:-1:1) fWs ]; % plies orientation of web 'symmetric
orientation'
fF=[fFs(end:-1:1) fFs ]; % plies orientation of web
nW=length(fW); % number of plies in the web
nF=length(fF); % number of plies in the flange

```

```

Tf=nF*t;           % thickness of flange (for upper and lower panel)
Tw=nW*t;           % thickness of web
a=width-Tw; b=height-Tf; % the dimension of the enclosed section
A=a*b;             % enclosed area
hw=hight-2*Tf;    % length of web
bfl=width;         % flange width
zw=(-nW*t/2):t:(nW*t/2); % ply coordinate based on the bottom of web
zf=(-nF*t/2):t:(nF*t/2); % ply coordinate based on the bottom of flange

%== web ABD =====
Aw = zeros(3,3); Bw = zeros(3,3); Dw = zeros(3,3); Ex_w=zeros(nW);
for i=1:nW
    clear Qbarw
    Qbarw = Qbar2(Q,fW(i));
    Aw = Amatrix(Aw,Qbarw,zw(i),zw(i+1));
    Bw = Bmatrix(Bw,Qbarw,zw(i),zw(i+1));
    Dw = Dmatrix(Dw,Qbarw,zw(i),zw(i+1));
end
Bw=Bw/2; Dw=Dw/3;
%== Flange ABD =====
Af = zeros(3,3); Bf = zeros(3,3); Df = zeros(3,3);
for i=1:nF
    clear Qbarf
    Qbarf = Qbar2(Q,fF(i));
    Af = Amatrix(Af,Qbarf,zf(i),zf(i+1));
    Bf = Bmatrix(Bf,Qbarf,zf(i),zf(i+1));
    Df = Dmatrix(Df,Qbarf,zf(i),zf(i+1));
end
Bf=Bf/2; Df=Df/3;
%=====
ABDw(1:3,1:3)=Aw; ABDw(1:3,4:6)=Bw; ABDw(4:6,1:3)=Bw; ABDw(4:6,4:6)=Dw;
abdw=inv(ABDw);
aw=abdw(1:3,1:3); bw=abdw(1:3,4:6); dw=abdw(4:6,4:6);
ABDf(1:3,1:3)=Af; ABDf(1:3,4:6)=Bf; ABDf(4:6,1:3)=Bf; ABDf(4:6,4:6)=Df;
abdf=inv(ABDf);
af=abdf(1:3,1:3); bf=abdf(1:3,4:6); df=abdf(4:6,4:6);
%=====
ExWb=12/(Tw^3*dw(1,1));
ExWm=1/(Tw*aw(1,1));
ExFm=1/(Tf*af(1,1));
If=2*(bfl*Tf^3/12+bfl*Tf*(b/2)^2);
Iw=2*Tw*hw^3/12;
EIxm=ExWm*Iw+ExFm*If;
%==== NEED TO BE CHECKED =====
Ify=2*Tf*bfl^3/12;
Iwy=2*(hw*Tw^3/12+hw*Tw*(a/2)^2);
EIym=ExWm*Iwy+ExFm*Ify;
%=====
qs=Q_shear*(2*ExFm*Tf*a*b+ExWm*Tw*b^2)/(8*EIxm); % this is max shear flow
at centre line
qs1=Q_shear*(1*ExFm*Tf*a*b)/(4*EIxm); % this is max shear flow
at top of web
qt=T/(2*A);
%=====
EIx=EIxm;
% Flange =====
z=hw/2;
gamaF=qt*af(3,3);
Taxy_f=(qs1)/Tf;
%-----

```

```

Ex_f=zeros(1,nF); Gxy_f=zeros(1,nF); Qx_flange=zeros(1,nF);
Q1b_F=zeros(1,nF); Q2b_F=zeros(1,nF); Tab_F=zeros(1,nF);
Q1t_F=zeros(1,nF); Q2t_F=zeros(1,nF); Tat_F=zeros(1,nF);
Q1S_F=zeros(1,nF); Q2S_F=zeros(1,nF); TaS_F=zeros(1,nF); Q1F=zeros(1,nF);
Q2F=zeros(1,nF); TaF=zeros(1,nF); failureF=zeros(1,nF);

for i=1:nF %-----
-
    m=cos(fF(i)*pi/180); n=sin(fF(i)*pi/180);
    Ex_f(i)=E1/(m^4+(E1/G12-2*NU12)*n^2*m^2+E1*n^4/E2);
    Gxy_f(i)=G12/(n^4+m^4+2*(2*G12/E1*(1+2* NU12)+2*G12/E2-1)*n^2*m^2);
    Qx_flange(i)=M*z*Ex_f(i)/EIx ; % at ply upper side

    % effect of Bending =====
    Q1b_F(i)=Qx_flange(i)*m^2; % if we assume that the ply has Qx only
    Q2b_F(i)=Qx_flange(i)*n^2;
    Tab_F(i)=-Qx_flange(i)*n*m;
    % effect of torsion =====
    Qbarf = Qbar2(Q,fF(i));
    sigx=Qbarf(3,1)*gamaF;
    sigy=Qbarf(3,2)*gamaF;
    txy=Qbarf(3,3)*gamaF;
    Q1t_F(i)=sigx*m^2+sigy*n^2+2*txy*m*n;
    Q2t_F(i)=sigx*n^2+sigy*m^2-2*txy*m*n;
    Tat_F(i)=(sigy-sigx)*n*m+txy*(m^2-n^2);
    % effect of shear =====
    Q1S_F(i)=Taxy_f*2*m*n;
    Q2S_F(i)=-Taxy_f*2*m*n;
    TaS_F(i)=Taxy_f*(m^2-n^2);
    % Principle Stresses =====
    Q1F(i)=Q1b_F(i)+(Q1S_F(i))+Q1t_F(i);
    Q2F(i)=Q2b_F(i)+(Q2S_F(i))+Q1t_F(i);
    TaF(i)=(Tab_F(i))+(TaS_F(i))+Tat_F(i);
    % Failure criterion =====
    fa1=abs(Q1F(i))/Xmin;
    fa2=abs(Q2F(i))/Ymin;
    fa3=abs(TaF(i))/S_Shear;
    failureF(i)=max([fa1,fa2,fa3]);
end
% Web =====
z=hw/2; % Here we will find the stress from bending in the web
gamaW=qt*aw(3,3);
Taxy_w=(qs)/Tw;
Taxy_w_top=(qs1)/Tw;
% allocate memory for matrices -----
Qx_wep=zeros(1,nW); Q1b_W_top=zeros(1,nW); Q2b_W_top=zeros(1,nW);
Tab_W_top=zeros(1,nW); Q1t_W=zeros(1,nW); Q2t_W=zeros(1,nW);
Tat_W=zeros(1,nW); Q1S_W=zeros(1,nW); Q2S_W=zeros(1,nW);
TaS_W=zeros(1,nW); Q1S_W_top=zeros(1,nW); Q2S_W_top=zeros(1,nW);
TaS_W_top=zeros(1,nW); Q1W=zeros(1,nW); Q2W=zeros(1,nW);
TaW=zeros(1,nW); Q1W_top=zeros(1,nW); Q2W_top=zeros(1,nW);
TaW_top=zeros(1,nW); failureW=zeros(1,nW); failureW_top=zeros(1,nW);
%-----
for i=1:nW
    m=cos(fW(i)*pi/180); n=sin(fW(i)*pi/180);
    Ex_w(i)=E1/(m^4+(E1/G12-2*NU12)*n^2*m^2+E1*n^4/E2);
    Qx_wep(i)=M*z*Ex_w(i)/EIx ; % stress at top of web
    % effect of Bending =====
    Q1b_W_top(i)=Qx_wep(i)*m^2; % at top of web
    Q2b_W_top(i)=Qx_wep(i)*n^2;
    Tab_W_top(i)=-Qx_wep(i)*n*m;

```

```

% effect of torsion =====
Qbarw = Qbar2(Q,fW(i));
sigx=Qbarw(3,1)*gamaW;
sigy=Qbarw(3,2)*gamaW;
txy=Qbarw(3,3)*gamaW;
Q1t_W(i)=sigx*m^2+sigy*n^2+2*txy*m*n;
Q2t_W(i)=sigx*n^2+sigy*m^2-2*txy*m*n;
Tat_W(i)=(sigy-sigx)*n*m+txy*(m^2-n^2);
% effect of shear at middle of web =====
Q1S_W(i)=Taxy_w*2*m*n;
Q2S_W(i)=-Taxy_w*2*m*n;
TaS_W(i)=Taxy_w*(m^2-n^2);
% effect of shear at top of web =====
Q1S_W_top(i)=Taxy_w_top*2*m*n;
Q2S_W_top(i)=-Taxy_w_top*2*m*n;
TaS_W_top(i)=Taxy_w_top*(m^2-n^2);
% Principle Stresses =====
%-- middle ----
Q1W(i)=(Q1S_W(i))+Q1t_W(i);
Q2W(i)=(Q2S_W(i))+Q2t_W(i);
TaW(i)=(TaS_W(i))+Tat_W(i);
%-- top -----
Q1Wtop(i)=Q1b_W_top(i)+(Q1S_W_top(i))+Q1t_W(i);
Q2Wtop(i)=Q2b_W_top(i)+(Q2S_W_top(i))+Q2t_W(i);
TaWtop(i)=(Tab_W_top(i))+TaS_W_top(i)+Tat_W(i);
% Failure criterion =====
%-- middle ----
fa1=abs(Q1W(i))/Xmin;
fa2=abs(Q2W(i))/Ymin;
fa3=abs(TaW(i))/S_Shear;
failureW(i)=max([fa1,fa2,fa3]);
%-- Top -----
fa1=abs(Q1Wtop(i))/Xmin;
fa2=abs(Q2Wtop(i))/Ymin;
fa3=abs(TaWtop(i))/S_Shear;
failureW_top(i)=max([fa1,fa2,fa3]);
end

%==== failure Criteria =====
FaCr=[max(failureW),max(failureF),max(failureW_top)];
%=== stop if no failure is detected =====
    if max(FaCr)<1
        break
    end
%=== increasing the plies in the failed element =====
    if FaCr(1)>1 || FaCr(3)>1
        ddw=ddw+1;
    end
%-----
    if FaCr(2)>1
        ddf=ddf+1;
    end
end
volume=(height*width-(hight-2*Tf)*(width-Tw))*L;
Weight_el=volume*density;
GJ=2*A/(a+b)^2*A*(b*(Aw(3,3)-Aw(2,3)^2/Aw(2,2))+a*(Af(3,3)-
Af(2,3)^2/Af(2,2)));
EA=ExFm*width*Tf+ExWm*hw*Tw;
end
%==== END of the SizeComp =====

```

ReducedStiffness.m

```
function y = ReducedStiffness (E1,E2,NU12,G12)
    NU21 = NU12*E2/E1;
    y = [E1/(1-NU12*NU21) NU12*E2/(1-NU12*NU21) 0 ; NU12*E2/(1-NU12*NU21)
        E2/(1-NU12*NU21) 0 ; 0 0 G12];
end
```

```
%-----
```

Qbar2.m

```
function y = Qbar2(Q,theta)
    m = cos(theta*pi/180);    n = sin(theta*pi/180);
    y(1,1) = Q(1,1)*m^4 + m^2*n^2*(2*Q(1,2) + 4*Q(3,3))+Q(2,2)*n^4;
    y(1,2) = m^2*n^2*(Q(1,1) +Q(2,2)- 4*Q(3,3))+Q(1,2)*(m^4+n^4);
    y(1,3) = m^3*n*(Q(1,1)-Q(1,2)- 2*Q(3,3))+m*n^3*(Q(1,2)-
        Q(2,2)+2*Q(3,3));
    y(2,1) =y(1,2) ;
    y(2,2) =Q(1,1)*n^4 + m^2*n^2*(2*Q(1,2) + 4*Q(3,3))+Q(2,2)*m^4;
    y(2,3) = n^3*m*(Q(1,1)-Q(1,2)- 2*Q(3,3))+m^3*n*(Q(1,2)-
        Q(2,2)+2*Q(3,3));
    y(3,1) = y(1,3);
    y(3,2) = y(2,3);
    y(3,3) = m^2*n^2*(Q(1,1) +Q(2,2)- 2*Q(1,2)- 2*Q(3,3))+Q(3,3)*(m^4+n^4);
end
```

```
%-----
```

Amatrix.m

```
function y = Amatrix(A,Qbar,z1,z2)
for i = 1 : 3
    for j = 1 : 3
        A(i,j) = A(i,j) + Qbar(i,j)*(z2-z1);
    end
end
y = A;
end
```

```
%-----
```

Bmatrix.m

```
function y = Bmatrix(B,Qbar,z1,z2)
for i = 1 : 3
    for j = 1 : 3
        B(i,j) = B(i,j) + Qbar(i,j)*(z2^2 -z1^2);
    end
end
y = B;
end
```

```
%-----
```

Dmatrix.m

```
function y = Dmatrix(D,Qbar,z1,z2)
for i = 1 : 3
    for j = 1 : 3
        D(i,j) = D(i,j) + Qbar(i,j)*(z2^3 -z1^3);
    end
end
y = D;
end
```

```
%-----
```

12 REFERENCES

- Alsahlani, A., T. Rahulan, and N. Abdulhassan, "Composite Structural Analysis of a High Altitude, Solar Powered Unmanned Aerial Vehicle". *International Journal of Mechanical Engineering and Robotics Research, IJMERR*, 2017. 6(1): p. 71-76.
- Alsahlani, A. and T. Rahulan, "Aerofoil Design for Unmanned High-Altitude Aft-swept Flying-Wings", *Journal of Aerospace Technology and Management*, accepted in April 2017.
- Alsahlani, A. and T. Rahulan. "A Mathematical Model of a Conceptual Design Approach of High Altitude Solar Powered Unmanned Aerial Vehicles", *International Review of Aerospace Engineering Journal*, Volume10, No.4, September 2017.
- Abbott, I. H., & Von Doenhoff, A. E. (1959). *Theory of wing sections, including a summary of airfoil data*: Courier Corporation.
- Ajaj, R. M., Smith, D., & Isikveren, A. T. (2013). A Conceptual Wing-Box Weight Estimation Model For Transport Aircraft. *AERONAUTICAL JOURNAL*, 177(1191), 533-551.
- Alsahlani, A., Johnston, L. J., & Atcliffe, P. A. (2015). Design of a High Altitude Long Endurance Flying-wing Solar-Powered Unmanned Air Vehicle. Paper presented at the 6TH European Conference for Aeronautics and Space Sciences (EUCASS2015), Krakow, Poland.
- Alsahlani, A., Johnston, L. J., & Atcliffe, P. A. (2017). Design of a High Altitude Long Endurance Flying-wing Solar-Powered Unmanned Air Vehicle. *Progress in Flight Physics*, 9, 3-24. doi: 10.1051/eucass/201709003
- Alsahlani, A., & Rahulan, T. (2016). Weight Estimation of a Conceptual Wing for a High Altitude, Solar Powered Unmanned Aerial Vehicle. Paper presented at the 5th Aircraft Structural Design Conference Manchester / UK.
- Alsahlani, A., & Rahulan, T. (2017). Conceptual and Preliminary Design Approach of A High Altitude, Long Endurance Solar-Powered UAVs. Paper presented at the CSE Annual PGR Symposium (CSE-PGSym 17), Salford, UK.
- Amadori, K. (2012). *Geometry Based Design Automation Applied to Aircraft Modelling and Optimization*. (Master Dissertations), Linköping University. (NO. 1418)
- Anderson, D. F., & Eberhardt, S. (2001). *Understanding Flight*. USA: McGraw-Hill New York.
- Anderson, R. F. (1934). NACA-report-627 The Experimental And Calculated Characteristics of 22 Tapered Wing: National Advisory Committee For Aeronautics.
- Anderson, R. F. (1935). NACA-report-572 Determination of the Characteristics tapered Wing: National Advisory Committee For Aeronautics.
- Ansys, I. (2013). *ANSYS FLUENT Theory Guide (Vol. Release 15.0)*. U.S.A: ANSYS, Inc.
- Austin, R. (2011). *Unmanned aircraft systems: UAVS design, development and deployment (Vol. 54)*: John Wiley & Sons.
- Bailey, M., & Bower, M. (1992). *High altitude solar power platform*: Citeseer.
- Baldock, N., & Mokhtarzadeh, M. R. (2006). A Study of Solar-Powered, High-Altitude Unmanned Aerial Vehicles. *Aircraft Engineering and Aerospace Technology*, 78(3), 187-193.
- Blot, M. (1945). *Horten Tailless Aircraft*: DTIC Document.
- Bolsunovsky, A., Buzoverya, N., Gurevich, B., Denisov, V., Dunaevsky, A., Shkadov, L., . . . Zhurihin, J. (2001). Flying wing—problems and decisions. *Aircraft design*, 4(4), 193-219.

-
- Boucher, R. (1984). History of solar flight. Paper presented at the 20th Joint Propulsion Conference, Ohio, USA.
- Brandt, S. A., & Gilliam, F. T. (1995). Design analysis methodology for solar-powered aircraft. *Journal of Aircraft*, 32(4), 703-709.
- Buckstrom, A. (1979). The Elements of Tailless Airplane Design. *Sport Aviation*, 39-44.
- Bureau, A. T. S. (2008). Fibre Composite Aircraft-Capability And Safety. Australia: Australian Transport Safety Bureau.
- Canale, G. (2010). Aeroelastic Tailoring of Aeroplane Wings Using Composite Laminates. (PhD Thesis), University of Bristol, UK.
- Cao, Y., & Wu, Q. (1999). Teaching Genetic Algorithm Using MATLAB. *International journal of electrical engineering education*, 36(2), 139-153.
- Cebeci, T., & Bradshaw, P. (2012). Physical and computational aspects of convective heat transfer: Springer Science & Business Media.
- Cerra, D. F., & Katz, J. (2008). Design of a High-Lift, Thick Airfoil for Unmanned Aerial Vehicle Applications. *Journal of Aircraft*, 45(5), 1789-1793. doi: 10.2514/1.36924
- Cesnik, C. E., Senatore, P. J., Su, W., Atkins, E. M., Shearer, C. M., & Pitcher, N. A. (2010). X-HALE: A Very Flexible UAV For Nonlinear Aeroelastic Tests. AIAA(2010-2715).
- Cesnik, C. E., & Su, W. (2011). Nonlinear Aeroelastic Simulation of X-HALE: A Very Flexible UAV. Paper presented at the 49th AIAA Aerospace Sciences Meeting including the New Horizons Forum and Aerospace Exposition, Orlando, Florida, USA.
- Cestino, E. (2006). Design of Solar High Altitude Long Endurance Aircraft For Multi Payload & Operations. *Aerospace Science & Technology*, 10(6), 541-550. doi: 10.1016/j.ast.2006.06.001
- Cestino, E., Frulla, G., & Romeo, G. (2007). Design of a High-Altitude Long-Endurance Solar-Powered Unmanned Air Vehicle for Multi-Payload and Operations. *Proceedings of the Institution of Mechanical Engineers, Part G: Journal of Aerospace Engineering*, 221(2), 199-216. doi: 10.1243/09544100jaero119
- Chintapalli, S. (2006). Preliminary Structural Design Optimization of an Aircraft Box-wing. (Master Thesis), Concordia University.
- Colella, N. J., & Wenneker, G. S. (1994). Pathfinder And The Development of Solar Rechargeable Aircraft. *Energy and Technology Review*, 1-9.
- Coley, D. A. (1999). An Introduction To Genetic Algorithms For Scientists And Engineers: World scientific Singapore.
- Colozza, A. J. (1993). Effect of Power System Technology and Mission Requirements on High Altitude Long Endurance Aircraft. Sverdup Technology Inc., NASA Lewis Group.
- Cook, M. V. (2013). Flight Dynamics Principles: A Linear Systems Approach To Aircraft Stability And Control (Third ed.): Butterworth-Heinemann, Elsevier.
- Craig L. Nickol , M. D. G., Lisa L. Kohout, and Thomas A. Ozoroski. (2007). High Altitude Long Endurance UAV Analysis of Alternatives and Technology Requirements Development.
- d'Oliveira, F. A., Melo, F. C. L. d., & Devezas, T. C. (2016). High-Altitude Platforms—Present Situation and Technology Trends. *Journal of Aerospace Technology and Management*, 8(3), 249-262.
- Datoo, M. H. (2012). Mechanics of Fibrous Composites: Springer Science & Business Media.
-

- Della Vecchia, P., Daniele, E., & D'Amato, E. (2014). An Airfoil Shape Optimization Technique Coupling PARSEC Parameterization And Evolutionary Algorithm. *Aerospace Science and Technology*, 32(1), 103-110. doi: 10.1016/j.ast.2013.11.006
- Derksen, R., & Rogalsky, T. (2010). Bezier-PARSEC: An Optimized Aerofoil Parameterization For Design. *Advances in engineering software*, 41(7), 923-930.
- Dorbath, F., Nagel, B., & Gollnick, V. (2010). Comparison of Beam and Shell Theory for Mass Estimation in Preliminary Wing Design. Paper presented at the 2nd Aircraft Structural Design Conference, London, UK.
- Drela, M. (1989). XFOIL: An Analysis And Design System For Low Reynolds Number Airfoils Low Reynolds Number Aerodynamics (pp. 1-12). Berlin, Heidelberg: Springer.
- Duffie, J. A., & Beckman, W. A. (1980). *Solar Engineering of Thermal Processes* (Second ed. Vol. 3). USA: Wiley New York etc.
- Duffie, J. A., & Beckman, W. A. (2013). *Solar engineering of thermal processes* (Vol. 3): Wiley New York.
- ESDU76003. (2012). Geometrical Properties of Cranked and Straight Tapered Wing Planforms Item No. 76003. London, UK: ESDU International plc.
- Frulla, G. (2002). HELIPLAT® Structural Analysis of High Altitude Very-Long Endurance Solar Powered Platform For Telecommunication And Earth Observation Applications. Paper presented at the 23rd congress of the international council of the aeronautical sciences (ICAS), Toronto.
- Frulla, G., & Cestino, E. (2008). Design, Manufacturing and Testing of A HALE-UAV Structural Demonstrator. *Composite Structures*, 83(2), 143-153. doi: 10.1016/j.compstruct.2007.04.008
- Gao, X.-Z., Hou, Z.-X., Guo, Z., Liu, J.-X., & Chen, X.-Q. (2013). Energy Management Strategy For Solar-Powered High-Altitude Long-Endurance Aircraft. *Energy Conversion and Management*, 70, 20-30. doi: 10.1016/j.enconman.2013.01.007
- Gay, D., Hoa, S. V., & Tsai, S. W. (2002). *Composite Materials: Design And Applications*: CRC press.
- Gibson, R. F. (2011). *Principles of Composite Material Mechanics*: McGraw-Hill, Inc.
- Goraj, Z., Frydrychewicz, A., Switkiewicz, R., Hernik, B., Gadomski, J., Goetzendorf-Grabowski, T., . . . Chajec, W. (2004). High Altitude Long Endurance Unmanned Aerial Vehicle of A New Generation-A Design Challenge For A Low Cost, Reliable And High Performance Aircraft. *Bulletin of Polish Academy of Sciences, Technical Sciences*, 52, 173-194.
- Greer, D., Hamory, P., Krake, K., & Drela, M. (1999). Design And Predictions For High-Altitude (Low Reynolds Number) Aerodynamic Flight Experiment: NASA Center for AeroSpace Information (CASI).
- Gregory, N., & O'Reilly, C. (1973). *Low-Speed Aerodynamic Characteristics Of NACA 0012 Aerofoil Section, Including The Effects of Upper-Surface Roughness Simulating Hoar Frost*. London, UK: Ministry of Defence, Aeronautical Research Council.
- Guardian, T. (2015). Facebook launches Aquila solar-powered drone for internet access. Retrieved 3rd May, 2016, from <https://www.theguardian.com/technology/2015/jul/31/facebook-finishes-aquila-solar-powered-internet-drone-with-span-of-a-boeing-737>
- Guarino, G. C., Stasi, S., Dassisti, M., & Chimienti, M. (2013). Multiobjective Optimization for Electric Drives Design in Solar-Powered Ultralight Aircrafts. *Recent Advances in Systems Science*, ISBN, 978-960.

-
- Hall, D. W., Fortenbach, C. D., Dimiceli, E. V., & Parks, R. W. (1983). A preliminary study of solar powdered aircraft and associated power trains.
- Hall, D. W., & Hall, S. A. (1984). Structural sizing of a solar powered aircraft. In N. C. R. Lockheed Missiles and Space Company, April 1984. (Ed.).
- Hantula, R. (2010). *How Do Solar Panels Work?* New York, USA: Infobase Publishing.
- Harris, B. (1999). *Engineering Composite Materials*. London, UK: The Institute of Materials.
- Hepperle, M. (1988). Neue Profile für Nurflügelmodelle. FMT Kolleg, 8.
- Holland John, H. (1992). *Adaptation In Natural And Artificial Systems: An Introductory Analysis With Applications To Biology, Control, And Artificial Intelligence*. USA: The MIT Press.
- Houghton, E. L., & Carpenter, P. W. (2003). *Aerodynamics for Engineering Students* (fifth ed.). UK: E.L. Houghton and P.W. Carpenter.
- Jemitola, P. O. (2012). *Conceptual Design and Optimization Methodology for Box Wing Aircraft*. (PhD thesis), Cranfield University.
- John, M., & Michael, H. (1980). Low-speed Single-Element Airfoil Synthesis. *Technical Soaring*, 6(2), 1-21.
- Jones, J. R., & Cesnik, c. E. S. (2015). Preliminary Flight Test Correlations of The X-HALE Aeroelastic Experiment. *THE AERONAUTICAL JOURNAL*, 119(1217).
- Jordan Hadjiev, H. P. (2013). Comparative Investigation of VLM Codes For Joined-Wing Analysis. *International Journal of Research in Engineering and Technology*, 2(12), 478-482.
- Katz, J., & Plotkin, A. (2001). *Low-Speed Aerodynamics* (Vol. 13): Cambridge University Press.
- Keidel, B. (2000). *Auslegung und Simulation von hochfliegenden, dauerhaft stationierbaren Solardrohnen*. (PhD), Technische Universität München, Universitätsbibliothek.
- Kennedy, G. J., & Martins, J. (2012). A Comparison of Metallic And Composite Aircraft Wings Using Aerostructural Design Optimization. Paper presented at the 14th AIAA/ISSMO Multidisciplinary Analysis and Optimization Conference, Indianapolis.
- Khan, F. A. (2010). *Preliminary Aerodynamic Investigation of Box-Wing Configurations Using Low Fidelity Code*. (Master Thesis), Luleå University of Technology.
- Khan, F. A., Krammer, P., & Scholz, D. (2010). Preliminary Aerodynamic Investigation of Box-wing Configurations Using Low Fidelity codes. DGLR: Deutscher Luft-und Raumfahrtkongress, DocumentID: 161308.
- Ko, W. L., Richards, W., & Tran, V. T. (2007). Displacement Theories for In-Flight Deformed Shape Predictions of Aerospace Structures. *National Aeronautics and Space Administration (NASA)*, 214612.
- Kroo, I. (1993). Tailless Aircraft Design- Recent Experiences. Paper presented at the Symposium on Aerodynamics and Acoustics, New Jersey, USA.
- Lei, J., Guo, F., & Huang, C. (2013). Numerical Study Of Separation On The Trailing Edge Of A Symmetrical Airfoil At A Low Reynolds Number. *Chinese Journal of Aeronautics*, 26(4), 918-925.
- Li, P., Zhang, B., Chen, Y., Yuan, C., & Lin, Y. (2012). Aerodynamic Design Methodology for Blended Wing Body Transport. *Chinese Journal of Aeronautics*, 25(4), 508-516. doi: 10.1016/s1000-9361(11)60414-7
- Lissaman, P. (1983). Low-Reynolds-Number Airfoils. *Annual Review of Fluid Mechanics*, 15(1), 223-239.
-

-
- M. Martínez, C. C. (2012). Preliminary Aerodynamic Investigation of An Unmanned Box-Wing Aircraft. Paper presented at the 28th International Congress of The Aeronautical Sciences ICAS, Brisbane, Australia.
- Ma, R., & Liu, P. (2009). Numerical Simulation Of Low-Reynolds-Number And High-Lift Airfoil S1223. Paper presented at the Proceedings of the World Congress on Engineering, London, UK.
- Mader, C., & Martins, J. (2012). Optimal Flying Wings: A Numerical Optimization Study. AIAA 2012-1758. doi: 10.2514/6.2012-1758
- Manuel, H. (2013). Design, Construction and Test of the Propulsion System of a Solar UAV (Master Thesis), Técnico Lisboa.
- Mariens, J. (2012). Wing Shape Multidisciplinary Design Optimization. (Master Thesis), Delft University of Technology.
- Mariens, J., Elham, A., & van Tooren, M. (2014). Quasi-Three-Dimensional Aerodynamic Solver for Multidisciplinary Design Optimization of Lifting Surfaces. *Journal of Aircraft*, 51(2), 547-558.
- Martinez-Val, R., Perez, E., Alfaro, P., & Perez, J. (2007). Conceptual Design of a Medium Size Flying Wing. *Proceedings of the Institution of Mechanical Engineers, Part G: Journal of Aerospace Engineering*, 221(1), 57-66.
- Martins, J. R. R. A. (2002). A Coupled-Adjoint Method For High-Fidelity Aero-Structural Optimization. (PhD Thesis), Stanford University.
- Mattos, B. S. d., Secco, N. R., & Salles, E. F. (2013). Optimal Design of a High-altitude Solar-Powered Unmanned Airplane. *Journal of Aerospace Technology and Management*, 5(3), 349-361. doi: 10.5028/jatm.v5i3.223
- McArthur, J. (2007). Aerodynamics of Wings At Lowreynolds Numbers. (PhD Thesis), University of Southern California, USA.
- Megson, T. H. G. (2012). *Aircraft Structures For Engineering Students*. UK: Butterworth-Heinemann, Elsevier.
- Meinel, A. B., Meinel, M. P., & McGowan, J. G. (1977). Applied Solar Energy: An Introduction. *American Journal of Physics*, 45(5), 499-499.
- Melin, T. (2001). User's Guide And Reference Manual For Tornado. Retrieved Sep 2014, from <http://www.redhammer.se/tornado/>
- Michael S. Selig, James J. Guglielmo, Andy P. Broeren, & Philippe Giguere. (1995). Summary of Low-Speed Airfoil Data Volume-1 (Vol. 4): Department of Aeronautical and Astronautical Engineering University of Illinois at Urbana-Champaign.
- MicroLink. (2017). Retrieved 15/07/2017, 2017, from <http://mldevices.com/index.php/product-services/photovoltaics>
- Min Chang, Zhou Zhou, Rui Wang, & Xu, X. (2014). A General Design Methodology for Year-Round Solar-Powered Stratospheric UAVs from Low to Middle Latitudes. Paper presented at the 29th Congress of The International Council of The Aeronautical Sciences, Russia.
- Mitchell, M. (1999). *An Introduction to Genetic Algorithms* (Fifth ed.). UK: Massachusetts Institute of Technology.
- Montagnier, O., & Bovet, L. (2010). Optimisation Of A Solar-Powered High Altitude Long Endurance UAV. Paper presented at the Proceedings of the 27th International Congress of The Aeronautical Sciences ICAS, Nice, France.
- Moran, J. (2003). *An Introduction to Theoretical and Computational Aerodynamics*: Dover Publications Inc.
- Morrissey, B. J. (2009). Multidisciplinary Design Optimization of an Extreme Aspect Ratio HALE UAV. (Master Thesis), California Polytechnic State University, USA.
-

- Mukesh, R., Lingadurai, K., & Selvakumar, U. (2012). Application of Nontraditional Optimization Techniques For Airfoil Shape Optimization. *Modelling and Simulation in Engineering*, 2012, 46. doi: 10.1155/2012/636135
- Najafi, Y. (2011). Design of A High Altitude Long Endurance Solar Powered UAV. (Master Thesis), San Jose State University.
- Nickel, K., & Wohlfahrt, M. (1994). *Tailless aircraft in theory and practice: Amer Inst of Aeronautics &*
- Nickol, C. L., Guynn, M. D., Kohout, L. L., & Ozoroski, T. A. (2007). High altitude long endurance air vehicle analysis of alternatives and technology requirements development. AIAA Paper, 1050, 2007.
- Niță, M., & Scholz, D. (2012). Estimation Oswald Factor from Basic Aircraft Geometry Parameters: Deutsche Gesellschaft für Luft-und Raumfahrt-Lilienthal-Oberth eV.
- Noll, T. E., Brown, J. M., Perez-Davis, M. E., Ishmael, S. D., Tiffany, G. C., & Gaier, M. (2004). Investigation of the Helios Prototype Aircraft. In T. H. M. I. Board (Ed.), (Vol. Volume I). USA: Langkey Research Center, NASA.
- Noth, A., Siegwart, R., & Engel, W. (2007). Design of Solar Powered Airplanes For Continuous Flight. ETHZ lecture, Version 1.1.
- Noth(a), A. (2008). History of Solar Flight. Autonomous Systems Lab, Switzerland: ETH Zürich.
- Noth(b), A. (2008). Design of Solar Powered Airplanes for Continuous Flight. (PhD Thesis), ETH ZÜRICH, Switzerland. (18010)
- Obert, E. (2009). Aerodynamic Design of Transport Aircraft. Netherlands: IOS Press under the imprint Delft University Press.
- P. Guarino, G. L. Cascella, S. Stasi, Dassisti, M., & Chimienti, M. (2014). Design of Solar Powered Ultra-light Aircrafts Realization of a Model and its Validation. *INTERNATIONAL JOURNAL OF ENERGY*, V8.
- P. Salunke, N., Ahamad R. A, J., & Channiwala, S. A. (2014). Airfoil Parameterization Techniques: A Review. *American Journal of Mechanical Engineering*, 2(4), 99-102. doi: 10.12691/ajme-2-4-1
- Park, K., Han, J.-W., Lim, H.-J., Kim, B.-S., & Lee, J. (2008). Optimal Design of Airfoil with High Aspect Ratio in Unmanned Aerial Vehicles. *World Academy of Science, Engineering and Technology*, 16.
- Pereira, R. L. (2012). Validation of Software For The Calculation of Aerodynamic Coefficients With A Focus on The Software Package. In F. Linköpings Universitet (Ed.), Degree Project.
- Pomeroy, B., & Visser, K. (2010). A Computational Study of Induced Drag Behavior for Spanwise Cambered Wings. Paper presented at the 28th AIAA Applied Aerodynamics Conference, Chicago, USA.
- Qin, N., Vavalle, A., Le Moigne, A., Laban, M., Hackett, K., & Weinerfelt, P. (2004). Aerodynamic Considerations of Blended Wing Body Aircraft. *Progress in Aerospace Sciences*, 40(6), 321-343. doi: 10.1016/j.paerosci.2004.08.001
- Raghavan, B. (2009). Flight Dynamics And Control of Highly Flexible Flying-Wings. (PhD Thesis), Virginia Polytechnic Institute and State University, USA.
- Rapinett, A. (2009). Zephyr A High Altitude Long Endurance Unmanned Air Vehicle. (Master Thesis), University of Surrey, UK.
- Rizzo, E., & Frediani, A. (2008). A Model For Solar Powered Aircraft Preliminary Design. *THE AERONAUTICAL JOURNAL*(February), 57-87.
- Romeo, G., Danzi, F., & Cestino, E. (2014). Multi-Objective Optimization Of The Composite Wing Box of Solar Powered HALE UAV. Paper presented at the 29 th

- Congress of International Council of The Aeronautical Sciences ICAS, St. Petersburg, Russia.
- Romeo, G., Pacino, M., & Borello, F. (2009). First Flight of Scaled Electric Solar Powered UAV For Mediterranean Sea Border Surveillance Forest And Fire Monitoring. *The Journal of Aerospace Science, Technology and Systems*, 88(1-2), 8-19.
- Rubio, S. R. (2013). Aerodynamic Analysis of A Sustainable-Energy Sailplane Using CEASIOM. (Master Thesis), Royal Institute of Technology, Sweden.
- Samareh, J. A. (1999). A Survey of Shape Parameterization Techniques. Paper presented at the CEAS/AIAA/ICASE/NASA Langley International Forum on Aeroelasticity and Structural Dynamics, Williamsburg.
- Selig, M. (2003). Low Reynolds number airfoil design lecture notes. VKI Lecture Series, November, 24-28.
- Selig, M. S., Gopalarathnam, A., Giguere, P., & Lyon, C. (2001). Systematic Airfoil Design Studies At Low Reynolds Numbers. *Progress in Astronautics and Aeronautics*, 195, 143-167.
- Selig, M. S., & Guglielmo, J. J. (1997). High-Lift Low Reynolds Number Airfoil Design. *Journal of Aircraft*, 34(1), 72-79.
- Sequeira, C. J., Willis, D. J., & Peraire, J. (2006). Comparing Aerodynamic Models For Numerical Simulation Of Dynamics And Control of Aircraft. Paper presented at the 44th AIAA Aerospace Sciences Meeting and Exhibit, Nevada, USA.
- Seywald, K. (2011). Wingbox Mass Prediction Considering Quasi-Static Nonlinear Aeroelasticity. (Diploma Thesis), Bauhaus Luftfahrt.
- Skoog, R. B. (1957). An Analysis of The Effects of Aeroelasticity on Static Longitudinal Stability and Control of a Swept-Wing Airplane (pp. 125-136): NACA Report.
- Sobieczky, H. (1997). Geometry Generator for CFD and Applied Aerodynamics. Paper presented at the New Design Concepts for High Speed Air Transport, Vienna.
- Sobieczky, H. (1999). Parametric airfoils and wings Recent Development of Aerodynamic Design Methodologies (pp. 71-87): Springer.
- Solarimpulse.com. (2017). Retrieved 21 April, 2017, from <http://www.solarimpulse.com/>
- Song, L., Yang, H., Zhang, Y., Zhang, H., & Huang, J. (2014). Dihedral Influence on Lateral-Directional Dynamic Stability on Large Aspect Ratio Tailless Flying Wing Aircraft. *Chinese Journal of Aeronautics*, 5(27), 1149-1155.
- Squire, H., & Young, A. (1938). The calculation of profile drag of airflow. Aeronautical Research Council.
- Sreher, G. G., & Wyatt, L. A. (1961). Boundary Layer Measurements at Low Speed on TWO Wings 45" and 55" Sweep. London, UK: Aeronautical Research Council / Ministry of Avitation.
- Stender, W. (1969). Sailplane weight estimation: Organisation scientifique et technique internationale du vol à voile.
- Symolon, W. E. (2009). High-Altitude, Long-Endurance UAVs vs. Satellites: Potential Benefits for U.S. Army Applications. (Master Thesis), Massachusetts Institute of Technology, USA.
- Torenbeek, E. (2013). *Advanced Aircraft Design: Conceptual Design, Technology and Optimization of Subsonic Civil Airplanes*. UK: John Wiley & Sons.
- Trips, D. (2010). Aerodynamic Design and Optimization of a Long Range Mini-UAV. (Master Thesis), Delft University of Technology.
- Vasiliev, V. V., & Morozov, E. (2013). *Advanced Mechanics of Composite Materials and Structural Elements*: Newnes. UK: Elsevier Ltd.
- Vasseur, P. (2014). Optimization Strategy For Conceptual Airplane Design. (Master Thesis), Delft University of Technology

-
- Voyiadjis, G. Z., & Kattan, P. I. (2005). *Mechanics of composite materials with Matlab*: Springer Science & Business Media.
- Wang, L., & Wang, L. (2012). Reconfigurable Flight Control Design for Combat Flying Wing with Multiple Control Surfaces. *Chinese Journal of Aeronautics*, 25(4), 493-499. doi: 10.1016/s1000-9361(11)60412-3
- Wang, Z., Chen, P. C., Liu, D. D., & Mook, D. T. (2010). Nonlinear-Aerodynamics/Nonlinear-Structure Interaction Methodology for a High-Altitude Long-Endurance Wing. *Journal of Aircraft*, 47(2), 556-566. doi: 10.2514/1.45694
- Wauquiez, C. (2009). *Shape Optimization of Low Speed Airfoils Using Matlab and Automatic Differentiation*: Royal Institute of Technology.
- Weyl, A. (1945). Tailless Aircraft and Flying Wings: A Study of Their Evolution and Their Problems. *Aircraft Engineering and Aerospace Technology*, 17(2), 41-46.
- Whitford, R. (2007). *Evolution of the Airliner*: Crowood Press.
- Wilson, E. L. (2002). *Three-Dimensional Static and Dynamic Analysis of Structures* (Third ed.). California, USA: Computers and Structures, Inc.
- Woehrle, T., Costerus, B., & Lee, C. (1994). *Modal Analysis of PATHFINDER Unmanned Air Vehicle* (pp. 1687-1693). USA: Lawrence Livermore National Lab.
- Zdobysław, G., Andrzej, F., & Jacek, W. (1999). Design Concept of a High-Altitude Long-Endurance Unmanned Aerial Vehicle. *Aircraft design*, 2(1), 19-44.
- Zetina, A. M., Jeong, S., & Obayashi, S. (2013). Airfoil Aerodynamic Optimization for A High-Altitude Long-Endurance Aircraft Using Multi-Objective Genetic-Algorithms. Paper presented at the IEEE Congress on Evolutionary Computation, Cancún, México.
- Zhu, X., Guo, Z., Fan, R., Hou, Z., & Gao, X. (2014). How High Can Solar-Powered Airplanes Fly. *Journal of Aircraft*, 51(5), 1653-1658. doi: 10.2514/1.C032333